Electron Bremsstrahlung Studies and Track Based Alignment of the ATLAS Detector

Anthony Keith Morley

Submitted in total fulfilment of the requirements
of the degree of Doctor of Philosophy

March 2010

School of Physics
The University of Melbourne

Abstract

The ATLAS Experiment [1] is one of the major experiments located at the Large Hadron Collider (LHC) at CERN in Geneva, Switzerland [2]. In 2010, ATLAS is expected to start collecting data from proton-proton collisions at a 7 GeV centre-of-mass energy, increasing to the design energy of 14 TeV after 2012.

The LHC and ATLAS have ambitious physics goals which require detectors that are both accurate and efficient. In the centre of the detector, the reconstruction of charged particle tracks is performed by silicon and drift tube based detectors. To attain the physics goals of ATLAS the resolutions of the measured track parameters must not be degraded by more than 20% due to detector misalignments. Thus, the relative positions of the silicon detector elements have to be known to an accuracy of better than 10 micrometers.

This requirement can be achieved by track based alignment algorithm techniques. A global χ^2 track-based alignment method has been developed and implemented into the ATLAS software. The difficulties of aligning a system with over thirty thousand degrees of freedom have been successfully overcome. Simulation studies have shown that the algorithm will be able to align the full detector with collision data to the required accuracy.

In addition to detector misalignments, bremsstrahlung of electrons prior to the calorimeters will be detrimental to electron track reconstruction, and hence the physics discovery capabilities of ATLAS. A method of accounting for the affects of bremsstrahlung using calorimeter cluster position information has been implemented and tested using Monte Carlo simulation.

Declaration

This is to certify that

1. the thesis comprises only my original work towards the Ph.D. except where indicated in the Preface,
2. due acknowledgement has been made in the text to all other material used, .
3. the thesis is less than 100,000 words in length, exclusive of tables, maps, bibliographies and appendices.

Anthony Morley

Acknowledgements

Despite the 200 pages that follow this I am not a man of many words so I will keep this brief.

I sincerely thank Geoff Talyor for giving me the opportunity to work on the ATLAS experiment, and for his support and guidance. Elisabetta Barberio for her co-supervision, for pushing me to do more and the good advice throughout the whole period, as well as for introducing me to the ATLAS e/γ community. To Jeff McCallum for the sound advice.

My Melbourne colleagues who have made my postgraduate study both more productive and enjoyable Nadia, Antonio, Will, Uli, Anna, Viv, Dave, Rob, Bryn etc.

The many people at CERN who have help me along the years especially Daniel, Thomas, Marcus, Andi S., Andi W. and Wolfgang. To the alignment group for all of the support and Pawel, Carlos, Salva, Sergio, Jochen and Muge.

Those friends who have supported, entertained, shared rooms with and sometimes worked with at CERN I also thank you. The guys from Sydney that I have had the pleasure of living with Anthony, Aldo and Jason thanks for putting up with me. Also those I grew to know whilst in St Genis, in particular: Ellie, Tina, Martin, Matt, Niel, Adam, Carl, Denver and John and many others who made my time there fun, and memorable.

To my parents, thank you for all your help and support throughout the years. To Emma for being a great sister. Last but certainly not least, to Renee, despite the many periods of spacial separation you have stuck by me and helped me throughout. Words can't express my gratitude to you.

Preface

The ATLAS collaboration comprises more than 2000 scientists from around the world. In a collaboration this size, one cannot work alone on any project. The work presented in this thesis was undertaken within the ATLAS Inner Detector alignment, tracking and e/γ groups.

The work in Section 5.7 on the solutions to large systems of linear equations is the sole work of the author. The work presented in Chapter 6 on the toy model alignment studies is also the is the sole work of the author.

The work in the first half of Chapter 7 is a modified version of the paper [3] in which the author had direct involvement. In particular the author was responsible for Section 7.4. This work is represented in order to set the scene for the work from Section 7.6 which is the sole work of the author.

The work presented in Chapter 8 is an extension of the ideas of collaborators, with the implementation of the technique being the sole work of the author. The application of the technique to physics processes, in Chapter 9, is sole work of the author.

CONTENTS

LIST OF FIGURES

LIST OF TABLES

1

CHAPTER

INTRODUCTION

The Large Hadron Collider (LHC) [2] has been created to study the nature of physics at very high energies. By investigating a previously inaccessible energy regime, physicists hope not only to find the missing piece the Standard Model, the Higgs Boson, but also investigate theories beyond it. The LHC is powerful enough to probe space-time more deeply than ever before, allowing us to take the next step in the understanding of our Universe.

This dissertation is arranged in two parts with conclusions being drawn at the end of each. Central to both parts is the operation of the innermost detector of the ATLAS [1] detector, named the Inner Detector. The Inner Detector is responsible for the measurement of the trajectory and momentum of charged particles that traverse it.

The motivation of the LHC and ATLAS is given in Chapter 2. A basic description of the LHC and the ATLAS detector is given in Chapter 3. An overview of track fitting, a central topic of this thesis, is presented in Chapter 4. A method of aligning the ATLAS Inner Detector using tracks is presented in Chapter 5. This method is applied to a toy model in Chapter 6 and to the full ATLAS Inner Detector in Chapter 7.

Further to the alignment, a method for accounting for the effects of bremsstrahlung is presented in Chapter 8. Its application to the reconstruction of a number of mass resonances is shown in Chapter 9.

2

CHAPTER

THEORETICAL MOTIVATION

The desire to understand and explain the world around us has been the driving force behind human innovation and discovery. Fundamental physics has attempted to reduce nature to its most essential traits. Currently we know of four basic forces; the *gravitational force*, the *electromagnetic force*, the *weak nuclear force*, and the *strong nuclear force*.

Gravity is best described by Einstein's theory of General Relativity [4]. This theory describes gravity as a geometric property of space and time, linking the geometry of the universe to the gravitational force. Although gravity is the weakest of all the four basic forces it dominates at large distances.

The other three forces and all known particles are described by a very different formalism, known as Quantum Field Theory (QFT). It merges ideas from quantum mechanics, classical field theory, and special relativity. The theory that collectively describes the three forces is known as the *Standard Model* (SM) of particle physics [5]. Physicists seek a single theory that describes all forces but as of yet all attempts to incorporate gravity into the Standard Model have failed.

The highly predictive nature of both General Relativity and the Standard Model has allowed for these models to be tested to high precision. Both have survived all confrontations with precision measurements. Nonetheless, there is a range of reasons for the hypothesis of a theory more fundamental than the Standard Model, and it is hoped that this theory will provide a unified description of particles and their interactions.

This chapter describes the physics motivation of the LHC and the ATLAS experiment.

2.1. The Standard Model

The Standard Model (SM) provides the best known description of the fundamental particles and their interaction, neglecting gravity. As it not feasible to provide a full description of the model here, only of some of the most valuable features will be detailed.

The SM is a gauge QFT which describes the interaction of point-like particles with half-integer spin, called fermions, whose interactions are mediated by integer spin gauge bosons. It combines the two QFT theories of electroweak and strong interactions. The electroweak theory is already a unification of the relativistic electromagnetic theory, quantum electrodynamics (QED) and the theory of the weak interactions, as initially proposed by Glashow [6], Weinberg [7], and Salam [8]. The theory of the strong interaction is called quantum chromodynamics (QCD).

One of the essential components of the SM is the group of local gauge symmetries $\mathrm{SU}(3)_C \otimes \mathrm{SU}(2)_L \otimes \mathrm{U}(1)_Y$ [9]. In QED for instance, the requirement that the electron field be invariant to local gauge transformation leads to the introduction of a gauge field. This field transforms just as Maxwell's equations and describes a massless spin-1 field, the photon. In a similar manner, local gauge invariance requirements in the SM predict the W^+, W^- and Z bosons of the weak interaction and the gluons of the strong interaction.

An immediate problem with the theory is that the presence of any mass term violates the chiral symmetry $SU(2)_L$. Higgs suggested a solution to this problem [10, 11]: the gauge invariance could be *spontaneously broken* with the addition of a complex scalar field doublet ϕ, with Lagrangian

$$\mathscr{L}_{\text{Higgs}} = \left(\partial_\mu \phi\right)^\dagger \left(\partial^\mu \phi\right) - V(\phi), \tag{2.1}$$

where the potential

$$V(\phi) = \mu^2(\phi^\dagger\phi) + \lambda\left(\phi^\dagger\phi\right)^2 \tag{2.2}$$

is the key[1]. When $\mu^2 < 0$ there will be spontaneous symmetry breaking. The λ term describes a quartic self-interaction between the scalar fields and is required to be greater than zero to ensure that the vacuum is stable.

This mechanism allowed Glashow, Weinberg and Salam to propose a unified electroweak theory for leptons. Through the use of the Higgs mechanism, this theory allows for massive $W^\pm$ bosons and leptons, and a massive Z boson while retaining a massless photon. Additionally, a massive Higgs boson is predicted, where the only free parameter is the Higgs mass. The $W^\pm$ and Z bosons were discovered at the CERN SPS by the UA1 and UA2 experiments [12, 13]. The Higgs boson is the only SM particle which has not yet been discovered.

Despite not being able to predict the mass of the Higgs boson, the SM is able to constrain it. Unitarity of the SM requires that $m_h \lesssim 780\,GeV$, unless there is new physics below the TeV scale [14]. Additionally, the Higgs boson mass can be indirectly limited from a global electroweak fit to a broad range of experimental measurements. This fit strongly favours a light Higgs mass [15] (see Figure 2.1).

Searches for the Higgs boson have been conducted at the Large Electron-Positron Collider (LEP) at CERN and at the Tevatron collider at FNAL. LEP provided a lower limit for the Higgs boson mass of $m_h > 114.4$ GeV[16]. Tevatron has recently excluded a Higgs boson mass between 163 and 166 GeV[17], both at 95% confidence level. The exclusion results, together with a global fit to precision electroweak measurements are shown in Figure 2.1.

The fundamental matter particles of the SM are all fermions. There are three generations of coloured up-type and down-type quarks, and three families of charged and neutral leptons. The quarks come in three colours, as described in the quark model developed by Gell-Mann [18]. Table 2.1 summarises the fermions of the SM. The question of why the fundamental fermions come in three generations cannot be answered by the SM. Theorists hope to address this question with more a fundamental theory containing additional symmetries.

---

[1] This is in fact the minimal solution to the problem. More complex potentials can also lead to spontaneous symmetry break but in general they would require a number of Higgs particles

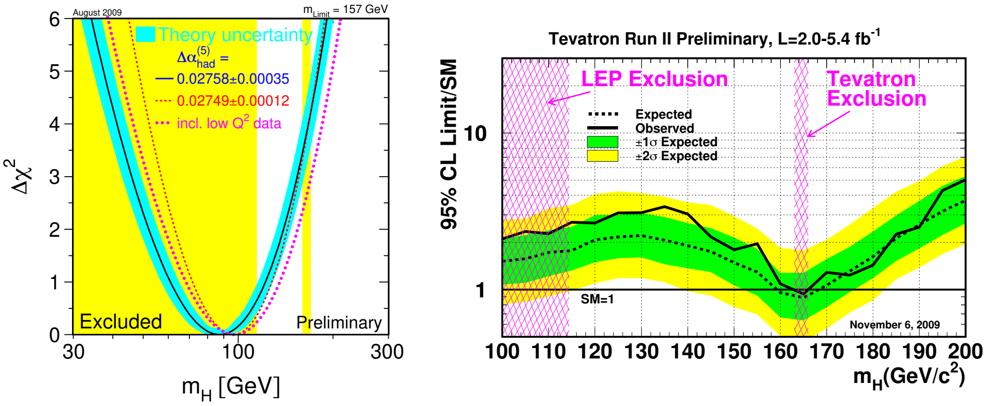

Figure 2.1.: Global fit to electroweak precision data (left) [15], and Higgs boson mass exclusions from LEP and Tevatron (right) [17].

Family	I	II	III
Leptons	$(e,\,\nu_e)_L$	$(\mu,\,\nu_\mu)_L$	$(\tau,\,\nu_\tau)_L$
	e_R	μ_R	τ_R
Quarks	$(u,\,d)_L$	$(c,\,s)_L$	$(t,\,b)_L$
(×3 colours)	$u_R,\,d_R$	$c_R,\,s_R$	$t_R,\,b_R$

Table 2.1.: The fundamental fermionic particles in the SM grouped according to family. Braces indicate weak isospin doublets. The subscripts L and R denote the left and right handed components respectively.

The quark mass eigenstates are not the weak eigenstates. The weak eigenstates are mixed states where a unitary 3×3 matrix, called the *Cabibbo-Kobayashi-Maskawa (CKM)* matrix [19, 20], governs the transformation between the weak basis and the mass basis states. The implications of this transformation are very important and result in the sole source of CP-violation in the SM. Finally, the requirement of local gauge invariance in QCD results in the eight massless spin-1 gluons of the strong force. The gauge symmetry group of QCD is $SU(3)_C$, describing three colour degrees of freedom.

In the formulation of the SM, it is also noteworthy that the $SU(2)$ and $SU(3)$ symmetry groups are non-abelian. An important consequence of this property is that the force carriers can self-couple, contributing to their self-energy and to the running of the coupling constants.

The QCD properties of confinement, the rapid increase of the strong force when trying to separate two coloured particles, and asymptotic freedom, where at very small distances coloured particles interact very weakly [21, 22], have very important consequences. Firstly they allow the use of perturbation theory for high-energy processes, but not in the low energy regime. When produced, coloured particles (gluons and quarks) will undergo “hadronisation”, where they group themselves into colour singlet objects which are hadrons or mesons. A collimated “jet” of hadrons and mesons is detected experimentally if the initial coloured particle, or “parton”, is generated with high momentum.

For completeness, the SM Lagrangian reads[23]

$$
\begin{aligned}
\mathscr{L}_{\mathrm{SM}} = \quad & \underbrace{-\frac{1}{4}W_a^{\mu\nu}W^a_{\mu\nu} - \frac{1}{4}B^{\mu\nu}B_{\mu\nu} - \frac{1}{4}G_a^{\mu\nu}G^a_{\mu\nu}}_{\text{Gauge bosons kinetic and self}-\text{interaction terms}} \\
+ \quad & \underbrace{\bar{L}\gamma^{\mu}\left(i\partial_{\mu} - \frac{1}{2}g\boldsymbol{\tau}_a W^a_{\mu} - \frac{1}{2}g'YB_{\mu}\right)L + \bar{R}\gamma^{\mu}\left(i\partial_{\mu} - \frac{1}{2}g'YB_{\mu}\right)R}_{\text{Fermions kinetic and electroweak interaction terms}} \\
+ \quad & \underbrace{\left|\left(i\partial_{\mu} - \frac{1}{2}g\tau_a W^a_{\mu} - \frac{1}{2}g'YB_{\mu}\right)\phi\right|^2 - \mu^2\phi^{\dagger}\phi - \lambda(\phi^{\dagger}\phi)^2}_{\text{Higgs doublet field } \phi \text{ with electroweak couplings}} \\
+ \quad & \underbrace{g_s G^a_{\mu}\bar{q}_i\gamma^{\mu}\mathbf{T}^a_{ij}q_j}_{\text{quark gluon interactions}} + \underbrace{\left(M_1\bar{L}\phi R + M_2\bar{L}\phi_c R + h.c.\right)}_{\text{Fermion mass and Higgs coupling terms}},
\end{aligned}
\tag{2.3}
$$

where L denotes left handed quark and lepton isospin doublets, R stands for right handed isospin singlets (quark or lepton), q is a quark field, (W, B, G) and (g, g', g_s) are the three gauge fields and the three coupling constants of the weak isospin, hypercharge, gluon fields. ϕ is the scalar Higgs field with μ and λ describing its potential. $(\tau, Y, \mathbf{T})$ are the symmetry group generators for the weak isospin, hypercharge, gluon fields. Finally M_1, M_2 contain the Higgs-Yukawa couplings to the fermions.

In its simplest version, the SM requires a total of 19 parameters: 9 fermion masses (quarks and charged leptons), 4 quark-mixing matrix (CKM) quantities, 2 gauge boson masses (for example the Z and Higgs boson masses), 3 coupling constants, and 1 strong CP parameter.

The SM has been extensively tested with many independent measurements and to date no inconsistencies have been found. Further tests of the SM will be performed at the LHC. For example, a precise measurement of the W boson mass will put in place a more stringent constraint on the mass of the Higgs. The measurement of the W mass will require a detailed knowledge of the detector. In particular the alignment of the Inner Detector of ATLAS will be required to be known to the micron level[24]. The alignment of the ATLAS Inner Detector is the focus of the first half of this thesis.

2.2. Phenomenology

The SM theory completely describes the basic interactions of the known fundamental particles and is very predictive. Experimental particle physics measures quantities such as cross sections, or kinematic variables. At hadron colliders, the calculation of these observables requires, in addition to the theoretical framework of the SM, two major phenomenological additions. These are required in the main part because protons are composite objects. Also, because QCD confinement causes perturbation theory to be inapplicable at low energies it cannot be used to make predictions in QCD.

The two additions are:

1. *Parton density functions* (PDF) that describe the probability of a given parton (quark and gluons) inside a proton, as a function of momentum transfer (Q^2) and the Bjorken x scaling variable [25].
2. *Fragmentation* and *Hadronisation* of the coloured particles. These non-perturbative processes are described by phenomenological shower models which have been tuned to agree with measured properties.

When the SM is augmented with PDFs and shower generators it allows the production cross sections as a function of centre-of-mass (CM) energy to be predicted for various physics processes as shown in Figure 2.2.

The total proton-proton ($p-p$) cross section at a CM energy of 14 TeV is predicted to be 102 mb [27]. This is split into elastic (23 mb) and inelastic (79 mb) parts. The inelastic cross section is strongly dominated by QCD processes, while the expected Higgs cross section is many orders of magnitude smaller.

QCD processes produce an environment at the LHC dominated by hadrons, making leptonic decay channels of particles, into electrons, muons and tauons, vital for accurate identification of the underlying physics process. Improving the reconstruction of electrons is the focus of the latter part of this thesis, with the early part of this focusing on the alignment of the detector.

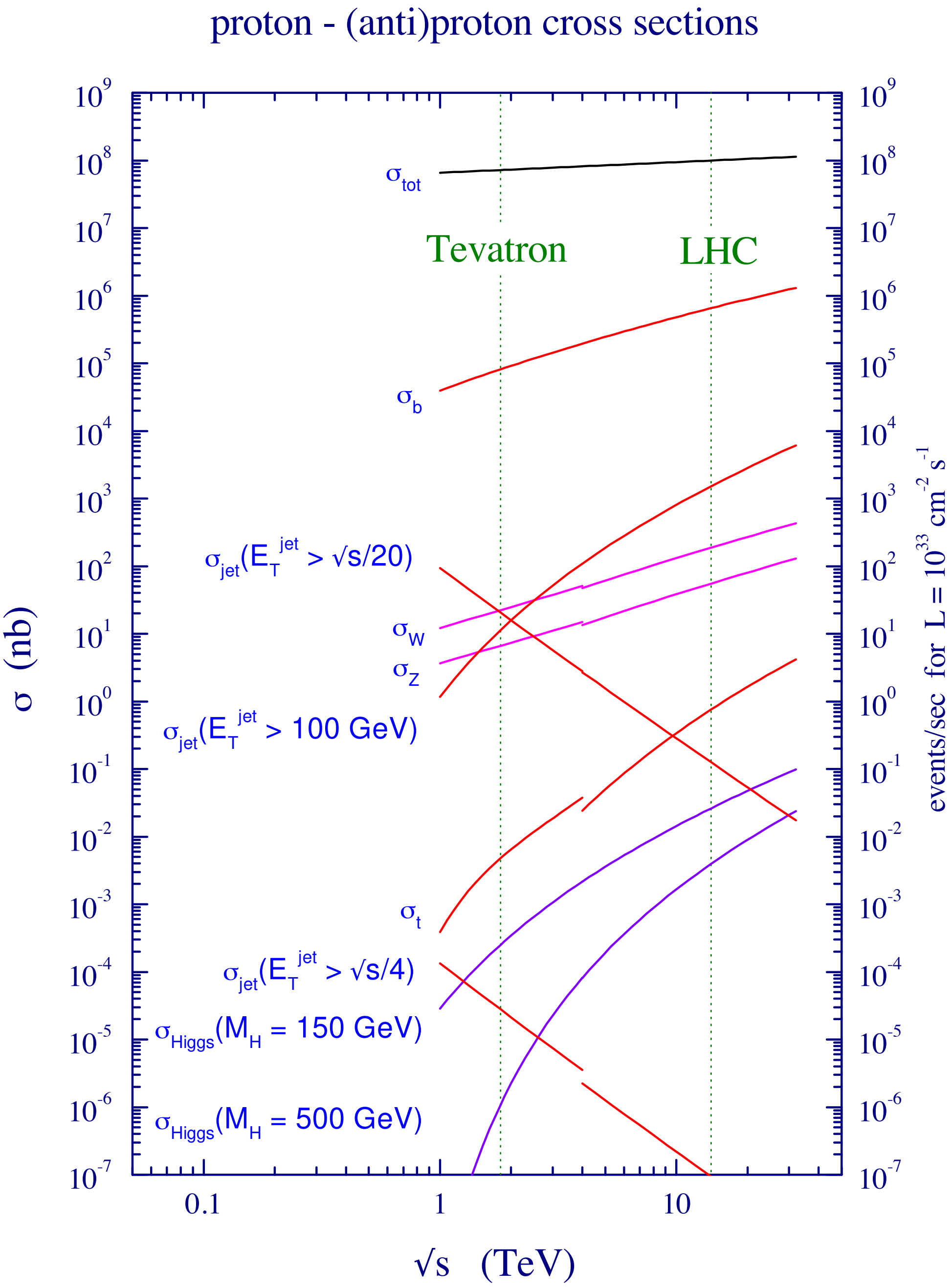

Figure 2.2.: Expected production cross sections and event rates (for $L = 10^{33}\ cm^{-2}s^{-1}$) for several SM physics processes at p–(anti)p colliders, as a function of the centre-of-mass energy [26]. The discontinuity at $\sqrt{s} \approx 4\,\text{TeV}$ indicates the transition from $p - \bar{p}$ to $p - p$

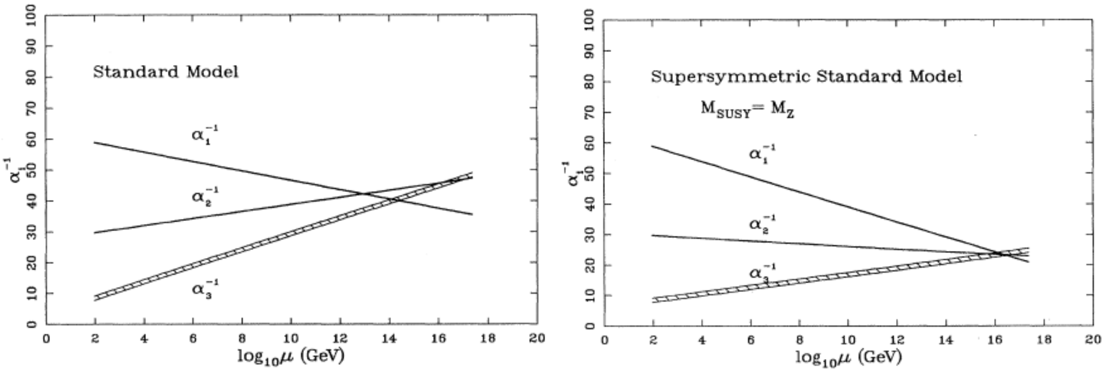

Figure 2.3.: The running of the coupling constants in the SM (left) and the Supersymmetric SM (right) [29]. The three gauge couplings correspond to the $U(1)_Y \otimes SU(2)_L \otimes SU(3)_C$ symmetries: α_1 (electromagnetic/hypercharge), α_2 (weak), α_3 (strong).

2.3. Beyond the Standard Model

As of yet there has been no clear experimental evidence of physics beyond the SM. However, it is evident that the SM needs to be extended to describe physics at higher energy scales. For example, a new model will be required at the energy scale where quantum gravitational effects become important. This energy scale is the so-called Planck scale, $M_{Planck} = \sqrt{\hbar c / G_{\text{Newton}}} \approx 10^{19}$ GeV. This energy scale is well beyond the reach of the LHC, but at the TeV scale there are also reasons for the emergence of new physics. For example in the SM the scattering amplitudes of vector bosons violate unitarity for a Higgs Boson mass $> 870\ GeV$ [28]. If a light Higgs Boson does not exist, some new physics must be present.

There are a number of other reasons which suggests physics beyond-SM:

- *Grand unification* of the gauge couplings. Although the strong interaction has been incorporated into the SM, the strong force has not merged with the electromagetic and weak forces. Estimates of the three SM gauge couplings at high energy suggest that they will not merge, but come close at 10^{15} GeV [29] (see Figure 2.3). The fact that they do not merge at high energy is unappealing from a theoretical standpoint, as it is contrary to the idea of a grand unified theory (GUT). The aim of a GUT is to encompass the SM theory within a symmetry group and thereby introduce new symmetries to reduce the number of free parameters. To date, no widely accepted GUT theory has been produced.

- The *Gauge hierarchy problem* is the question of why the Higgs boson is expected to be so much lighter than the Planck mass or the grand unification energy.

  The bare Higgs mass will receive large quantum loop corrections from virtual effects of every particle that couples directly or indirectly to the Higgs field. These quantum corrections are quadratically divergent [28]. All of the fermions of the SM play a role in the quadratically divergent correction with the largest contribution coming from the top quark (as it is the heaviest). If the cut-off to these corrections (which sets the scale for new physics), Λ_{UV}, is set at the GUT scale ($\sim 10^{16}\, GeV$) or Planck scale ($\sim 10^{19}\, GeV$), the huge discrepancy between the cut-off and the Higgs mass scale will require what is known as *fine tuning* to keep a light and stable Higgs mass.

  To ensure vacuum stability and that the theory is non trivial; upper and lower limits can be placed on m_h depending on the value of Λ_{UV}, for example $m_h < 180\, GeV$ if $\Lambda_{\text{UV}} = 10^{19}\, GeV$ [30].

  It should be noted that there is no reason that fine tuning is not in fact what keeps the Higgs mass stable. In addition fine tuning would suggest that there is no new physics between the energy scale of the SM and that of the cut-off.

- *Dark matter* and *dark energy*. Over the years much evidence for the existence of dark matter has been accumulated. These include the rotational speed of spiral galaxies [31], discrepancies between gravitational potential mater density derived from gravitational lensing and observable matter [32], and anisotropy measurements of the cosmic microwave background [33]. Many dark matter candidates have been proposed and most have been discarded. However, all remaining candidates can account for only a small fraction of dark matter present in the universe. As it is unlikely that many different factors are contributing, the most likely scenario is that a new unknown fundamental particle is responsible for dark matter.

  Dark matter particles produced in the big bang which survive until today are generically called weakly interacting massive particles (WIMPS). Any such particle are beyond the SM.

- There are questions of why there are so many different types of matter particles, why the quark and neutrino flavours mix in the way they do, and why the matter particles are grouped in three generations. All three are present in the SM but there is no intrinsic reason for them. Idealistically it would be hoped that the model would explain the reason why there so many particles.

- Matter-Antimatter Asymmetry: Dirac predicted the existence of antimatter particles with the same masses as conventional particles, but opposite internal properties such as electric charges. It has been predicted and verified experimentally that every known kind of particle has a corresponding antiparticle. However, it is puzzling that the universe does not have equal amounts of matter and antimatter. Moreover there is no evidence that there are any major concentrations of antimatter in the universe. To account for this disparity either the universe began with a small preference for matter, or the universe was originally perfectly symmetric, but somehow a set of phenomena contributed to a small imbalance in favour of matter over time. *Baryogenesis and leptogenesis* are the proposed processes that created the asymmetry between baryons and the asymmetry between leptons in the early universe resulting in the observed dominance of matter over antimatter. Sakharov proposed three conditions that are necessary for the baryogenesis[34]: Baryon number violation, C- and CP-violation, as well as the departure from thermodynamic equilibrium. The first, and to a lesser extent the second condition are difficult to realise in the SM with the required rates and suggest physics beyond the SM.

The significance of these problems varies. The gauge hierarchy is essentially not a flaw in the SM but rather a disturbing sensitivity of the Higgs potential to new physics in almost any imaginable way. Possible solutions include [35]:

- the existence of new physics at energies not much above the electroweak energy scale which would regularise the quadratic divergences.
- a cut-off Λ_{UV} which is much closer to the electroweak scale than currently anticipated.
- the SM is simply finely tuned.

Supersymmetry is one of the popular and attractive scenarios for physics beyond the SM. It solves the hierarchy problem through cancellation between the various contributions (known as regularisation by new physics). All SM fermion correction terms are accompanied by corresponding scalar terms, with opposite sign, from supersymmtery. To avoid the need for fine tuning, the masses of the supersymmetric particles need to be less than approximately a few TeV[36].

The additional supersymmetric particles can alter the three gauge couplings in such a way that their strengths merge at approximately $10^{16}\,GeV$. Figure 2.3 compares the SM with the supersymmetry predictions for the running of the gauge couplings.

Finally, supersymmetry can provide a candidate for dark matter. The lightest supersymmetric particle would, in many supersymmetry models, provide a suitable WIMP candidate for dark matter. In order to generate the observed relic dark matter density, the mass of such a WIMP should not exceed $\mathcal{O}(1\,TeV)$[37].

Another proposed theory for dealing with the hierarchy problem is that there are additional dimensions of space. In addition to the three spatial dimensions that we know, postulated additional dimensions are curled up so small that they are invisible. This idea is not new (first proposed by Kaluza and Klein over 80 years ago), but has been gaining favour in recent years when it was realised that string theory predicts the existence of extra dimensions of space[38]. According to string theory, elementary particles are not point like, but are objects extended along one dimension (a string) or are membranes with more dimensions[39].

Until only recently string theory was thought to be a very elegant model but had no physical manifestation. It was then realised that at least some of the new dimensions might be much larger than originally believed and possibly observable at the LHC. It is speculated that gravity is strong when extra dimensions appear and according to some variations of string theory, microscopic black holes might be produced by the LHC[40]. However, they would be short-lived, decaying rapidly through thermal "Hawking" radiation.

To determine the true solutions to these problems further evidence and hence experimentation is required. The LHC is now the key project capable of producing and searching for the Higgs and physics beyond the SM.

3

CHAPTER

THE LHC AND THE ATLAS EXPERIMENT

The construction of the Large Hadron Collider (LHC) and its detectors has been completed and both machine and detectors are now ready for operation. Low energy collisions began at the LHC in November 2009.

This chapter provides a brief overview of the LHC machine and the ATLAS detector. Section 3.1 details the machine parameters and the effects of minimum bias and pile-up. Section 3.2 introduces the ATLAS detector, the motivations for the chosen detector design, and lists the key performance goals.

3.1. The Large Hadron Collider

The Large Hadron Collider, based at CERN in Geneva, is designed to provide proton–proton (p–p) collisions at a centre-of-mass energy of 14 TeV, with a luminosity of $10^{34}\,cm^{-2}\,s^{-1}$ and a proton bunch-crossing rate of 40 MHz. The LHC has also been designed to collide heavy ions (lead nuclei), with an energy of 2.8 TeV per nucleon at a peak luminosity of $10^{27}\ cm^{-2}\,s^{-1}$.

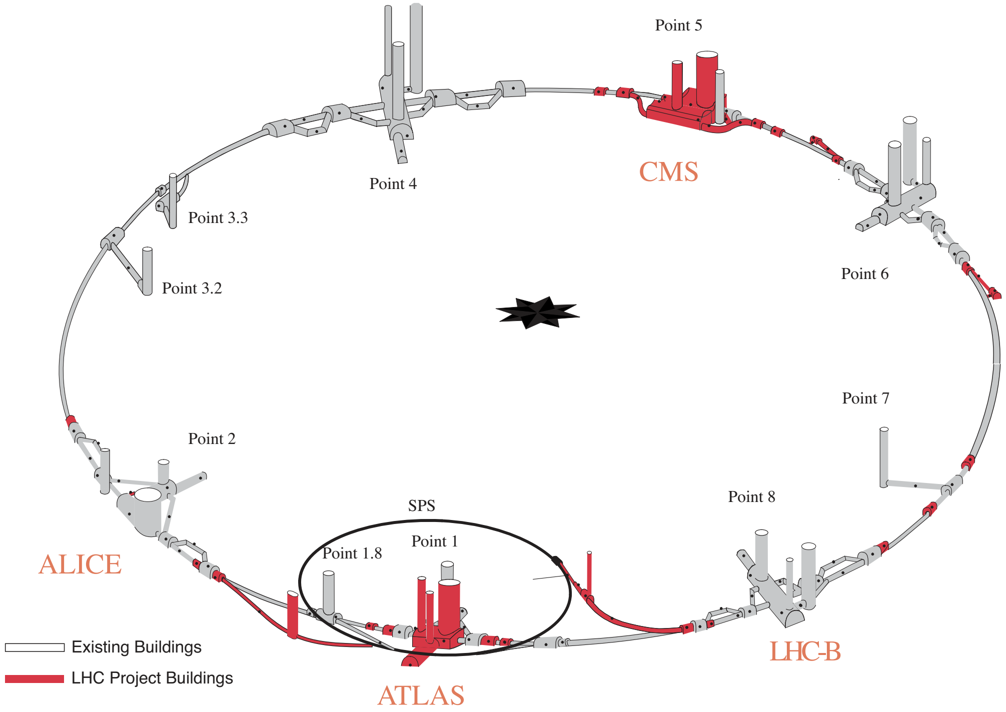

Figure 3.1.: Civil engineering structure of the LHC tunnel and underground structures housing the detectors [2]. Structure originally from LEP are shown in white while new structures for the LHC are in red.

While a brief overview is given here, a detailed description of the design of the LHC machine can be found in [2], as well as in the Design Reports [41–43].

The construction of the accelerator made use of the extensive infrastructure already in place at CERN in order to save costs. As such the LHC ring has been installed in the 26.7 km long and 3.7 m wide (in the arcs) tunnel that was constructed earlier for the CERN Large Electron–Positron (LEP) machine. It lies between 45 m and 170 m below the surface on a plane inclined at 1.4%.

Driven by physics aims, namely the discovery of rare processes, the LHC has been designed to provide a high luminosity at high energy. The rate at which a given physics process is generated is given by $R = L\sigma$, where L is the machine luminosity and σ is the cross section of the physics process in question. The cross section is a purely physics quantity dependant upon the collision energy, whereas the luminosity is entirely dependent on the machine parameters. Hence the study of rare processes requires high beam energies and high beam currents.

Beam parameters	
Collision type	proton–proton
Centre-of-mass energy	14 TeV
Bunch-crossing rate	40.08 MHz
Number of bunches (N_B)	2808
Number of particles per bunch (N_p)	$1.15 \cdot 10^{11}$
Stored energy per beam	362 MJ
Full crossing angle (θ_C)	285 μrad
Luminosity related parameters	
RMS bunch length (σ_z)	7.55 cm
RMS beam size (σ_t)	16.7 μm
Nominal peak luminosity L	10^{34}

Table 3.1.: Summary of the key LHC parameters[41]. The parameters θ_C, σ_z, σ_t, F, and L displayed are specific to the ATLAS and CMS interaction points.

The luminosity of a collider can be approximated by

$$L = \frac{n_b N_p^2 f_{rev}}{4\pi\sigma_t^2},$$

where n_b denotes the number of bunches, f_{rev} is the revolution frequency, N_p is the number of particles per bunch, and σ_t is the transverse beam size at the interaction point (IP). The crossing angle θ_C of the beams at the IP reduces the luminosity by a geometric factor (F), which at small crossing angles be approximated to

$$F \approx \left(1 + \left(\frac{\theta_C \sigma_z}{2\sigma_t}\right)^2\right)^{-1/2},$$

where σ_z is the longitudinal beam size at the IP. Table 3.1 lists the key parameters of the LHC accelerator.

The LHC accelerator is a two-ring, superconducting, hadron accelerator and collider. The majority of the LHC is comprised of 1232 superconducting dipole magnets which bend the beams of charged particles around the LHC ring. The magnets are twin bore, consisting of two sets of coils and beam channels within the same mechanical structure and cryostat. This design was required to accelerate two beams of equally charged particles in opposite directions within a small area. The dipole magnets can generate magnetic fields of up to 8.33 T. The coils are made of niobium-titanium (NbTi), a material that is superconducting at 1.9 K. In addition to the dipole magnets there are also 392 quadrupole magnets for beam focusing and beam corrections and also sextupole, octupole and decapole magnets which are mainly used to compensate for systematic non-linearities.

The LHC machine is supplied with protons or heavy ions from the existing accelerator complex at CERN. This comprises both linear and ring accelerators, which have all been upgraded to meet the demanding requirements of the LHC to provide a proton injection energy of 450 GeV into the main LHC ring.

The LHC will provide collisions at four interaction points (IPs). At each IP a detector is located (see Figure 3.1):

- *ATLAS* (A Toroidal LHC Apparatus) [1] is a general-purpose detector located at point 1 on the LHC (see also Section 3.2);
- *CMS* (Compact Muon Solenoid) [44] is a general-purpose detector and located at point 5;
- *LHCb* [45] is a dedicated detector for precision measurements of CP violation and rare decays of B hadrons and is located at point 8;
- *ALICE* (A Large Ion Collider Experiment) [46] is a general-purpose, heavy-ion detector which focuses on QCD and the strong-interaction sector of the SM at very high energy densities, located at point 2.

In addition to the main experiments the LHC accommodates two smaller experiments, located some distance from the IPs:

- *LHCf* [47] is an experiment dedicated to the measurement of neutral particles emitted in the very forward region of LHC collisions;
- *TOTEM* [48] is an experiment to measure the total p–p cross section with a luminosity independent method and study elastic and diffractive scattering at the LHC.

The experimental conditions produced by the proton–proton collisions of the LHC are quite challenging. As the total inelastic p–p cross section at the nominal LHC energy ($\sqrt{s} = 14$ TeV) is expected to be approximately 79 mb [27], the expected p–p interaction rate is nearly 1 GHz at high luminosity ($L = 10^{34}\, cm^{-2}\ s^{-1}$) which translates to an average of 25 interactions per bunch-crossing [49]. The vast majority of these interactions, however, are soft and generate little transverse momentum (p_T) as they stem from long-range p–p interactions.

So called "Minimum-bias" events, make up the majority of events produced by the LHC and are dominated by the soft interactions mentioned above (due to their huge abundance), but hard interactions can contribute. Experimentally, the definition of minimum-bias events depends on the experiments trigger, however it is usually associated to non-single-diffractive events, given by $\sigma_{\text{NSD}} = \sigma_{\text{inel.}} - \sigma_{\text{SD}} = 65\,\text{mb}$ [50].

The soft interactions which are found in every event, can be seen as noise superimposed upon all events. Furthermore, if a detector element has a readout latency that exceeds the bunch spacing (25 *ns* at the LHC) it will result in detector signals arising from previous bunch-crossings in the current event. The combination of both effects form what is known as called "pile-up". The effects of pile-up have had a strong impact on the design of all LHC detectors and will influence physics analyses.

As the LHC is generally endeavouring to find high mass particles the events that are of interest will involve a hard scattering. However, with every hard scattering there is an associated underlying event which is called the "soft" part of the event. Unlike minimum-bias interactions, the underlying event arises from the same p–p interaction as the hard scattering of interest. The typical definition of the underlying event is that it is everything that arises from the p–p collision except the hard scattered particles.

3.2. The ATLAS Detector

The following section introduces the ATLAS detector and its main sub-detectors. A comprehensive description of ATLAS can be found in [1] as well as in the Technical Design Reports (TDRs) for the overall technical design [51]. Details of the expected performance of ATLAS can be found in [49].

The design of the ATLAS detector has been driven by its main physics goals: the search for the origin of electroweak symmetry breaking and the search for new physics beyond the SM. These physics studies coupled with the challenging conditions at the LHC determine the requirements for the performance of ATLAS [49, 51].

The high rate of collisions at the LHC requires that event selection (triggering) is very fast, with precise timing and low latency. Given that the interaction rate, at peak luminosity, is expected to be about $\sim$ 1 GHz (40 MHz $\times$ $\sim$ 25 interaction per bunch crossing) the initial trigger (Level 1) will be required to have efficient pattern recognition to reduce the data rate to a more manageable rate (75 kHz). Two next trigger levels are the Level-2 trigger and the event filter and are collectively known as the High Level Trigger (HLT). The HLT continues the processing and selection, prior to the event being stored onto disk (200 Hz) (see Section 3.2.6 for more details on the Trigger). The number of events being written to disk coupled with an events size $\mathcal{O}$(1.5 MB/event) results in a data rate of $\sim$ 300 MB/s. This requires powerful data processing and distributed analysis.

At full luminosity the charged particle multiplicity in a bunch crossing is expected to be $\mathcal{O}$(1000). In order for the detector to be able to discriminate between events the detector must have a very highly granulated tracking detector.

The high flux of particles through the detector ensures that the rate of irradiation over the lifetime of the experiments at the LHC is phenomenal ($5 \times 10^{14}\,\mathrm{n_{eq}/cm^2}$ over 10 year). This high dose requires that all components of the detector are radiation hard and all electronics are radiation tolerant.

In addition to the proton–proton collisions there will also be a high background rate from beam halo, neutron and beam-gas collisions. These mainly effect the muon detector system, requiring that the detector timing is precise, pattern recognition is redundant and the detector is radiation hard.

Table 3.2 summarises the ATLAS detectors key performance goals [1]. The overall ATLAS detector layout is shown in Figure 3.2. With a diameter of 25 m, a length 44 m and a total weight of approximately 7000 tonnes, ATLAS is the world's largest collider experiment. In the following sections, the main detectors and components of the ATLAS experiment are introduced.

3.2.1. ATLAS coordinates system

Within ATLAS there are a number of different right-handed coordinate frames being used. Of particular importance to the alignment and tracking are the global frame, the local module frame and the measurement frame [52–54].

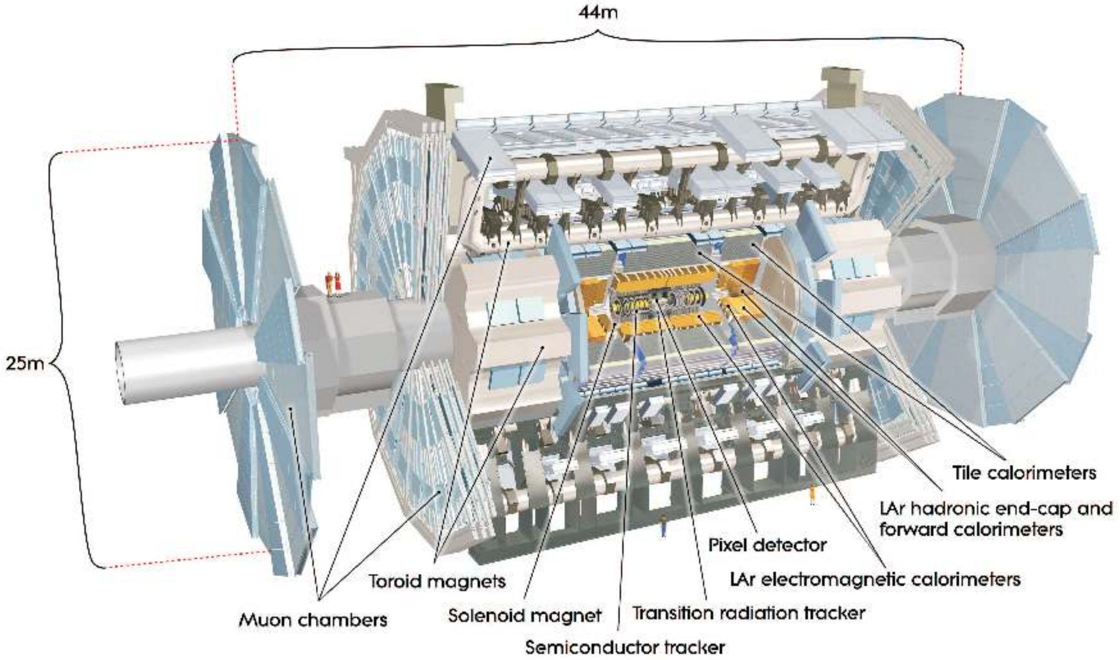

Figure 3.2.: Cut-away view of the ATLAS detector[1].

Detector component	Required resolution	η coverage
Tracking	$\sigma_{p_T}/p_T = 0.05\% \oplus 1\%$	±2.5
EM calorimeter	$\sigma_E/E = 10\%/\sqrt{E} \oplus 0.7\%$	±3.2
Hadronic calorimeter (jets)		
barrel and end-cap	$\sigma_E/E = 50\%/\sqrt{E} \oplus 3\%$	±3.2
forward	$\sigma_E/E = 100\%/\sqrt{E} \oplus 10\%$	$3.1 < \lvert\eta\rvert < 4.9$
Muon spectrometer	$\sigma_{p_T}/p_T = 10\%$ at $p_T = 1$ TeV	±2.7

Table 3.2.: Summary of the key ATLAS performance goals[1]. The units for Energy, E, and Transverse momentum, p_T, are in GeV. Note that for high-p_T muons, the muon spectrometer can work independently of the Inner Detector system.

ATLAS Global Frame

The ATLAS global frame (x, y, z) is the frame in which the origin lies at the nominal IP of the proton-proton collisions. This origin is also the nominal center of the ATLAS detector as shown in Figure 3.3, where the z-axis is along the beam direction, the y-axis points to the surface and the x-axis is the horizontal axis pointing towards the centre of the LHC tunnel.

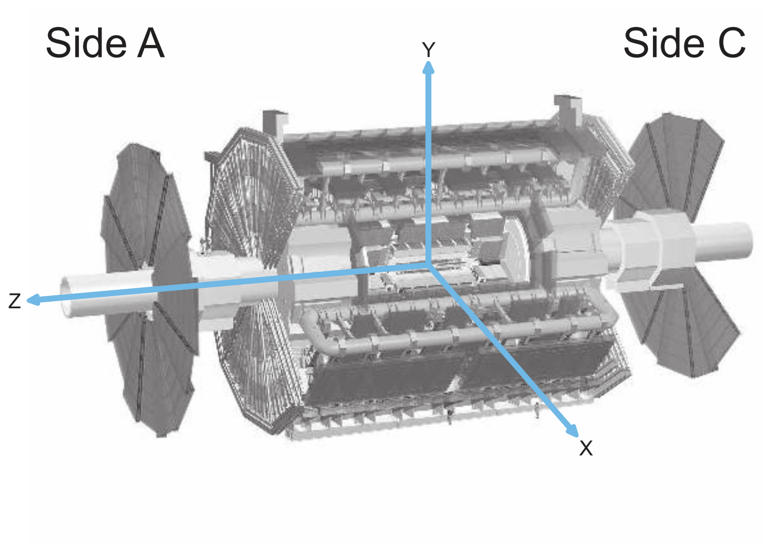

Figure 3.3.: Global coordinate frame of ATLAS.

In this coordinate frame the $+z$ direction (also known as side-A) points in the direction of the nominal solenoid B-field. In the global frame a cylindrical coordinate system is created where the polar angle θ is measured from the positive z-axis covering the range $\theta \in [0, \pi)$, the azimuthal angle ϕ is measured in the x-y-plane so that the positive x-axis has an azimuthal angle of $\phi = 0$ and the positive y-axis an azimuthal angle of $\phi = \pi/2$, when ϕ covers the range $\phi \in [0, 2\pi)$. The azimuthal and polar angles can be calculated via the momentum components using the following relations

$$\tan\phi = \frac{p_y}{p_x}, \tag{3.1}$$

$$\cot\theta = \frac{p_z}{p_T}, \tag{3.2}$$

where p_x , p_y and p_z denote the components of the momentum corresponding to the global frame and p_T is the transverse momentum with respect to the beam axis, i.e. $p_T = \sqrt{p_x^2 + p_y^2} = p \sin\theta$.

The pseudorapidity, η, is defined to be

$$\eta = -\log_e\left(\tan\left(\frac{\theta}{2}\right)\right). \tag{3.3}$$

Local Module Frame

The local module frame (x', y' and z') is different for each detector element. The origin is placed in the centre of each detector module (The various modules that make up the Inner Detector of ATLAS are the pixel, SCT and TRT modules and are described in Section 3.2.3). The x'-axis is parallel to the most sensitive measurement direction within the modules. For the pixel wafers, the x'-axis across the direction of the short side of the modules, and in the direction crossing the strips and the straws for the SCT and for the TRT, respectively. The y'-axis parallel to long side of modules is in the pixel wafer, parallel to the strip direction on the non-stereo side in the SCT and parallel to the straw direction in the TRT.

Therefore for all Inner Detector module types, in the barrel part of the detector, the y'-axis in the module frame is always parallel to the z-axis of the global reference frame and in the end-cap regions y'-axis is radial. The x'-axis is in the $r\phi$ direction in the global frame. Finally in this frame the z'-axis is perpendicular to the module plane in all cases and it is orientated to give a right-handed system. This is going outward radially in the barrel and in the negative global z-axis direction in the end-cap.

Measurement Frame

The measurement frame is the coordinate frame in which the residuals are calculated [55]. For the pixel detector the measurement frame is equal to the module frame. For the SCT there are two separate sides to the wafer that have are slight stereo rotation, and as a result each SCT module has two separate measurement frames. Both frames are defined such that the y-axis is aligned parallel to the strip direction, and the x axis is perpendicular to the strips. The TRT measurement frame has the x-axis perpendicular to both track and straw, the y-axis parallel to the straw and the

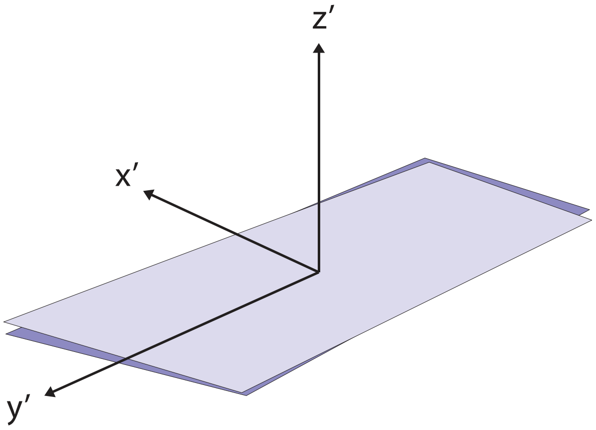

Figure 3.4.: Schematic diagram of the local coordinate frame.

z-axis perpendicular to x and y. In this case, the origin is the middle of the straw wire. Defining the TRT frame in this manner is motivated by the fact that the drift time of the TRT hit is a measurement of the distance between track and wire, i.e. $|x|$ in the measurement frame.

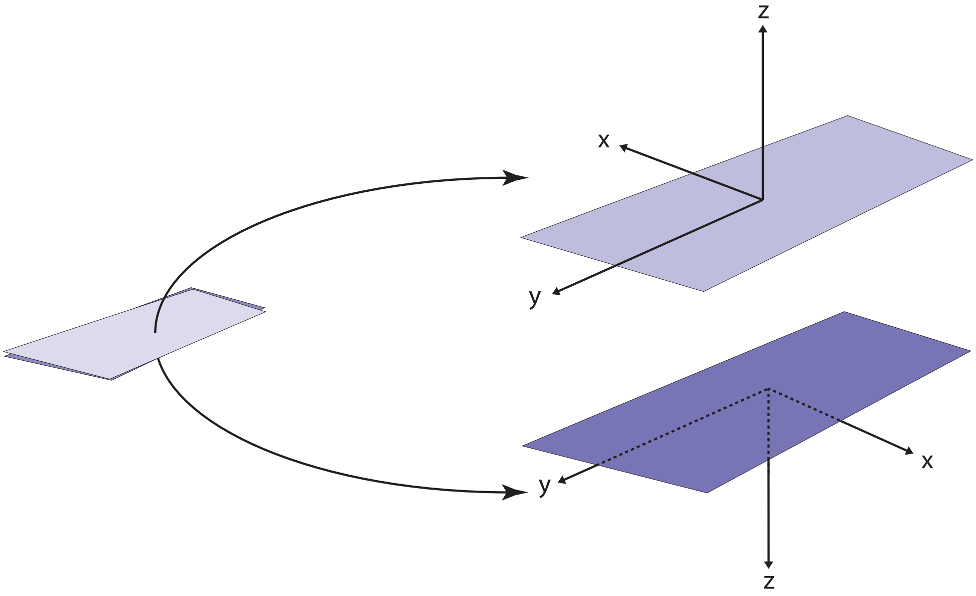

Figure 3.5.: Schematic diagram of the measurement frame for a SCT. The two sides of the module can been seen due the small stereo angle between them.

3.2.2. Magnet System

On of they design elements of the ATLAS detector is its magnet system, shown in Figure 3.6. Consisting of three large air-core toroids (two end-caps and one barrel) and a solenoid, the magnet system has been one of ATLAS' most challenging engineering accomplishments due to its unusual configuration and large size[56].

The toroidal design of the muon magnet system is one the unique aspects of the ATLAS detector. As one of the performance goals of ATLAS is to measure muon momentum to within 10% at 1 TeV, a strong magnetic field over a large volume is required. Each of the three toroids consist of eight superconducting coils powered by a 20.5 kA power supply[57, 58]. The barrel toroid coils are individually housed in their own cryostats, while the each end-cap toroid is housed in one a large cryostat. The barrel toroid system weights 830 tonnes and is 25.3 m in length and has an inner and outer diameter of 9.4 m and 20.1 m respectively. The two end-cap toroids are each 5 m in length and have an outer diameter of 10.7 m and weigh 240 tonnes.

The magnetic field of the toroidal magnet system is quite inhomogeneous as bending power is lower in the transition region where the magnets overlap. However, the bending power of the magnets is considerable; $\int Bdl$ is 1.5 to 5.5 Tm in the range $|\eta| < 1.4$ (barrel toroid) and approximately 1 to 7.5 Tm in the region $1.6 < |\eta| < 2.7$ (end-cap toroids).

The central solenoid is designed to provide a 2 T axial magnetic field for the Inner Detector and is powered by an $\sim$ 8 kA power supply[59]. Located in between the electromagnetic calorimeter and the Inner Detector, it has been designed to minimise the upstream material which degrades the performance of the electromagnetic calorimeter. As such, it requires that the solenoid windings and the electromagnetic calorimeter share a common vacuum vessel. The magnetic flux of the solenoid is returned in the steel of the hadronic calorimeter and its support structure. The inner (outer) diameter of the solenoid is 2.46 m (2.56 m), the axial length is 5.8 m and weighs 5.4 tonnes.

The solenoid is shorter than the ID itself, which makes the field quite inhomogeneous in the forward region. Figure 3.7 shows the z and R components of the magnetic field (referred as B_z and B_R) as a function of z and radius (R). One can see that the z component of the field drops from 2 T to 1 T at the end of the tracker, while the R component reaches up to 0.6 T in the forward region. The inhomogenity of

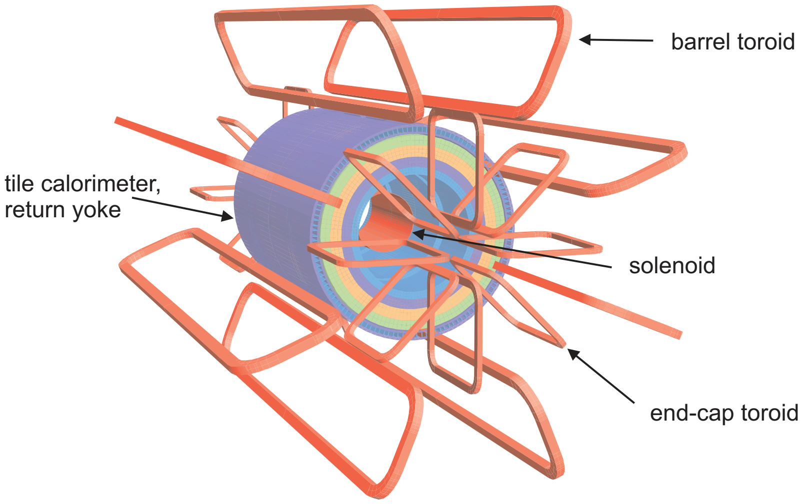

Figure 3.6.: Arrangement of the ATLAS magnet windings and the tile calorimeter steel [1]. The solenoid windings are situated inside the calorimeter volume. The tile calorimeter is modelled by four layers with different magnetic properties, plus an outside return yoke.

the magnetic field at the end-caps enforces the use of a field map in simulation and reconstruction.

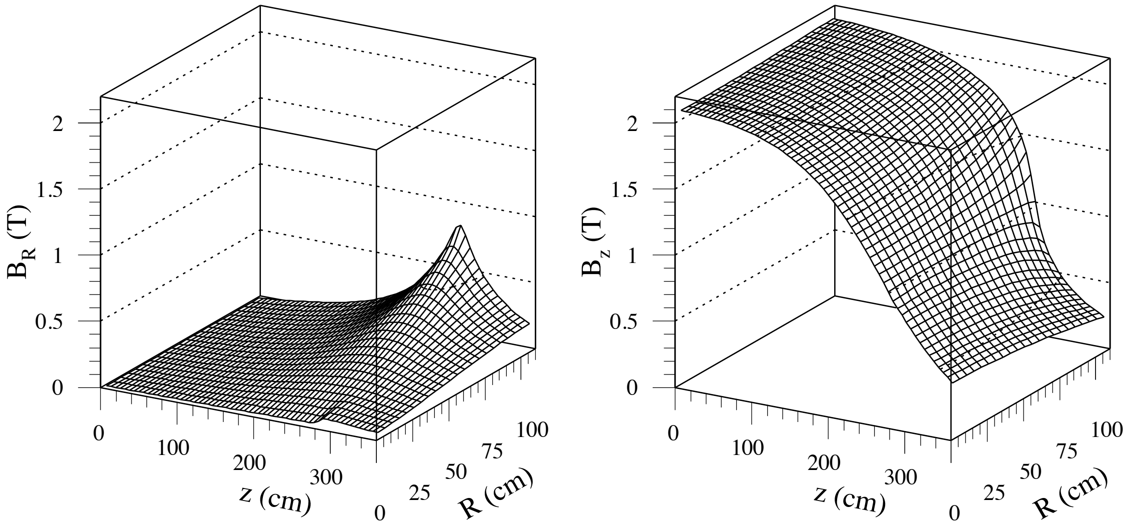

(a) B_R component **(b)** B_z component

Figure 3.7.: B_R and B_z fields of the solenoid as a function of R and z respectively [49].

In the ATLAS solenoid magnet, the integral $\int Bdl$ drops from about 2 Tm at $|\eta| = 0$ to about 0.5 Tm at $|\eta| = 2.5$, for two reasons: the field strength in the end-caps is lower than in the barrel, and tracks in the very forward region ($|\eta| > 1.85$) exit the tracker before reaching the solenoid.

The resolution of the reconstructed momentum of particles in the Inner Detector is directly related to the bending power of the magnet. The reconstructed momentum p is related to the magnetic field by

$$p = 0.299792458\, B\rho, \tag{3.4}$$

where p is measured in GeV/c, B the value of the magnetic field given in Tesla and ρ the radius of the track curvature given in meter. As such, for a particle to escape the solenoid field it must have a momentum in the transverse direction of at least ≈ 0.66 GeV/c.

As the transverse momentum of a particle increases it will be deflected less by an axial magnetic field. Combining this with the fact that the detector modules have a finite resolution provides a theoretical limit on the maximum momentum that can be measured.

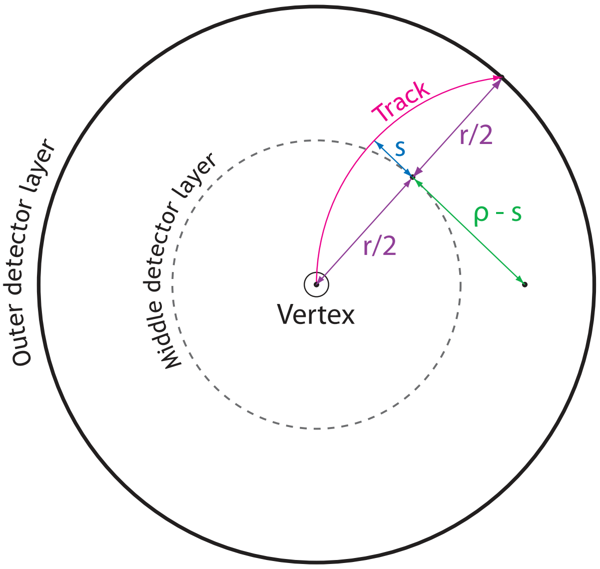

Figure 3.8.: Sagitta definition of a track in the x-y plane (global frame).

The sagitta, s, describes the maximal deflection of the track from a purely linear path (see Figure 3.8). A chord, constructed in the transverse plane, connects the vertex point with the track position at the outer most point of the detector. The sagitta is defined to be the distance between the midpoint of the chord and the arc of the trajectory. The relationship between s and ρ can be obtained using Pythagoras Theorem

$$\rho = \frac{(r/2)^2 + s^2}{2s}. \tag{3.5}$$

Given that the detector radius is 1.1 m, and if we assume that the smallest statistically significant sagitta we can measure is 50 μm, an upper limit of $\sim 2TeV$ is determined.

3.2.3. Inner Detector

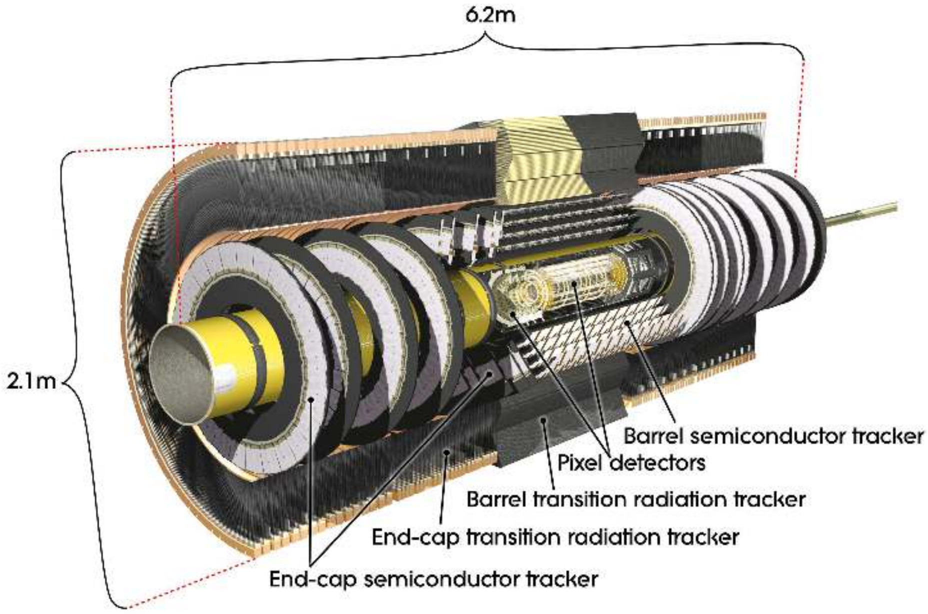

Figure 3.9.: Cut-away view of the ATLAS Inner Detector[1].

The ATLAS Inner Detector (ID), immersed in the 2 T magnetic field generated by the central solenoid, is designed to provide robust pattern recognition, excellent momentum resolution and accurate vertex measurements for charged particles above a nominal p_T threshold of 0.5 GeV. The Inner Detector is able to provide precision measurements over a range of $|\eta| < 2.5$ which is matched by the precision measurement range of the electromagnetic calorimeter.

It consists of three sub-detectors: the pixel detector, a semiconductor tracker (SCT), and a transition radiation tracker (TRT), shown in Figure 3.9. The three independent sub-detectors of the ID are complementary; the combination of precision trackers at

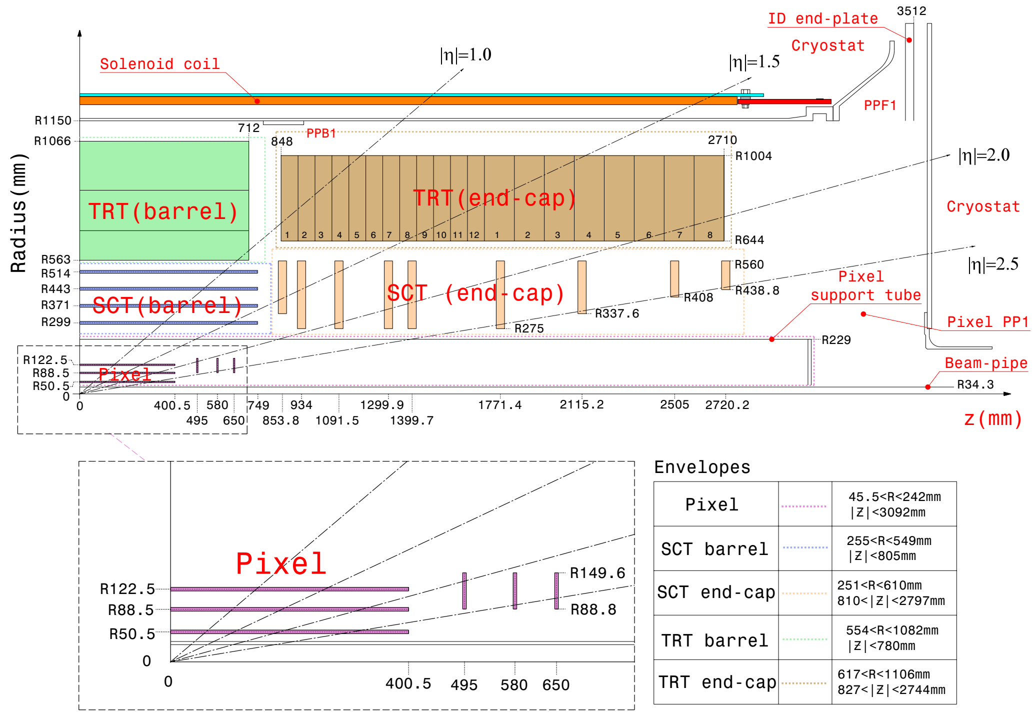

Envelopes

Pixel	⋯	45.5<R<242mm |Z|<3092mm
SCT barrel	⋯	255<R<549mm |Z|<805mm
SCT end-cap	⋯	251<R<610mm 810<|Z|<2797mm
TRT barrel	⋯	554<R<1082mm |Z|<780mm
TRT end-cap	⋯	617<R<1106mm 827<|Z|<2744mm

Figure 3.10.: Schematic view of a quarter-section of the ATLAS Inner Detector showing each of the major detector elements with its active dimensions and envelopes [1]

small radii together with the TRT at larger radius gives robust pattern recognition and high precision in both $r\phi$ and z coordinates.

A comprehensive description of the ATLAS ID can be found in [1, 60–65]. A brief summary of the ID sub-detectors is given in the following.

Pixel Detector

The pixel detector is designed to perform high-precision particle tracking in a hostile environment. It is vital for the accurate reconstruction of primary and secondary vertices, which in turn are crucial for the identification of long lived particles such as b-quarks and τ-leptons.

The pixel detector will have a higher flux density of particles through it than any of the other detectors (158 kGy/year or 0.2×10^{15} n_{eq} cm^{-2} per year at high luminosity compared with 8 kGy/year for the next subdetector [1]) and as such it needs to be radiation hard. To ensure that particle trajectory is not perturbed too much by material interactions the modules have been designed to ensure that a single pixel module does not exceed 1.2% of a radiation lengths, X_0 (see Appendix A for details about particle material interactions)

The detector is comprised of three cylindrical layers in the barrel, and three disks in each of the forward regions. This ensures complete coverage of the region $|\eta| <2.5$. The distances of the three barrel layers to the beamline are 5.05, 8.85 and 12.25 cm respectively, while the distance of the end-cap disks to the centre of the detector is 49.5, 58.0 and 65.0 cm (see Figure 3.10). The layers and disks are fitted with identical silicon pixel modules like the one shown in Figure 3.11.

Each pixel module consists of a single silicon sensor which has highly doped n^+ implants on a n-type substrate. Each sensor has a active area of 16.4 $mm \times 60.8$ mm and are 250 μm of thick. The sensors are divided into 47268 pixels which are connected to 16 front-end readout chips. There the majority of the pixels are, 50 $\mu m \times$ 400 μm (41984 pixels in total) while a small number are larger and 50 $\mu m \times 600$ μm (5284 pixels in total) (see Figure 3.11). The lager sized pixels are necessary to cover the gap between the readout chips. These front-end chips are arranged in two rows and bump bounded to the sensor (46080 channels in total).

As there is an inadequate number of readout channels per module to allow for every pixel to read out, the last eight pixels rows are connected to only four channels ("ganged" pixels). This leads to a two-fold ambiguity in 5% of the hits which is resolved offline. The intrinsic resolution of the pixel modules is 10 μm in the $r\phi$ (transversal) direction and 115 μm in the z (longitudinal) direction, and is a direct two dimensional readout.

There are 1744 identical pixel modules in ATLAS, 1456 in the barrel and 288 in the end-cap disks. The barrel modules are arranged along staves (112 staves in total with 13 modules per stave). Overlaps between sensitive wafers are achieved by having modules tilted by 1^o relative to the global z-axis (see Section 3.2.1 for the coordinate system definition). The staves lie parallel to the beam axis, overlap with each other and are mounted at a tilt angle of -20^0 . In addition to this the staves are grouped on carbon fibre half-shells which form the barrel layers. Finally, there are 48 end-cap sectors with 8 sectors per disk, each containing 6 modules.

The complete pixel detector has a sensitive area of 2.2 m^2 with $\sim$80 million readout channels as can be seen in Table 3.3.

Structure	Layer/Disk	R/Z (mm)	Staves/Sectors	Modules	Pixels
Barrel	Layer-0	50.5	22	286	$13.2 \cdot 10^6$
	Layer-1	88.5	38	494	$22.8 \cdot 10^6$
	Layer-2	122.5	52	676	$31.2 \cdot 10^6$
End-cap	Disk 1	495	8	48	$2.2 \cdot 10^6$
	Disk 2	580	8	48	$2.2 \cdot 10^6$
	Disk 3	650	8	48	$2.2 \cdot 10^6$
Total				1744	$80.4 \cdot 10^6$

Table 3.3.: Summary table of the Pixel detector for each of the barrel layers and end-cap disks.

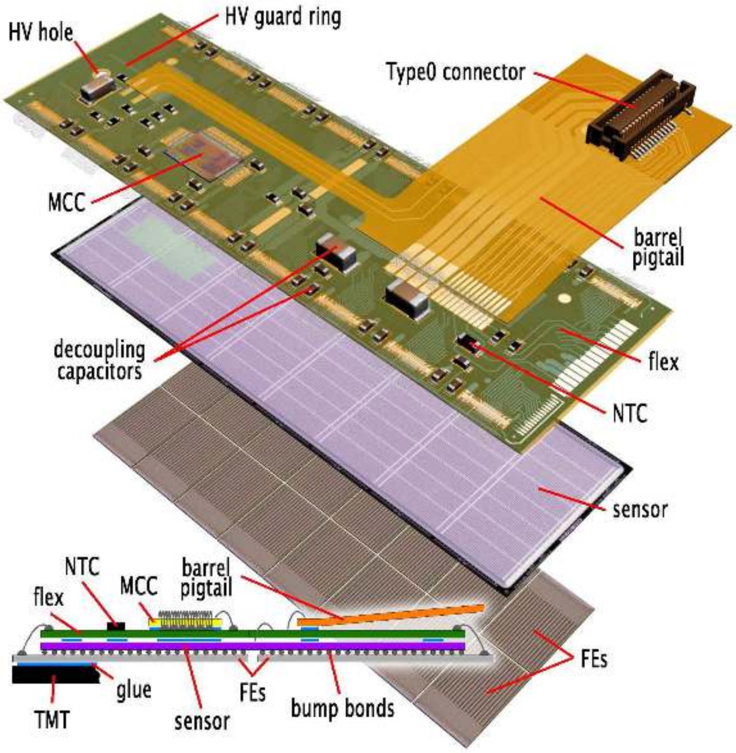

Figure 3.11.: Schematic view of a pixel module illustrating the major pixel hybrid and sensor elements. At the bottom there is a plan view showing the bump-bonding of the silicon pixel sensors to the polyimide electronics substrate[1].

SCT

The SemiConductor Tracker (SCT) is a silicon microstrip detector and surrounds the pixel detector covering a pseudorapidity range of $|\eta| < 2.5$. The purpose of the SCT is to provide precision track measurements in the intermediate radial region, contributing to the measurements of the momentum and vertex position. The detector consists of four cylindrical layers in the barrel and nine end-cap disks on each side. The distances of the four barrel layers with respect to the beamline are 29.9 cm, 37.1 cm, 44.3 cm and 51.4 cm and are symmetric around the IP while the distance of end-cap disks are 85.38 cm, 93.40 cm, 109.15 cm, 129.99 cm, 139.97 cm, 177.14 cm, 211.52 cm, 250.50 cm and 272.02 cm (see Figure 3.10). The layers and disks are mounted on carbon-fibre structures and are filled with silicon microstrip modules.

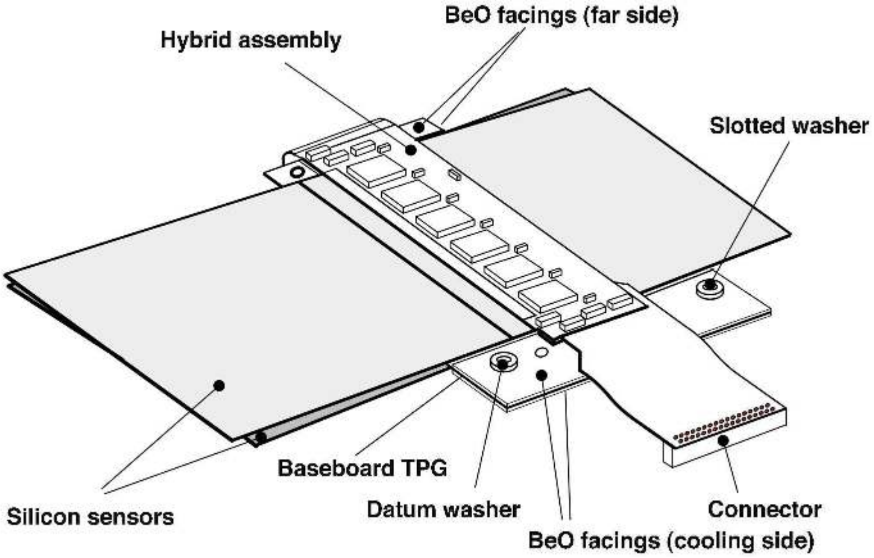

Figure 3.12.: Schematic view of a SCT barrel module illustrating its different components including the silicon wafers[1].

There are a number of different types of SCT modules used within the SCT. Generally a module consists of four silicon wafers, two each on the top and bottom side. Each side has 768 silicon microstrips each which are glued together back-to-back at a 40 mrad stereo angle. The silicon wafers are 285 μm thick, single sided and consist of highly doped $p+$ readout implants in a $n-$type silicon bulk. Each silicon wafer provides a one dimensional position measurement.

In the barrel, the module side parallel to the global z is called $r\phi$ side and the other is known as the stereo side. Each side is built from two bonded 6 cm × 6 cm silicon sensors (to reduce the construction costs). The readout is performed by means of 12 (6 per side) binary front-end chips. Figure 3.12 shows a schematic view of a SCT barrel module where its different components are labeled.

The SCT has 4088 modules in total, 2112 barrel modules and 1976 end-cap modules. All barrel modules are identical and rectangular in shape while there are three different module shapes for the end-caps, namely outer, middle and inner according to their position in the end-cap wheels.

The strip pitch is only constant in the barrel module, which is 80 μm. The end-cap modules have a fan-out structure where the strip pitch varies from 54.53 μm to 90.34 μm, depending the wafer position. The resulting resolution of the barrel modules is 23 μm precision in $r\phi$. The combination of measurements for either side (at a small stereo angle) allows for the reconstruction of a three dimensional spacepoint. Once a three dimensional spacepoint is built, the intrinsic resolution of a whole SCT module is 17 μm in $r\phi$ direction and 580 μm in the z/r direction .

The tables 3.4 and 3.5 contain a summary of the main properties of the SCT detector for the barrel and the end-caps respectively. The SCT modules cover a surface of 61.1 m^2 of silicon with ∼6.3 million readout channels providing almost hermetic coverage with at least four precision spacepoint measurements per crossing particle over the ID coverage.

In the barrel of the SCT the modules were mounted onto staves. These staves were mounted on the barrel with a tilt angle of 11^o leading to an overlap of 4 mm between modules. The final construction of the end-cap disks is quite complicated as each disk have a different number and type of SCT end-cap modules as can be seen in Table 3.5.

Layer	**Radius (mm)**	**Modules**	**Area (m^2)**		
1	300.0	12 × 32	6.26	Barrel length:	1.4934 m
2	373.0	12 × 40	7.82	Strip pitch:	80.0 μm
3	447.0	12 × 48	9.4	No. of modules:	2112
4	520.0	12 × 56	10.96	Total area:	34.4 m^2
				No. of channels:	3244032

Table 3.4.: Summary of the properties SCT Barrel.

Module z (mm)	**Radius (mm) [*Inner*/*Outer*]**	**Modules [I / M / O]**	Strip pitch [min/max] (μm)	
835.0	336 / 560	- / 40 / 52	*Inner:*	54.53 / 69.43
925.0	259 / 560	40 / 40 / 52	*Middle:*	70.48 / 94.74
1072.0	259 / 560	40 / 40 / 52	*Outer:*	70.92 / 90.34
1260.0	259 / 560	40 / 40 / 52		
1460.0	259 / 560	40 / 40 / 52	No. of modules:	1976
1695.0	259 / 560	40 / 40 / 52	Total area:	26.7 m^2
2135.0	336 / 560	- / 40 / 52	No. of channels:	3035136
2528.0	401 / 560	- / 40 / 52		
2788.0	440 / 560	- / - / 52		

Table 3.5.: Summary of the properties SCT end-caps.

TRT

The *TRT* consists of straw tubes, 4 mm in diameter, that cover a range up to $|\eta| < 2.1$. The TRT will provide on average more than 30 measurements per track. It measures precisely only $R-\phi$ coordinates with an intrinsic accuracy of 130 μm per straw. In the barrel region, the 144 cm long straws are parallel to the beam axis. Their wires are divided into two halves at approximately $\eta = 0$. In the end-cap region, the 37 cm long straws are arranged radially in wheels. The total number of TRT readout channels is approximately 351 thousand. The TRT's capability to detect transition-radiation photons enhances the overall ATLAS electron identification performance.

The TRT straw hits contribute significantly to the momentum measurement, since the lower precision per point is compensated by the larger number and longer measured track length.

Material budget

Particles that traverse the ID will interact, to varying degrees, with the material of the makes up the ID (e.g. sensors, cables, support structures etc.). The effect of such interactions need to be taken into account during the reconstruction of these particles. The dominant effects are:

- Multiple Coulomb Scattering (MCS), causing particles to deviate from their ideal trajectory (see Section A.2).
- Bremsstrahlung, causing charged particles, especially electrons, to radiate energy (see Section A.1.3).
- Photon conversion, causing photons to convert into an electron-positron pair ($\gamma \rightarrow e^+e^-$).
- Hadronic interactions, between hadrons and the detector material can cause the hadrons to produce a stream of secondary particles.

With an overall weight of ∼4.5 tonnes, the ATLAS ID has much more material than any previous tracking detector. The amount of material has kept to a minimum by using light-weight, low-Z materials like carbon fiber for the support structures. Figure 3.13 shows the amount of material that a particle traverses as a function of the pseudorapidity. The material is expressed in terms of radiation lengths (X_0)(see Appendix A). This amount of material placed before the electromagnetic calorimeters has a detrimental effect on their performance as some particles may lose significant amounts of energy prior to entering the calorimeters.

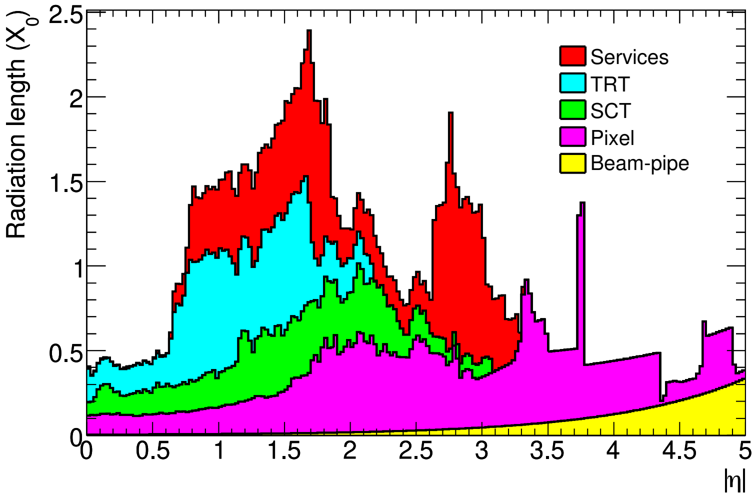

Figure 3.13.: Material distribution within the Inner Detector as a function of $|\eta|$ and averaged over ϕ. Including the services and thermal enclosures. The breakdown indicates the contributions of external services and of individual subdetectors, including services and their thermal enclosures in their active volume[1].

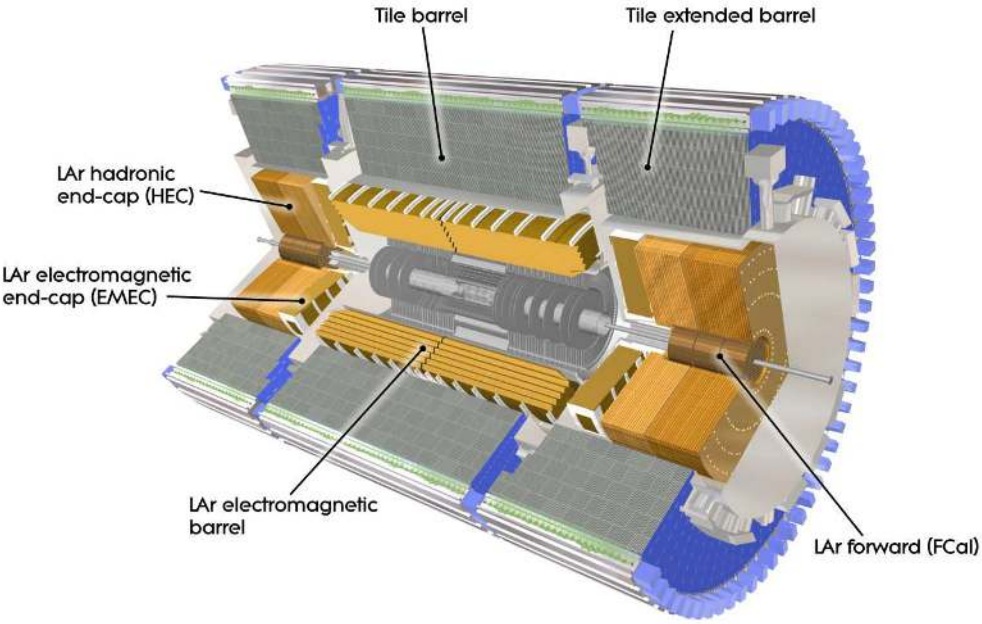

Figure 3.14.: Cut-away view of the ATLAS calorimeter system[1].

3.2.4. Calorimetry

The ATLAS calorimeter system, shown in Figure 3.14, covers a range of $|\eta| < 4.9$ using different techniques suited to the widely varying requirements of the physics processes of interest and of the radiation environment over this large η-range. It accommodates an electromagnetic (EM) calorimeter, a hadronic calorimeter, and forward calorimeters (FCal).

The ATLAS calorimeters, with $22 - 24X_0$ and about 10 interaction lengths (λ) for the EM and hadronic detectors respectively, provide good containment for EM and hadronic showers, which is vital to provide good energy resolution, and also for limiting punch-throughs into the muon system. The large η-coverage ensures good missing energy measurements, which is particularly important for searches of beyond the standard model physics. A brief description of each of the sub-detectors follows but a full description can be found in [1] and in the ATLAS calorimeter TDRs[66–68].

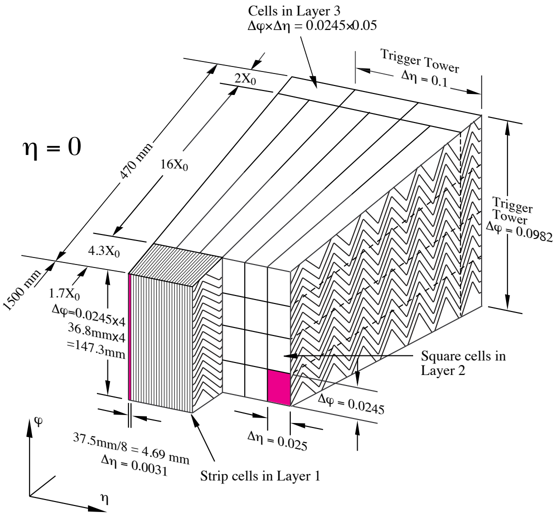

Figure 3.15.: Sketch of an EM calorimeter barrel module. The granularity in η and ϕ of the cells of each of the three layers and of the trigger towers is indicated [1].

EM calorimeter

The EM calorimeter is constructed in two main sections; a barrel section covering the region $|\eta| < 1.475$ and two end-caps (EMEC) covering the region $1.375 < |\eta| < 3.2$. The EM calorimeter is a liquid-argon (LAr) sampling detector with accordion-shaped kapton electrodes and lead absorber plates which provides complete ϕ symmetry without azimuthal cracks (see Figure 3.15). The barrel is divided into two identical half-barrels that are separated by a small gap (4 mm) at $z = 0$. Each EMEC is mechanically divided into two coaxial wheels. The barrel and two EMECs are each housed in their own cryostat. The total thickness of the EM calorimeter is $> 22\,X_0$ in the barrel and $> 24\,X_0$ in the end-caps.

The EM calorimeter is segmented for precision measurements within $|\eta| < 2.5$ region (to match the ATLAS ID). It is segmented into three longitudinal sections with varying granularities depending on η. The middle section, for instance, consists of square towers of $\Delta\eta \times \Delta\phi = 0.025 \times 0.025$ for $|\eta| < 2.5$, see Figure 3.15.The EMEC inner wheel ($|\eta| > 2.5$) is segmented into two longitudinal sections and has a coarser lateral granularity.

To account for the significant amount of material in front of the calorimeter a presampler detector (active LAr layer) is used to correct for energy losses due to up-stream material. In total there are more than 170 thousand readout channels in the EM calorimeter.

Hadronic calorimeter

The hadronic calorimeter consists of a barrel covering the region $|\eta| < 1.0$, two extended barrels covering the region $0.8 < |\eta| < 1.7$, and two hadronic end-caps (HEC) covering the region $1.5 < |\eta| < 3.2$. The barrel and extended barrels, known as the Tile barrel and Tile extended barrel, are sampling tile detectors using steel as the absorber and scintillating tiles as the active material. The HEC is a sampling LAr detector.

The Tile barrel and extended barrels are placed directly outside the EM calorimeter. All Tile calorimeters are divided into 64 modules in the azimuthal direction and into three layers longitudinally. The longitudinal divisions are approximately 1.5, 4.1, and 1.8 λ thick in the barrel and 1.5, 2.6, and 3.3 λ in extended barrels. The scintillating tile is read out by wavelength shifting fibres into two separate photomultiplier tubes. The granularity is $\Delta\eta \times \Delta\phi = 0.1 \times 0.1$ for the barrel and extended barrels in the first two layers and $\Delta\eta \times \Delta\phi = 0.2 \times 0.1$ for the last layer.

The HEC calorimeter consists of two independent wheels per end-cap and are located located directly behind the EMEC and share the same cryostat. Each wheel is built from 32 identical wedge-shaped modules, and is divided into two longitudinal segments. The granularity is $\Delta\eta \times \Delta\phi = 0.1 \times 0.1$ in the region $1.5 < |\eta| < 2.5$ and $\Delta\eta \times \Delta\phi = 0.2 \times 0.2$ in the region $2.5 < |\eta| < 3.2$.

FCal calorimeter

The FCal is a LAr copper or tungsten detector and is integrated into the end-cap cryostats. It is approximately 10 λ deep, and consists of three modules in each end-cap: the first is made of copper, and is optimised for EM measurements, while the other two, made of tungsten, predominantly measure the energy of hadronic interactions.

3.2.5. Muon Spectrometer

The ATLAS muon spectrometer, shown in Figure 3.16, is designed to provide precision muon momentum measurements and a stand-alone trigger subsystem[69]. The muon spectrometer consists of separate trigger and high-precision tracking chambers, and

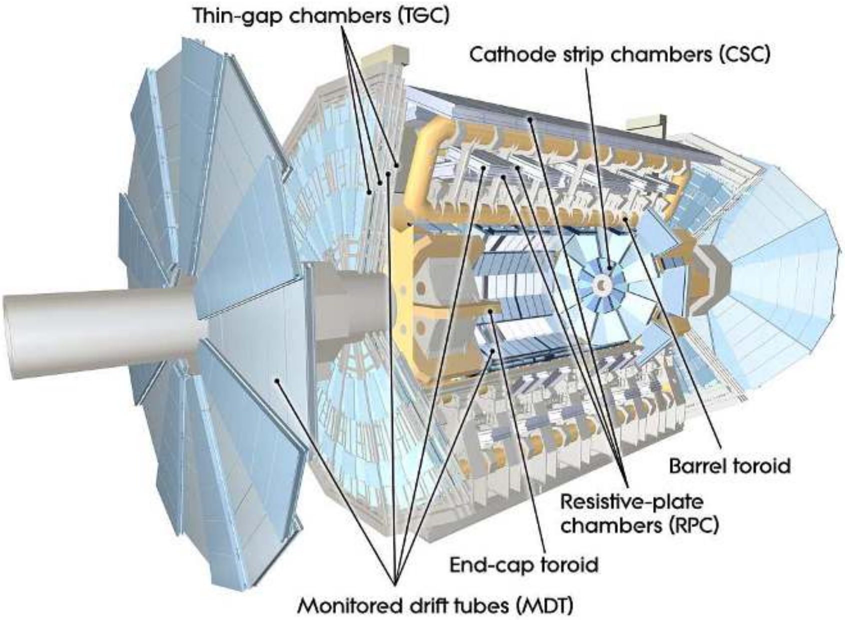

Figure 3.16.: Cut-away view of the ATLAS muon spectrometer[1].

utilises the large superconducting air-core toroid magnets to deflect muon tracks that pass through it. In the barrel region, tracks are measured in chambers arranged in three cylindrical layers around the beam axis; in the end-cap regions, the chambers are installed in planes perpendicular to the beam again in three layers.

Precision measurements of the track coordinates in the bending direction of the magnetic field are provided by the Monitored Drift Tubes (MDTs) and by Cathode Strip Chambers (CSCs) in the region $|\eta| < 2.7$. The CSCs are multiwire proportional chambers with cathodes segmented into strips. The stringent requirements on the relative alignment of the muon chambers are met by a combination of precision mechanical-assembly techniques and optical alignment systems.

The muon trigger subsystem consists of Resistive Plate Chambers (RPCs) in the barrel and Thin Gap Chambers (TGCs) in the end-cap regions. A trigger subsystem provides well-defined p_T thresholds through the systems excellent time resolution and measures the muon coordinate in the direction orthogonal to that determined by the precision-tracking chambers.

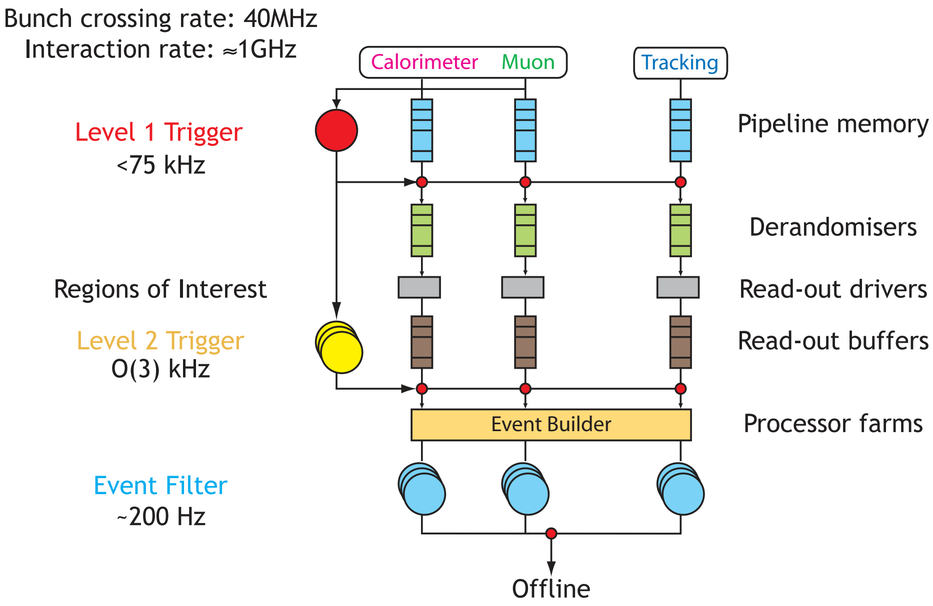

Figure 3.17.: Schematic view of the ATLAS TDAQ system.

3.2.6. Trigger and Data Acquisition

The ATLAS trigger and data acquisition system (TDAQ) is based on three distinct levels of on-line event selection: level-1 (LVL1), level-2 (LVL2), and event filter (EF) (see Figure 3.17) [70, 71]. LVL2 and EF together form the high-level trigger (HLT).

Each trigger level refines the decision made at the previous level, reducing the data rate at each level by adding additional selection criteria. The trigger system follows an early rejection approach so that as soon as an event fails all trigger criteria of a given level, it is rejected and will not and cannot be resurrected. Accepted events must have passed through all processing steps. As nearly all events must be rejected (1 GHz → 200 Hz), this approach saves valuable processing time. In the following, a brief overview is presented, also introducing the data acquisition system (DAQ).

The LVL1 trigger, based upon custom-made electronics, is designed to search for high-p_T muons, electrons, photons, jets, and hadronically decaying τ-leptons, as well as large amounts of missing transverse energy and larger amounts of transverse energy. The selection is based on information from a subset of detectors present in ATLAS: muons are identified using the muon trigger chambers (RPCs and TGCs), the remaining objects are identified using coarsely granulated information from the calorimeters. The ID is not used in the LVL1 trigger. The LVL1 decision is made in less than $2.5\,\mu$s and has a maximum output rate of 75 kHz.

The HLT is a software based system running on large computing farms. The LVL2 trigger refines the LVL1 trigger objects (muons, electrons etc.). The full detector is read out at full granularity and precision, however, only detector information around the given LVL1 trigger objects (known as a Region Of Interest (ROI)) is actually processed. This limits the required data transfers to an average of approximately 2% of all available data. The LVL2 trigger is designed to reduce the rate to 3 kHz, with an event processing time in the order of 40 ms (when averaged over all events).

The final trigger level, the event filter, further reduces the trigger rate to approximately 200 Hz, with an average processing time of order of four seconds. The selection mechanisms are derived from off-line analysis procedures and utilises all detector data.

The DAQ controls the movement of data down the trigger selection chain, as seen in Figure 3.17. After LVL1 trigger accepts the event, it is buffered from the detector-specific readout electronics. The requested event data is then transfered to the LVL2 trigger. If accepted by LVL2, all parts of the event data are combined and assembled in the event builder nodes. The full event data is then moved by the DAQ to the EF trigger. In case of an EF passing, the full event data is moved to permanent storage.

3.2.7. ATLAS Software: *Athena*

The amount of data produced by ATLAS, the complex nature of the detector and the long lifetime of the experiment requires a flexible and adaptable software framework that will ensure that the data is usable in the future and improvements can be made to the software and detector.

An object orientated approach was deemed the optimal solution for such a complex problem and C++ was chosen as the programming language for the majority of the software development. Named Athena [72], the ATLAS software is based on the framework known as Gaudi [73]. It ensures modularity by separating algorithms and data structures. The framework itself provides a set of abstract and template base classes while Athena is the collection of concrete implementations. Athena performs tasks such as simulation, data reconstruction, analysis and monitoring.

Athena is also linked to a number of external packages: Geant4 [74, 75] is the simulation engine used predominantly to determine the detector response; physics generators such as Pythia[76] are integrated into Athena to study specific processes arising from proton-proton collisions.

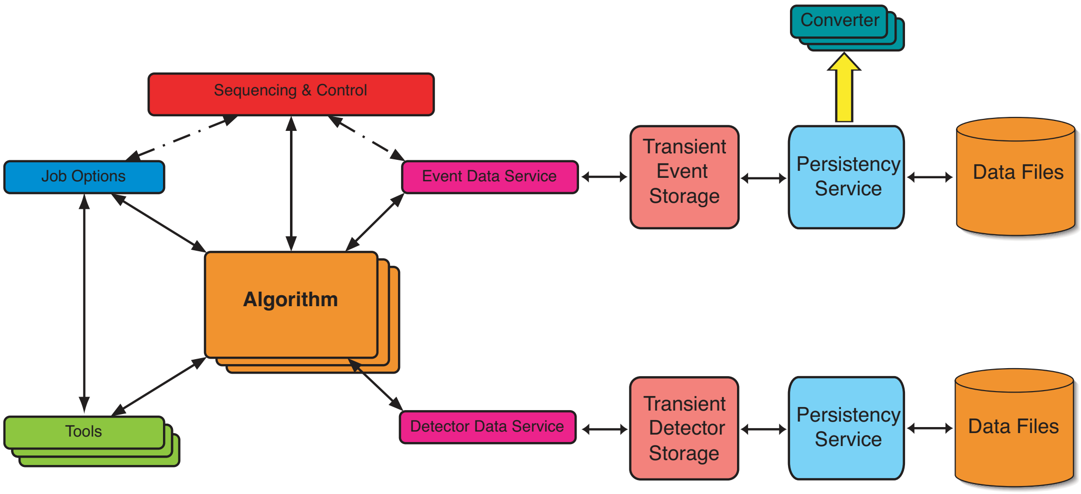

Figure 3.18.: The structure of the Gaudi framework[73].

The framework ensures that the requested algorithms are run in the correct order, while offering common services and tools like message logging, access to data on disk or remote disk servers to reduce unnecessary duplication of said tools and services.Job options scripts, written in Python, supply instructions to the sequencing and control block as well as providing algorithms and helper tools with run-time information.

In this framework algorithms are responsible for the manipulation of data objects. An algorithm may call on a number of tools and services that may be common to a number of different algorithms. The output of an algorithm is stored in a common memory area, called the “Transient Event Store” (TES), from where the next algorithm can retrieve the output for further processing. From the TES data can be written out to disk (persistified) through the use persistency service.

The ATLAS offline software contains several databases which are needed in order to allow the Athena to form its tasks. Storing information like the position, size and orientation of each volume detector, calibration constants for the numerous detector elements, and material locations within the detector, the databases combine in Athena to give the status of the detector at any particular time.

The alignment constants are stored in a conditions database which is used by the detector description to correct the nominal positions of the sensors from the previous database. It also holds the calibration constants, which are needed, for example, to convert the drift times in the TRT straws and the MDT tubes into drift radii. The calibration constants also comprise the list of dead or noisy silicon channels.

A distributed analysis paradigm has been kept in mind during the software design as the amount of data and the number of users is too large for a single cluster and so are divided across the computing resources of many institutions (see Section 3.2.8 for more details).

3.2.8. LHC Computing Grid

The LHC project has an additional element that is common for all of the main LHC experiments. This is the LHC Computing Grid. Which is aimed at building and maintaining a distributed data storage and analysis infrastructure for the entire LHC community.

When the LHC begins its operations it will produce roughly 15 PB of raw data annually[1] which is combined with the processed data, user data, and Monte-Carlo simulation. Given the large amounts of data and the fact that over 6000 scientists spread across the globe will need access to this data, it must be ensured that access to the data be as efficient and stable as possible. These requirements could not be satisfied just by CERN, so an international distributed Grid infrastructure was launched.

The Grid is a hierarchical distributed computing model based on sites called “Tiers”. For the LHC data, a primary backup will be recorded on tape at CERN which will be the unique Tier-0 centre. After the initial processing, this data will be distributed to a series of Tier-1 centres (11 sites worldwide) which are large computer centres with sufficient storage and access capacity. The Tier-1 centres will make data available to Tier-2 centers (140 LCG sites worldwide) within their “clouds”, each consisting of one or several collaborating computing facilities, which can store sufficient data and provide adequate computing power for specific analysis tasks. Transfers between Tier-2 centers are just done within a cloud. Finally, physics analysis will be facilitated through a users closest Tier-3 computing resources. The main goal of this model is that the jobs should run where the requested data is, avoiding long data transmission.

---

[1] ATLAS will produce ~ 3.2 PB/year of raw data at high luminosity considering that it will see 2×10^9 events/year where each event is ~ 1.5 MB

4

CHAPTER

TRACK RECONSTRUCTION

To analyse the underlying physics processes at ATLAS complete reconstruction of the event (collision) is required. The multiple overlaying proton-proton collisions at the LHC produce an environment with a large number of tracks, making track reconstruction a very challenging task. Stringent requirements on the reconstruction performance are defined by the physics we desire to study.

Determination of the trajectories of the charged particles plays a vital role for the physics that is wished to be performed. Accurate track reconstruction allows for:

- long lived charged particle momentum and origin to be reconstructed accurately with known uncertainty,
- Identification of short lived particles from their decay products
- the identification of primary and secondary vertices which is vital in the evaluation of the particles lifetimes and is of particular interest in the identification of τ's and B hadrons.

Precise measurements of the positions of charge particles as well a track model which accurately describes the trajectory of charged particles within the tracking detector are required to determine the trajectory of the particles. To ensure that momentum of the particle is measured accurately a detailed understanding of the magnetic field is also important. Knowledge of the material located within the detector is vital to take into account multiple scattering and potential energy losses caused by the particle interacting with matter. Finally knowledge of the resolution of the individual detector components is required to ensure that the trajectory estimation is unbiased.

In this chapter the model which describes the passage of a charged particle in the magnetic field is also discussed.

4.1. ID Data Preparation

The raw ID data ("hits") have to be pre-processed into something more tangible in order to perform a high performance track reconstruction. This process, known as data preparation, transforms the hits on a detector into a position in the detectors reference frame. The steps involved in the data preparation for the ID are discussed below.

4.1.1. Clusterisation

Neighboring pixels/strips with hits that are designated to have been produced by the same particle within a wafer plane are grouped into clusters. This clusterisation is performed at hardware level for the SCT and at software level for Pixels. During the offline reconstruction the clusterisation algorithm performs the grouping of the pixels that share at least one edge and the cluster position is corrected by charge interpolation from the Time-over-Threshold (ToT) measurement. This software also checks if there are ganged pixels or bad/dead strips (using information from the conditions database) in the cluster candidate and removes them.

The position of the cluster is calculated by taking a simple centre of gravity of all the pixels or strips in that cluster.

A correction is made to the cluster position to take into account the deflection of the charge carriers (electrons and holes) caused by the magnetic field present (known as Lorentz shift). Finally a position measurement uncertainty is assigned. The SCT procedure is similar to the Pixels procedure but using the strips information. The precision achieved using the clusterisation technique is higher than the resolution of a single pixel or strip.

4.1.2. Silicon Spacepoint Formation

A spacepoint (SP) is a three dimensional point created from the pixel and SCT cluster positions. Defined in the global frame, a SP requires only a simple transformation from the local to global frame to be created for pixels. However for the SCT SP formation is a little more involved.

Created using information from both sides of the module measurements (see Figure 3.5) a SP is calculated to be where the two strips or two clusters overlap. As the two sensors in an SCT module are ~ 1 mm apart the constructed SPs depend on the incidence angle of the track with respect to the module. A SP can also be created from two single measurements of two different overlapping modules on the same layer or disk. For tracks originating from collisions, the SP formation assumes that the track comes from the ATLAS origin.

The SP are used during offline pattern recognition in ATLAS, but due to their dependence on the incident angle of the track, track fitters use the SCT clusters instead of the SP's in the final fit.

4.1.3. TRT Drift Circle Formation

For the TRT hits, the recorded drift time needs to be converted into a drift radius. First, the drift time is corrected by subtracting the t_0 (the time offset of the straw in the readout electronics). The value of t_0 is in principle determined for each individual straw by a calibration procedure. In the reconstruction this fitted value is read from the conditions database. Using this corrected drift time the radius is calculated.

4.2. Pattern Recognition

The role of pattern recognition in the ID is to assign the measurements in the tracking detector into sets, where all measurements in a set are believed to have come from one charged particle.

The occupancy of each of the detector channels is defined as the fraction of detector channels with a hit. The efficiency of detector channels is defined as the probability for a hit in a channel where the active detection area is crossed by a charged particle. In addition the fraction of channels (in a local area) with hits caused by electronic noise is referred to as the noise level occupancy.

A group of hits created by a single charged particle is called a track. Pattern recognition is the process of finding tracks while minimising the number of fake tracks and eliminating wrong hits. Wrong hits are those incorrectly associated to a track. Fake tracks are reconstructed tracks where no particle has been and mostly consist of several hits randomly lining up. Fake tracks are very dependent on the occupancy of the detector and are often defined as a track comprised of mainly random hits. Once the hits have been associated to the track, an estimation of the trajectory of the original particle is constructed in the track fitting procedure.

Each bunch crossing at the LHC, at high luminosity, will create many hundred charged particles that pass into the Inner Detector. When the occupancy in a detector rises the rate of fake tracks rises sharply. The detector has been designed in such a way to ensure that high occupancy is avoided. For example the pixel detectors, which have been chosen for the three innermost silicon layers of the ATLAS detector, endure their occupancy is low by having each pixel small enough that the track denisty is not too high.

The default pattern recognition for the Inner Detector in ATLAS is called New Tracking (NEWT) [77]. Other packages include iPatRec [78] and xKalman [79]. NEWT is based upon using a combinatorial Kalman Filter technique and is designed to identify tracks with momentum > 0.5 GeV in the SCT and pixel (“silicon portion”) of the ID. Seeding tracks with hits from the silicon portion of the ID, NEWT solves the possible ambiguities, and provides estimates of the track parameters. The silicon portions are then matched to TRT track segments. After extrapolation to the TRT, the track fitting algorithm uses all compatible measurements and estimates the trajectory of the particle that created the track. In addition to the silicon seeded tracking of the NEWT there is complementary TRT seeded algorithm that starts from the unused TRT segments and fits "outside in".

4.3. Track Model

For track fitting, the track model needs to describe the motion of a charged particle in a static magnetic field $\mathbf{B}(\vec{x})$. This model needs to be accurate and easily linearised to allowed for the trajectory to be well estimated. The force exerted on the particle is given by

$$\mathbf{F} = \frac{d\vec{p}}{dt} \sim q\mathbf{v} \times \mathbf{B}(\vec{x}), \tag{4.1}$$

where $\vec{p}$ denotes a three-dimensional momentum vector, $\vec{x}$ denotes a three-dimensional position vector, $\mathbf{v} = d\vec{x}/dt$ is the velocity of the particle and q is the charge of the particle[80]. Since $\mathbf{F}.\mathbf{v} = 0$ the magnetic force does no work on the particle and hence $|\vec{p}| = p =$ constant.

It is useful to rewrite Equation 4.1 in terms of the path-length, $s(t)$

$$\begin{aligned} \frac{ds}{dt} &= v, \\ \mathbf{v} &= v\hat{\alpha}, \qquad \hat{\alpha} \equiv \frac{d\vec{x}}{ds}, \\ \vec{p} &= \gamma m\mathbf{v}, \\ \frac{d\vec{p}}{ds} &= \kappa q\hat{p} \times \mathbf{B}(\vec{x}), \\ \frac{d\hat{\alpha}}{ds} &= \frac{\hat{\alpha} \times \hat{B}}{\rho}, \quad \rho = p/\kappa qB, \end{aligned} \tag{4.2}$$

where the κ is a constant of proportionality, which is proportional to the speed of light. The value of $\kappa = 0.299792458\ GeV/cT^{-1}m{-}1$ where the strength of B is expressed in tesla, momentum is given in GeV/c, distances in meters and charge in units of elementary charge. Unit vectors are indicated by the ˆ symbol. This equation of motion indicates that the motion of the particle will be circular with radius ρ about the direction of the magnetic field.

If it is assumed that the magnetic field is uniform and orientated parallel to the z-axis: $\mathbf{B} = (0, 0, B)$. Equation 4.2 reduces to

$$\begin{aligned} \frac{d\alpha_x}{ds} &= \frac{\alpha_y}{\rho} \\ \frac{d\alpha_y}{ds} &= -\frac{\alpha_x}{\rho} \\ \frac{d\alpha_z}{ds} &= 0. \end{aligned} \tag{4.3}$$

By differentiating Equation 4.3 again we decouple the x and y components.

$$\begin{aligned} \frac{d^2\alpha_x}{ds^2} &= \frac{1}{\rho}\frac{d\alpha_y}{ds} = -\frac{\alpha_x}{\rho^2} \\ \frac{d^2\alpha_y}{ds^2} &= \frac{1}{\rho}\frac{d\alpha_x}{ds} = \frac{\alpha_y}{\rho^2} \\ \frac{d^2\alpha_z}{ds^2} &= 0. \end{aligned} \tag{4.4}$$

The solutions to this set of differential equations are sinusoidal in the x and y components

$$\begin{aligned} \alpha_x &= \alpha_{x0}\cos\phi - \alpha_{y0}\sin\phi \\ \alpha_y &= \alpha_{x0}\sin\phi + \alpha_{y0}\cos\phi \\ \alpha_z &= \alpha_{z0}, \end{aligned} \tag{4.5}$$

where $\phi = s/\rho$. ϕ can physically be interpreted as the angle which the momentum vector is rotated, perpendicular to the magnetic field $\mathbf{B}$, when the particle moves a distance s. Obtaining the position of the particle in the field is found simply by integrating Equation 4.5. Given that at $s = 0$ we are located at some reference point $\vec{x}_0 = (x_0, y_0, z_0)$

$$\begin{aligned} x(\phi) &= x_0 + \alpha_{x0}\rho\sin\phi - \alpha_{y0}\rho\left(1 - \cos\phi\right) \\ y(\phi) &= y_0 + \alpha_{y0}\rho\sin\phi + \alpha_{x0}\rho\left(1 - \cos\phi\right) \\ z(\phi) &= z_0 + \alpha_{z0}\rho\phi. \end{aligned} \tag{4.6}$$

It should be remembered that $\hat{\alpha}$ is just the unit vector of the momentum vector i.e. $\vec{p} = \gamma m v\hat{\alpha}$ and the radius of curvature $\rho = p/\kappa qB$. In an effort to simplify the system of equations they can be rewritten

$$
\begin{aligned}
p_x &= p_{x0}\cos\phi - p_{y0}\sin\phi \\
p_y &= p_{x0}\sin\phi + p_{y0}\cos\phi \\
p_z &= p_{z0} \\
x &= x_0 + \frac{p_{x0}}{a}\sin\phi - \frac{p_{y0}}{a}(1-\cos\phi) \\
y &= y_0 + \frac{p_{y0}}{a}\sin\phi + \frac{p_{x0}}{a}(1-\cos\phi) \\
z &= z_0 + \frac{p_{z0}}{a}\phi,
\end{aligned}
\tag{4.7}
$$

where $a = \kappa q B$. Although these solutions are for the relatively unrealistic case of a perfectly homogenous field they are still useful. For example, if we follow a particle through an inhomogeneous field with a series of small steps, treating the field in each step as if it was homogenous we can apply the exact solutions to our equations of motion.

4.3.1. Track Parameters for a Helical Model

The solution to Equation 4.4 gives six constants of integration

$$\mathbf{p} = (x_0, y_0, z_0, p_{x0}, p_{y0}, p_{z0}). \tag{4.8}$$

Using the identity

$$\left(\frac{dx}{ds}\right)^2 + \left(\frac{dy}{ds}\right)^2 + \left(\frac{dz}{ds}\right)^2 = 1, \tag{4.9}$$

it is possible to remove one degree of freedom leaving only five free parameters. These remaining parameters are a representation of the five free *track parameters*, two coordinates describing the impact position on a given surface, two describing the direction at that point and the radius of curvature (or transverse alternatively momentum)(see Figure 4.1).

The choice of parameterisation for the track parameters is arbitrary however it is governed by two factors: the underlying track model; and the geometry of the detector.

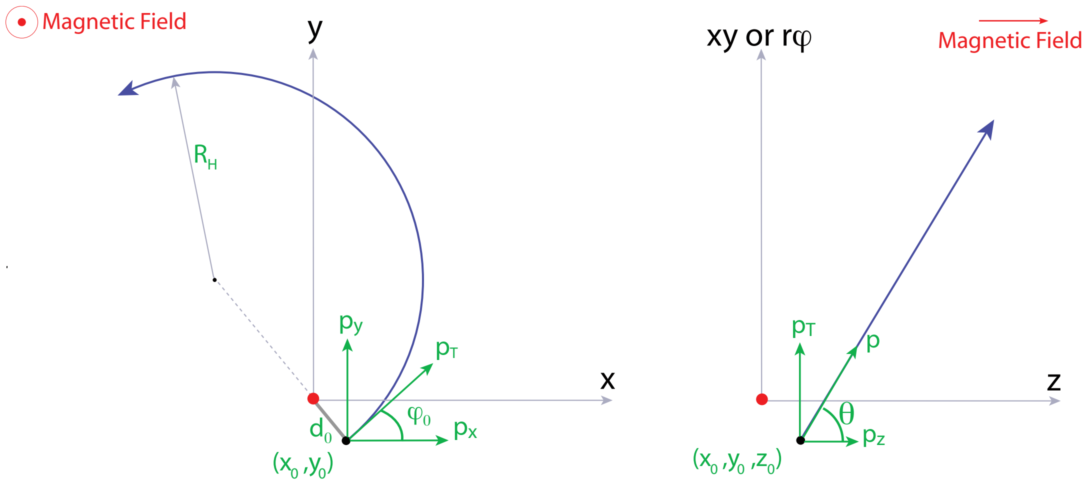

Figure 4.1.: A graphical representation of the helix parameters in the transverse plane (left) and the longitudinal plane(right)

If we assume that our detector geometry is cylindrical then it is practicable to write the track parameters in terms of the five parameters

$$\mathbf{p} = (d_0, z_0, \varphi_0, \theta, h.R_H). \tag{4.10}$$

The signed impact parameter, d_0, is the radius of point of closest approach to the origin in the x-y plane, and is positive when the φ of the position is greater than that of the direction of motion at the point of closest approach. z_0 is the z of the track at the point of closest approach to the origin in the x-y plane. The angle φ_0 is the φ of the track momentum at the point of closest approach. θ is the polar angle between the positive z axis and the particles direction. The direction of rotation for the helix in the transverse plane, h, is given by $h = -\mathrm{sign}(qB_z) = \mathrm{sign}(d\varphi/ds) = \pm 1$.

For completeness some useful relationships between the parameters

$$\begin{array}{cc}
\varphi_0 = \tan^{-1}(p_{y0}/p_{x0}) & p_T = \sqrt{p_x^2 + p_y^2} \\
\theta = \tan^{-1}(p_T/p_z) & p_x = p_T \cos\varphi_0 \\
p_y = p_T \sin\varphi_0 & |d_0| = \sqrt{x_0^2 + y_0^2} \\
x_0 = -d_0 \sin\varphi_0 & y_0 = d_0 \cos\varphi_0 \\
z_0 = z_0 & R_H = p_T/(|\kappa q B|).
\end{array} \tag{4.11}$$

Additionally the change in the direction of the charged particle

$$sin(\varphi - \varphi_0) = \frac{d_0}{r} + \frac{R_H/2r(r^2 + d_0^2)}{1 + 2R_H d_0} \quad (4.12)$$

$$cos(\varphi - \varphi_0) = \pm\sqrt{\frac{1 - d_0^2/r^2[(1 + R_H d_0/2)^2 - r^2 R_H^2/4]}{1 + R_H d_0}}. \quad (4.13)$$

4.3.2. Track Parameters for a Linearised Helical Model

It is useful, for fitting purfoses, to have a track model that is approximately linear. If we consider the case of a high momentum particle where the deflection by the magnetic field ($\Delta\varphi$) is small and the tracks begin near the origin of the coordinate system then:

$$\varphi = \varphi_0 + \Delta\varphi, \quad (4.14)$$

and since dr/ds if effectively constant there is no deflection in the longitudinal plane:

$$\theta = \text{constant}.$$

When $\Delta\varphi$ and d_0 are small then

$$\varphi - \varphi_0 \propto \frac{q}{p_T} r.$$

In this case, the track model is approximately linear in the parameters $(\varphi_0, \cot(\theta), q/p_T)$. The track parameters based on a linearised helical model in cylindrical coordinates are

$$\mathbf{p} = \left(r\varphi, z, \varphi_0, \cot(\theta), q/p_T\right). \quad (4.15)$$

The radius of curvature can be used instead of p_T if desired.

4.3.3. Parabolic representation of Track Model

At high momentum a parabola can approximate the helix in the bending plane while a straight line in the $r - z$ plane[81]

$$\begin{aligned} r\phi &= -d_0 + \phi_0 r + \frac{1}{2R} r^2 \qquad (4.16) \\ z &= z_0 + \tan(\theta)\, r. \qquad (4.17) \end{aligned}$$

Where R is the radius of curvature which is proportional to p_T, ϕ_0 is the direction of the track in the x-y plane at the point of closest approach, d_0 is the impact parameter defined as the distance of closest approach to the beam line, z_0 is the value of z at the point on the track where d_0 is evaluated and θ is the dip angle.

4.3.4. Track Parameters for the ATLAS Tracking Detectors

The track parameters of the linearised helical model are not appropriate for the ATLAS tracking systems for a number of reasons:

- The magnetic field is not uniform throughout the tracking volume. Therefore p_T is not a constant of the motion hence the more appropriate choice of q/p.
- The layout detector and the geometry of individual sensors are not cylindrical so $r\phi$ is no longer a well linearised term.
- Corrections for energy loss are calculated as a function p, not p_T. Corrections are also applied directly to p. It is undesirable to continuously switch between representation, as it is computationally expensive and may lead to numerical inaccuracies.
- Multiple scattering is most naturally corrected using (ϕ, θ) and also requires knowledge of the current momentum. Again, the undesirable nature of switching between representations arises.

To try and accommodate these factors, the chosen parameter set in ATLAS is[82]

$$\mathbf{x}_{ATLAS} = (loc1, loc2, \phi, \theta, q/p), \qquad (4.18)$$

where the impact point of the track on a surface is given in local coordinates by $(loc1, loc2)$.

4.4. Estimation Theory

Estimation Theory (ET) deals with the basic problem of inferring some relevant features of an experiment based on observation of the experiment outcomes. Track fitting is an implementation of estimation theory. The relevant feature we are interested in is the state vector, $\mathbf{p}$, which describes the trajectory of a particle i.e. the helix parameters. Assuming that we have an accurate track model, $\mathbf{f}$, we are able to determine the path of the track as a function of the track parameters $\mathbf{p}$. This is in contrast to experimental observations, which are normally the result of recording the position of charged particles passing through sensitive detectors. These measurements of the track, $\mathbf{m}$, are a function of the true state vector degraded by experimental limitations (e.g. noise). The experimental limitations are described by a vector of random variables, $\boldsymbol{\epsilon}$. Hence

$$\mathbf{m} = \mathbf{f}(\mathbf{p}_{true}) + \boldsymbol{\epsilon}. \tag{4.19}$$

The task of ET and track fitting is to find a meaningful mapping, $\mathbf{F}$, of the set of measured coordinates, $\{\mathbf{m}\}$, onto the set of track parameters, $\{\mathbf{p}\}$, with minimum variance and without bias for the fitted parameters:

$$\begin{aligned} \tilde{\mathbf{p}} &= \mathbf{F}(\mathbf{m}), & (4.20)\\ \langle \tilde{\mathbf{p}} \rangle &= \mathbf{p}_{true}, & (4.21)\\ \sigma^2(\tilde{\mathbf{p}}_i) &\equiv \langle (\tilde{\mathbf{p}}_i - (\mathbf{p}_{true})_i)^2 \rangle \rightarrow Minimum, & (4.22) \end{aligned}$$

where $\tilde{\mathbf{p}}$ and $\mathbf{p}_{true}$ and the fitted and trues values of $\mathbf{p}$ respectively. For each individual track the true value of the track parameters, $\mathbf{p}_{true}$, is an unknown but fixed value, while the value of $\tilde{\mathbf{p}}$ is a function of random quantity $\mathbf{m}$ and is hence a random quantity also. The variance is to be considered as the experimental error on our measured quantities and may vary dependent on $\mathbf{p}_{true}$. If our measurements $\mathbf{m}$ were not random variables then calculating $\mathbf{F}$ would be an inversion problem, i.e. $\mathbf{F} = \mathbf{f}^{-1}$, and not an estimation problem at all.

The conditional probability density function d describing the detector measurement resolution can be constructed using the definition of the track model and the randomly displaced measurements. The conditional probability density function is dominated by the difference between the measurement vector and the appropriate quantities of the track $\mathbf{f}(\mathbf{p})$, i.e. $\varepsilon = \mathbf{m} - \mathbf{f}(\mathbf{p})$. This value often depends on the measurement vector itself.

$$\begin{aligned} d(\mathbf{m};\mathbf{p}_{true}) &= d'(\varepsilon,\mathbf{m}) = d'(\mathbf{m}-\mathbf{f}(\mathbf{p}),\mathbf{m}) && (4.23)\\ d(\mathbf{m};\mathbf{p}) &\geq 0 && (4.24)\\ \int_{-\infty}^{\infty} d(\mathbf{m};\mathbf{p}).d\mathbf{m} &= 1 && (4.25)\end{aligned}$$

Explicit estimators are defined by a function of the measurement vector, and implicit estimators determine quantities that can only be implicitly defined by the measurement vector.

4.4.1. Cramér-Rao Lower Bound (CRLB)

In its simplest form, the CRLB expresses the lower bound on the variance of estimators of a deterministic parameter, i.e. the best parameter resolution we could hope to obtain using our detector. Although this lower bound may be impossible to achieve it does serve a purpose in evaluating the overall efficiency of our estimator.

The CRLB states that, in the multivariate case

$$\sigma^2(\tilde{p}_i) \geq (\mathbf{I}^{-1})_{ii}, \tag{4.26}$$

where $\mathbf{I}$ is the Fisher information for our system it is defined as

$$(\mathbf{I}(\mathbf{p}_{true}))_{ij} = \left\langle \frac{\partial \ln d(\mathbf{m};\mathbf{p})}{\partial p_i} \times \frac{\partial \ln d(\mathbf{m};\mathbf{p})}{\partial p_j} \right\rangle. \tag{4.27}$$

4.4.2. Maximum Likelihood Estimator (MLE)

The MLE is one of the most common implicit estimators. It has the very favourable properties of being asymptotically unbiased, asymptotically efficient (i.e. achieves the

CRLB), and having a Gaussian probability distribution function. The idea is to choose a set of parameters **p** which maximises the likelihood of the model having generated the data. This is achieved by inspecting the Likelihood ratio **R**

$$\mathbf{R_m}(\mathbf{p}) = d(\mathbf{m};\mathbf{p})/d(\mathbf{m};\mathbf{p_0}). \tag{4.28}$$

To estimate the value of **p** it is required that the likelihood ratio be a maximum, or equivalently, that the natural log of the ratio be a maximum.

$$\frac{\partial \ln \mathbf{R_m}(\mathbf{p})}{\partial \mathbf{p}} = 0 \tag{4.29}$$

If an efficient estimator exists (i.e. satisfies the CRLB), the maximum likelihood procedure will produce it. Track fitting with a MLE is often rather impractical due to the computation time required.

4.4.3. Gauss-Markov theorem

The Gauss-Markov theorem states that for a linear model, e.g. a linearised track model,

$$\mathbf{p} = \mathbf{H}\boldsymbol{\theta} + \varepsilon, \tag{4.30}$$

where $\boldsymbol{\theta}$ is a vector of parameters to be estimated, ε is a noise vector which is unbiased ($\langle\varepsilon\rangle = 0$) and has covariance **C**. The least squares method will then produce an unbiased estimate for θ and amongst a class of unbiased linear estimators it will produce the result with smallest variance (i.e. the best possible result).

4.5. Track fitting with the Least Squares Method (LSM)

The LSM has a long history of being used for the purpose of track fitting particle physics experiments. It is numerically simple, has convenient statistical properties and is relatively fast.

The track model, which is the solution of the equations of motion for a charged particle in magnetic filed, is required to be linearised to be used in the LSM. As such the function $\mathbf{f}(\mathbf{p})$ is expanded around the point $\mathbf{p_0}$

$$\mathbf{f}(\mathbf{p}) = \mathbf{f}(\mathbf{p_0}) + \mathbf{A} \cdot (\mathbf{p} - \mathbf{p_0}) + \mathcal{O}((\mathbf{p} - \mathbf{p_0})^2), \tag{4.31}$$

where $\mathbf{f}$ is an $(n \times 1)$ vector of observations, $\mathbf{A}$ is a $(n \times k)$ matrix of known coefficients and is defined by

$$\mathbf{A} = \frac{\partial \mathbf{f}(\mathbf{p})}{\partial \mathbf{p}} \text{ at } \mathbf{p} = \mathbf{p_0}. \tag{4.32}$$

The range in which this linearised model actually stays closely related to the full model depends strongly on the choice of track parameterisation (see Section 4.3). If the track model can be well approximated by a linear model in the neighborhood of the measurements and errors vary little with track parameters (so they can be considered constant in the region of the track path), the LSM has minimum variance among the class of linear and unbiased estimates (see Section 4.5.1). In addition to the linearised track model (Equation 4.31), another key component, called the covariance matrix ($\mathbf{V}$), must be calculated

$$\mathbf{V} = \langle (\mathbf{m} - \langle \mathbf{m} \rangle)(\mathbf{m} - \langle \mathbf{m} \rangle)^T \rangle, \tag{4.33}$$

where $\mathbf{m}$ is the measurement vector defined in Equation 4.19. The weight matrix is defined as the inverse of the covariance matrix:

$$\mathbf{W} \equiv \mathbf{V}^{-1}. \tag{4.34}$$

At this stage it would be pertinent to say it is expected that $\mathbf{m}$ has been corrected for possible biases i.e.$\langle \mathbf{m} \rangle = \mathbf{f}(\mathbf{p}_{true})$. In the case of totally independent measurements the weight matrix is diagonal and of the form $\mathbf{W}_{ii} = 1/\sigma_i^2$. This is certainly not the usual case. In general the weight matrix will have off diagonal terms and matrix inversion is required to obtain it.

The LSM tries to minimise M which is the weighted scalar sum of the squares of the measurement residuals. In matrix notation this can be written as:

$$M = \mathbf{r}^T \cdot \mathbf{W} \cdot \mathbf{r}, \tag{4.35}$$

where the residual **r** is the difference between the measurement and the linear model predication

$$\begin{aligned} \mathbf{r} &= \mathbf{f}(\mathbf{p}) - \mathbf{m} && (4.36) \\ &= \mathbf{f}(\mathbf{p_0}) + \mathbf{A} \cdot (\mathbf{p} - \mathbf{p_0}) - \mathbf{m}. && (4.37) \end{aligned}$$

The effect of the weight of the matrix is to give higher or lower emphasis to certain measurements, for example if some data is deemed to be more reliable.

In order to minimise M with respect to our track parameters **p** we differentiate M with respect to **p** and take advantage of the matrix property $\partial \boldsymbol{\theta}^T \mathbf{A} \boldsymbol{\theta} / \partial \boldsymbol{\theta} = \mathbf{2A}\boldsymbol{\theta}$

$$\frac{\partial M}{\partial \mathbf{p}} = 2\mathbf{A}^T \mathbf{W}(\mathbf{f}(\mathbf{p_0}) + \mathbf{A} \cdot (\mathbf{p} - \mathbf{p_0}) - \mathbf{m}). \tag{4.38}$$

Setting $\partial M / \partial \mathbf{p} = 0$ we obtain a solution to our track parameters

$$\begin{aligned} \frac{\partial M}{\partial \mathbf{p}} = 0 &= 2\mathbf{A}^T \mathbf{W}(\mathbf{f}(\mathbf{p_0}) + \mathbf{A} \cdot (\mathbf{p} - \mathbf{p_0}) - \mathbf{m}) \\ \mathbf{A}^T \mathbf{W} \mathbf{A} \cdot (\mathbf{p} - \mathbf{p_0}) &= \mathbf{A}^T \mathbf{W} \cdot (\mathbf{m} - \mathbf{f}(\mathbf{p_0})) \\ \tilde{\mathbf{p}} &= \mathbf{p}_0 + (\mathbf{A}^T \mathbf{W} \mathbf{A})^{-1} \mathbf{A}^T \mathbf{W} \cdot (\mathbf{m} - \mathbf{f}(\mathbf{p_0})) && (4.39) \\ &= \mathbf{p}_0 - (\mathbf{A}^T \mathbf{W} \mathbf{A})^{-1} \mathbf{A}^T \mathbf{W} \cdot \mathbf{r}(\mathbf{p_0}). && (4.40) \end{aligned}$$

If the derivative of **A** is dependent on **p**, the problem would be non-linear. In this case $\tilde{\mathbf{p}}$ would not be the value of **p** that minimizes M, but would be closer than $\mathbf{p}_0$. To obtain a better solution the values of the derivative should be updated by substituting $\mathbf{p_0} = \tilde{\mathbf{p}}$ into Equation 4.40. In doing so a new estimate of the value $\tilde{\mathbf{p}}$ would be obtained. This procedure is repeated until the solution has converged, which is usually defined by a minimum change in M.

An understanding of the measurement uncertainty, hence detector resolution, is very important for the correct estimation of track parameters and must be checked during data acquisition and offline analysis. Although not detailed here it should be noted that it can estimated through:

- Theoretical consideration
- Measurements from a calibration experiment (e.g. test beam)
- The tracks themselves

4.5.1. Properties of LSM

There are a number of key properties of the LSM which make it suitable for track fitting. Firstly, it is an unbaised estimator. From Equation 4.40

$$\begin{aligned}
\langle \tilde{\mathbf{p}} \rangle &= \langle \mathbf{p}_0 - (\mathbf{A}^T\mathbf{W}\mathbf{A})^{-1}\mathbf{A}^T\mathbf{W}\cdot(\mathbf{m}-\mathbf{f}(\mathbf{p_0}))\rangle \\
&= \langle \mathbf{p}_0 - (\mathbf{A}^T\mathbf{W}\mathbf{A})^{-1}\mathbf{A}^T\mathbf{W}\cdot(\mathbf{f}(\mathbf{p_{true}})+\epsilon-\mathbf{f}(\mathbf{p_0}))\rangle .
\end{aligned}$$

In the case where we have a linear model for our measurements

$$\begin{aligned}
&= \langle \mathbf{p}_0 - (\mathbf{A}^T\mathbf{W}\mathbf{A})^{-1}\mathbf{A}^T\mathbf{W}\cdot(\mathbf{A}(\mathbf{p_{true}}-\mathbf{p_0})+\epsilon\rangle \\
&= \langle \mathbf{p}_{true}\rangle - \langle(\mathbf{A}^T\mathbf{W}\mathbf{A})^{-1}\mathbf{A}^T\mathbf{W}\cdot(\epsilon)\rangle \\
&= \langle \mathbf{p}_{true}\rangle - (\mathbf{A}^T\mathbf{W}\mathbf{A})^{-1}\mathbf{A}^T\mathbf{W}\cdot\langle(\epsilon)\rangle .
\end{aligned}$$

Using the fact that our measurements are unbiased i.e $\langle\epsilon\rangle = 0$

$$\langle \tilde{\mathbf{p}} \rangle = \mathbf{p}_{true}. \tag{4.41}$$

The covariance matrix of our newly found track parameters, **C**, is

$$\begin{align}
\mathbf{C} &= \langle(\tilde{\mathbf{p}}-\langle\mathbf{p}\rangle)(\tilde{\mathbf{p}}-\langle\mathbf{p}\rangle)^T\rangle \tag{4.42}\\
&= \langle[(\mathbf{A}^T\mathbf{W}\mathbf{A})^{-1}(\mathbf{A}^T\mathbf{W}\mathbf{r}(\mathbf{p_0}))][(\mathbf{A}^T\mathbf{W}\mathbf{A})^{-1}(\mathbf{A}^T\mathbf{W}\mathbf{r}(\mathbf{p_0}))]^T\rangle \notag\\
&= (\mathbf{A}^T\mathbf{W}\mathbf{A})^{-1}\mathbf{A}^T\mathbf{W}\langle\mathbf{r}(\mathbf{p_0})\mathbf{r}(\mathbf{p_0})^T\rangle\mathbf{W}\mathbf{A}(\mathbf{A}^T\mathbf{W}\mathbf{A})^{-1} \notag\\
&= (\mathbf{A}^T\mathbf{W}\mathbf{A})^{-1}(\mathbf{A}^T\mathbf{W}\mathbf{W}^{-1}\mathbf{W}\mathbf{A})(\mathbf{A}^T\mathbf{W}\mathbf{A})^{-1} \notag\\
&= (\mathbf{A}^T\mathbf{W}\mathbf{A})^{-1}(\mathbf{A}^T\mathbf{W}\mathbf{A})(\mathbf{A}^T\mathbf{W}\mathbf{A})^{-1} \notag\\
&= (\mathbf{A}^T\mathbf{W}\mathbf{A})^{-1}. \tag{4.43}
\end{align}$$

If we truely have a linear model then we can rewrite our $N \times 1$ vector of observations (Equation 4.19) as

$$\mathbf{m} = \mathbf{A}\mathbf{p} + \epsilon, \tag{4.44}$$

where the $N \times m$ matrix **A** is the observation matrix, **p** is a $m \times 1$ vector of the parameters we wish to estimate, and ϵ is the noise vector with a covariance matrix **V** and $\langle\epsilon\rangle = 0$. If it is assumed that the probability distribution function of **m** is

Gaussian, and given by

$$d(\mathbf{m};\mathbf{p}) = \frac{1}{\det^{1/2}(\mathbf{V})(2\pi)^{N/2}} \exp\left[-\frac{1}{2}(\mathbf{m}-\mathbf{A}\mathbf{p})^T\mathbf{V}^{-1}(\mathbf{m}-\mathbf{A}\mathbf{p})\right], \tag{4.45}$$

the CRLB can be found for this specific case.

$$\begin{aligned} \frac{\partial \ln d(\mathbf{m};\mathbf{p})}{\partial \mathbf{p}} &= (\mathbf{A}^T\mathbf{V}^{-1}\mathbf{A})((\mathbf{A}^T\mathbf{V}^{-1}\mathbf{A})^{-1}\mathbf{A}^T\mathbf{V}^{-1}\mathbf{m}-\mathbf{p}) & (4.46)\\ &= (\mathbf{A}^T\mathbf{V}^{-1}\mathbf{A})(\hat{\mathbf{p}}-\mathbf{p}). & (4.47) \end{aligned}$$

So $\hat{\mathbf{p}}$ is a minimum variance unbiased estimator, where the minimum variance is given by the diagonal elements of the covariance matrix

$$\mathbf{C} = (\mathbf{A}^T\mathbf{V}^{-1}\mathbf{A})^{-1}. \tag{4.48}$$

To find the maximum likelihood estimator we need to maximise $d(\mathbf{m};\mathbf{p})$, or equivalently minimise:

$$(\mathbf{m}-\mathbf{A}\mathbf{p})^T\mathbf{V}^{-1}(\mathbf{m}-\mathbf{A}\mathbf{p}), \tag{4.49}$$

which leads to

$$\hat{\mathbf{p}} = (\mathbf{A}^T\mathbf{V}^{-1}\mathbf{A})^{-1}\mathbf{A}^T\mathbf{V}^{-1}\mathbf{m}, \tag{4.50}$$

which has been shown to be the minimum variance unbiased estimator (Equation 4.46) and is also the least squares estimator. Showing that since an efficient estimator exists, i.e. satisfies the CRLB, the maximum likelihood procedure produces it. If the errors, ϵ, were not Gaussian, $\hat{\mathbf{p}}$ would not be minimum variance unbiased estimator. However it would still be best linear unbiased estimator.

It can be explicitly shown that LSM is the estimator with minimum variance among all unbiased linear estimators, as has been shown in Plackett[83] who notes that the fundamental results are due to Gauss[84].

Another important property for any estimator is to be relatively insensitive to measurements that deviate from the expected behavior, i.e. robust. There are two options for measurements that significantly deviate from the expected behavior, they can be removed, or they left as long as they do not unduly influence the estimate. These measurements can occur from process noise signal wrongly associated to the track in pattern recognition, or just be a measurement with very low probability of occurrence, referred to as outliers. Identification of such measurements is detailed in Section 4.6.

4.6. Goodness of Fit tests

As stated before three things are required to get a good estimate of the track parameters

- The track model must be correct.
- Covariance matrix of the measurements must be correct.
- The estimation method must work.

To ensure that this is the case a couple tests can be constructed from the results of the LSM.

4.6.1. Pull Quantities

The pull quantities or reduced residuals are a check of the proper use of the LSM. It is the difference between the measurement (or true value) $\mathbf{m}$ and the track hypothesis at that surface $\mathbf{f}(\tilde{\mathbf{p}}) = \tilde{\mathbf{c}}$ (or estimated track parameters)

$$p_i = \frac{m_i - \tilde{c}_i}{\sqrt{C_{ii}}}, \tag{4.51}$$

where C_{ii} is the i^{th} diagonal element of the covariance matrix of the residual measurement.

The pull quantities should have a distribution with a mean of 0 and variance of 1, and are sensitive to wrong error assumptions and possible misalignments of the detector. If constantly monitored the pull quantities are able to determine if particular parts of the detectors performance are beginning to deteriorate.

4.6.2. χ^2

A less sensitive but more global check is to observe the $\langle\chi^2\rangle$. The χ^2 is a value that is automatically obtained from the LSM and is actually the value which we are trying to be minimise. The χ^2 is defined as

$$\chi^2 = \sum_{i=1}^{n} \left(\frac{m_i - f(p_i)}{\sigma_i} \right)^2, \tag{4.52}$$

or in vector notation

$$\chi^2 = \mathbf{r}^T \cdot \mathbf{W} \cdot \mathbf{r}. \tag{4.53}$$

To see why this value is important, consider a case where the deviation of the measurement from its true value is gaussian. Here the probability of making a certain observation is given by:

$$p(x) = \frac{1}{\sigma\sqrt{2\pi}} \exp\left[-1/2 \left(\frac{y_i - f(x_i)}{\sigma_i} \right)^2 \right], \tag{4.54}$$

where the y_i is the observation and $f(x_i)$ is the expectation value. The total probability of obtaining a set of n measurements , $\{y_i, x_i\}$, is given by the product of the probability

$$\begin{aligned} p_{\{y_i,x_i\}} &= \prod_n P(x_i) \\ &= \prod_n \left[\frac{1}{\sigma\sqrt{2\pi}} \right] \cdot \exp\left[-1/2 \sum_{i=1}^{n} \left(\frac{m_i - f(x_i)}{\sigma_i} \right)^2 \right]. \end{aligned} \tag{4.55}$$

An understanding of the usefulness of the χ^2 can be obtained from Equation 4.55. As can be seen, maximising the probability is the same as minimising the sum in the exponential, which in turn is the definition of the χ^2.

The probability distribution function (PDF) of the χ^2 distribution is given by

$$p_{\chi^2}(x) = \frac{(1/2)^{n/2}}{\Gamma(n/2)} x^{n/2-1} e^{-x/2}, \tag{4.56}$$

where n is the number of degrees of freedom of the system and x is the χ^2. The PDF of the χ^2 distribution can be shown via central limit theorem, to tend to a Gaussian with $\mu = n$ and $\sigma = \sqrt{2n}$ as $n \rightarrow \infty$. This property can be exploited to observe the effects of having a limited number of observations via the use of the reduced χ^2.

The reduced χ^2 is defined as

$$\chi^2_{Reduced} = \chi^2 / n_{DOF}, \tag{4.57}$$

where n_{DOF} is the number of degrees of freedom and is defined by

$$\begin{aligned} n_{DOF} &= \text{number of measurements} + \text{number of constraints} \\ &\quad - \text{number of free parameters}. \end{aligned} \tag{4.58}$$

The reduced χ^2 measures both the deviations between the data, and the mean of the parent distribution. These deviations occur because there are less than an infinite number of observations, and there is a discrepancy between the mean of the parent distribution and the mean as predicted by the model f.

The cumulative distribution function (CDF) of the χ^2 of the distribution is given by

$$P_{\chi^2}(x) = \int_{-\infty}^{x} p_{\chi^2}(x) = \frac{\gamma(k/2, x/2)}{\Gamma(n/2)}. \tag{4.59}$$

As such the probability of a fit being correct can be calculated and track quality selection criteria can be made. It is useful under reasonable assumptions, as easily calculated quantities can be proven to have distributions that approximate to the χ^2 distribution if the null hypothesis is true.

Outlier removal

It has been assumed that all measurements in our set **m** have been produced by the same particle. However this might not always be the case, for example if a small fraction of coordinates have been associated incorrectly, or the measurements have been associated together although there was no track at all. If we have the null hypothesis, p_0, which assumes all measurements do indeed belong to the track and

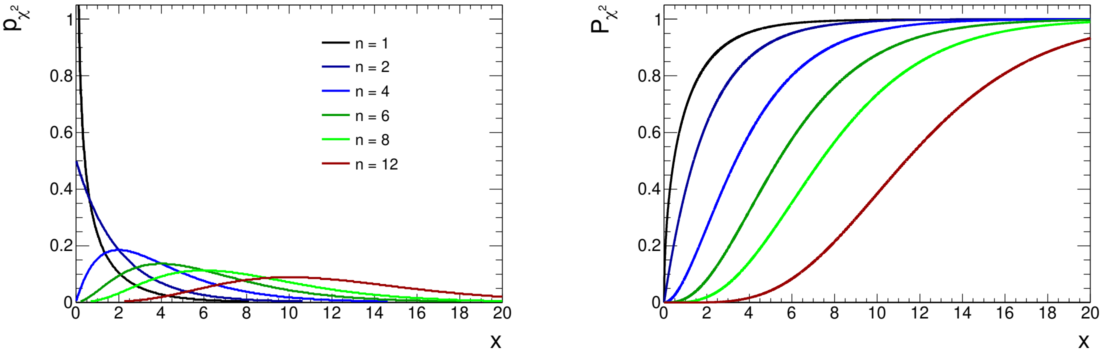

(a) χ^2 PDF **(b)** χ^2 CDF

Figure 4.2.: The χ^2 probability distribution function and cumulative distribution function with $n = 1, 2, 4, 6, 8, 12$

compare to an alternative hypothesis, p_1, we may be able to ascertain if the hits in the null hypothese are correctly assigned.

4.7. Recursive track fitting

The estimator described in Section 4.5 is a *global fitter*; it requires knowledge of all the measurements prior to the commencement of the calculation of the solution. In the general case of n measurements the LSE computes the inverse of a $n \times n$ matrix. Due to the effects of the multiple scattering, this matrix will not be diagonal and as a result the CPU time for this calculation grows $\propto n^3$. A *recursive track fitter* incorporates measurements into the estimate of the track parameters in a stepwise manner, avoiding the need for the inversion of large matrices. The recursive least squares estimator is called the Kalman filter (KF) [85, 86].

The KF is generally a method of estimating the states of dynamic systems, where the dynamic system, is an evolving model of the *time* varying phenomenon. The concept of time in this case should be interpreted as a univariate parameter to which the system state is dependent. In the case of track fitting the univariate parameter is the path length. At a point in space, s_k, let us assume that the track intersects a measurement surface. The trajectory between two adjacent measurement surfaces, $k-1$ and k, is given by the *system equation*

$$\mathbf{p}(s_k) \equiv \mathbf{p}_k = \mathbf{f}_k(\mathbf{p}_{k-1}) + \mathbf{w}_k, \tag{4.60}$$

where the function $\mathbf{f}_k$ is the track model between the surface $k-1$ and k. The random disturbances which may arise due to multiple scattering and energy loss mechanisms between the two measurement surfaces, are taken into account by the vector of random variables $\mathbf{w}_k$. Any bias introduced can be corrected for, and without loss of generality it can be stated that

$$\langle \mathbf{w}_k \rangle = 0, \;\; cov(\mathbf{w}_k) \equiv \mathbf{Q}_k. \tag{4.61}$$

Generally the track model $\mathbf{f}_k$ will be nonlinear and as such will need to be approximated by a linear function. This is done a by a Taylor series expansion to first order (See Equation 4.31). In the case of a linear track model, Equation 4.60 can be rewritten as

$$\mathbf{p}_k = \mathbf{A}_k \mathbf{p}_{k-1} + \mathbf{w}_k. \tag{4.62}$$

The constant term from the linear expansion has been suppressed for convenience. The covariance matrix for the track model at surface k is represented by the matrix $\mathbf{C}_k$.

It is worth restating that the track state is generally not observed directly, and the relationship between the track parameters and the measurement is described by the measurement Equation 4.63

$$\mathbf{m}_k = \mathbf{h}_k(\mathbf{p}_k) + \epsilon_k \tag{4.63}$$

$$\langle \epsilon_k \rangle = 0, \;\; cov(\epsilon_k) \equiv \mathbf{V}_k, \tag{4.64}$$

where $\mathbf{m}_k$ is the measurement vector at surface k and ϵ_k is the measurement noise. The properties of measurement vector see that it is unbiased, with a well defined covariance matrix. It is clear that the purpose of the function $\mathbf{h}_k$ is to map $\mathbf{p}_k$ on to $\mathbf{m}_k$. As in ATLAS this is a linear mapping, and as such can be represented by the derivative matrix $\mathbf{H}_k$. Again the constant term has been suppressed for the sake of convenience.

4.7.1. Kalman Filter Operations

The KF invokes three types of operation; prediction, filtering and smoothing. The prediction operation provides an estimate of a future state, filtering provides an estimate of the current state and includes the current measurement, and smoothing provides an estimate of the previous state.

The Prediction

The prediction is the estimate of the state vector at the point of the next measurement. Starting from an estimate of the state vector at measurement surface $k-1$ which is based upon all previous measurements $m_1, ..., m_{k-1}$, we wish to predict the state at the next surface

$$\mathbf{p}_{k|k-1} = \mathbf{A}_k \mathbf{p}_{k-1} + \mathbf{w}_k. \tag{4.65}$$

In addtion to the state vector, the covariance matrix of the state must also be extrapolated from s_{k-1} to s_k. This is given by linear error propagation

$$\mathbf{C}_{k|k-1} = \mathbf{A}_k \mathbf{C}_{k-1} \mathbf{A}_k^T + \mathbf{Q}_k. \tag{4.66}$$

The residual of the prediction is given by

$$\mathbf{r}_{k|k-1} = \mathbf{m}_k - \mathbf{H}_k \mathbf{p}_{k|k-1}, \tag{4.67}$$

and the covariance matrix of the predicteion residuals

$$\mathbf{R}_{k|k-1} = \mathbf{V}_k + \mathbf{H}_k \mathbf{C}_{k|k-1} \mathbf{H}_k^T. \tag{4.68}$$

Filtering

Once the predicted state has been extrapolated to the next surface, $\mathbf{x}_{k|k-1}$, it is combined with measurement $\mathbf{m}_k$:

$$\mathbf{p}_{k|k} = \mathbf{p}_{k|k-1} + \mathbf{K}_k \left(\mathbf{m}_k - \mathbf{H}_k \mathbf{p}_{k|k-1}\right), \tag{4.69}$$

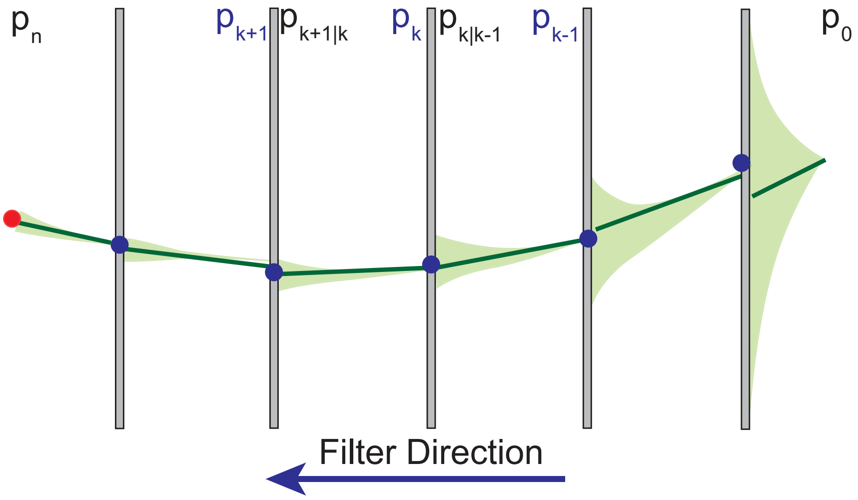

Figure 4.3.: A schematic representation of the Kaman filter process. The track is represented by the green line while uncertainty of the track is represented by shaded green area.

where $\mathbf{K}_k$ is the *Kalman gain matrix*:

$$\mathbf{K}_k = \mathbf{C}_{k|k-1}\mathbf{H}_k^T \left(\mathbf{V}_k + \mathbf{H}_k\mathbf{C}_{k|k-1}\mathbf{H}_k^T\right)^{-1}. \tag{4.70}$$

The filtered covariance matrix is given by

$$\mathbf{C}_{k|k} = \left(\mathbf{I} - \mathbf{K}_k\mathbf{H}_k\right)\mathbf{C}_{k|k-1}, \tag{4.71}$$

where $\mathbf{I}$ is the identity matrix. The residual of the filtered state is given by

$$\mathbf{r}_{k|k} = \mathbf{m}_k - \mathbf{H}_k\mathbf{p}_{k|k} = \left(\mathbf{I} - \mathbf{H}_k\mathbf{K}_k\right)\mathbf{r}_{k|k-1}, \tag{4.72}$$

and the covariance matrix of the filtered residuals

$$\mathbf{R}_k = \mathbf{V}_k + \mathbf{H}_k\mathbf{C}_k\mathbf{H}_k^T. \tag{4.73}$$

A schematic representation of the Kaman filter process can been seen in Figure 4.3.

Smoothing

After all measurement information have been incorporated into the filter the optimal track parameters ($\mathbf{p}_{n|n}$) have been determined at the surface with the last measurement that was included ($\mathbf{m}_n$). It is also possible to calculate the optimal description of the trajectory on all other surfaces ($\mathbf{p}_{k|n}$). The is accomplished in the smoothing process by incorporating information from both the filter running in the forwards direction, $(m_1, m_2, ..., m_n)$, and a second filter running in the opposite direction, $(m_n, m_{n-1}, ..., m_1)$. This allows the trajectory description on all surfaces to utilise the information of all measurements.

From the forward filtered state ($\mathbf{p}_{k|k}$), and the difference between the next forward prediction ($\mathbf{p}_{k+1|k}$) and next smoothed state ($\mathbf{p}_{k+1|n}$), the smoothed state at surface k can be determined

$$\mathbf{p}_{k|n} = \mathbf{p}_{k|k} + \mathbf{S}_k \left(\mathbf{p}_{k+1|n} - \mathbf{p}_{k+1|k} \right), \tag{4.74}$$

where $\mathbf{S}_k$ is the *smoother gain matrix*

$$\mathbf{S}_k = \mathbf{C}_{k|k} \mathbf{F}_{k+1}^T \left(\mathbf{C}_{k+1|k} \right)^{-1}. \tag{4.75}$$

The covariance matrix of the smoothed state ($\mathbf{C}_{k|n}$) is

$$\mathbf{C}_{k|n} = \mathbf{C}_{k|k} + \mathbf{S}_k \left(\mathbf{C}_{k+1|n} - \mathbf{C}_{k+1|k} \right) \mathbf{S}_k^T. \tag{4.76}$$

The residual of the smoothed state is given by

$$\mathbf{r}_{k|n} = \mathbf{r}_k - \mathbf{H}_k(\mathbf{p}_{k|n} - \mathbf{p}_k) = \mathbf{m}_k - \mathbf{H}_k \mathbf{p}_{k|n}, \tag{4.77}$$

and the covariance matrix of the smoothed residuals

$$\mathbf{R}_{k|n} = \mathbf{V}_k + \mathbf{H}_k \mathbf{C}_{k|n} \mathbf{H}_k^T. \tag{4.78}$$

4.7.2. Kalman Filter Goodness of Fit

As the KF is a recursive MSE it would be expected that a χ^2 for the fit could be calculated. This can be simply done by summing each χ^2 increment, χ_k^2, for each smoothed state

$$\chi^2 = \sum \chi_{k|n}^2 = \mathbf{r}_{k|n}^T \mathbf{R}_{k|n}^{-1} \mathbf{r}_{k|n}. \tag{4.79}$$

4.7.3. Gaussian Sum Filter

The Gaussian Sum Filter (GSF) [87–89] is a non linear generalisation of the KF. The GSF approximates non Gaussian noise by a weighted sum of Gaussians allowing it to take into account non Gaussian contributions. The GSF is implemented as a series of KF's running in parallel, where each KF acts as one of the components of the Gaussian sum. The weights of each component are computed independently. As with the KF, the GSF alternates propagation and filtering steps. At each stage the track parameters are allowed to be described as a mixture of Gaussians.

Three possible applications of the GSF have been identified, to take into account:

- Tails in measurement error distributions.
- Tails in multiple scattering distributions.
- Electron bremsstrahlung, which is described by the Bethe-Heitler distribution.

Only small gains in performance can be expected by modelling multiple scattering and measurement error distributions as Gaussian mixtures. For the strongly non-Gaussian process of radiative energy loss the most significant improvements are predicted and observed. Within ATLAS a version of the GSF has been developed which utilises a Gaussian-sum approximation of the Bethe-Heitler distribution to model radiative energy loss of electrons with ATLAS [90] (see Figure 4.4). At each material surface, the track parameters (described by a sum of Gaussians) are convolved with a Gaussian mixture describing the potential energy losses. This leads to an exponential explosion in the number of components describing the track parameters. In order to limit the number of components, hence the computation time, the components that are sufficiently similar to each other are merged together. A detailed explanation of the GSF in ATLAS can be found in [90]

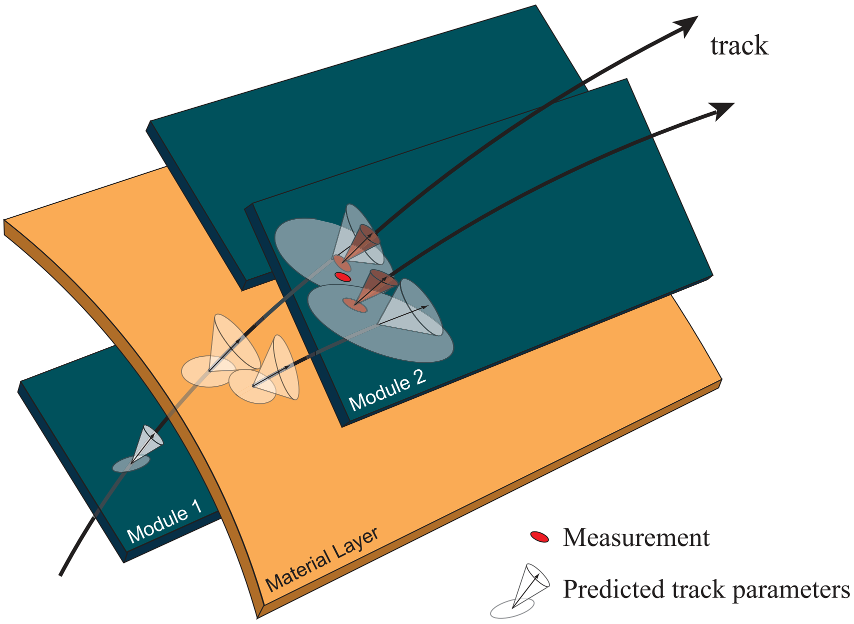

Figure 4.4.: A simplified illustration of a typical extrapolation process within a GSF filter step. The track, on the detector module 1, is propagated onto the next measurement surface, which requires the track to pass through a material layer. The material layer between the two modules causes an increase of the track direction uncertainties. These uncertainties model by a weight sum of Gaussian (in this case 2 Gaussians). This now means that track parameters are represented by a weight sum of Gaussians which are propagated to the measurement surface and updated in manner identical to that of the Kalman filter.

5

CHAPTER

ALIGNMENT OF DETECTORS WITH TRACKS

To make use of the high spatial resolution of the Inner Detector, (in particular the Pixel and SCT detectors), the knowledge of the location of modules must better the spatial resolution in terms of precision. The alignment of the detector is the process of determining the position of the active detector modules within a global reference frame. These positions are then taken into account during the tracking and event reconstruction.

Track based alignment techniques all rely on the minimisation of residual distributions, where residual is defined as the distance between between a track and its hit on a module surface. At present a number of independent alignment approaches have been developed for the Inner Detector of ATLAS.

One such method is known as the Global χ^2 Alignment. This chapter presents the details of this method. In section 5.1 the details of how to extract the alignment parameters from the results of multiple track fits is presented. Section 5.2 introduces two ways of incorporating the effects of multiple scattering into the track and alignment parameter fit. Section 5.3 details how to align a structures comprised of multiple detector modules. Section 5.4 provides a detailed example of how to calculate the derivative of the alignment parameters with respect to the track parameters and residuals. The final portion of the chapter focusses on obtaining reliable solutions from the large system of linear equations produced by the alignment procedure.

There are two other alignment methods implemented in ATLAS:

- The **Robust Alignment** [91, 92] is an iterative method aimed at aligning any kind of silicon detector by re-centring residual distributions using the module overlapping information.

  In each iteration alignment corrections (given in the local module plane) are calculated from the measurements of mean residual $\bar{R}_i$ and mean $\phi(z)$ overlap residuals $\bar{OR}_i^{\phi}$ ($\bar{OR}_i^{z}$), where i stands for either x' or y' (the local axes of the module). The method aims at correcting the inplane DoF only as it is not sensitive to movements perpendicular to the surface of the module.

  This method has been tested and successfully applied to the simulation challenges [3, 93], testbeams [94] and cosmic ray data taking [95, 96]. Although it is not as powerful as the Local χ^2 or Global χ^2 techniques it provides invaluable information for cross-checking results obtained from the other two techniques.

- **Local χ^2 Alignment** [97, 98] is based on the minimisation of the χ^2 with respect to the alignment parameters. The χ^2 is defined as

  $$\chi^2 = \sum_{Tracks} \mathbf{r}^T \mathbf{V}^{-1} \mathbf{r}.$$

  Where $\mathbf{r}$ is the vector of residuals to the fitted track and $\mathbf{V}$ is its covariance matrix. The residuals will depend on the track parameters ($\mathbf{p}$) as well as the alignment parameters related to the modules intersected by that track ($\boldsymbol{\alpha}$).

  It is assumed that the corrections are small and as such the problem can be lineriased for which the generic solution for alignment corrections is

  $$\delta\boldsymbol{\alpha} = \left(\sum_{Tracks} \left(\frac{d\mathbf{r}}{d\boldsymbol{\alpha}} \right)^T \mathbf{V}^{-1} \frac{d\mathbf{r}}{d\boldsymbol{\alpha}} \right)^{-1} \sum_{Tracks} \left(\frac{d\mathbf{r}}{d\boldsymbol{\alpha}} \right)^T \mathbf{V}^{-1} \mathbf{r}. \tag{5.1}$$

  The track parameters dependence on the alignment parameter corrections is neglected in this method hence $d\mathbf{r}/d\boldsymbol{\alpha} = \partial \mathbf{r}/\partial \boldsymbol{\alpha}$. This assumption makes that the covariance matrix diagonal as a resulting system of equations breaks down to 6 × 6 blocks.

These approximations made are justifiable as long as uncertainty on the track parameters is smaller than that of the measurements. As all correlations between modules are ignored the method is inherently iterative and as such needs a large number of iteration to converge.

The Local χ^2 method has been tested on CTB[94] and cosmic ray data[95,96] in addition the simulation challenges[3,93].

5.1. Global χ^2 Alignment

The Global χ^2 Alignment algorithm is quite similar in principal to the Millepede[99] alignment procedure. Developed for the H1 [100] at HERA , Millepede has been shown to work well and has been adopted by a number of other high energy physics experiments [101–103]. The basic principal of this algorithm is to minimise a χ^2 with respect to all of the alignment parameters simultaneously.

In Section 4.5 the method of track fitting using the LSM was described. The procedure minimises the χ^2 (Equation 4.52) with respect to all track parameters and coordinates measurements simultaneously producing an unbiased estimate of the track parameters. In reality, the measurement residual (Equation 4.36) $\mathbf{r}$ is not only dependent upon the track parameters $\mathbf{p}$ but also upon the alignment parameters $\boldsymbol{\alpha}$ which are the same for all tracks. In this section a procedure of how to extract the alignment parameters from a large sample of tracks is described. This is followed by a discussion of the properties of the alignment problem.

5.1.1. Alignment Details

As mentioned previously, the track residuals are dependent on $\mathbf{p}$ and $\boldsymbol{\alpha}$. There is an ambiguity as to whether the alignment parameters are seen as part of the track model $\mathbf{f}$ or should be used to correct the position the measurements themselves. This detail is rather inconsequential in the development of the formalism as it is suffice to say that the residuals are dependent on track parameters, alignment parameters and measurements.

$$\mathbf{r}(\mathbf{p},\boldsymbol{\alpha},\mathbf{m}) = \mathbf{f}(\mathbf{p},\boldsymbol{\alpha}) - \mathbf{m} \;\; or \;\; \mathbf{f}(\mathbf{p}) - \mathbf{m}(\boldsymbol{\alpha}) \tag{5.2}$$

In order to determine the alignment parameters we define a metric that is sensitive to changes of the alignment parameters and minimise this with respect to the alignment parameters. Our chosen metric is the χ^2:

$$\chi^2 = \sum_{Tracks} \mathbf{r}^T \mathbf{V}^{-1} \mathbf{r}. \tag{5.3}$$

Upon first inspection it may seem possible to minimise Equation 5.3 using the procedure outlined in the previous section to obtain the alignment parameters. This naive observation negates the effect of the nested track parameters. If the procedure used to find the track parameters (Section 4.5) is followed, replacing **p** with a vector containing both the alignment parameters and the track parameters, the technique quickly becomes impractical. Assume that N alignment parameters are wished to be found. Each time a track is added the $N \times N$ matrix will increase in size to $(N+n) \times (N+n)$ where n is the number of parameters in the track fit. As we will need a significant number of tracks to reduce the statistical error on the alignment parameters, the matrix size could be very large. For example, if using 100000 tracks, the matrix size would be $(N + n \times 100000) \times (N + n \times 100000)$. A matrix of this size is impractical to solve without using specialised computing systems.

In order to avoid this problem it is possible to find a solution for $\boldsymbol{\alpha}$ without explicitly solving the large set of track parameters at the same time. To do this the fact that the track parameters are not common to all of the tracks while the alignment parameters are is utilised. An initial solution for the track parameters for any arbitrary track fit is found, and its derivative used to predict how the track parameters change as a function of the alignment parameters. This can be done in two equivalent ways, by using an alternative definition of the full derivative when minimising the χ^2 [55] (see also Appendix B) or by explicitly finding the solution for the track parameters and inserting them into the χ^2 derivative for the alignment parameters (as done in [104]).

Following the derivation of[104] we start by taking the full derivative of the χ^2 with respect to the alignment parameters

$$\frac{d\chi^2}{d\boldsymbol{\alpha}} = 2 \sum_{Tracks} \frac{d\mathbf{r}^T}{d\boldsymbol{\alpha}} \mathbf{W} \cdot \mathbf{r}, \tag{5.4}$$

where the weight matrix $\mathbf{W} = \mathbf{V}^{-1}$.

If the measurements are independent, the matrix **W** will be diagonal and hence the derivative to any alignment parameter α_i will only receive contributions from the residuals where $\partial \mathbf{r}/\partial \alpha_i$ are non zero. Therefore only the measurements occurring in the module which coincides with the alignment parameter α_i will contribute to the first derivative of the χ^2.

As a first step to determining the alignment parameters, the track parameters need to be determined for some arbitrary alignment. This is just the regular least squares track fit as described in the previous chapter

$$\tilde{\mathbf{p}} = \mathbf{p}_0 - (\mathbf{A}^T\mathbf{W}\mathbf{A})^{-1}\mathbf{A}^T\mathbf{W} \cdot \mathbf{r}(\mathbf{p}_0, \boldsymbol{\alpha}), \tag{4.40}$$

where **A** is the partial derivative of the residual with respect to the track parameters ($\partial \mathbf{r}/\partial \mathbf{p}$) evaluated at some arbitrary initial value $\mathbf{p}_0$, **W** is the weight matrix (defined by $\mathbf{W} = \mathbf{V}^{-1}$) and the residuals **r** now depend on the alignment parameters. This now provides a solution of the track parameters as a function of our alignment parameters $\boldsymbol{\alpha}$ which can be used in conjunction with the definition of the global χ^2 (Equation 5.3) to obtain a solution for the alignment. Proceeding in an analogous way that was used to extract the solution of the track parameters (i.e linearisation of the problem), we can begin to solve for the alignment parameters.

$$\begin{aligned} \frac{d\chi^2}{d\boldsymbol{\alpha}} &= 2\left(\sum_{Tracks} \frac{d\mathbf{r}^T}{d\boldsymbol{\alpha}} \mathbf{W} \cdot \mathbf{r}\right) \\ &= 2\left(\sum_{Tracks} \frac{d\mathbf{r}^T}{d\boldsymbol{\alpha}} \mathbf{W}\left(\mathbf{r}(\mathbf{p}_0, \boldsymbol{\alpha}_0) + \frac{d\mathbf{r}}{d\boldsymbol{\alpha}_0}(\boldsymbol{\alpha} - \boldsymbol{\alpha}_0)\right)\right). \end{aligned} \tag{5.5}$$

Setting $d\chi^2/d\boldsymbol{\alpha} = 0$

$$\begin{aligned} 0 &= \sum_{Tracks} \frac{d\mathbf{r}^T}{d\boldsymbol{\alpha}} \mathbf{W}\left(\mathbf{r}(\mathbf{p}_0, \boldsymbol{\alpha}_0) + \frac{d\mathbf{r}}{d\boldsymbol{\alpha}_0}(\boldsymbol{\alpha} - \boldsymbol{\alpha}_0)\right) \\ &= \left(\sum_{Tracks} \frac{d\mathbf{r}^T}{d\boldsymbol{\alpha}} \mathbf{W} \frac{d\mathbf{r}}{d\boldsymbol{\alpha}_0}\right)(\boldsymbol{\alpha} - \boldsymbol{\alpha}_0) + \sum_{Tracks} \frac{d\mathbf{r}^T}{d\boldsymbol{\alpha}} \mathbf{W} \cdot \mathbf{r}(\mathbf{p}_0, \boldsymbol{\alpha}_0). \end{aligned} \tag{5.6}$$

However, there is now a nested dependancy on the track parameters. The full derivative can be rewritten as

$$\frac{d\mathbf{r}}{d\boldsymbol{\alpha}} = \frac{\partial \mathbf{r}}{\partial \boldsymbol{\alpha}} + \frac{\partial \mathbf{r}}{\partial \mathbf{p}} \frac{d\mathbf{p}}{d\boldsymbol{\alpha}}. \tag{5.7}$$

The derivative $d\mathbf{p}/d\boldsymbol{\alpha}$ can be obtained by differentiating Equation 4.40

$$\frac{d\mathbf{p}}{d\boldsymbol{\alpha}} = -\left(\mathbf{A}^T\mathbf{W}\mathbf{A}\right)^{-1}\mathbf{A}^T\mathbf{W}\frac{\partial \mathbf{r}}{\partial \boldsymbol{\alpha}}, \tag{5.8}$$

hence

$$\frac{d\mathbf{r}}{d\boldsymbol{\alpha}} = \left(1 - \mathbf{A}\left(\mathbf{A}^T\mathbf{W}\mathbf{A}\right)^{-1}\mathbf{A}^T\mathbf{W}\right)\frac{\partial \mathbf{r}}{\partial \boldsymbol{\alpha}}. \tag{5.9}$$

From equations 5.6 and 5.9 the alignment corrections can be derived

$$\begin{aligned}
\boldsymbol{\alpha} - \boldsymbol{\alpha}_0 &= -\left(\sum_{Tracks} \frac{d\mathbf{r}^T}{d\boldsymbol{\alpha}}\mathbf{W}\frac{d\mathbf{r}}{d\boldsymbol{\alpha}}\right)^{-1} \sum_{Tracks} \frac{d\mathbf{r}^T}{d\boldsymbol{\alpha}}\mathbf{W}\cdot\mathbf{r}(\mathbf{p}_0,\boldsymbol{\alpha}_0) \\
&= -\left(\sum_{Tracks} \frac{\partial\mathbf{r}^T}{\partial\boldsymbol{\alpha}}\hat{\mathbf{W}}\frac{\partial\mathbf{r}}{\partial\boldsymbol{\alpha}}\right)^{-1} \sum_{Tracks} \frac{\partial\mathbf{r}^T}{\partial\boldsymbol{\alpha}}\hat{\mathbf{W}}\cdot\mathbf{r}(\mathbf{p}_0,\boldsymbol{\alpha}_0), \qquad (5.10)
\end{aligned}$$

where all partial derivatives are evaluated at some initial values for the track parameters $\mathbf{p}_0$ and alignment parameters $\boldsymbol{\alpha}_0$. $\hat{\mathbf{W}}$ is defined by

$$\begin{aligned}
\hat{\mathbf{W}} &= \left(1 - \mathbf{A}\left(\mathbf{A}^T\mathbf{W}\mathbf{A}\right)^{-1}\mathbf{A}^T\mathbf{W}\right)^T\mathbf{W} \\
&= \mathbf{W} - \mathbf{W}\mathbf{A}\left(\mathbf{A}^T\mathbf{W}\mathbf{A}\right)^{-1}\mathbf{A}^T\mathbf{W}. \qquad (5.11)
\end{aligned}$$

It is useful to note the following simplifying relationship

$$\hat{\mathbf{W}}\mathbf{W}\hat{\mathbf{W}} = \hat{\mathbf{W}}. \tag{5.12}$$

To simplify notation, 5.10 can be re-expressed as

$$\boldsymbol{\alpha} - \boldsymbol{\alpha}_0 = -\mathscr{M}^{-1}\mathscr{V}. \tag{5.13}$$

We have effectively reduced the alignment problem down to n coupled linear equations, where our solution is the inverse of a matrix $\mathscr{M}$ multiplied a vector $\mathscr{V}$.

5.1.2. $\mathscr{M}$ and $\mathscr{V}$

The properties and meaning of the matrix $\mathscr{M}$ and vector $\mathscr{V}$ are of paramount importance when trying to solve our problem. It can be easily shown that $\mathscr{M}^{-1}$ is the covariance matrix of the alignment parameters.

As is $\mathscr{M}^{-1}$ is a covariance matrix it would be hoped that $\mathscr{M}$ would be symmetric positive definite so that all eigenvalues are positive. By default this is not the case as the alignment equations will not give the detector a fixed frame of reference meaning that the matrix will be singular. After fixing the alignment systems frame of reference (e.g. the position of a single module) the matrix will be symmetric positive definite and the results will be valid.

The density of the matrix $\mathscr{M}$ also plays a vital role in how the problem is solved (See Section 5.7). When aligning modules the level of correlation, and hence the density of the matrix, will depend on the degree of overlap between modules on a single structure and the diversity of angles that tracks pass through modules.

$\mathscr{M}$ is effectively the second derivative of the χ^2 with respect to the alignment parameters, assuming that all higher order terms are ignored while $\mathscr{V}$ is the first derivative, thus

$$\boldsymbol{\alpha} - \boldsymbol{\alpha}_0 = -\left(\frac{d^2\chi^2}{d\boldsymbol{\alpha}^2}\right)^{-1}\frac{d\chi^2}{d\boldsymbol{\alpha}}. \tag{5.14}$$

When stated in this manner it clear that alignment parameters are arrived via the Newton-Raphson method to find the roots of the function $d\chi^2/d\boldsymbol{\alpha}$. This technique is not perfect and can behave poorly near asymptotes or a local extremum. However, with a good initial choice of the root's position, the algorithm will converge. It can be shown that when this method converges it converges quadratically (see Appendix C).

For the alignment of n parameters the minimum χ^2 condition consists of n coupled equations. In general, $\partial\mathbf{r}/\partial\boldsymbol{\alpha}$ are non linear, and consequently the equations that make up the minimum χ^2 condition are also non linear. It will be shown later that the technique will require a number of iterations to account for these nonlinearities.

From this position is is also worth mentioning the "Local χ^2 Alignment", which searches for a solution for the alignment parameters of individual modules without taking into account the correlations between modules. This removes the problem of solving one large system by solving smaller systems many times. This simplification does come at a cost, as correlations are ignored and many iterations are necessary to account for them. In the Local χ^2 method, parameters for each module are calculated under the assumption that all other modules do not move (i.e. perfectly aligned), and as such requires that the multiple iterations be performed. The solution to the local χ^2 alignment can be reproduced by the global method if intermodule correlations are ignored in the matrix $\mathscr{M}$.

There are a number of advantages of the global method over the local technique: firstly since the matrix $\mathscr{M}$ is complete it would be expected that the alignment problem would converge in one iteration if the problem is linear. Secondly the systems of equations, if inverted, can provide the full covariance matrix for the alignment parameters allowing for the uncertainty on the alignment parameters to be estimated. Finally if the matrix is inverted via diagonalisation, the eigenvectors and eigenvalues of system can be used to identify and remove poorly constrained degrees of freedom. These poorly constrained degrees of freedom are of particular concern for alignment and in both the local and global methods can lead to poor convergence or oscillatory behaviour in the solution between iterations. When applied to the ATLAS Inner Detector the alignment problem is not perfectly linear so a number of iterations will be required to solve the alignment problem.

5.2. Treatment of Multiple Scattering

In the normal track fitting scenario the covariance matrix ($\mathbf{V}$) of the residuals is a diagonal matrix corresponding to the measurement errors. If a material description is available then Multiple Coloumb Scattering (MCS) effects can be incorporated in the track model by allowing the track to kink on a finite number of scattering surfaces. Taking MCS into account introduces correlations between the scattering planes and therefore measurements between them. MCS is most needed to be taken into account in high material regions of the detector or when the momentum of the particle is low.

To introduce the MCS contribution two approaches can be followed and in both cases the residuals will also depend (explicitly or implicitly) on the scattering angles $\boldsymbol{\theta}$ hence $\mathbf{r} = \mathbf{r}(\mathbf{p}, \boldsymbol{\theta}, \boldsymbol{\alpha})$. The results of both methods have been shown to be equivalent and hence both techniques are suitable methods.

Explicit scattering effects dependence

To introduce the scattering angles explicitly the χ^2 (Equation 5.3) is redefined and an extra term is added

$$\chi^2 = \mathbf{r}^T \mathbf{V}^{-1} \mathbf{r} + \mathbf{r}_\theta^T \Theta^{-1} \mathbf{r}_\theta, \tag{5.15}$$

where the first term is the normal track χ^2 (where the residuals ($\mathbf{r}$) depend explicitly on the scattering angles, $\boldsymbol{\theta}$), and the second term represents the contribution from the scattering angles. In this term, $\mathbf{r}_\theta = (\boldsymbol{\theta} - \boldsymbol{\theta}')$ represents the residual vector for the scattering angles ($\boldsymbol{\theta}'$ is the expected value and $\boldsymbol{\theta}$ the measured value). $\Theta = \sigma_{\boldsymbol{\theta}} \sigma_{\boldsymbol{\theta}}^T$ is the covariance matrix for the MCS contribution. Θ is diagonal as the expectations for the scattering angles are independent of each other. The elements can be calculated according to Equation A.8 which evaluates an expectation value for the scattering angle based upon the momentum of the track and the amount of material between each measurement.

As $\sigma_\theta \propto 1/p$, multiple scattering is very important in the reconstruction of low momentum tracks. The computations of the multiple scattering covariance matrix requires that there has been prior momentum determination and as such can not be applied to tracks that have no momentum knowledge.

In this approach the covariance matrices, $\mathbf{V}$ and Θ, remain diagonal in the track fit but now the χ^2 has to be minimized with respect to the track parameters ($\mathbf{p}$) and scattering angles ($\boldsymbol{\theta}$), simultaneously.

By redefining terms that are included in the χ^2 such that

$$\tilde{\mathbf{p}} = \begin{pmatrix} \mathbf{p} \\ \boldsymbol{\theta} \end{pmatrix}, \quad \tilde{\mathbf{r}}(\tilde{\mathbf{p}}, \alpha) = \begin{pmatrix} \mathbf{r}(\mathbf{p}, \boldsymbol{\theta}, \alpha) \\ \mathbf{r}_\theta(\boldsymbol{\theta}) \end{pmatrix} \text{ and } \tilde{\mathbf{V}} = \begin{pmatrix} \mathbf{V} & 0 \\ 0 & \Theta \end{pmatrix}. \tag{5.16}$$

The equation for the χ^2 track fit including the multiple scattering simply written as

$$\chi^2 = \tilde{\mathbf{r}}^T \tilde{\mathbf{V}}^{-1} \tilde{\mathbf{r}} \quad \text{where} \quad \tilde{\mathbf{r}} = \tilde{\mathbf{r}}(\tilde{\mathbf{p}}, \mathbf{a}). \tag{5.17}$$

So in effect the track is not defined just by the five parameters of its helix but also by a sequence of scattering angles attributed to each scattering plane it traverses.

This approach is used in the Global χ^2 track fitter [105] [106]. MCS effects are incorporated in the track model by allowing the track to kink on a finite number of multiple scattering planes.

Implicit scattering effects dependence

This approach eliminates the scattering angles from the χ^2 minimisation by directly including their contribution in the covariance matrix and residual vector. This is the approach used in the Global χ^2 alignment algorithm. The χ^2 used is the one in Equation 5.3 however the modifications are made. The covariance matrix is modified to take into account MCS

$$\mathbf{V} \rightarrow \mathbf{V} + \mathbf{V}_{MCS} \text{ where } \mathbf{V}_{MCS} = \frac{\partial \mathbf{r}}{\partial \boldsymbol{\theta}} \Theta \left(\frac{\partial \mathbf{r}}{\partial \boldsymbol{\theta}} \right)^T , \tag{5.18}$$

where $\mathbf{V}$ describes the intrinsic resolution of the measurement devices and it is diagonal by construction and $\mathbf{V}_{MCS}$ contains the scattering effects contribution. The vector $\partial \mathbf{r} / \partial \theta$ are the derivatives relating the deflection angles, $\boldsymbol{\theta}$, to the change of residual on the extrapolation to the consecutive measurement planes and $\boldsymbol{\Theta}$ is, as before, a diagonal matrix describing the expectations for the scattering angles derived from the expression A.8.

In addition to the changes to the covariance matrix the residuals have to be redefined to accommodate the scattered trajectory

$$\mathbf{r} \rightarrow \mathbf{r} + \frac{\partial \mathbf{r}}{\partial \boldsymbol{\theta}} \boldsymbol{\theta}. \tag{5.19}$$

As can be seen the new residuals again have a $\boldsymbol{\theta}$ dependence (i.e. $\mathbf{r} = \mathbf{r}(\mathbf{p}, \boldsymbol{\theta}, \boldsymbol{\alpha})$). As the scattering angles have not be calculated directly to use this technique a prior knowledge of the scattering angles is needed. In ATLAS the scattering angles are obtained from the initial track fit performed by the Global χ^2 track fitter.

5.3. Alignment of Super Structures

The alignment of “super structures” constructed from multiple modules plays an important role in the alignment of the ATLAS Inner Detector. By aligning the structures the statistical significance of the solution is increased, allowing for systematic effects to be studied in more detail and in a simpler manner. Using logical physical structures as super-structures, for example layers, discs etc., allows for the alignment results to be directly compared with survey measurements. Aligning super-structures also reduces the number of degrees of freedom of the system allowing for the solutions to the system to be calculated in a timely manner. This does have the effect of increasing the density of the matrix as reducing the number of structures that are being aligned will increase the correlation between the structures that being aligned.

The solution to the alignment parameters given in Equation 5.10 is a general solution to the alignment problem. To align the super-structures we can reinterpret Equation 5.10 so that we are now solving the alignment of the super structures, $\boldsymbol{\beta}$,

$$\boldsymbol{\beta}-\boldsymbol{\beta}_0 = -\left(\sum_{Tracks}\left(\frac{\partial \mathbf{r}}{\partial \boldsymbol{\beta}}\right)^T \hat{\mathbf{W}} \left(\frac{\partial \mathbf{r}}{\partial \boldsymbol{\beta}}\right)\right)^{-1} \sum_{Tracks}\left(\frac{\partial \mathbf{r}}{\partial \boldsymbol{\beta}}\right)^T \hat{\mathbf{W}}\cdot\mathbf{r}. \tag{5.20}$$

However, hidden in Equation 5.20 there is a dependence on the individual module alignment parameters ($\boldsymbol{\alpha}$) as the residuals are generally calculated in the local frame of reference of the individual modules. Rewriting

$$\frac{\partial \mathbf{r}}{\partial \boldsymbol{\beta}} \quad \text{as} \quad \frac{\partial \mathbf{r}}{\partial \boldsymbol{\alpha}}\frac{\partial \boldsymbol{\alpha}}{\partial \boldsymbol{\beta}},$$

Equation 5.20 transforms to

$$\begin{aligned}
\boldsymbol{\beta}-\boldsymbol{\beta}_0 &= -\left(\sum_{Tracks}\left(\frac{\partial \mathbf{r}}{\partial \boldsymbol{\alpha}}\frac{\partial \boldsymbol{\alpha}}{\partial \boldsymbol{\beta}}\right)^T \hat{\mathbf{W}} \left(\frac{\partial \mathbf{r}}{\partial \boldsymbol{\alpha}}\frac{\partial \boldsymbol{\alpha}}{\partial \boldsymbol{\beta}}\right)\right)^{-1} \cdot \\
&\quad \sum_{Tracks}\left(\frac{\partial \mathbf{r}}{\partial \boldsymbol{\alpha}}\frac{\partial \boldsymbol{\alpha}}{\partial \boldsymbol{\beta}}\right)^T \hat{\mathbf{W}}\cdot\mathbf{r} \qquad (5.21)\\
&= -\left(\left(\frac{\partial \boldsymbol{\alpha}}{\partial \boldsymbol{\beta}}\right)^T \sum_{Tracks}\left(\frac{\partial \mathbf{r}}{\partial \boldsymbol{\alpha}}\right)^T \hat{\mathbf{W}} \left(\frac{\partial \mathbf{r}}{\partial \boldsymbol{\alpha}}\right)\left(\frac{\partial \boldsymbol{\alpha}}{\partial \boldsymbol{\beta}}\right)\right)^{-1} \cdot \\
&\quad \left(\frac{\partial \boldsymbol{\alpha}}{\partial \boldsymbol{\beta}}\right)^T \sum_{Tracks}\left(\frac{\partial \mathbf{r}}{\partial \boldsymbol{\alpha}}\right)^T \hat{\mathbf{W}}\cdot\mathbf{r} \\
&= -\left(\left(\frac{\partial \boldsymbol{\alpha}}{\partial \boldsymbol{\beta}}\right)^T \mathscr{M} \left(\frac{\partial \boldsymbol{\alpha}}{\partial \boldsymbol{\beta}}\right)\right)^{-1} \left(\frac{\partial \boldsymbol{\alpha}}{\partial \boldsymbol{\beta}}\right)^T \mathscr{V}. \qquad (5.22)
\end{aligned}$$

The matrix $\partial\alpha/\partial\beta$ is a Jacobian describing how the local alignment parameters (α) vary with respect to that of the super structures alignment parameters (β). The solution of the super structure alignment parameter is a projection of the original problem and can be calculated in one of two ways. Using Equation 5.21 where the alignment parameters are calculated directly. Alternatively, one can define a matrix and vector with respect to the individual module alignment parameters and perform the projection onto the smaller system after all tracks have been processed. In this way, it is required to only once process the data to get many possible interpretations of the results. Comparison of these results can gain some insight into the systemic of the problem.

For the alignment of a super structure the residuals that are provided by the individual modules need to be translated into the reference frame of the super structure. The derivatives of the alignment parameters need to be determined with respect to the super-module parameters instead of the individual modules parameters.

5.4. Alignment Derivative Calculations

A key component of the least squares fit is the calculation of the derivative of the residuals with respect to the alignment parameters. This can be done either analytically or numerically. The choice of technique will depend on the individual situation. If working in a highly non linear magnetic field then analytical derivatives are very difficult to compute and thus a numerical calculation would be the clear choice. Exploring the analytical calculation of the derivatives helps in the understanding of the alignment procedure.

5.4.1. Transformation between coordinate frames

Consider the transformation between the global coordinate frame $\mathbf{x}$ to the local frame $\mathbf{x}'$ such that

$$\mathbf{x} = T + R\mathbf{x}', \tag{5.23}$$

where R and T are rotations and translations respectively. The combined operation of the rotation and translation will be called a transformation and represented by the symbol $\mathscr{T}$.

The subsequent transformations do not commute and as such

$$\mathscr{T}_0\mathscr{T}_1 \neq \mathscr{T}_1\mathscr{T}_0, \tag{5.24}$$

unless the rotations in either transformation are null.

5.4.2. Translations and Rotations

To define the position and orientation of a three dimensional object from a known reference point requires the knowledge of the transformation between the two reference frames. To define this transformation requires the knowledge of six parameters, those being three translations and a rotation describe by three parameters. In ATLAS the translations have been selected to be defined by movements in the cartesian frame (T_x, T_y, T_z) and by rotations around the cartesian axes (R_x, R_y, R_z).

It should be noted that although there are six possible degrees of freedom (DoF) per detector module, it might be impossible to determine all six of those DoF. The ability to determine all DoF is dependant on the read out geometry of the detector. For example if trying to align a drift tube it is impossible and also useless to determine the rotation of the wire long the wire axis.

A general rotation in three-dimensional Euclidean space can be decomposed into three successive rotations about the three orthogonal axis. In this case it was chosen to represent them as a rotation by an angle ϕ around the x-axis

$$R_x(\phi) = \begin{pmatrix} 1 & 0 & 0 \\ 0 & \cos\phi & -\sin\phi \\ 0 & \sin\phi & \cos\phi \end{pmatrix},$$

a rotation by an angle θ around the y-axis

$$R_y(\theta) = \begin{pmatrix} \cos\theta & 0 & \sin\theta \\ 0 & 1 & 0 \\ -\sin\theta & 0 & \cos\theta \end{pmatrix},$$

and a rotation by an angle ψ around the z-axis

$$R_z(\psi) = \begin{pmatrix} \cos\psi & -\sin\psi & 0 \\ \sin\psi & \cos\psi & 0 \\ 0 & 0 & 1 \end{pmatrix}.$$

The full rotation matrix $R = R_x R_y R_z$ can be expressed as

$$R(\phi,\theta,\psi) = \begin{pmatrix} \cos\theta\cos\psi & -\cos\theta\sin\psi & \sin\theta \\ \cos\phi\sin\psi + \sin\phi\sin\theta\cos\psi & \cos\phi\cos\psi - \sin\phi\sin\theta\sin\psi & -\sin\phi\cos\theta \\ \sin\phi\sin\psi - \cos\phi\sin\theta\cos\psi & \sin\phi\cos\psi - \cos\phi\sin\theta\sin\psi & \cos\phi\cos\theta \end{pmatrix}.$$

For the sake of simplicity it is often useful to consider the case when all angles are small. As such R can be approximated to

$$R = \begin{pmatrix} 1 & -\psi & \theta \\ \psi & 1 & -\phi \\ -\theta & \phi & 1 \end{pmatrix}.$$

5.4.3. Analytical derivatives

The accuracy of the residual derivatives with respect to the track and alignment parameters plays a very important role in the construction of the equations that describe the alignment problem. The residuals are calculated in the local measurement frame and it is wished to correct the misalignments of modules in the local measurement frame. The analytical calculation of the derivatives for alignment corrections in the local module frame can be found in this section (a derivation of the derivatives for alignment corrections in the global frame can be found in[55]).

Defining the track position in the measurement frame (local frame) as $\mathbf{x}' = (x', 0, 0)$ and consider a small change in position $(\delta_x, \delta_y, \delta_z)$. Then the change in the x component of point at which the track intersects the x-y plane of the becomes

$$\Delta x' = \delta_x - \delta_z \frac{n_x}{n_z}, \tag{5.25}$$

where (n_x, n_y, n_z) is the vector parallel to the track at the measurement planes surface. Hence the derivative of a residual with respect to a change in the position of the track in the measurement frame is given by

$$\begin{pmatrix} \partial r/\partial x' \\ \partial r/\partial y' \\ \partial r/\partial z' \end{pmatrix} = \begin{pmatrix} 1 \\ 0 \\ -n_x/n_z \end{pmatrix}.$$

Now consider the infinitesimal rotation $\delta R = 1 + \varphi$ and the infinitesimal translation $\delta T = \tau$ of the measurement frame

$$\mathbf{x}' \quad \rightarrow \quad \tau + (1+\varphi)\mathbf{x}'.$$

Observed in the global frame this becomes

$$\mathbf{x} \quad = \quad T + R(\tau + (1+\varphi)\mathbf{x}'), \tag{5.26}$$

for which the inverse transformation is given by

$$\begin{aligned} \mathbf{x}' &= (1+\varphi^T)R^T(\mathbf{x} - T - R\tau) \\ &= R^T(\mathbf{x} - T) - \tau + \varphi^T R^T(\mathbf{x} - T) + O(\varphi\tau). \end{aligned} \tag{5.27}$$

As such the results of the derivatives with resect to the translations are

$$\begin{pmatrix} \partial r/\partial \tau_x \\ \partial r/\partial \tau_y \\ \partial r/\partial \tau_z \end{pmatrix} = \begin{pmatrix} -1 \\ 0 \\ n_x/n_z \end{pmatrix}.$$

The result for the residual derivatives with respect to the rotations are

$$\begin{pmatrix} \partial r/\partial \varphi_x \\ \partial r/\partial \varphi_y \\ \partial r/\partial \varphi_z \end{pmatrix} = \begin{pmatrix} n_x/n_z\left[R^T_{xy}\Delta T_x + R^T_{yy}\Delta T_y + R^T_{zy}\Delta T_z\right] \\ -(R^T_{xz} + \frac{n_x}{n_z}R^T_{xx})\Delta T_x - (R^T_{yz} + \frac{n_x}{n_z}R^T_{yx})\Delta T_y - (R^T_{zz} + \frac{n_x}{n_z}R^T_{zx})\Delta T_z \\ R^T_{xy}\Delta T_x + R^T_{yy}\Delta T_y + R^T_{zy}\Delta T_z \end{pmatrix}, \quad (5.28)$$

where ΔT_i is the i^{th} component of the vector $\mathbf{x} - T$.

The expressions for the derivatives of the y-residual can be obtained in a similar fashion as the derivatives to those of the x-residuals. The result for the residual derivatives with respect to the translation are

$$\begin{pmatrix} \partial r/\partial \tau_x \\ \partial r/\partial \tau_y \\ \partial r/\partial \tau_z \end{pmatrix} = \begin{pmatrix} 0 \\ -1 \\ n_y/n_z \end{pmatrix}.$$

The result for the residual derivatives with respect to the rotations are

$$\begin{pmatrix} \partial r/\partial \varphi_x \\ \partial r/\partial \varphi_y \\ \partial r/\partial \varphi_z \end{pmatrix} = \begin{pmatrix} (R^T_{xz} + n_y/n_z R^T_{xy})\Delta T_x + (R^T_{yz} + n_y/n_z R^T_{yy})\Delta T_y + (R^T_{zz} + n_y/n_z R^T_{zy})\Delta T_z \\ -n_y/n_z(R^T_{xx}\Delta T_x + R^T_{yx}\Delta T_y + R^T_{zx}\Delta T_z) \\ -R^T_{xx}\Delta T_x - R^T_{yx}\Delta T_y - R^T_{zx}\Delta T_z \end{pmatrix}.$$

5.5. Constraining Systems of Linear Equations

The matrix produced by the alignment procedure is unfortunately symmetric semi positive definite. The singular nature of the matrix is a result of unconstrained global degrees of freedom, for example global rotations or translations of the system. These movements do not effect the residuals of the system, and hence the minimisation is not sensitive to them. In order to have a viable solution the unconstrained DoF need to be constrained. In the following section a number of different techniques will be presented for constraining the system of equations produced by the alignment procedure.

5.5.1. Alignment Parameter Constraints

How to apply constraints directly to the alignment parameters. Redefining the χ^2 to include the alignment parameter constraint

$$\chi^2 = \sum_{Tracks} \mathbf{r}^T \mathbf{V}^{-1} \mathbf{r} + (\boldsymbol{\alpha} - \boldsymbol{\alpha}')^T \mathbf{S}^{-1} (\boldsymbol{\alpha} - \boldsymbol{\alpha}'), \tag{5.29}$$

where $\boldsymbol{\alpha}'$ is the value of the alignment parameters which is wished to constrain and $\mathbf{S}$ is the covariance matrix of the constraint. Minimising the χ^2 with respect to the alignment parameters leads to

$$0 \ = \ \sum_{Tracks} \frac{d\mathbf{r}^T}{d\boldsymbol{\alpha}} \mathbf{W} \left(\mathbf{r}(\mathbf{p}_0, \boldsymbol{\alpha}_0) + \frac{d\mathbf{r}}{d\boldsymbol{\alpha}_0} (\boldsymbol{\alpha} - \boldsymbol{\alpha_0}) \right) + \mathbf{S}^{-1} (\boldsymbol{\alpha} - \boldsymbol{\alpha}'). \tag{5.30}$$

If it is assume that we wish to constrain the parameters to current positions i.e. $\boldsymbol{\alpha}' = \boldsymbol{\alpha}_0$ then solution is quite simple.

$$0 = \left(\sum_{Tracks} \frac{d\mathbf{r}^T}{d\boldsymbol{\alpha}} \mathbf{W} \frac{d\mathbf{r}}{d\boldsymbol{\alpha}_0} + \mathbf{S}^{-1} \right) (\boldsymbol{\alpha} - \boldsymbol{\alpha_0}) + \sum_{Tracks} \frac{d\mathbf{r}^T}{d\boldsymbol{\alpha}} \mathbf{W} \cdot \mathbf{r}(\mathbf{p}_0, \boldsymbol{\alpha}_0). \tag{5.31}$$

Upon comparing this result to the basic alignment solution shown in Equation 5.6 it is clear that $\mathscr{M} \rightarrow \mathscr{M} + \mathbf{S}^{-1}$. Evidently the better defined the matrix $\mathscr{M}$ is (i.e. the more tracks used) the lower the influence of the alignment parameter constraint.

The matrix $\mathscr{M}$ can be diagonlised and written as $\mathscr{M} = \mathbf{PDP}^T$ (see Section 5.6.1). Also as $\mathbf{P}$ is a square matrix, assuming that the constraint covariance matrix $\mathbf{S} \propto 1$ then it can be written that

$$\mathbf{PDP}^T \rightarrow \mathbf{P}(\mathbf{D} + \mathbf{S}^{-1})\mathbf{P}^T. \tag{5.32}$$

Therefore constraining the alignment parameters has the effect of increasing the eigenvalues of the matrix $\mathscr{M}$. As the eigenvalues of $\mathscr{M}$ are non-negative any addition of an identity like matrix is going to ensure that the matrix is positive definite and hence the problem becomes soluble.

This method of constraining the track parameters is the simplest form of the constraint, but can be generalised so that movements of groups of modules are constrained to some level of certainty and as such the χ^2 for this constrained system is represented by

$$\chi^2 = \sum_{Tracks} \mathbf{r}^T \mathbf{V}^{-1} \mathbf{r} + \mathbf{G}(\alpha)^T \mathbf{S}^{-1} \mathbf{G}(\alpha), \tag{5.33}$$

where $\mathbf{G}(\alpha)$ describes the constraint and $\mathbf{S}$ is the covariance matrix for the constraint.

5.5.2. Track Parameter Constraints

Constraining the individual parameters of each track is useful when trying to remove systematic distortions and/or reduce the chance of introducing them. If there is a reliable secondary measurement of a track parameter, for example the momentum, it is possible to constrain the momentum of the track by adding an appropriate term to the matrix. However, any systematic biases in the secondary measurement would result in biases to the system alignment. Biases must be identified and understood before the use of such a technique.

χ^2 is redefined to include the track parameter constraint:

$$\chi^2 = \sum_{Tracks} \mathbf{r}^T \mathbf{V}^{-1} \mathbf{r} + (\mathbf{p} - \mathbf{p}')^T \mathbf{S}^{-1} (\mathbf{p} - \mathbf{p}'), \tag{5.34}$$

where $\mathbf{p}'$ is the track parameter to be constrained and $\mathbf{S}$ is the covariance which defines the constraint of the track parameters, $\mathbf{p}$. The solution to the constrained track fit is

$$\begin{aligned} \tilde{\mathbf{p}} - \mathbf{p}_0 &= -(\mathbf{A}^T \mathbf{W} \mathbf{A} + \mathbf{S}^{-1})^{-1} (\mathbf{A}^T \mathbf{W} \cdot \mathbf{r}(\mathbf{p_0}) + \mathbf{S}^{-1} (\mathbf{p_0} - \mathbf{p}')) \\ &= -\mathbf{J}^{-1} (\mathbf{A}^T \mathbf{W} \cdot \mathbf{r}(\mathbf{p_0}) + \mathbf{S}^{-1} (\mathbf{p_0} - \mathbf{p}')). \end{aligned} \tag{5.35}$$

Following in a manner similar used to obtain basic solution of the alignment parameters (Equation 5.10), it can shown that the solutions to the alignment parameter corrections, with application of a track parameter constraint[104] can be represented as

$$\begin{aligned}\boldsymbol{\alpha}-\boldsymbol{\alpha}_0 = -&\left(\sum_{tracks}\frac{\partial \mathbf{r}^T}{\partial \boldsymbol{\alpha}}\hat{\mathbf{W}}\frac{\partial \mathbf{r}}{\partial \boldsymbol{\alpha}}\right)^{-1}\\ &\left[\sum_{tracks}\frac{\partial \mathbf{r}^T}{\partial \boldsymbol{\alpha}}\left(\hat{\mathbf{W}}+\mathbf{WAJ}^{-1}\mathbf{S}^{-1}\mathbf{J}^{-1}\mathbf{A}^{\mathrm{T}}\mathbf{W}\right)r\right.\\ &\left.+\sum_{tracks}\frac{\partial \mathbf{r}^T}{\partial \boldsymbol{\alpha}}\mathbf{WAJ}^{-1}\mathbf{S}^{-1}(\mathbf{J}^{-1}\mathbf{S}^{-1}-\mathbf{1})(\mathbf{p}-\mathbf{p}')\right],\end{aligned}$$

where $\hat{\mathbf{W}}$ is now defined as

$$\hat{\mathbf{W}} = \mathbf{W} - \mathbf{WAJ}^{-1}\mathbf{A}^{\mathrm{T}}\mathbf{W}. \tag{5.36}$$

Clearly if one wanted to completely fix a track parameter it would be possible to do so by removing it from the matrix **A** which contains the first derivative track parameters. This technique can be used to apply a vertex constraint if the prior knowledge of the vertex is known.

5.5.3. Lagrange Multipliers

The method of Lagrange multipliers (LM) is a powerful tool for finding the maxima or minima of function for a given constraint. In general the constraint can be non-linear, and linearised using a Taylor series expansion around initial values with higher terms being ignored.

To illustrate how LM are applied to a χ^2 problem consider a simplified example

$$\chi^2 = \mathbf{r}^T\mathbf{V}^{-1}\mathbf{r}, \tag{5.37}$$

where $\mathbf{r}$ is the residual and is defined by $\mathbf{r} = \mathbf{m} - \mathbf{Hx}$. Where $\mathbf{m}$ is a measurement vector, $\mathbf{H}$ is the linear measurement model and $\mathbf{x}$ is the vector of parameters to be estimated. Finding the minimum of χ^2 we obtain

$$\Delta\mathbf{x} \quad = \quad -(\mathbf{H}^T\mathbf{V}^{-1}\mathbf{H})^{-1}\mathbf{H}^T\mathbf{V}^{-1}\mathbf{r}(\mathbf{x}_0). \tag{5.38}$$

Applying a linearised constraint of the form $\mathbf{Bx}-\mathbf{b}=0$ transforms the χ^2 to

$$\chi^2 = \mathbf{r}^T\mathbf{V}^{-1}\mathbf{r} + 2\boldsymbol{\lambda}^T(\mathbf{Bx}-\mathbf{b}), \tag{5.39}$$

where $\boldsymbol{\lambda}$ are the Lagrange multipliers and are just constants which indicate the amount of work required to enforce the constraint. When minimised with respect to $\mathbf{x}$ yields the following

$$\begin{aligned} \frac{d\chi^2}{d\mathbf{x}} &= 0 \\ 0 &= \mathbf{Cx}-\mathbf{c}+\mathbf{B}^T\boldsymbol{\lambda} && (5.40) \\ & && (5.41) \end{aligned}$$

where $\mathbf{C}=\mathbf{H}^T\mathbf{V}^{-1}\mathbf{H}$ and $\mathbf{c}=\mathbf{H}^T\mathbf{V}^{-1}\mathbf{r}(\mathbf{x}_0)$. Solving for the parameters of the system:

$$\begin{aligned} \Delta x_c &= -(\mathbf{H}^T\mathbf{V}^{-1}\mathbf{H})^{-1}\mathbf{H}^T\mathbf{V}^{-1}\mathbf{r}(\mathbf{x}_0) + (\mathbf{H}^T\mathbf{V}^{-1}\mathbf{H})^{-1}\mathbf{B}^T\boldsymbol{\lambda} && (5.42) \\ &= \Delta\mathbf{x} + (\mathbf{A}^T\mathbf{V}^{-1}\mathbf{H})^{-1}\mathbf{B}^T\boldsymbol{\lambda}. && (5.43) \end{aligned}$$

Solving for $\boldsymbol{\lambda}$ yields

$$\boldsymbol{\lambda} = \left[\mathbf{B}(\mathbf{H}^T\mathbf{V}^{-1}\mathbf{H})^{-1}\mathbf{B}^T\right]^{-1}(\mathbf{Bx}-\mathbf{b}). \tag{5.44}$$

The Lagrange Multipliers constrained χ^2 estimator can be seen as just a corrected version of the unconstrained least squares estimator.

This can be applied to the system of equations in the following way

$$\begin{pmatrix} \mathbf{C} & \mathbf{B}^T \\ \mathbf{B} & 0 \end{pmatrix} \begin{pmatrix} \mathbf{x} \\ \boldsymbol{\lambda} \end{pmatrix} = \begin{pmatrix} \mathbf{c} \\ \mathbf{b} \end{pmatrix}. \tag{5.45}$$

The big advantage of this technique lies in the fact that the sparsity of the matrix is well preserved although the size of the matrix will increase by the number of constraints applied. There is a price to be paid which is the freezing of the constrained shape into the detector. As no uncertainty can be applied to the constraint it is absolute. This is not ideal for alignment. Each constraint must be evaluated to ensure that the shape is not in fact a true misalignment of the detector. However, LM can be used to give the system of equations a frame of reference and to remove degrees of freedom that the system is relatively insensitive to thereby allowing for a well defined solution.

5.5.4. Eliminating/Fixing modules

Often there is a need to eliminate certain modules from the alignment problem. This may be because the modules do not have enough hits or the data from a module is deemed to be unreliable.

There are two very different ways to remove modules:

- Removing the unwanted modules from the detector setup, the tracks are fit without the hit information corresponding to the eliminated modules.
- Removing the corresponding modules from the solution, by discarding the rows and columns from the matrix $\mathscr{M}$ and contracting the vector $\mathscr{V}$.

The difference between the two methods have direct consequences for the properties of the alignment solution. In the first method the removal of a module is complete and the removed modules will have no influence on the final alignment and the remaining system preserves all genuine features.

In the second method, the *a posteriori* removal of the module will alter the basic properties of the solution. In particular the singularity of the solution may be eliminated. Consider a χ^2-invariant mode which is described by an eigenvector $\mathscr{S}$ (see Section 5.6.1 for further details). Assume that the mode involves the module l that we want to discard from the solution. We have

$$\mathscr{M}\mathscr{S} = 0. \tag{5.46}$$

We can discard the rows and columns associated to the module l from the matrix $\mathscr{M}$ as well as from the eigenvector S, and call them $\mathscr{M}$ and $\mathscr{S}$ respectively. If $\mathscr{S}$ was to remain a singular mode of M, it is needed for each i $\sum_j \mathscr{M}_{ij}S_j = 0$ and for each $i \neq l$ $\sum_{j \neq l} \mathscr{M}_{ij}\mathscr{S}_j = 0$. This implies that for each $i \neq l$ $\mathscr{M}_{il} = \mathscr{M}_{li} = 0$, and as such module l has no correlation to any other module. Such a situation would be impossible in this alignment procedure. Consequently, the mode $\mathscr{S}$ will cease to be singular due to elimination of a relevant degree of freedom. Technically, such an *a posteriori* elimination is equivalent to freezing of the corresponding degrees of freedom, which has consequences for the rest of the system. In particular the system will not be free to move in its global six DoF's as some elements have been pinned down and immobilised.

5.6. Linear equation manipulation

To find the correction to the alignment parameters, Equation 5.10 needs to be solved for $\Delta\alpha$. Using this alignment technique on a detector system as large and complex as the ATLAS Inner Detector will require the solution of a large system of equations ($\sim 35000 \times 35000$). There are a number of ways to solve such problems, but firstly let's simplify the notation by defining the minimization problem in the simplified form $\mathscr{M}\delta\boldsymbol{\alpha} = \mathscr{V}$. Solving such a large system in the general case on a single computer is practically impossible due to the memory requirements and the CPU time required to solve such a problem. The amount of memory used and time required to solve the problem can be reduced by utilizing some of the properties of the matrix $\mathscr{M}$.

5.6.1. Eigenvalues

The eigenvalue distribution of the matrix provides information about the "weak modes" of the system. These weak modes are linear combinations of alignment parameters that are relatively poorly constrained or χ^2-invariant. The matrix $\mathscr{M}$ is square and can be written as

$$\mathscr{M} = \mathbf{P}\mathbf{D}\mathbf{P}^{-1}, \tag{5.47}$$

and in the case of a real symmetric matrix

$$\mathscr{M} = \mathbf{P}\mathbf{D}\mathbf{P}^{T}, \tag{5.48}$$

where $\mathbf{P}$ is an orthogonal matrix (i.e. $\mathbf{P}^T = \mathbf{P}^{-1}$) whose columns are the eigenvector of $\mathscr{M}$, and $\mathbf{D}$ is a diagonal matrix whose entries are the eigenvalues of $\mathscr{M}$. This process is called diagonalisation and it is clear to see that the matrix $\mathscr{M}$ is invertible (hence a solution for x can be found) only if all of the eigenvalues are non-zero.

Diagonalisation is a non trivial process, however there are a number of packages that provide a solution, for example, LAPACK's `DSPEV`[107]. Assuming diagonalisation can be performed, the solution is quite trivial.

$$\delta\boldsymbol{\alpha} = \mathscr{M}^{-1}\mathscr{V} = \mathbf{P}\mathbf{D}^{-1}\mathbf{P}^{T}\mathscr{V}. \tag{5.49}$$

As the reciprocal of the eigenvalues can be seen to appear in the solution, the smallest eigenvalues will lead to a large statistical uncertainty in $\delta\boldsymbol{\alpha}$. To illustrate this inspect the covariance matrix for $\delta\boldsymbol{\alpha}$, which is the inverse of matrix $\mathscr{M}$.

$$COV(\delta\boldsymbol{\alpha}) = \mathscr{M}^{-1} = \mathbf{P}\mathbf{D}^{-1}\mathbf{P}^{T}. \tag{5.50}$$

The diagonal elements of the matrix $\mathscr{M}^{-1}$ are the variance of the alignment parameters. Thus if any of the eigenvalues of $\mathscr{M}$ are small, this will then translate to a large value in D^{-1} and hence the variance of $\delta\boldsymbol{\alpha}$.

In the case of an under-constrained system a number of the eigenvalues can be near-zero with a subset or all of the parameters $\boldsymbol{\alpha}$ having infinitely large uncertainty. An example of such a situation is a global transformation. This would leave the χ^2 unchanged. If such degrees of freedom are not removed from the system of equations, the number of solutions would be infinite (see Section 5.5 for further details).

A method of removing the poorly constrained degrees of freedom is by omitting certain eigenmodes from the solution. This is accomplished by limiting the sum in the Equation 5.51, which is just a reinterpretation of Equation 5.49

$$\delta\boldsymbol{\alpha} = \sum_{j} \frac{\langle p^{j}, \mathscr{V} \rangle}{d_{j}} p^{j}, \tag{5.51}$$

where $\langle , \rangle$ is the inner product, $d_j \equiv D_{jj}$ and $p_i^j \equiv P_{ij}$. This seems quite a simple solution but it is necessary to determine at what point to set the threshold. In addition it should be noted that the scale of eigenvalues can be changed.

5.6.2. Rescaling the System

Rescaling the eigenvalue spectrum can help iterative techniques reach a solution quicker by transforming the matrix $\mathscr{M}$ into something closer to the identity matrix. The key to any preconditioning is that it must be quick.

Rescaling with approximate solutions

$$S\mathscr{M}\delta\alpha = S\mathscr{V}. \tag{5.52}$$

If S is approximately $\mathscr{M}^{-1}$ then the matrix $S\mathscr{M}$ will approximately equal I. This situation is ideal for iterative solvers, but as the matrix is no longer symmetric, it will generally make calculation of the solution more computationally intensive

Rescaling with approximate Cholesky factorization

To leave the matrix symmetric the following transforms need to be applied

$$(S\mathscr{M}S^T)(S^{-T}x) = S\mathscr{V}, \tag{5.53}$$

where S is a square matrix of rank equal to that of $\mathscr{M}$. If the matrix is symmetric positive definite it is possible to decompose the matrix to

$$\mathscr{M} = LL^T, \tag{5.54}$$

where L is a lower triangular matrix. This is known a Cholesky decomposition. A full Cholesky decomposition can take as long as a matrix inversion . Using an approximate Cholesky factorization technique we are able rescale the matrix and keep it symmetric.

Giving the eigenvalues meaning

The matrix can not only be rescaled to reduce the computation time required, but can also be rescaled to give the eigenvalues meaning. Defining S in Equation 5.53

$$S_{i,i} = \sqrt{\frac{N_{hits}}{\mathscr{M}_{i,i}}}, \tag{5.55}$$

the system has been rescaled proportional to the number of hits in each module, N_{hits}. In the extreme, and unlikely, case when $\mathscr{M}$ is diagonal the eigenvalues of the matrix are equal to the number of hits in the module.

5.7. Solving Large Systems of Linear Equations

When solving a linear system of equations the properties of the matrix determine which solution technique should be used. As described earlier, the matrix produced during alignment is symmetric, and without constraints, singular. The various constraint techniques can change the matrix type into a positive definite or a definite matrix. Practical experience shows that without any preconditioning the matrix will also be poorly conditioned i.e. the eigenvalues are spread over in excess of ten orders of magnitude.

Finding a solution to a system with a large number of DoF is both computationally and memory intensive. The size and condition of the matrix machine may also require machine precision to be taken into account when choosing a solution technique.

5.7.1. Diagonalisation of the matrix

There are a number of software packages that are able to provide a solution, for example, LAPACK's `DSPEV`[107]. The computation time for diagonalisation in general, scales as $O(DoF^3)$. Solving for very large systems soon becomes untenable on a single machine, so studies have been performed with parallel computing[108]. Parallel computing, given enough resources, will allow for digonalisation to be performed on large systems of equations. They do however require some effort to setup and operate but given the recent trend towards multi-core CPU development this type of technique might again become favorable.

5.7.2. Solvers

Linear equation solvers have been developed to solve large systems of linear equations for a variety of different applications. Most of the techniques have been developed with a rather specific problem in mind so the selection of the correct technique can improve the computation time significantly. A common feature seen in almost all of the solvers is that they do not directly invert the matrix but obtain a solution to the problem, in the process reducing the computation time and memory required. The solvers discussed utilise the matrix's sparsity to reduce the computation time of the solution.

Iterative Solvers

Iterative solvers, in general, do not try and compute the inverse of the matrix but rather try to calculate the solution vector x which minimises $\parallel Ax - b \parallel$, where A is the matrix and b is the vector. Computation time for this type of procedure varies but generally scales as $O(DoF^2)$ or better. The memory requirements for iterative solvers are considerably lower than that of diagonalisation or inversion. `MINRES`[109] is one such package that solves sparse symmetric linear.

It has been reported by the CMS alignment team that for a 12015 × 12015 matrix, an inversion took ~ 12 hours while the MINRES only took 32 seconds[101]. Initial trials using `MINRES` were quite disappointing taking almost as long to solve the system using the iterative approach as the full inversion.

To reduce the computation time, approximate solutions to the matrix inversion can be used to improve the condition of the matrix. It was found that preconditioning the matrix using an approximate Cholesky factorization routine significantly reduced the number of iterations required for the system to converge but the performance was still nowhere near what the CMS team were able to obtain. Other iterative packages optimized for such a process include the routines `F11JAF` `F11JCF` in the NAG package[110]. Using this package it was possible to solve the system in a time that was comparable to that of the CMS result.

Singularities within the matrix can pose a significant problem for iterative solvers as $\| \Delta x \|$, which generally serves as part of the termination criteria, can continue to be large whilst the magnitude of the residual ($\| Ax - b \|$) can be small.

A comparison of the performance of two iterative techniques as applied to the ATLAS alignment problem a can be seen in Figure 5.1. It shows that time taken is significantly lower than that of full diagonalisation. However beyond 10,000 DoF the algorithms struggle.

Direct Solvers

In recent years a number of direct solvers for large, sparse and symmetric systems have been developed. A critical review of the performance of a number of solvers was undertaken in[111]. Two of the solvers evaluated `MA57`[112] and `PARDISO`[113, 114], produced the best results for indefinite matrixes.

Both `PARDISO` and the precursor to `MA57`, `MA27` [115], were tested on matrices created using the global alignment procedure. Both were found to be very efficient at solving a problem that took nearly an hour using diagonalization in less than ten seconds. Using such a procedure on a 35000×35000 matrix takes less than 2 minutes (see Figure 5.1). It is also clear to see that the more modern `PARDISO` has a significant advantage over `MA27` once the matrix is larger than $15,000 \times 15,000$.

Unlike the majority of iterative techniques, singularities do not pose a significant problem for the majority of direct solvers as most have been developed to identify singularities and remove them from the solution.

It is possible to calculate some of the eigenvalues and their corresponding eigenvectors of the system by combining `PARDISO` and `ARPACK`[116]. This can be useful in identifying the lingering χ^2-invariant modes of the system. The time required to calculate the eigenvalues and eigenvectors is very dependant of the structure the eigenvalue spectrum. For example, if the ten smallest eigenvalues are relatively close to each other and the eleventh is orders of magnitude larger it would take a considerably longer to calculate the first eleven eigenvalues than the first ten.

A cautionary note about sparse direct solvers. The amount of time and memory required to compute a solution is heavily dependant on the density and structure of the matrix. If for example the density of the matrix > 10% then for a 20k×20k the memory requirements will exceed the capabilities of a 32 bit machine. In general use of a sparse symmetric solver was found to be very advantageous when solving for large systems (DoF> 5000) as it allowed a solution to be calculated in reasonable time on a single computer.

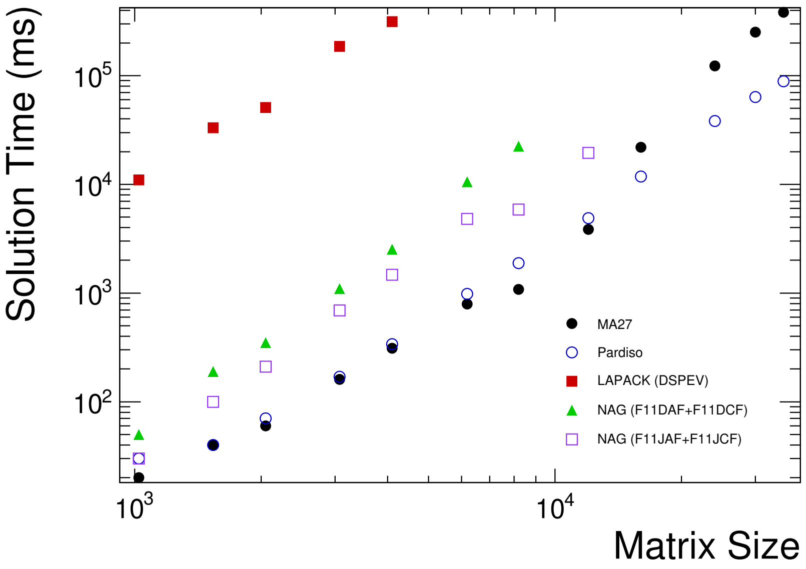

Figure 5.1.: Solution time of various linear equation solvers. The `LAPACK` diagonalisation routine `DSPEV` is represented by red solid squares. Two iterative solution techniques from NAG are shown. `F11DAF+F11DCF` a conjugate gradient squared method using incomplete LU factorisation preconditioning (solid green triangles). `F11JAF+F11JCF` iterative Lanczos method with incomplete Cholesky factorisation preconditioning (open violet squares). The sparse direct techniques `MA27` and `PARDISO` are represented by the solid black circles and the open blue circles, respectively. All test were performed using symmetric positive definite matrices with 32-bit binaries on an Intel Core 2 Duo CPU E6850 running at 3.0 GHz with 8 GB of memory.

6

CHAPTER

ALIGNMENT OF A TOY MODEL

To improve our understanding of properties of the alignment problem and their implications, a study of the alignment of a "toy model" is performed and presented in this chapter. This simplified model allowed for an in-depth study of the properties of the alignment problem in a very controlled manner. In the first section a description of the toy model and its geometrical properties are outlined. In Section 6.2 the derivatives of the alignment parameters of the toy model are presented. In Section 6.3 the properties of the alignment matrix are discussed, and in Section 6.4 possible methods of constraining the detector are investigated. Finally in Section 6.5 the accuracy of the alignment parameters are explored in addition to their impact on the quality of the reconstructed tracks.

6.1. Toy Model Geometry

To investigate the properties of the alignment problem a simplified model was created. The model consisted of ten planes each with one module, each separated by 50 *mm*

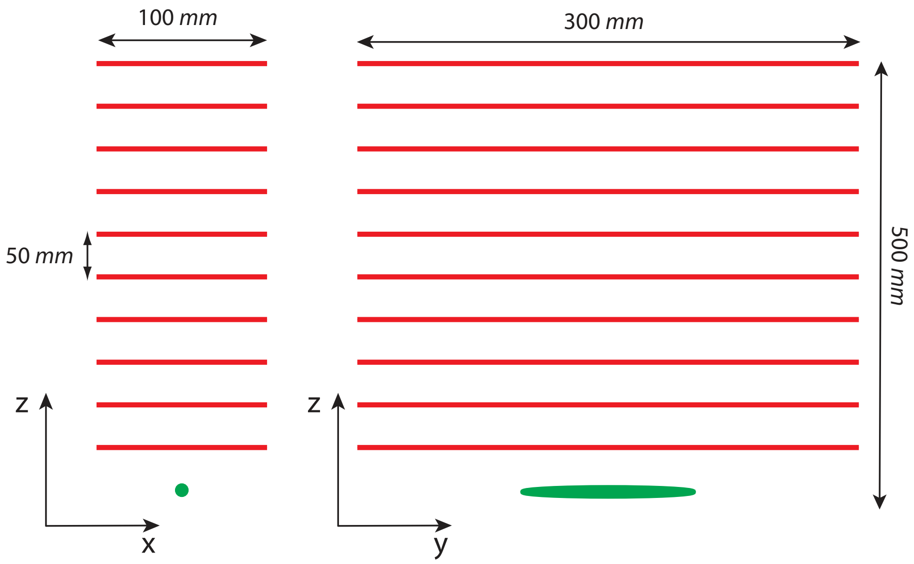

Figure 6.1.: Schematic diagram of the layout of the toy model containing 10 planes. The green dots represent the beam spot and the red line represent the detector planes.

Description	Value
Module Dimensions	Width = 100 mm
	Height = 300 mm
	Separation = 50 mm
Hit Resolution	x = 10 μm
	y = 30 μm
Module Hit Efficiency	98%
Misalignment Magnitudes	$x, y, z \sim 100\ \mu m$
	$R_x, R_y, R_z \sim 2\ mrad$

Table 6.1.: The toy model's geometrical parameters

(see Figure 6.1). The dimensions of each detector module are 100 $mm \times 300\ mm$ with a resolution 10 μm in the x direction and 50 μm in the y direction.

Each detector module was randomly misaligned in the local frame of the module. All translational misalignments were taken from Gaussian distribution with a mean of zero and $\sigma = 100\ \mu m$. All rotational misalignment were taken from a Gaussian distribution with a mean of zero and $\sigma = 2\ mrad$.

The study presented here uses a linear track model of a particle in the absence of any magnetic field giving the track four degrees of freedom. The tracks originate from $x = 0 \pm 50\ mm$, $y = 0 \pm 50\ mm$, $z = 0 \pm 10\ \mu m$, with the first detector plane 50 mm from the beam spot. This is similar to the situation expected in the barrel of the ATLAS Inner Detector.

6.2. Derivatives in the Toy Model

The derivatives of the track parameters are quite simple as the track model is linear. As such

$$f(\mathbf{p}) = f(m_x, c_x, m_y, c_y). \tag{6.1}$$

The x position of the track at any given the z position is

$$x = m_x\, z + c_x. \tag{6.2}$$

Similarly the y position is given by

$$y = m_y\, z + c_y. \tag{6.3}$$

Hence the derivatives of the track with respect to the track parameters are

$$\begin{aligned} \frac{df(\mathbf{p})}{dm_x} &= z, & \frac{df(\mathbf{p})}{dc_x} &= 1, \\ \frac{df(\mathbf{p})}{dm_y} &= z, & \frac{df(\mathbf{p})}{dc_y} &= 1. \end{aligned} \tag{6.4}$$

To calculate the derivatives of the alignment parameters of the toy model we exploit the inherit simplicity of the model. To transform a measurement from the local frame of the module to the global frame of the detector only a simple translation is required $(0, 0, z_{plane})$. Thus making $\Delta T = (x, y, 0)$ (see Equation 5.28).

Hence the derivatives of the x residuals with respect to the translations are

$$\begin{pmatrix} \partial r/\partial \tau_x \\ \partial r/\partial \tau_y \\ \partial r/\partial \tau_z \end{pmatrix} = \begin{pmatrix} -1 \\ 0 \\ n_x/n_z \end{pmatrix},$$

and the residual derivatives with repsect to the rotations are

$$\begin{pmatrix} \partial r/\partial \phi_x \\ \partial r/\partial \phi_y \\ \partial r/\partial \phi_z \end{pmatrix} = \begin{pmatrix} (n_x/n_z)y \\ -(n_x/n_z)x \\ y \end{pmatrix}. \tag{6.5}$$

Similarly the derivatives for the y residual with respect to the translations are

$$\begin{pmatrix} \partial r/\partial \tau_x \\ \partial r/\partial \tau_y \\ \partial r/\partial \tau_z \end{pmatrix} = \begin{pmatrix} 0 \\ -1 \\ n_y/n_z \end{pmatrix},$$

and the derivatives with respect to the rotations are

$$\begin{pmatrix} \partial r/\partial \phi_x \\ \partial r/\partial \phi_y \\ \partial r/\partial \phi_z \end{pmatrix} = \begin{pmatrix} (n_y/n_z)y \\ -(n_y/n_z)x \\ -x \end{pmatrix}. \tag{6.6}$$

The derivatives indicate that three alignment parameters(T_x, T_y and R_z) are directly related to the measurement and three (T_z, R_x and R_y) are indirectly related. As a result the alignment procedure is more sensitive to parameters T_x, T_y and R_z and less sensitive T_z, R_x and R_y.

6.3. Properties of the Alignment Matrix

The properties of the alignment matrix (see Equation 5.13) play a vital role in assessing techniques for the calculation of the alignment parameters. Without any modifica-

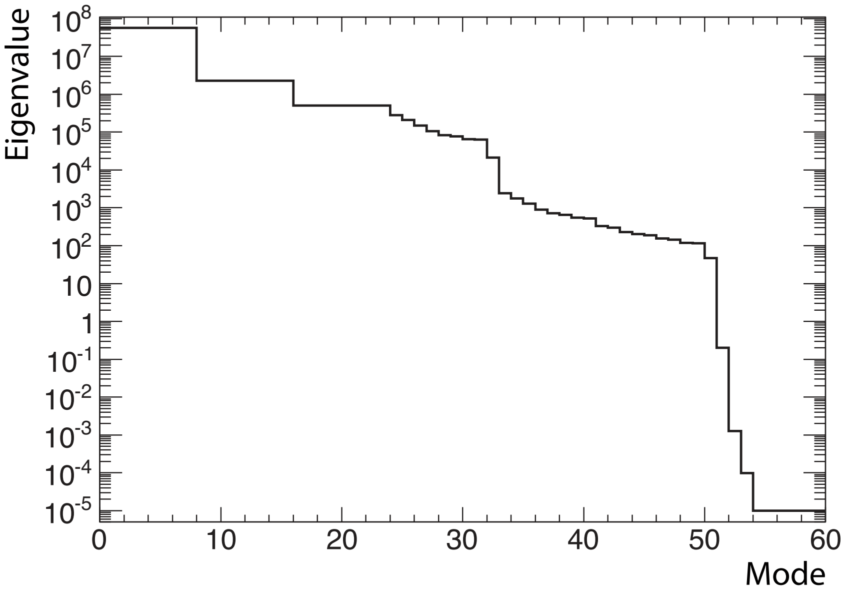

Figure 6.2.: The eigenvalues of the toy model. Note to aid the visulisation, eigenvalues below 10^{-5} have been set to 10^{-5}

tion the matrix is singular and consequently the problem is ill defined. To understand why the matrix is singular it is informative to look at the eigenvalues and eigenvectors of the matrix.

6.3.1. Eigenvalues and Eigenvectors

The alignment matrix is symmetric and can be diagonalised to obtain the eigenvalues and associated eigenvector of the matrix (see Section 5.6.1 for details). Shown in Figure 6.2 are the eigenvalues of the toy model for a perfectly aligned detector using 10,000 tracks. Of note are the nine eigenvalues (Mode 50 and above in Figure 6.2) which are significantly smaller than the remainder of the eigenvalues. These eigenvalues correspond to nine poorly constrained degrees of freedom. The eigenvectors associated to the small eigenvalues show which of the detector movements are not constrained by the data. Figure 6.3 displays the eigenvectors corresponding to the nine smallest eigenvalues. Six of the eigenvectors display the global translations or rotations of the detector and are a direct result of the alignment system not having a frame of reference fixed in space.

The remaining three poorly constrained degrees of freedom are caused by the choice of track model. There are coordinated movements of the detector modules that leave the final χ^2 of all tracks invariant but will distort the measured track parameters. These are exactly the type of detector distortions which need to be controlled and understood as they are not able to be corrected via track based alignment. The distortions that will allow for the χ^2 to be invariant are of the same type as the track model, and hence are linear ($T_i \propto mz + c$). This leads to six degrees of freedom, three of which (the constant translations) are identical to the global translations ($T_i \propto c$) while the other three are new degrees of the system and are of the form $T_i \propto mz$.

If, instead, the track model is helical, and thus approximately parabolic in the bending plane and linear in the non bending plane (see Section 4.3.3), an additional unconstrained degree of freedom arises. Assuming a barrel like system, with $x \sim r\phi$, $z = r$ and $y = z$. There is an additional degenerate degree of freedom corresponding to detector movements of the type $T_{r\phi} \propto r^2$. This additional degree of freedom can be removed if a mix of both straight and parabolic tracks are used. However, in reality turning off the magnetic field may cause the detector move so cannot be considered. As such it should be treated like all other poorly constrained degrees of freedom.

The other noteworthy observation is the structure of the eigenvalue spectrum. There is a number of distinct steps in the spectrum where each block of eigenvalues corresponds to movements of particular degrees of freedom of the system. For example the first eight eigenvalues correspond to the translations in the x direction of the module. The cause of these steps is quite simple to explain. The eigenvalues are inversely proportional to the uncertainty of the movement represented in the eigenvector. Given that each module has the same number of hits in it the statistical uncertainty of each like correction is going to be approximately same for each module. Hence the eigenvalues associated to each movement type are similar in magnitude. The small variations in them seen beyond the first three plateau's are caused by the fact that the derivatives of the alignment parameters depend on the position at which the track intersects the surface of the module. As each module is not illuminated in a spatially uniform manner, the eigenvalues differ.

As each module has six degrees of freedom and there are ten modules, it would be expected that there would six blocks each consisting of ten eigenvalues. However, some movements are degenerate (e.g. global rotations) which reduces the number of eigenvalues per block. In order to have a stable and viable solution the nine

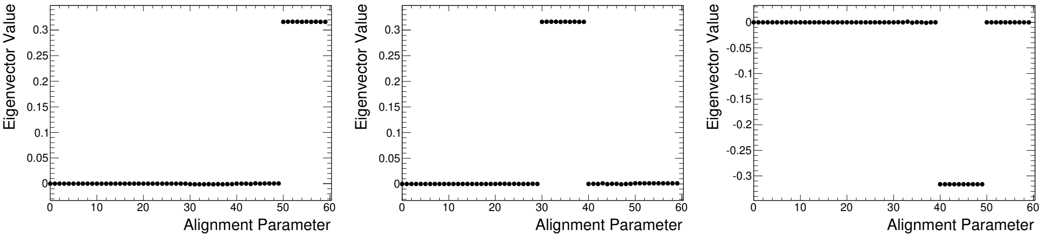

(a) Eigenvector 60: $\Delta R_z \approx c$ **(b)** Eigenvector 59: $\Delta R_x \approx c$ **(c)** Eigenvector 58: $\Delta R_y \approx c$

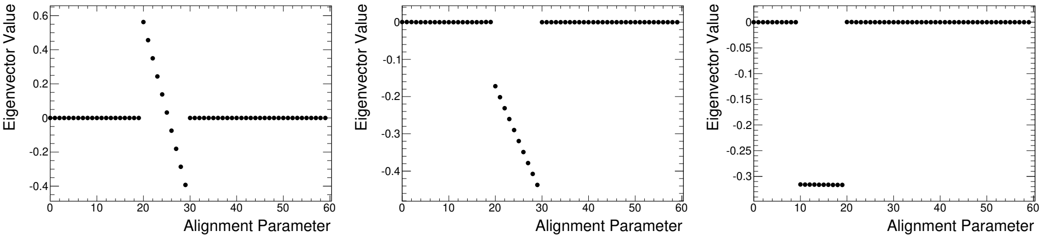

(d) Eigenvector 57: $\Delta T_z \propto z$ **(e)** Eigenvector 56: $\Delta T_z \propto z$ **(f)** Eigenvector 55: $\Delta T_y \approx c$

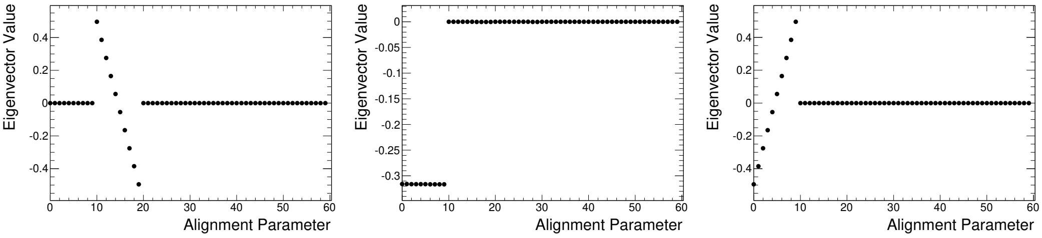

(g) Eigenvector 54: $\Delta T_y \propto z$ **(h)** Eigenvector 53: $\Delta T_x \approx c$ **(i)** Eigenvector 52: $\Delta T_x \propto z$

Figure 6.3.: The eigenvectors of the alignment matrix corresponding to the nine smallest eigenvalues from the unconstrained toy model. Along the x axis of each plot are the alignment parameters while the y axis shows magnitude of the correction. The first ten parameters correspond to a translations in the x direction of the 10 modules, parameters 11-20 correspond to the translation in the y direction, parameters 21-30 correspond a translation in z direction, parameters 31-40 correspond to a rotations around the x-axis, parameters 41-50 correspond the rotations around the y-axis, and parameters 51-60 correspond a rotation around the z-axis

unconstrained degrees of freedom need to be constrained using one of a number of techniques.

6.3.2. The Effect of Detector Inefficiencies

Up to this point it was assumed that the detector and all of its elements were 100% efficient. In reality there is no such thing as a perfect detector and effects like hit

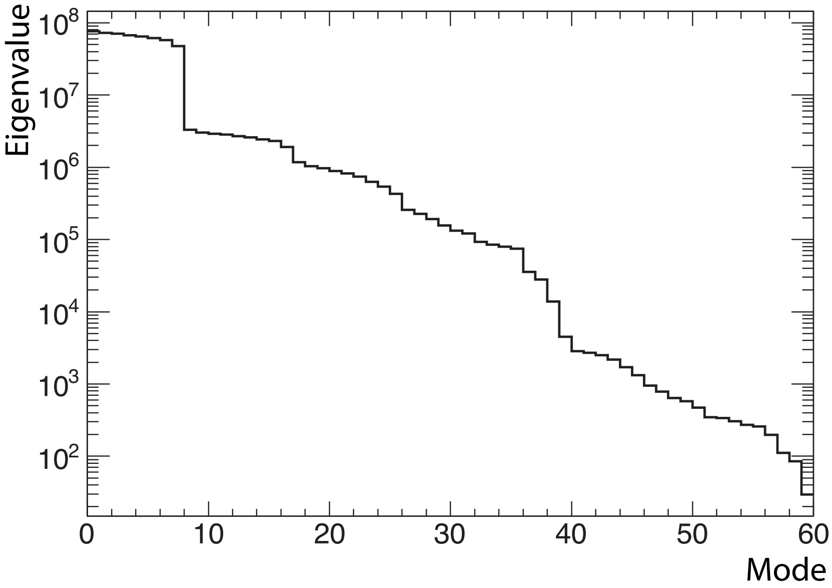

Figure 6.4.: Eigenvalues of the alignment matrix from the unconstrained toy model that is 98% efficient

efficiency, multiple scattering and energy loss need to be taken into account. Although it is a bit beyond the scope of the toy model to take into account the multiple scattering and energy loss, it is quite a simple task to take into account detector efficiencies.

To investigate the effect of detector efficiencies, the more realistic conditions that each detector module is 98% efficient is imposed and a minimum of five hits out of a possible ten is required to form a track. The eigenvalues of such a system differ significantly from that of the perfect system (see Figure 6.2 for the perfect system and Figure 6.4 for the imperfect system).

No longer is there a strong differentiation between the unconstrained degrees of freedom and the well defined, which makes identifying the poorly constrained degrees of freedom much more difficult. Nor are there clear and distinct steps in the spectrum. A possible reason for this is that the tracks become less well defined (fewer hits) and resultantly the corrections are less well defined.

The nine unconstrained degrees of freedom identified for the perfectly efficient detector are present but are buried amongst the other random movements of the detector modules making identification of the unconstrained degrees of freedom quite difficult. This is especially the case when it is practically impossible inspect all of the mode of the detector.

6.4. The Effect of Constraining the System

In order to have a non singular matrix, and hence a viable solution, the unconstrained degrees of freedom need to be removed from the problem. There are a number possible techniques that have been proposed (see Section 5.5). In this section the effectiveness of each of the techniques is investigated. Unless otherwise stated, the results shown are based upon of nine iterations using 10,000 tracks.

6.4.1. Lagrange Multipliers

As the unconstrained degrees of freedom of the alignment problem have been identified (see Section 6.3.1) it is possible to explicitly constrain them through the use of Lagrange Multipliers (LM). There are nine unconstrained degrees of freedom, requiring nine LM to ensure that system is not singular.

To fix each of the global shifts we can apply the following three constraints to the alignment parameters

$$\sum_{Module} T_i = 0 \;\text{ where }\; i = x, y, z. \tag{6.7}$$

Similarly the global rotations of the system can be constrained by insisting that the sum of the rotations is zero:

$$\sum_{Module} R_i = 0 \;\text{ where }\; i = x, y, z. \tag{6.8}$$

Finally the three additional unconstrained degrees of freedom introduced by the track model can be constrained

$$\sum_{Module} T_i \cdot z_{Module} = 0 \;\text{ where }\; i = x, y, z. \tag{6.9}$$

As a direct consequence of using LM, the matrix now has both positive and negative eigenvalues. It is an indefinite matrix (see Figure 6.5). Although this will not fundamentally change the interpretation of the problem it may influence the solution technique chosen.

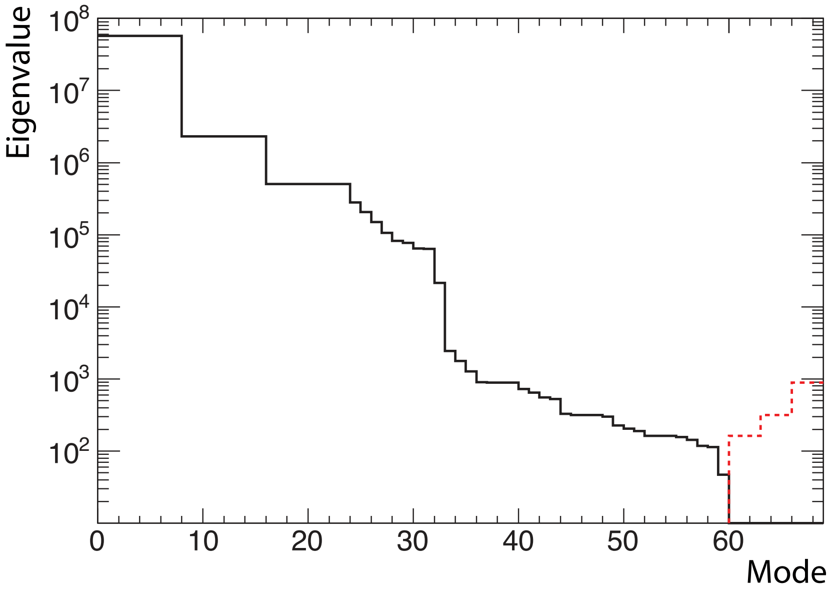

Figure 6.5.: The eigenvalue spectrum for the misaligned toy model that has been constrained with Lagrange Multipliers. To simplify the visulisation, eigenvalues with negative values are shown by the dashed red line while solid black line represents positive eigenvalues.

The results of the alignment procedure can be seen in Figure 6.6. They show no signs of global misalignments or systematic distortions. The resolution obtained on the alignment parameters that are directly measured, T_x and T_y, indicates an alignment resolution much greater than that of the module measurement read out, which is expected given that each module has $\sim \mathcal{O}(10k)$ hits.

Caution must be taken when using LM constraints as they may lock in any pre-existing systematic deformation of the detector. If only movements that are truly χ^2-invariant are restricted then this method is completely valid as those movements are unable to be corrected by track-based alignment alone. It should be noted that identifying all χ^2-invariant modes of the detector may prove to be more difficult than in this very simple case.

6.4.2. Eigenvalue Selection

As shown previously the eigenvalues of the system can be used to identify the unconstrained degrees of freedom of the system. By limiting the sum in Equation 5.51 those poorly constrained degrees of freedom can be excluded from the solution.

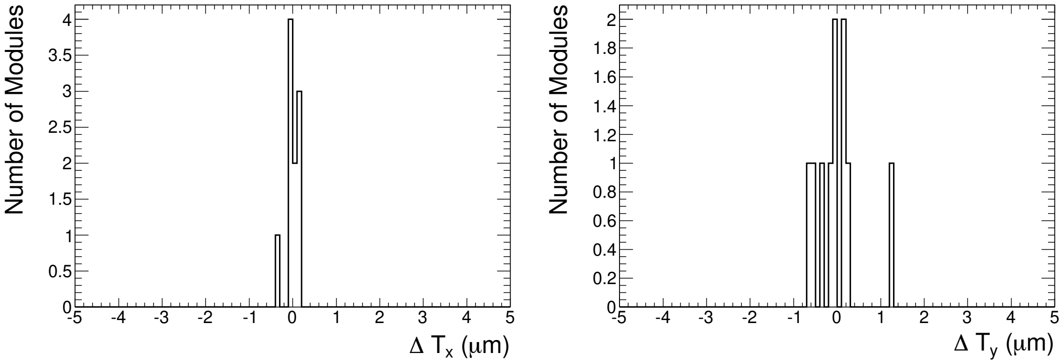

(a) Final ΔT_x **(b)** Final ΔT_y

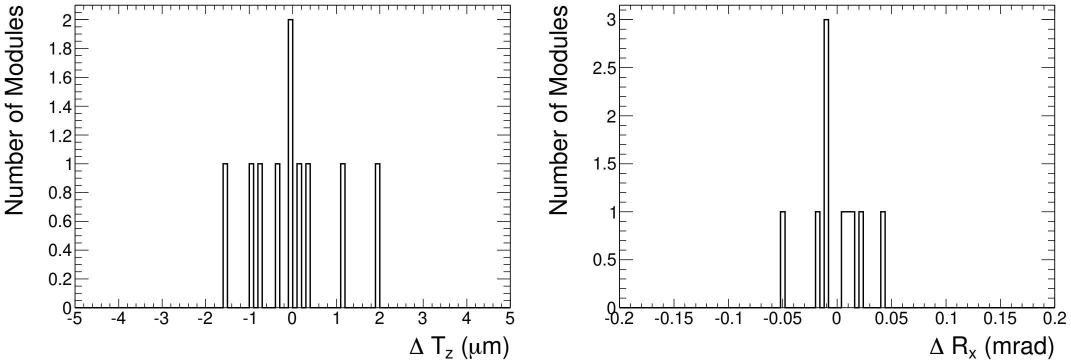

(c) Final ΔT_z **(d)** Final ΔR_x

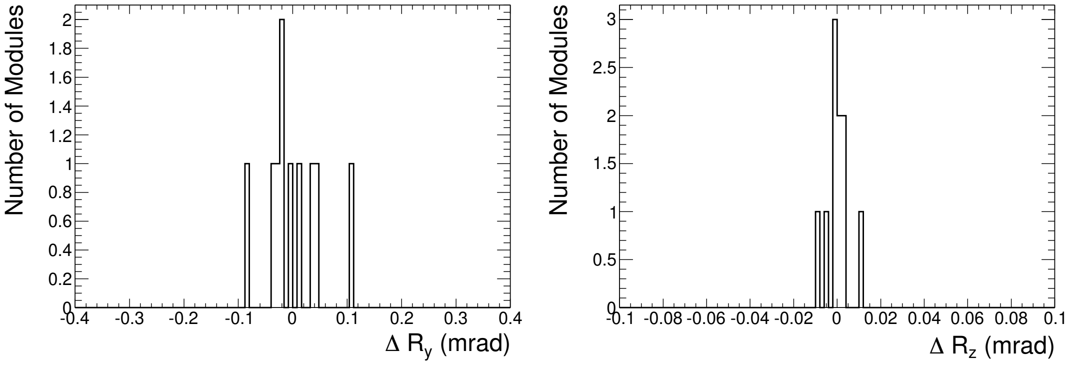

(e) Final ΔR_y **(f)** Final ΔR_z

Figure 6.6.: The difference between the true positions and the positions calculated by the alignment procedure for the misaligned toy model which has been constrained with Lagrange Multipliers.

In the case of a 100% efficient perfect detector selecting the appropriate cut position is quite obvious as there is clear separation between the constrained movements and the unconstrained movements. For this reason an eigenvalue cut of 1 was selected as it would eliminate the 9 unconstrained degrees of freedom. The results are shown in

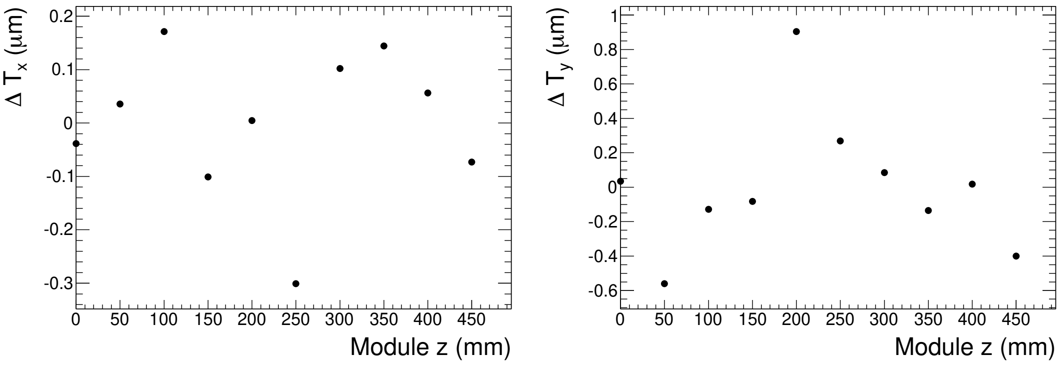

(a) Final ΔT_x **(b)** Final ΔT_y

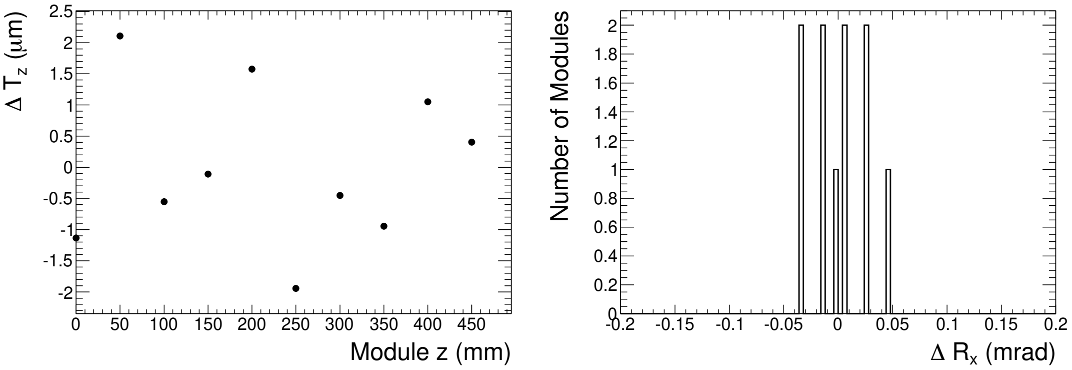

(c) Final ΔT_z **(d)** Final ΔR_x

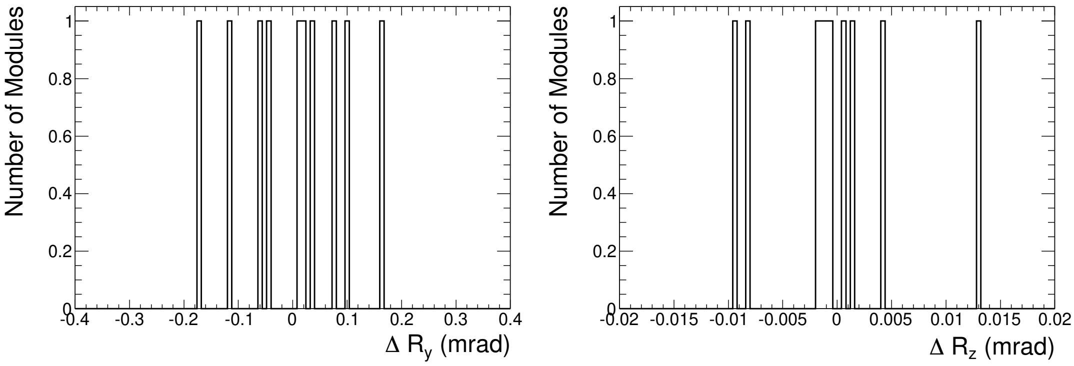

(e) Final ΔR_y **(f)** Final ΔR_z

Figure 6.7.: The difference between the true positions and the positions calculated by the alignment procedure for the misaligned toy model with 100% detector efficiency when a eigenvalue cut of 1 is applied.

Figure 6.7, and as hoped the corrections show no systematic distortions and the final parameter resolution is good.

When the detector is not 100% efficient, the eigenvalues don't exhibit a clear choice for the eigenvalue cut. By setting the cut at 100 only 2 modes are not included in the solution. The results are shown in Figure 6.8 and clearly exhibit strong systematic biases of all parameters.

By selecting the cut at 1000 the lowest 15 modes are not included in the solution (see Figure 6.9) and the results still exhibit strong biases. This suggests that not all of the poorly constrained modes are excluded results (inspecting the eigenvectors confirms this). Another significant observation is that the alignment parameters R_x and R_y are not corrected. This suggests that these corrections associated to these parameters have rather low eigenvalues.

Knowing exactly how many unconstrained degrees of freedom there are in this system, it would be hoped that an *a priori* cut on the eigenvectors would remove these unconstrained degrees of freedom. However without any clear indication of where to place this it somewhat negates the effectiveness of this technique. The use of this technique will need to be studied on a case by case basis as there is no grantee that the system will be free from systematic distortions.

6.4.3. Alignment parameter constraints

The action of constraining the alignment parameters to their original position is another technique to ensure that the matrix is not singular. If the correct uncertainty on the alignment parameters is used to constrain them the system converges at a similar rate as to that using Lagrange Multipliers and final parameter resolution is similar. However three of the alignment parameters, the rotations, are significantly biased (see Figure 6.10).

As it is unlikely that the uncertainty on the alignment parameters is going to be known exactly, the effects of under or over estimating the uncertainty on the alignment parameters was investigated. The uncertainties of the alignment parameters were scaled by varying amounts on the alignment system using 1000 tracks. It should be noted that the number of tracks used changes the effectiveness of this technique as the more tracks used the better defined the matrix $\mathscr{M}$ becomes, while the effect of the alignment parameter constraint reduces.

Figure 6.11 shows the mean and the RMS of the rotations around the z axis varied as a function of the error scaling. It is clear that if the assumed uncertainty on the alignment parameters is significantly underestimated then the alignment parameters may

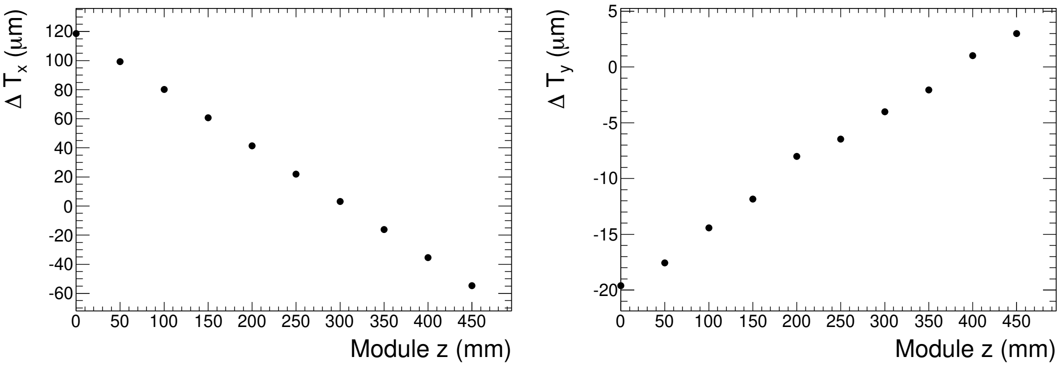

(a) Final ΔT_x **(b)** Final ΔT_y

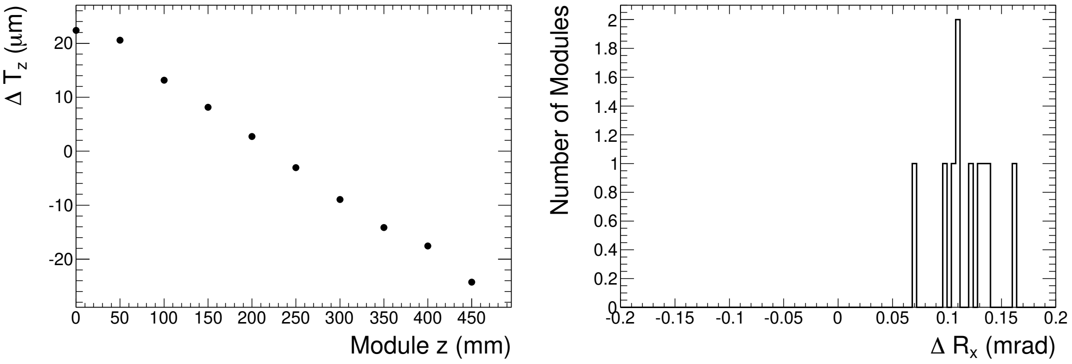

(c) Final ΔT_z **(d)** Final ΔR_x

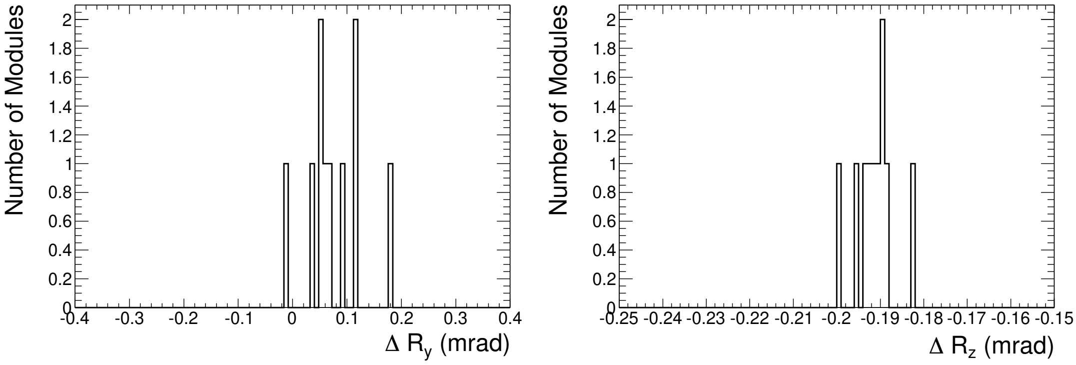

(e) Final ΔR_y **(f)** Final ΔR_z

Figure 6.8.: The difference between the true positions and the positions calculated by the alignment procedure for the misaligned toy model with 98% detector efficiency when a eigenvalue cut of 100 is applied.

not completely converge within the given iterations. Over estimating the uncertainty resulted in the complete rotations of the detector becoming magnified.

However, the uncertainty needs to be unreasonably incorrect to affect the final track quality. In fact even being an order of magnitude out does not really affect the con-

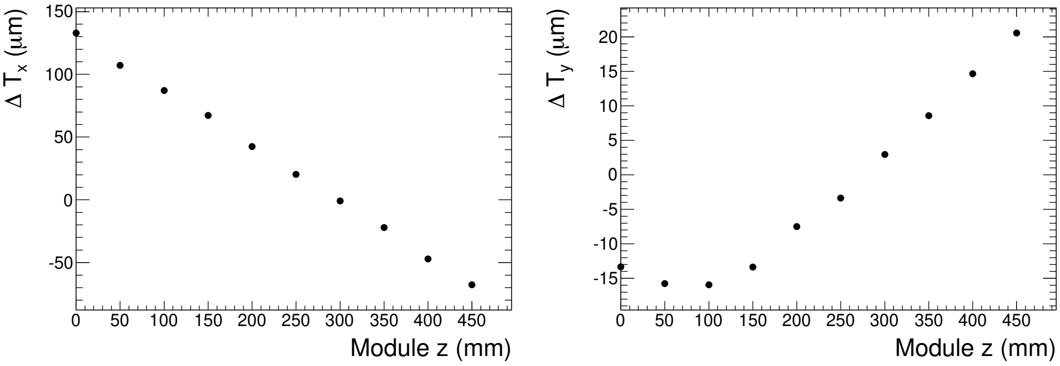

(a) Final ΔT_x **(b)** Final ΔT_y

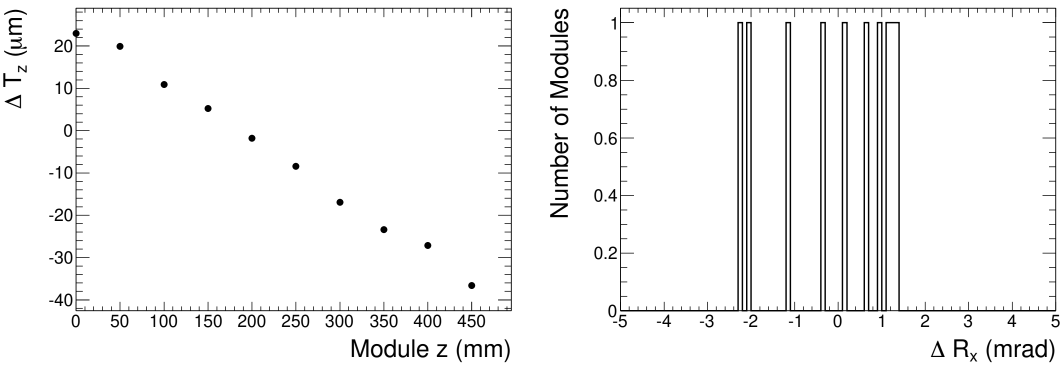

(c) Final ΔT_z **(d)** Final ΔR_x

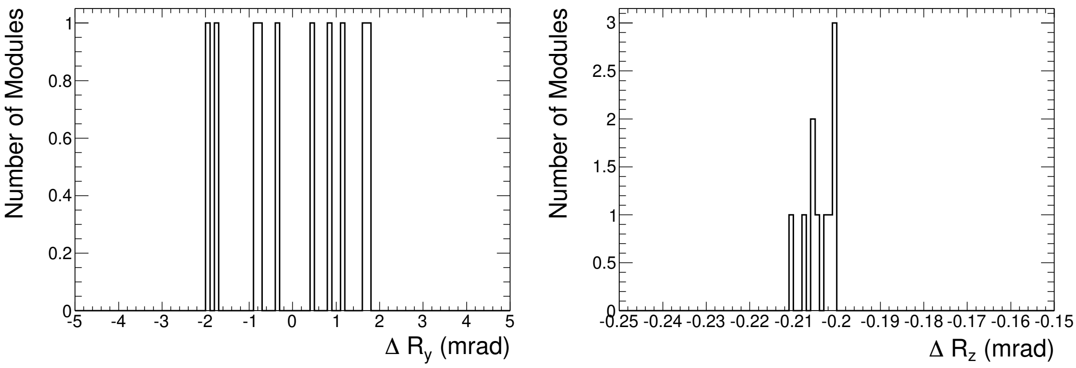

(e) Final ΔR_y **(f)** Final ΔR_z

Figure 6.9.: The difference between the true positions and the positions calculated by the alignment procedure for the misaligned toy model with 98% detector efficiency when a eigenvalue cut of 1000 is applied.

vergence of the alignment at all. It is not until the assumed uncertainty is incorrectly estimated by more than an order of magnitude that the effects can be seen. Overestimating the assumed uncertainty does not constrain the alignment equations enough allowing χ^2-invariant movements of the detector to effect the final result. Note that

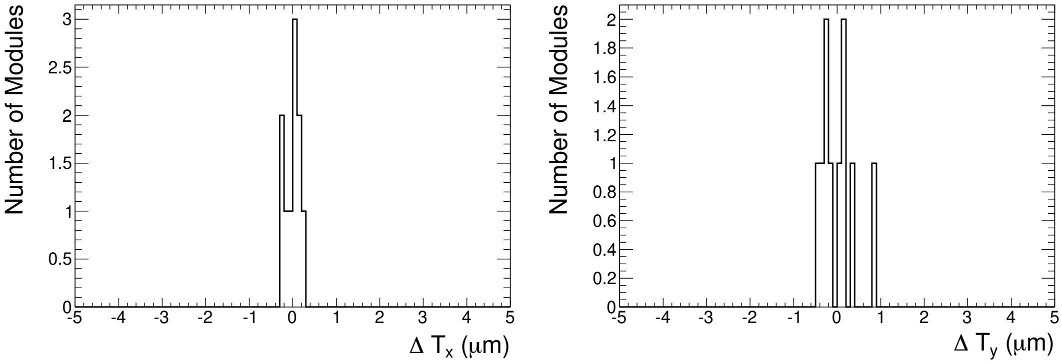

(a) Final ΔT_x **(b)** Final ΔT_y

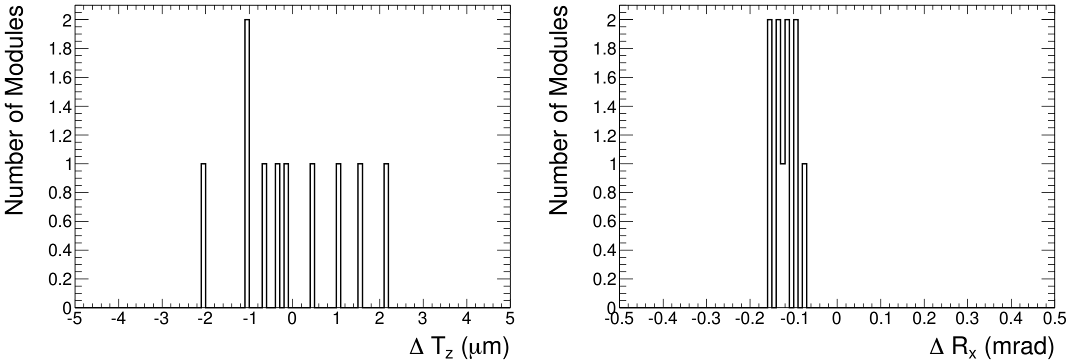

(c) Final ΔT_z **(d)** Final ΔR_x

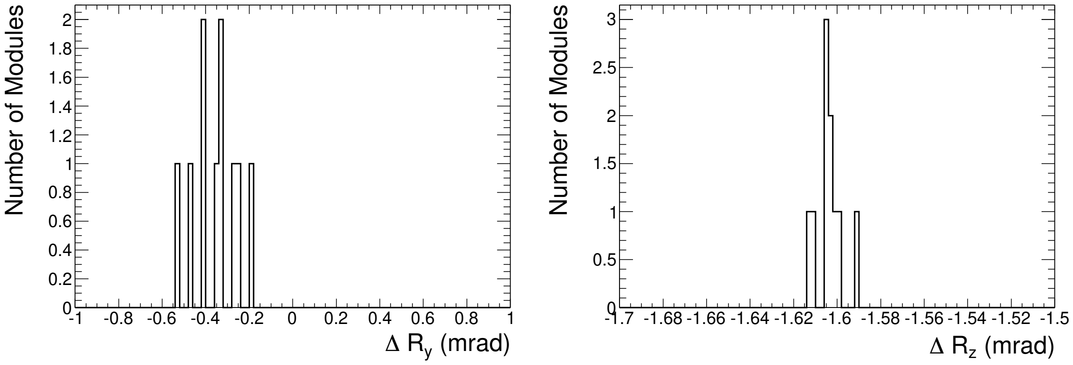

(e) Final ΔR_y **(f)** Final ΔR_z

Figure 6.10.: The difference between the true positions and the positions calculated by the alignment procedure for the misaligned toy model which has had an alignment parameter constraint.

in Figure 6.12 when the system is poorly constrained that the track χ^2/DoF slowly drifts away from ideal values during later iterations. Underestimating the assumed uncertainty of the alignment parameters will slow the convergence of the system and

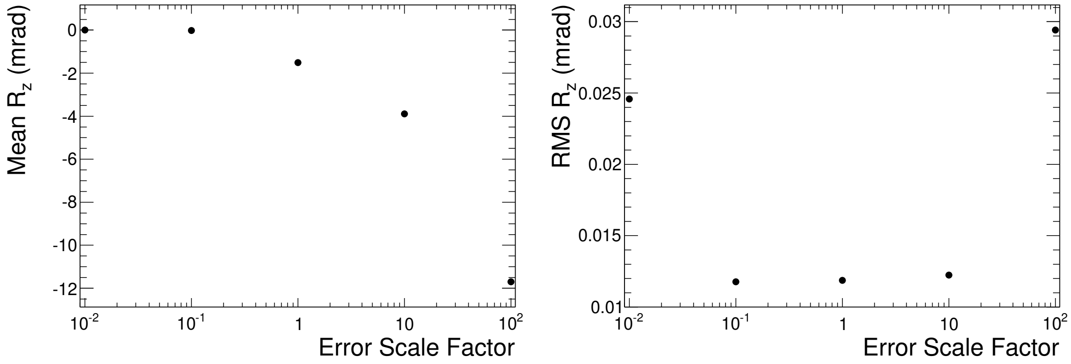

(a) Mean z Rotation **(b)** RMS z Rotation

Figure 6.11.: The effect of scaling assumed uncertainty on the alignment parameters on the average and RMS of final R_z.

may not allow the system to reach the ultimate minima which can be seen in Figure 6.12b.

6.4.4. Fixing modules

A very simple way to give the system a fixed frame of reference is to fix one or more modules in place. Fixing one module will effectively constrain six degrees of freedom and stop the global rotation and translation, but will not constrain the remaining three higher order modes. In order to constrain those modes a second module needs to be

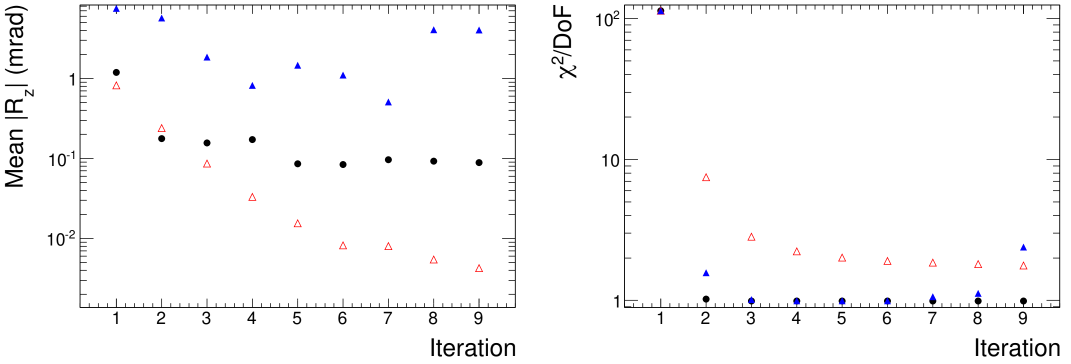

(a) Mean z Rotation **(b)** Mean χ^2/DoF

Figure 6.12.: The the tracks average χ^2/DoF versus the iteration. Correct error estimation (solid black circles), error estimation ×0.01 (open red triangle) and error estimation ×100 (solid blue triangle).

fixed, or at least the three translational degrees of freedom need to be constrained. Fixing enough modules will result in the matrix being symmetric positive definite.

This method, although technically very simple to implement, does have some undesirable features. In particular the misalignments of the fixed modules are never corrected and the remaining system is aligned with respect to these misaligned modules. This problem can be negated by changing the modules that are fixed each iteration. However in doing this there is no guarantee that the detector will not, after iterating, see the effect of the original unconstrained degrees of freedom.

If for example two modules are randomly selected to be fixed during each iteration of the alignment of the toy model then the results exhibit strong systematic distortions (see Figure 6.13). It was noted that the problem took significantly longer to converge when compared with the other techniques. This can be explained simply as each iteration does not solve for all alignment parameters, just eight tenths of them (as two of the ten modules are fixed).

Even starting from a perfectly aligned detector (see Figure 6.14) there are signs that systematic distortions are be introduced into the system after nine iterations especially in the T_y parameters (see Figure 6.14b).

6.5. Alignment Parameter Accuracy

There are a number of factors that will determine the final accuracy of the alignment parameters. The most obvious is the number of tracks used to find the alignment parameters. Others include the diversity and the quality of the tracks used.

From the derivatives of the alignment parameters, the only two parameters that are solely dependent on the detector resolution are the translations in the direction of the measurements (i.e. T_x and T_y). The accuracy of all of the other alignment parameters depend on not only the resolution of the detector measurements but also on the geometry of the detector and the diversity of the tracks used. The resolutions of the T_z corrections are dependent on (in addition to the measurement resolution) the gradient of the tracks at the surface of the associated module. The rotation of the modules around the z axis depends upon the position of the hit on the module. The further the hit from the axis of rotation the better defined the rotational corrections.

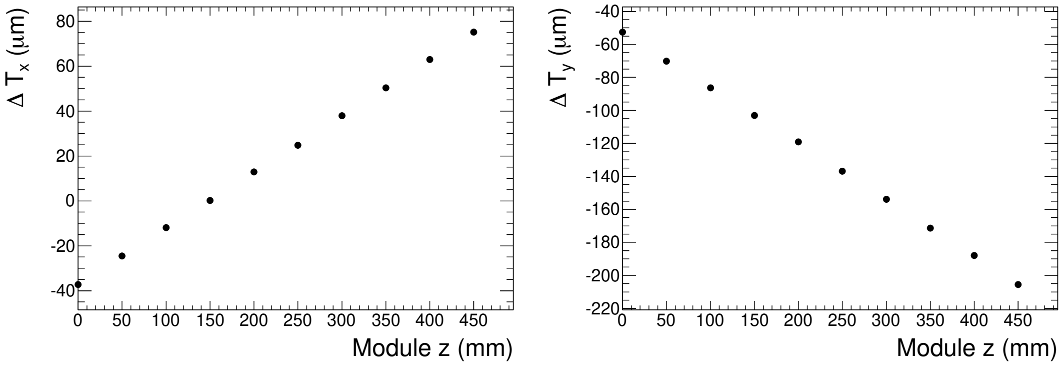

(a) Final ΔT_x **(b)** Final ΔT_y

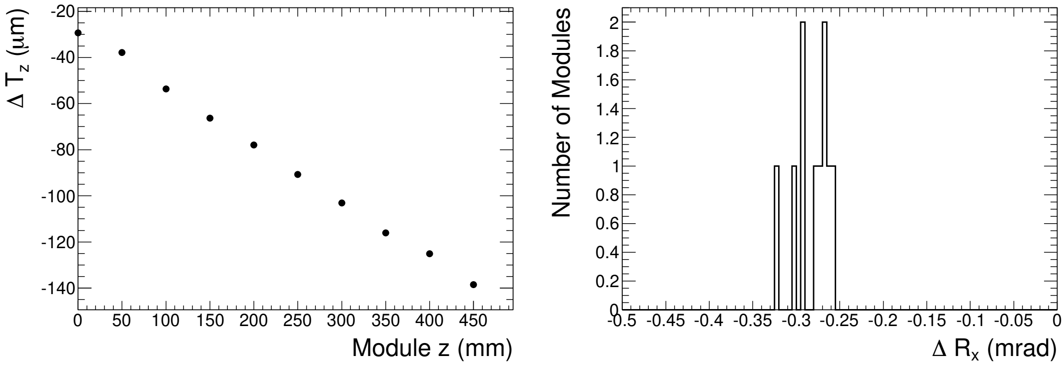

(c) Final ΔT_z **(d)** Final ΔR_x

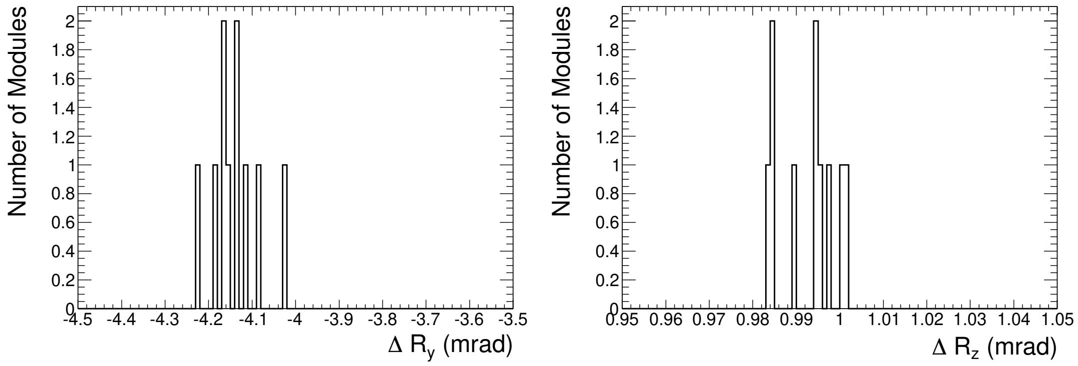

(e) Final ΔR_y **(f)** Final ΔR_z

Figure 6.13.: The difference between the true positions and the positions calculated by the alignment procedure for the misaligned toy model when two modules are randomly selected, each iteration, to be fixed.

The final two rotations, R_x and R_y, depend upon both the gradient of the tracks and position of the hits on the modules.

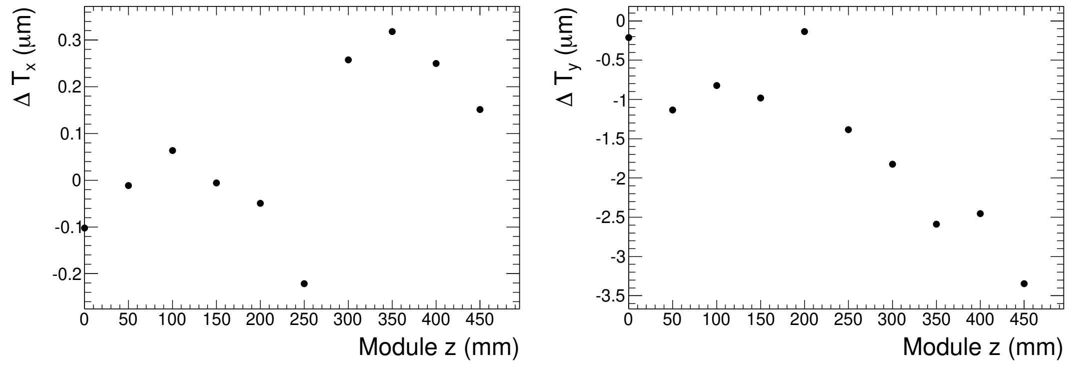

(a) Final ΔT_x

(b) Final ΔT_y

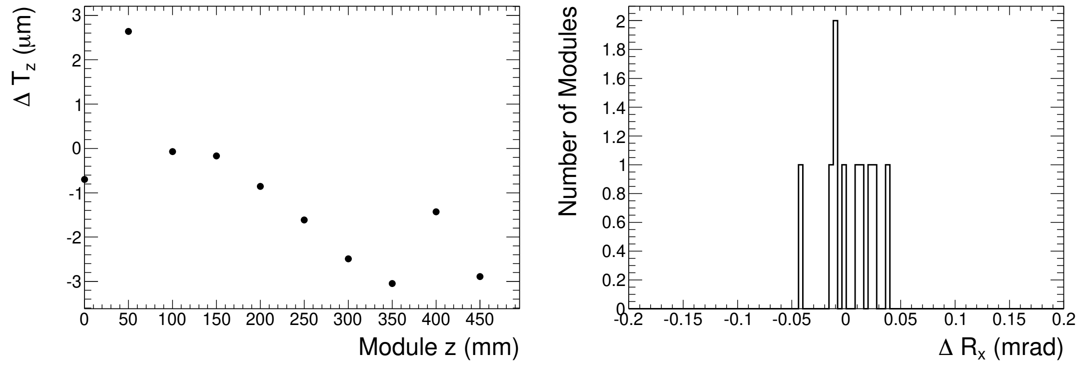

(c) Final ΔT_z

(d) Final ΔR_x

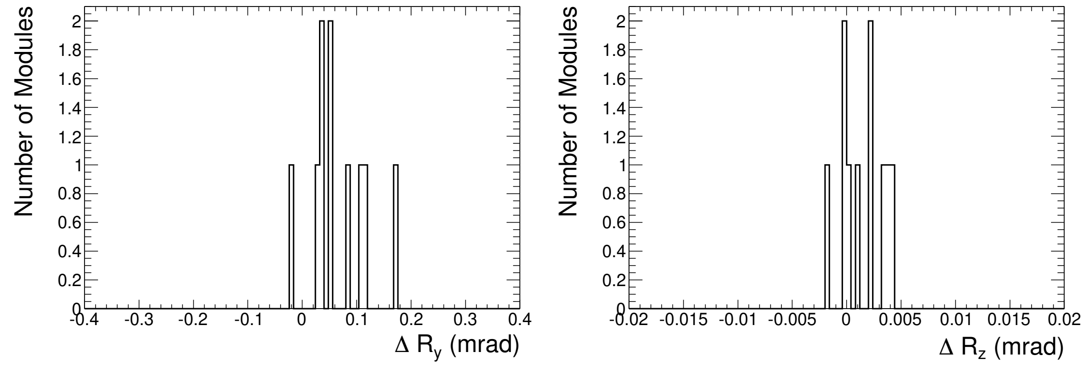

(e) Final ΔR_y

(f) Final ΔR_z

Figure 6.14.: The difference between the true positions and the positions calculated by the alignment procedure for starting with a perfectly aligned toy model when two random modules are fixed

As most modules are positioned to maximise the surface area of the detector, tracks pass through the detector perpendicular to the modules surface. Hence the, T_z, R_x, and R_y corrections require large statistics to become well defined.

6.5.1. Statistics

As would be expected from a linear system like this, the accuracy of the alignment parameters depends strongly upon the amount of information used; in this case the number of tracks used.To study the effect of the number tracks used on the final results the same misaligned system constrained with Lagrange Multipliers was aligned with 10 to 100,000 tracks. Figure 6.15 demonstrates the effect that the number of tracks have on the accuracy of the alignment parameters. All parameters exhibit the same feature, $\sigma \propto n^{-1}$, where n is the number of tracks used. As there have only been ten modules aligned, these results have significant statistical fluctuations.

These results cannot be taken at face value, as this a toy model, but give an indication of the statistics required to obtain a certain resolution in a real detector. Given the resolution in the x direction (y direction) was 10 μm (50 μm) it only takes 100 tracks to obtain an alignment resolution one fifth of the measurement resolution. Even with only 10 tracks the alignment of these parameters has been improved from the initial misalignment of 100 μm.

With only 10 tracks the translational alignment parameters T_z (initial misalignment 10 μm) show no improvement and similarly the R_x and R_y (initial misalignment 2 $mrad$) parameters are not corrected. In fact the R_y corrections have degraded the alignment. This shows the need to understand the magnitude of the initial misalignments (so that the parameters can be constrained correctly).

This of course is a very ideal situation in which there is no material effects which generally degrade the track quality. Higher statistics would be required to obtain similar alignment parameter resolution in a true to life problem which has additional degradation.

6.5.2. Geometrical effects

The toy model geometry was chosen to reflect the basic properties of the barrel of the Inner Detector. The end-cap geometry presents additional challenges as the tracks trajectory become very similar (very little beam spot spread in the x-y plane when compared to the r-z plane). This means that the alignment parameters, with sensitivity dependent on the gradient of the tracks crossing the modules (T_z, R_x and R_y), will be adversely effected.

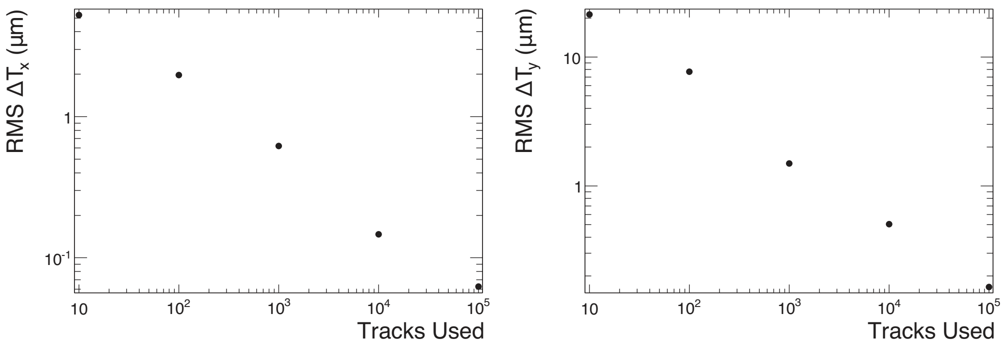

(a) Final ΔT_x **(b)** Final ΔT_y

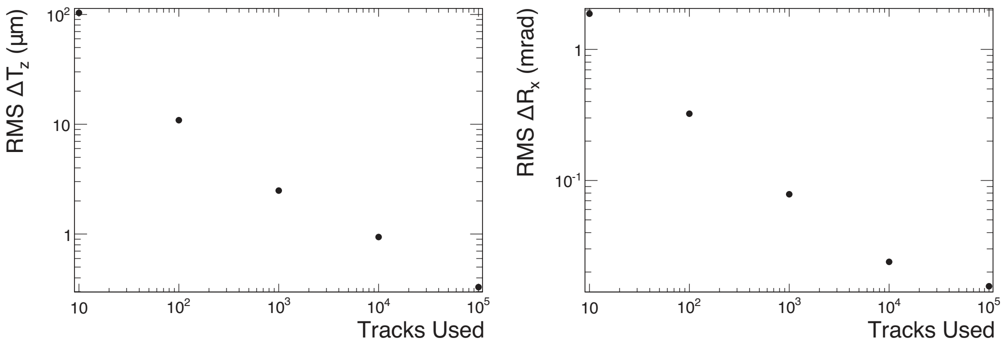

(c) Final ΔT_z **(d)** Final ΔR_x

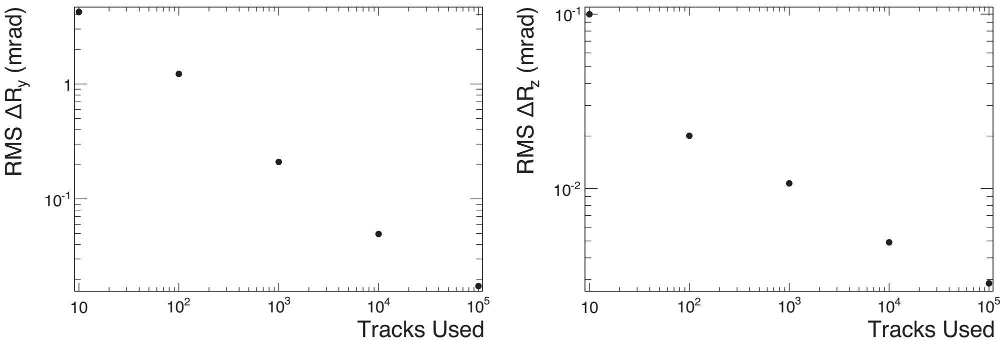

(e) Final ΔR_y **(f)** Final ΔR_z

Figure 6.15.: The difference the true positions and the positions calculated by the alignment procedure for the misaligned toy model which has been constrained Lagrange Multipliers using varying numbers of tracks.

It is also interesting to note that when the tracks come from a common position, an additional poorly constrained degree of freedom enter the system. The eigenvector (see Figure 6.16a) associated to this eigenvalue shows that the rotations around the x (parameters 30-40) and y axes (parameters 40-50) have a χ^2-invariant mode propor-

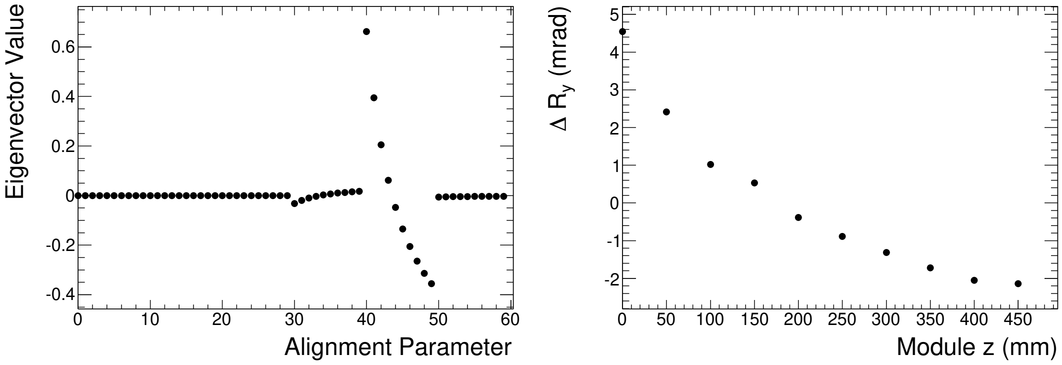

(a) Eigenvector

(b) ΔR_y vs z

Figure 6.16.: The eigenvector and resulting displacements of the detector after nine iterations of the alignment procedure (see text for details).

tional to $1/z$. This new degree of freedom results in very strong systematic distortions of the R_y parameters (see Figure 6.16b)

To understand how such a movement can be χ^2-invariant consider a small rotation, ϕ, around the y axis. This will effectively change the z position of the hit to

$$z_i \rightarrow z_i + \phi x_i, \tag{6.10}$$

where x_i and z_i are the x and z position of the track at surface of module i. As the track is linear, the x position of the track is related to the z position via

$$x_i = m z_i + c, \tag{6.11}$$

where m and c are constants. Substituting Equation 6.11 into Equation 6.10 results in

$$z_i \rightarrow z_i + \phi(m z_i + c). \tag{6.12}$$

A constant shift of all modules in any direction will leave the χ^2 of the track unchanged. In order for a rotation around the y axis to leave the track χ^2 unchanged, it must translate all measurements a constant distance in the z direction. Assuming the constant $c \ll m z_i$, the rotation required at each surface should be

$$\phi_i \propto 1/z_i, \tag{6.13}$$

as was observed.

If all tracks originate from a common position then this rotation is unconstrained. This is something to be mindful of particularly when aligning the end-caps. If only tracks from collisions are to be used, this characteristic can become problematic.

6.5.3. Track Quality

The track quality after alignment should be optimal if the system has converged to the correct solution and as such the residuals and track χ^2 distributions should exhibit the same properties of the perfectly aligned (ideal) system. However having ideal residuals and track χ^2 distribution does not mean that the alignment of the detector is correct.

Measurement Residuals

	Mean (μm)	σ (μm)
Ideal System	-0.032 ± 0.098	8.705 ± 0.065
Misaligned System	-58.483 ± 0.558	37.551 ± 0.545
Aligned System (Biased)	0.051 ± 0.099	8.746 ± 0.068
Aligned System (Unbiased)	0.003 ± 0.097	8.684 ± 0.065

Table 6.2.: Results of a Gaussian fit to the x residuals on the 6th module.

Table 6.2 shows the results to a gaussian fit of the residuals for the perfectly aligned system (ideal), the misaligned system, and the aligned system when there are strong systematic effect and no systematic effects. The residuals of both of the aligned systems are very close to those of the perfectly aligned system. They are both unbiased (i.e. mean ≈ 0) and have the same resolution as the ideal case. Despite the presence of a strong bias the final alignment results of the residuals look identical to the ideal system. This is to be expected as the systematic biases are χ^2-invariant and hence “pull” and residual invariant.

Track χ^2

The tracks' χ^2 should be distributed according to the the χ^2 PDF (see Equation 4.56). Selecting tracks which have hits in all modules (i.e. 10 Hits), results in tracks with 16 DoF (20 measurements minus 4 track parameters). Figure 6.17 displays the fitted χ^2 of tracks that have hits in every layer for the four separate cases. The results of a fit to the χ^2 PDF are displayed in table 6.3. The results for all three cases are very similar, showing that fits return a value for the number of DoF of the track consistent with actual DoF of the track. This suggests that both alignment parameter sets have been estimated well and that the measurement error estimates are correct.

Again despite the presence of a strong bias in the final alignment results, the χ^2 distribution looks identical to that of the ideal system. This again shows the χ^2-invariant nature of the detector movements.

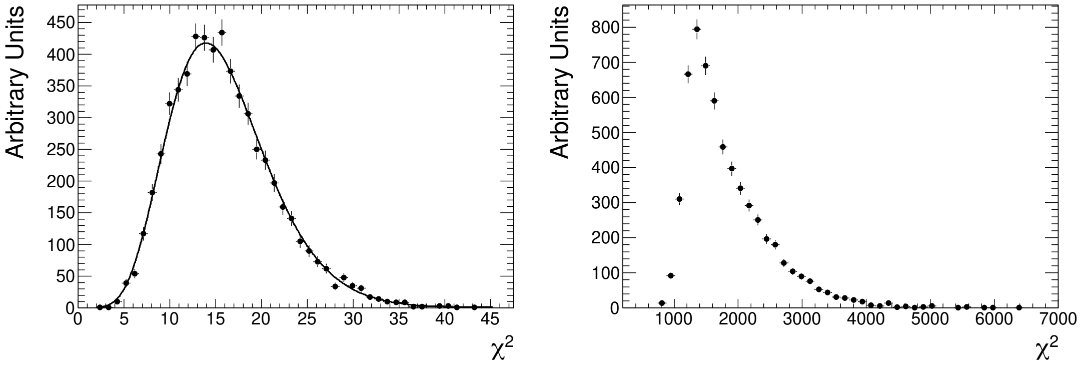

(a) Perfect **(b)** Misaligned

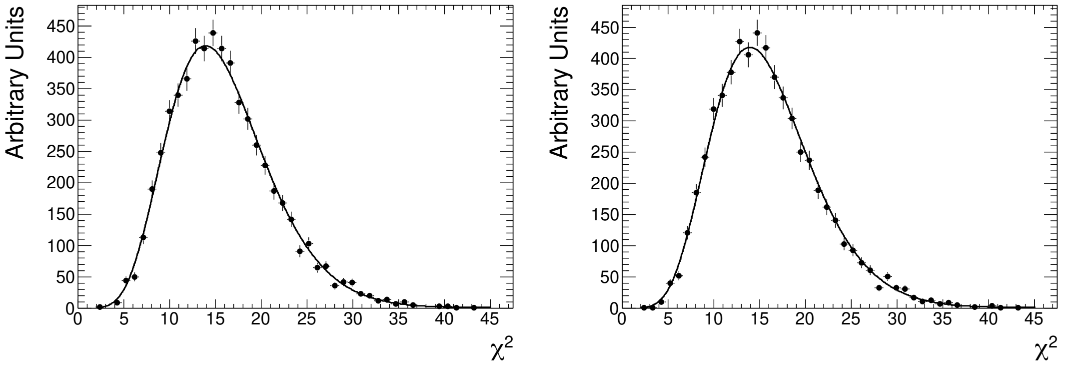

(c) Aligned (Biased) **(d)** Aligned (Unbiased)

Figure 6.17.: χ^2 distribution for the tracks having 16 DoF

	Degrees of Freedom
Ideal	15.947 ± 0.068
Aligned (Biased)	15.925 ± 0.070
Aligned (Unbiased)	15.946 ± 0.068

Table 6.3.: Results of a fit to the χ^2 distribution of tracks with 16 DoF from the toy model for four different alignments

Track Parameters

The resolution of the reconstructed track parameters is ultimately what is of concern. Figure 6.18 displays the difference between the reconstructed and true gradient of a track for various situations. The most striking observation is that in the “unbiased” aligned case there is still a small bias of the track parameters (although it is significantly smaller than the biased aligned case). There is also a degradation of the resolution of the gradient (see Table 6.4). The constant of the reconstructed line in the y-z plane is also biased (see Table 6.5).

As the track χ^2 and residuals are virtually ideal it suggests that there are some small biases remaining in the "unbiased" solution. This is not surprising as the initial random misalignment of the modules is undoubtedly a little biased given that there are only 10 modules. Given that the alignment technique is insensitive to such misalignment, an external source of information is needed to remove there distortions. This could come from a secondary measurement of the track parameters from a known well calibrated detector (for example the muon detector).

	Mean (μm/mm)	RMS (μm/mm)
Perfect	0.0018	0.1377
Misaligned	-0.0012	0.2420
Aligned (Biased)	-0.2703	0.2104
Aligned (Unbiased)	0.0597	0.1416

Table 6.4.: The Mean and RMS of the difference between the true and reconstructed gradient of the track in the y-z plane

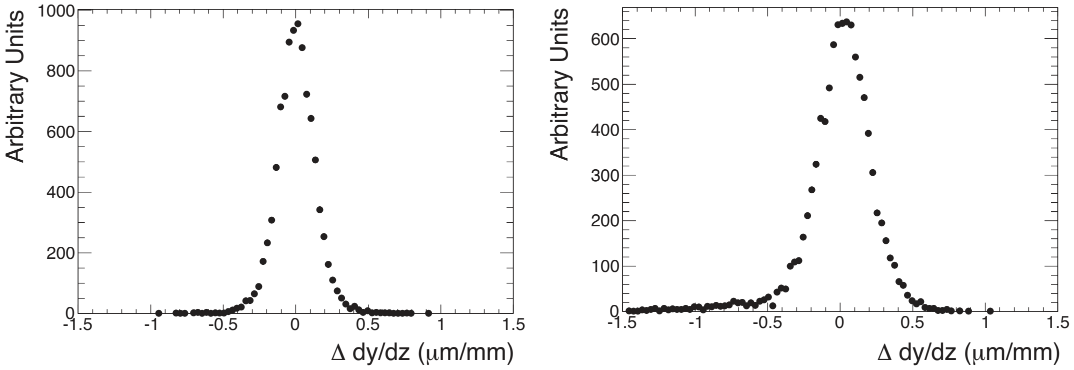

(a) Perfect **(b)** Misaligned

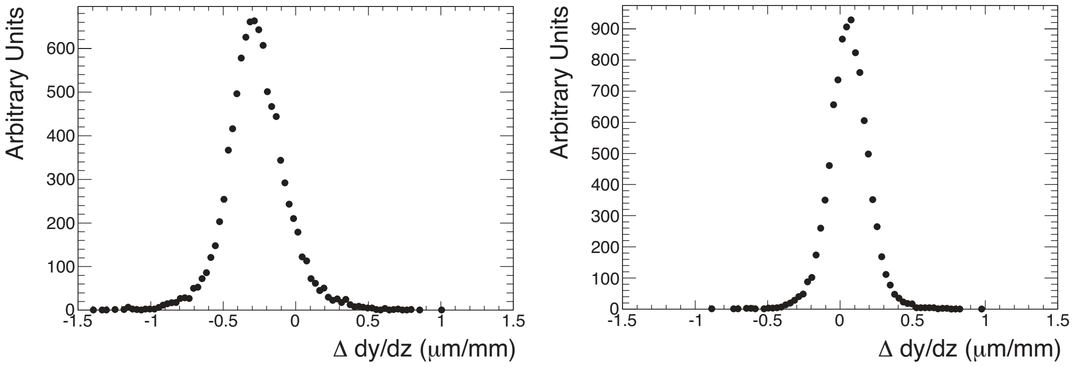

(c) Aligned (Biased) **(d)** Aligned (Unbiased)

Figure 6.18.: The difference between the true and reconstructed gradient of the track in the y-z plane

	Mean (mm)	RMS (mm)
Perfect	-0.0005	0.0416
Misaligned	0.0097	0.0749
Aligned (Biased)	-0.0519	0.0694
Aligned (Unbiased)	0.0003	0.0431

Table 6.5.: The Mean and RMS of the difference between the true and reconstructed constant of the track in the y-z plane

6.6. Summary

In the end all methods result in similar alignment parameter resolutions once global distortions have been removed. The technique that was shown to be least reliable

Constraint	ΔT_x	ΔT_y	ΔT_z	ΔR_x	ΔR_y	ΔR_z
Lagrange Multipliers	0.147	0.504	0.943	23.86	49.543	4.910
Eigenvalue Cut Ideal	0.131	0.376	1.211	25.21	95.541	5.934
Eigenvalue Cut Realistic	63.68	12.63	19.37	1312.1	1274.1	3.376
Alignment Parameter	0.168	0.379	1.25	25.787	94.531	5.977
Randomly Fixed Modules	35.87	48.68	35.34	19.19	54.183	6.397

Table 6.6.: Summary of the performance of the various constraint techniques used in the global χ^2 alignment algorithm. The table presents the RMS of the difference between the alignment parameters and their true value

was eigenvalue cut. The lack of a clear location to place the cut could result in some parameters not being corrected and systematic distortions being present. This technique resulted in the worst alignment of all of the techniques tested.

Lagrange multipliers provide the best method to stop the introduction of χ^2-invariant distortions as it explicitly restricts their introduction. However, for this technique to work, all modes must be known before the commencement of the alignment procedure. A constraint on the alignment parameters is a foolproof way of ensuring the matrix is not singular but does not guarantee that detector will not be systematically deformed.

Constraints on the alignment parameters provide a foolproof method of reducing the extent that χ^2-invariant distortions factor in the final result. A combination of both alignment parameters constraints and Lagrange multipliers could be applied to ensure that all know and unknown χ^2-invariant deformations are reasonably constrained.

In all cases it would be useful to a have a method of removing the systematic deformations that are initially present. For example a constraint on the track parameters.

7

CHAPTER

ALIGNMENT OF THE ATLAS INNER DETECTOR

In this chapter methods for aligning the ATLAS Inner Detector using the Global χ^2 alignment algorithm are presented. In Section 7.1 the goals of the alignment are outlined along with their motivation. The details of the ATLAS CSC simulation alignment challenge are discussed in Section 7.2 with the alignment procedure presented in 7.3 and the results in 7.4. This work was collaborative effort that is documented in[3]. An extension of the standard alignment procedure is presented in Section 7.6 which is developed by gaining an understanding of the properties of the alignment (Section 7.5). This work is the sole work of the author

7.1. Aims of Alignment

The ATLAS detector is constructed of very high precision sub-detectors. This high precision allows for the determination trajectories and momentum of jets and lepton to the accuracy required by a range of possible physics processes. However, as with any high precision device, it must be well calibrated in order to take full advantage of its intrinsic high precision.

The ATLAS Inner Detector has the capability of measuring space points along the path of a charged particle to within a $\sim 20\ \mu m$. However, any misalignment of the components of the ATLAS Inner Detector will prevent this potential accuracy of being attained. A direct result of any misalignment is that track-measurement residuals generally increase and track parameter resolution is degraded. Furthermore, if misalignments are severe enough to degrade residuals beyond expected values, some hits may be mistakenly excluded from the track fit.

One of the requirements of ATLAS is that alignment imprecision should not degrade the resolution of reconstructed track parameters beyond that expected from the inherent space point resolution. The ATLAS Inner Detector Technical Design Report[117] stated that the resolution of the track parameter be degraded by no more than 20%. Device misalignments significantly affect the intrinsic detector resolution and therefore also will directly degrade the pattern recognition capability of the Inner Detector. This in turn will degrade the physics performance and discovery potential of the whole experiment. Furthermore, severe misalignments may effect the measured efficiency of the detector[117]. Studies with simulated Monte Carlo events in the ATLAS detector established that to ensure that the track parameter resolution was not degraded by more than 20%. An alignment precision of 7 μm for Pixel modules, and about 12 μm for SCT modules is required[118].

Beyond the effects on track reconstruction performance, the misalignments of the detector elements will impact many aspects of the ATLAS physics performance, including the muon and tau reconstruction and identification, the electron identification, jet calibrations, primary and secondary vertex reconstruction and b-tagging performance.

For example in the Higgs decay channels $H \rightarrow ZZ \rightarrow 4\ell$ with an expected mass (180 $< m_H <$ 400) GeV, with its four final state leptons, will require very good lepton reconstruction and identification and efficiency in order to maximise its discovery potential.

Misalignment also impacts the measurement of secondary vertices from decays of long-lived particles such as b-mesons. The accurate measurement of vertices is strongly dependant on a precise measurement of the track impact parameters. The distance between the primary and secondary vertex is one of the key b hadron jet identification (b-tagging) measurements. It has been found that a random misalignment of 10 μm will result in a 10% reduction of the b-tagging efficiency[119].

The measurement of the W boson mass has been extensively studied and will require the accurate measurement of tracks if it is to be performed with the desired accuracy.

An accurate measurement of the W mass will test the SM itself if the Higgs is found. To achieve the desired accuracy (15-20 MeV/c^2) on the W mass measurement, it will be necessary to[24]:

- Understand the position of the modules to an accuracy of $\mathscr{O}(1)$ μm in the $r\phi$ plane in order to achive the maximum hit resolution.
- Understand the solenoid magnetic field to better than 0.02%, to compute correctly the momentum.
- Determine the distribution of material within the ID detector to an accuracy of 1%, to account for Multiple Coulomb Scattering effects.
- Understand the transverse momentum (p_T) resolution to 1%.

The alignment requirements for the W mass measurement are the most stringent.

Several recent studies have further explored the impact of misalignments on physics analyses using Monte Carlo simulations[120–122].

7.2. The ATLAS CSC Challenge

The Computing System Challenge (CSC) [27] provided a testing ground for the full scale alignment procedures of the ATLAS detector. The alignment was performed on a simulated misaligned detector that contained systematic distortions and random detector element misalignments. The details of the generated misalignments are detailed in Section 7.2.2.

7.2.1. Description of the Simulated Data Samples

Muons from the Collision Point

For the alignment of the detector muons were selected to be used due to their near ideal tracking properties. Muons act as *minimum ionising particles* through the detector and have minimal interactions with hadronic particles in comparison to pions. The sample consisted of almost 10^5 simulated events, each containing 10 muons. Within each event the muons had the same charge and originated from the same point corresponding to the primary vertex of that event. Positive and negative muons alternated from one event to the next. The events were simulated a magnetic field with initial displacements and misaligned geometry (CSC misalignment for the Inner Detector can be seen in the section 7.2.2. Greater detail is given in[123, 124]).

The muon tracks were randomly assigned their p_T, η and ϕ from uniform flat distributions, as seen in figure 7.1, with the following parameter ranges:

- The transverse momentum spectrum range is p_T = [2, 50] GeV/c.
- The pseudorapidity range is η = [-2.7, 2.7]
- The azimutal angle range is ϕ = [0, 2π]

In order to simulate the expected beam spot spread the event primary vertex distribution was generated from Gaussian distributions centred at zero and with the following widths (see Figure 7.2):

- transverse plane (v_x and v_y): $\sigma = \sqrt{2} \cdot 15\ \mu m$
- along the beam axis (v_z): $\sigma = \sqrt{2} \cdot 56\ mm$

In figure 7.2 one can see the distributions for each vertex coordinate (top plots) and the correlations between the coordinates (on the bottom). These plots were obtained from the numbers that the particle generator produced.

Cosmic Rays

In addition to the sample of simulated muons originating from the primary vertex cosmic rays were also simulated. The cosmics rays were simulated at the surface then were propagated through the earth to the ATLAS cavern. To speed up the simulation

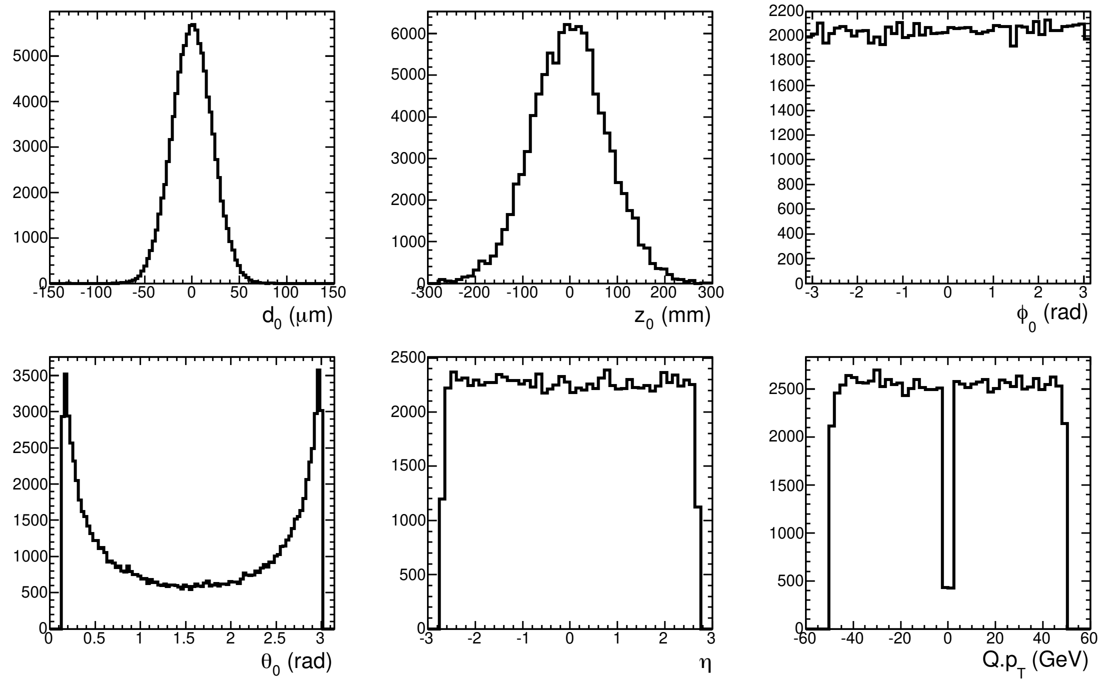

Figure 7.1.: True generated parameters of the multimuon sample.

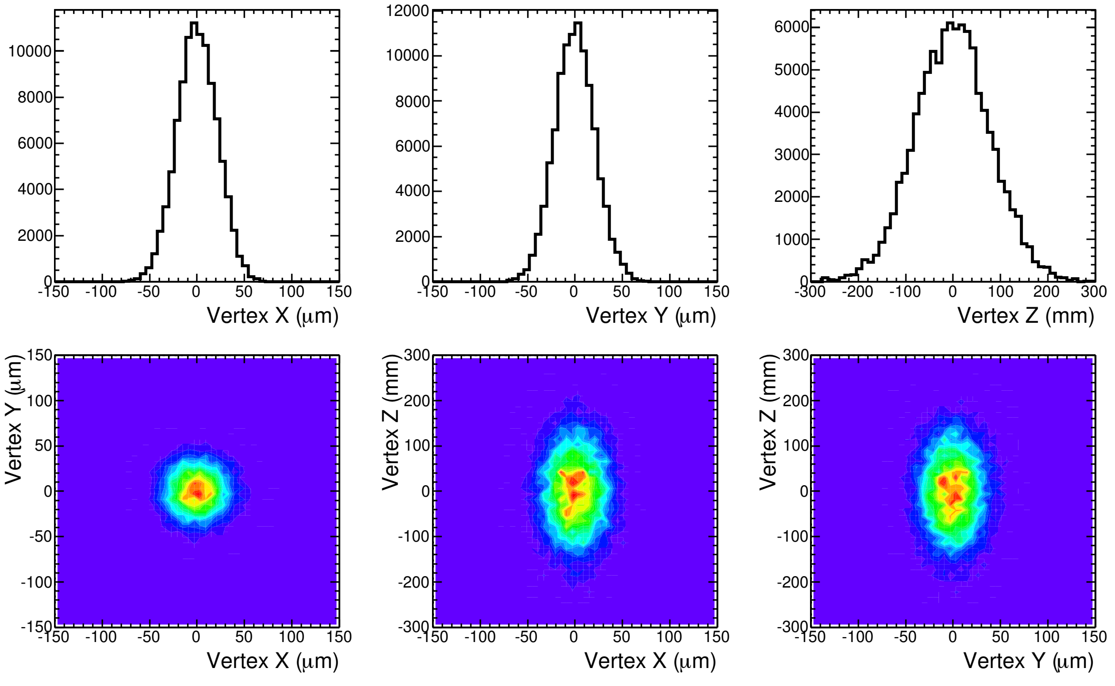

Figure 7.2.: True generated vertex of the multimuon sample.

of such events a volume filter was introduced, with the main sample ensured the particle traversed the TRT volume. Cosmic events were produced with both the solenoid magnetic field on and the magnetic field off.

Once the tracks from the comic muons reach the ID they are no longer spatially uniform as the probability of Cosmic ray reaching the ATLAS detector will be heavily increased if the particle passes through access shafts rather the 100 m of earth. In addition to this the majority of the tracks will be almost perpendicular to the beam line there are very few tracks that have hits in the end-cap of the Silicon tracker.

7.2.2. Silicon misalignments for CSC

For the CSC exercise misalignments of the Inner Detector were designed to be as realistic as possible. Hence different levels of misalignment were generated in order to simulate a realistic detector, as close as possible to the real as-built experiment. The details of the misalignment of the detector can be found in [3, 125] but are summarised here.

Three different levels of misalignments were introduced into the Silicon Tracker which reflected the construction of the detector:

- Level 1 transforms: transformation of each silicon subsystems.
- Level 2 transforms: transformation of detector layers/disks.
- Level 3 transforms: transformation of individual detector modules.

The approximate magnitude of the transforms can be seen in Table 7.1. The exact deformations for the Level 1 and 2 tranformatios can be found in Appendix D.

7.2.3. The Effect of the Misalignment on Reconstructed Track Parameters

Such gross misalignments of the detector have a significant effect on the reconstructed track parameters. Figure 7.3 displays the effects of the misalignments on the reconstructed track parameters. All of the track parameters are biased to varying degrees and all have compromised resolutions. The shifts of the detector at Level 2 and 1 are

Level 1 Transforms		
System	Translations (mm)	Rotations ($mrad$)
Pixel detector	1.0	0.5
SCT Barrel	1.0	0.5
SCT End-cap	1.0	0.5
Level 2 Transforms		
System	Translations	Rotations
Pixel Barrels/Disks	1.0	1.0
SCT Barrel modules	0.1	0.1
SCT End-cap modules	0.1	0.1
Level 3 Transforms		
System	Translations	Rotations
Pixel Barrel modules	0.03	1.0
Pixel End-cap modules	0.03	1.0
SCT Barrel modules	0.15	1.0
SCT End-cap modules	0.10	1.0

Table 7.1.: Approximate sizes of the silicon displacements at each level

the major cause of the biasing of the reconstructed parameters, and the compromised resolution is a result of the random movements of the modules at Level 3.

The transverse impact parameters are expected to be consistent with zero as the tracks originate from (0,0,0), however they exhibit a sinusoidal dependence on the reconstructed track ϕ_0. This is indicative of the movement of the pixel detector with respect to the nominal beam position.

Although the total number of reconstructed tracks drops only by 1.8%, the quality of those tracks is significantly affected. The average number of silicon hits per track (see Figure 7.4) drops from 11.62 to 8.26. The average number of *holes* on track increasing from just 0.05 to 1.36.

In addition, the tracks χ^2 per DoF is also affected. The χ^2 indicates that the calculated uncertainty of the measurements is about three times too small as a result of the detector misalignment. This is a result of the measurement uncertainties not taking into account misalignments and miscalibrations. To combat this effect and to improve tracking efficiency the errors of the hits are inflated. This procedure is known as *Track*

Error Scaling. This feature is used during the initial stages of the alignment procedure to help “kick start” the alignment procedure. Details of the error scaling are provided in[3].

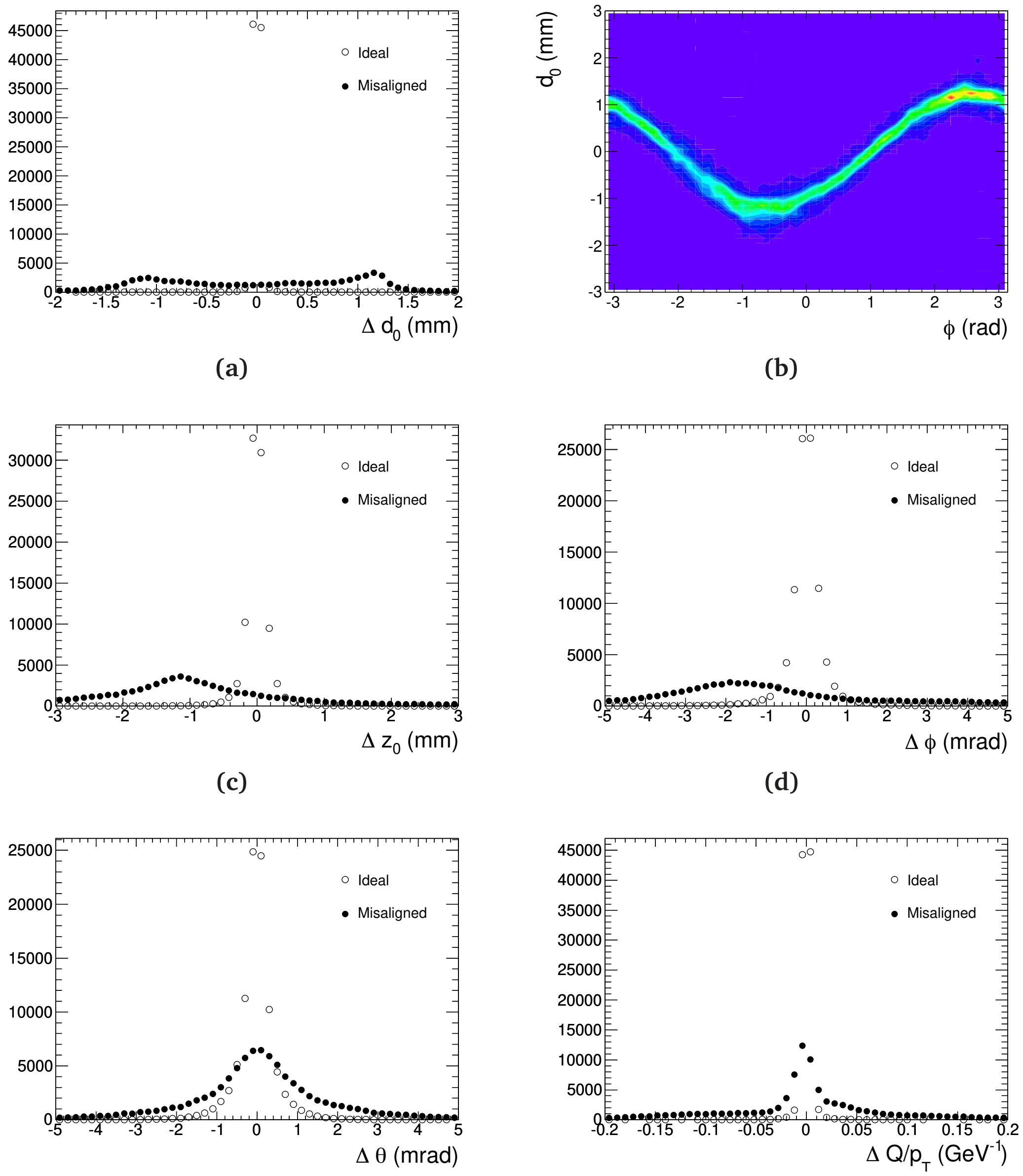

(a) (b) (c) (d) (e) (f)

Figure 7.3.: The effect of the CSC misalignments on the reconstructed track parameters

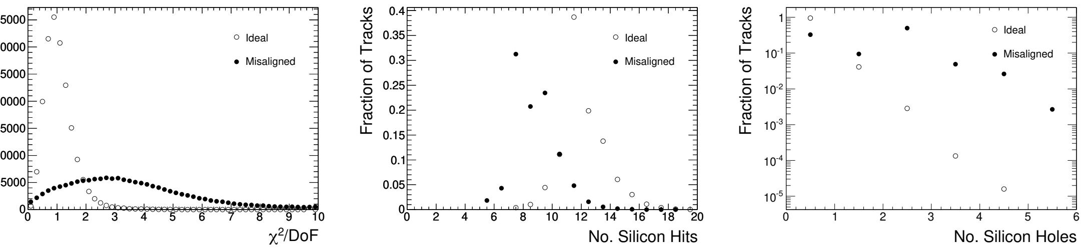

(a) χ^2/DoF **(b)** Hits per track **(c)** Missing hits per track

Figure 7.4.: The effect of the CSC misalignments on some measures of the track quality.

7.3. Standard CSC Alignment Procedure

The standard alignment procedure for the Silicon Tracker is presented here and is a reproduction of[3]. It involves running the Global χ^2 alignment algorithm iteratively starting from the misaligned geometry (as defined in Section 7.2.2) using the data described in Section 7.2.1. Tracks were fit with global χ^2 track fitter without any additional constraints.

For all iterations, tracks with momenta above 10 GeV/c were constrained to be consistent with the beam line, assumed at (0,0) in the x-y plane. This constraint was applied in the form of a track parameter constraint on the transverse impact parameter d_0. This constraint was softened by increasing the error on the d_0 constraint and was set to a value 10 times larger than the error on the transverse impact parameter (d_0) obtained from the track fit.

A number of iterations were required to ensure that the alignment had converged. The iterations can be divided in three phases:

1. An initial four iterations involving the degrees of freedom (DoF's) of barrel cylinders and end-cap discs all considered as rigid objects (6 DoF's per object). This corresponds to the Level 2 geometry description of the ID (see Section 7.2.2 and [123, 124]).

   The solution was obtained by means of diagonalisation with the smallest four eigenvectors removed for the solution. These were assumed to correspond to the four near-singular modes of the solution, i.e. the three rotations and the translation along z of the whole system. Note, that the freedom of the x and y translations have been removed by the beam line constraint. The iterations used 10,000 muon events each (approximately 100,000 muon tracks) with error scaling turned on.

2. Two iterations involving the entire set of 34,922 DoF's of the ATLAS silicon system. Known as Level 3 alignment, the solution was obtained using `MA27` direct fast solver [115] (see Section 5.7.2 for further details). Each iteration used 50,000 multiple muon events leaving each module with at least 500 hits. The limited statistics of the tracks passing through each module and the solving method necessitated the need for matrix preconditioning. To control the statistical error of the solution a constraint on the alignment parameters was introduced. The constraint values were motivated by the CSC misalignments and are shown in Table 7.2.

	Pixel	SCT
x' error	0.010 mm	0.050 mm
y' error	0.010 mm	0.050 mm
z' error	0.015 mm	0.050 mm
$R_{x'}$ error	0.0003 rad	0.0003 rad
$R_{y'}$ error	0.0003 rad	0.0003 rad
$R_{z'}$ error	0.0003 rad	0.0003 rad

Table 7.2.: Alignment parameter constraint values used in the CSC alignment exersice

3. Two futher iterations of the Level 2 alignment were performed. The procedure for these iterations was identical to that of the first four. The purpose of this last step was two-fold: align any residual distortions that might have been introduced by the Level 3 iterations and confirm the convergence.

This procedure makes no attempt to remove the various types of systematic /χ^2-invariant distortions that could be introduced during the alignment procedure. As described in Chapter 6, in order to remove some of the χ^2-invariant distortions additional information provided by the simulated cosmic muons was used. This information provided by the cosmic muons allowed for distortions of the type $R_z \propto r$ and where $T_z \propto r$ to be removed from the system (see Figure 7.5). Section 7.5 and 7.6 detail a method for all forms of χ^2-invariant distortions.

To incorporate the information obtained from cosmic tracks an additional iteration was performed at Level 2 combining 10,000 multiple muon events with the simulated

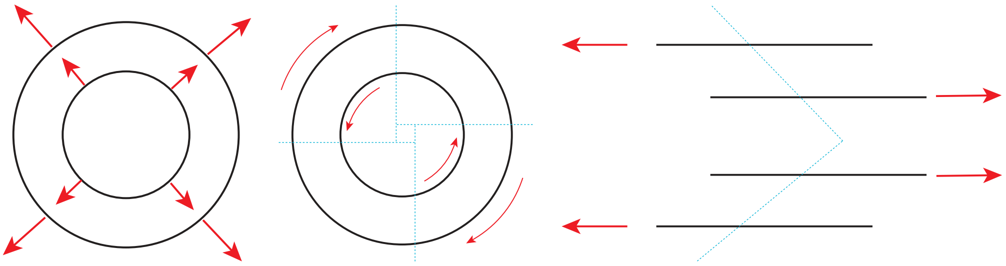

(a) $\Delta r \propto r$ (b) $\Delta R_z \propto r$ (c) $\Delta T_z \propto r$

Figure 7.5.: First order systematic distortions of barrel like detector in r, ϕ and z with respect to r.

cosmic. The cosmics rays provide tracks with differing coverage to that of collisions muons. The muons were processed in an identical manner to those in the previous iterations and cosmic events were processed using the same alignment settings as the collision event but without the impact parameter constraint. The matrices and vectors produced by the collision muons and the cosmic muons were then merged and the final corrections were obtained by diagonalising and solving the combined system and removing the eigenvector associated to the lowest four eigenvalues. Two different samples of simulated cosmic rays were tried: without and with the magnetic field inside the ID. Both gave qualitatively similar results.

7.4. Standard CSC Alignment Results

A number of checks were performed to confirm the stability of the solution, the validity of the beam line constraint, the suitability of the alignment parameter constraints, and the quality of the alignment solution. This section describes validation and the quality of the resulting alignment (see also [3]).

7.4.1. Validity of Beam Line Constraint

To test the validity of the beam line constraint the alignment was performed at Level 2 starting from the nominal alignment with the error parameters of the constraint on track parameter d_0 scaled by varying amounts. The resulting alignment constants were checked for their ability to reconstruct the beam line correctly. In particular the dependence of the reconstructed d_0 on the track direction in the x-y plane (track

ϕ_0) was inspected, in addition to the transverse impact parameters resolution. The ϕ dependence on the position of the track parameter d_0 indicates one of two things (see Figure 7.3b). Either that all tracks are not originating from the nominal collision position (0,0,0) or that the detector (in particular the first layer of the pixel detector) is misaligned.

Figure 7.8 demonstrates that the resolution of d_0 is relatively independent of the strength of the constraint imposed. The resolution is relatively unaffected by scaling the error on the beam line constraint. As expected a constraint on d_0 provides an effective method of correctly defining the position of the detector relative to the IP.

7.4.2. Validity of Alignment Parameter Constraints

The strength of the alignment parameter constraints were scaled up and down in the range $\times 0.01 \rightarrow \times 1000$ in order to verify stability of the Level 3 alignment. A plateau of workable cut values was identified, as seen in Figures 7.9, 7.10 and 7.11. Convergence was slowed as the constraints were tightened, while systematic deformations dominated the solution if the constraints were relaxed too much in a similar manner to that shown in the toy model (see Section 6.4.3).

The greatest concern with these results is that the alignment converges to marginally different solutions depending on the strength of the constraint (evident in the differing momentum scale biases as seen in Figure 7.9). Converging to the same result regardless of constraint strength, as would be the case if it converged to the true global minimum of the problem, would be the best outcome. Given that the alignment begins from a biased position, and the Level 3 alignment is not expected to correct for these biases, it would be expected that any bias which could not be addressed during the alignment at Level 2 would be present after the Level 3 alignment. However the alignment at Level 3 can reduce and or increase the biases present depending on the constraints applied to the system. This suggests that χ^2-invariant deformations of the system are introduced during the Level 3 alignment.

7.4.3. Solution Stability

To study the stability of the solution further iterations of both the Level 2 and Level 3 alignment were performed in order to verify the convergence of the method and lack of uncontrolled runaway. Figures 7.6 to 7.8 show that the Level 2 alignment has converged to a stable solution, albeit after six iterations instead of the four that was selected in the alignment procedure due to time constraints.

Inspection of the change of the alignment parameters over those iterations presents a slightly different picture, as alignment parameters continue to vary. This could be due to a number of reasons. Firstly, the modules on the substructures are misaligned and as a result the track parameters are still poorly defined and hence the alignment parameters are unable to determined to sufficient accuracy. Secondly, as the modules that comprise the super structure being aligned are themselves misaligned with respect to the super structure, the Jacobain describing the movement of the super structure with respect to the composite module is inaccurate. As such the derivative matrix that describes the movement of the super structure with respect to the track is inaccurate, leading to an unreliable calculation of the alignment parameters. Finally, the super structures could be moving in a χ^2-invariant manner which of course would need to be restricted through some form of constraint. As the first two possibilities are due to random misalignments it would be expected that the movement would be random, and the final case corrections would be systematic or would lead to a systematic solution. No clear evidence was found to suggest that these movements were systematic.

When aligning all modules individually (Level 3 alignment) there is also the possibility that the detector will move in a χ^2-invariant manner. To combat this constraints on the alignment parameters were used to subdue these movements (see Figure 7.9). To be noted is the behaviour of the momentum scale when the constraint is relaxed; it is able to shift significantly (especially in the end-caps) which is an indication that the detector is moving in a χ^2-invariant manner. This emphasises again that the detector needs to have the χ^2-invariant modes constrained. Figures 7.11 and 7.10 show that the system at Level 3 converges after no more than 3 iterations, when using the standard constraint strength.

7.4.4. Final Solution Performance

A number of figures of merit were used to gauge the quality of the resulting alignment. A comparison of reconstructed to generated track parameters was performed. A test for any remaining global sagitta distortion was of the primary interest. The

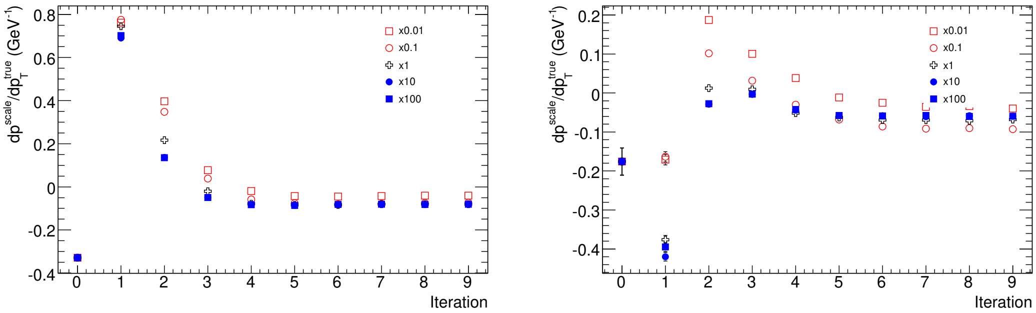

(a) $|\eta| < 0.8$

(b) $|\eta| > 1.5$

Figure 7.6.: The momentum scale in the central barrel, (a), and end-caps, (b), for silicon only tracks during Level 2 iterations with the collision muon sample. The strength of the beam spot constraint were scaled by the amounts indicated.

quantity $(Q/p_T^{\text{rec}})/(Q/p_T^{\text{true}})$, which will be referred to as the momentum scale (p^{scale}), was plotted in the form of a profile histogram against the signed track transverse momentum. The slope of this dependence gives direct evidence of a sagitta distortion.

Other methods need to be used to check for such distortions. One such check is to inspect the charge asymmetry ($N_{\mu^+} - N_{\mu^-}/N_{\mu^+} + N_{\mu^-}$) of tracks originating from mass reassurances that decay into oppositely signed leptons, for example the Z boson. Checking the asymmetry with respect to the track parameters (especially track momentum and direction) will give an indication of any systematic distortions present in the detectors alignment.

Inspecting the results of charge asymmetry as a function of track momentum of muons originating from Z boson decays shows a distinct bias that has not been corrected for during the alignment process. As it has not been corrected it suggests that it is χ^2-invariant deformation of the detector.

The resolution of the reconstructed transverse momentum after the Level 3 alignment is significantly worse than the ideal value. For example there is a 75% degradation for $p_T = 50$ GeV tracks found in the end-caps. This has a significant effect on the reconstructed mass of the Z boson (see Figure 7.15), degrading the mass resolution by 50%

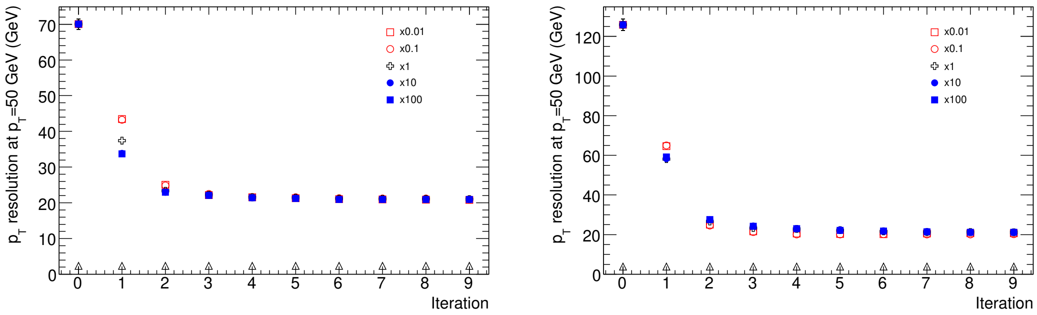

(a) $|\eta| < 0.8$ **(b)** $|\eta| > 1.5$

Figure 7.7.: The p_T resolution in the central barrel, (a), and end-caps, (b), for silicon only tracks during Level 2 iterations with the collision muon sample. The strength of the beam spot constraint was modified by the amounts indicated. The open triangles show the ideal alignment resolution of the silicon tracker

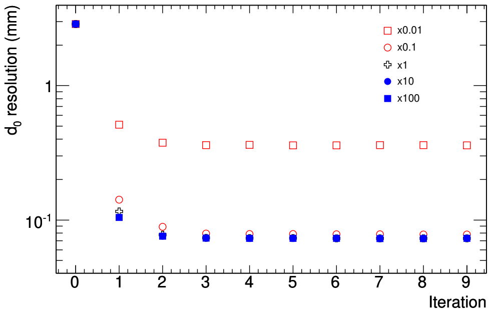

Figure 7.8.: The resolution of the transverse impact parameter for silicon only tracks during Level 2 iterations the collision muon sample. The strength of the beam spot constraint were scaled by the amounts indicated. The strength of the beam spot constraint was modified by the amounts indicated.

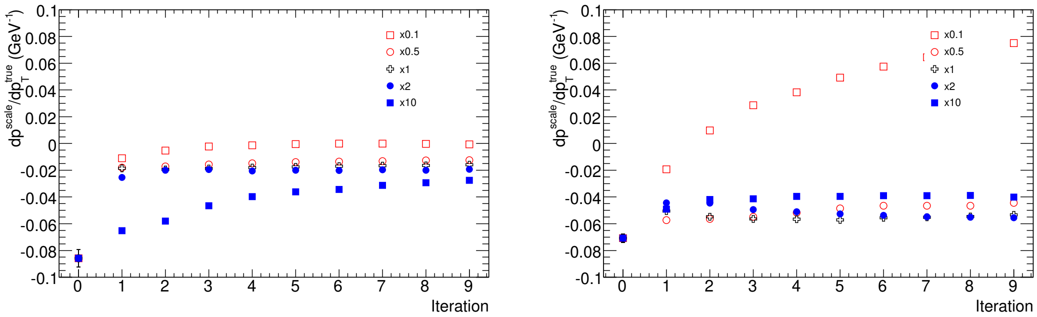

(a) $|\eta| < 0.8$ **(b)** $|\eta| > 1.5$

Figure 7.9.: The momentum scale in the central barrel, (a), and end-caps, (b), for silicon only tracks during Level 3 iterations with the collision muon sample. The strength of the alignment parameter constraint was scaled by the amounts indicated.

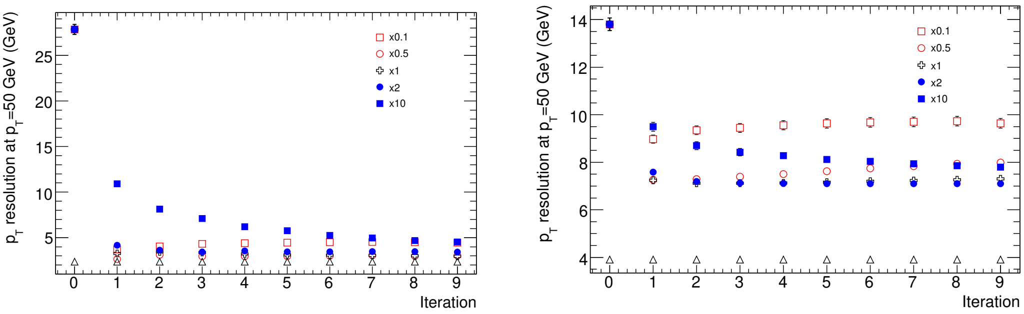

(a) $|\eta| < 0.8$ **(b)** $|\eta| > 1.5$

Figure 7.10.: The p_T resolution in the central barrel, (a), and end-caps, (b), for silicon only tracks during Level 3 iterations with the collision muon sample. The strength of the alignment parameter constraint was scaled by the amounts indicated. The open triangles show the ideal alignment resolution of the silicon tracker

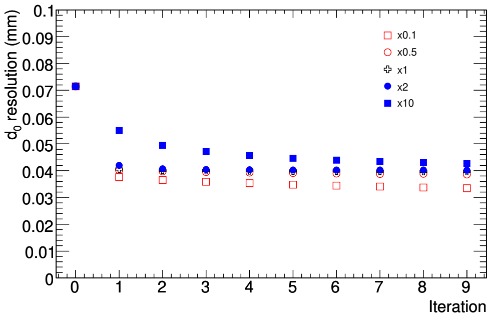

Figure 7.11.: The resolution of the transverse impact parameter for silicon only tracks during Level 3 iterations the collision muon sample. The strength of the alignment parameter constraint was scaled by the amounts indicated.

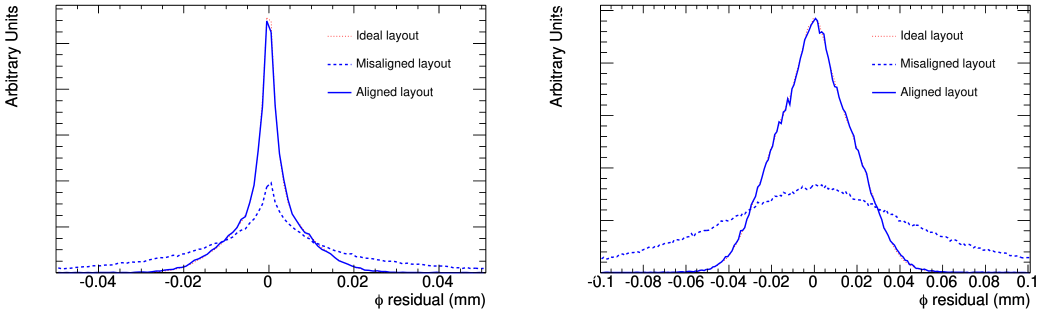

(a) Pixel barrel **(b)** SCT barrel

Figure 7.12.: The local $r\phi$ residual distribution for the barrel of the (a) Pixel and (b) SCT detectors

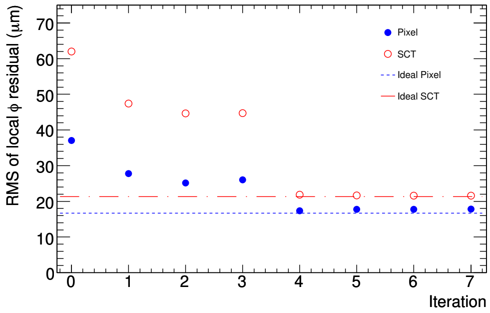

Figure 7.13.: The RMS of the local ϕ residuals for barrel modules of the Pixel an SCT detectors as a function of the iteration during the CSC exercise.

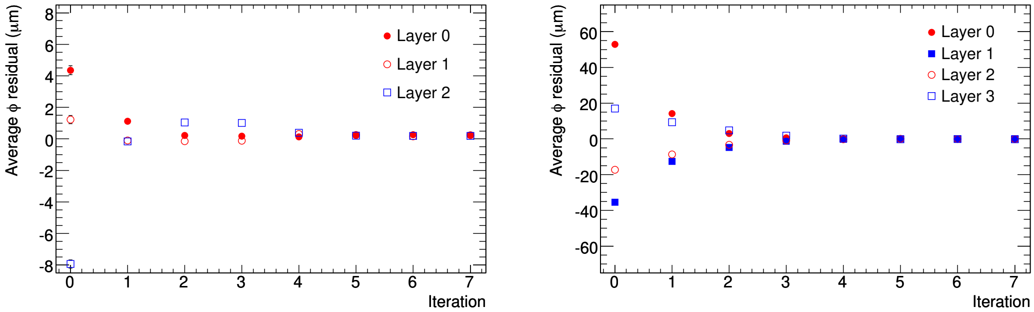

(a) Pixel barrel

(b) SCT barrel

Figure 7.14.: The average local ϕ residual for each layer in the barrel of the (a) Pixel and (b) SCT detectors

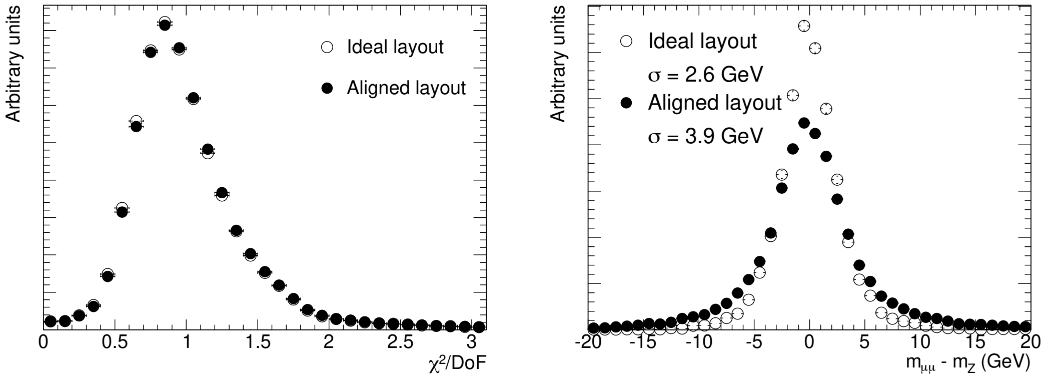

(a) χ^2/DoF

(b) Z mass resolution

Figure 7.15.: The track χ^2/DoF and reconstructed Z mass resolution for the ideal and aligned detector[1] [3]

7.5. Properties of the Alignment system

The standard alignment procedure shown in Section 7.3 made no attempt to remove χ^2-invariant deformations of the detector beyond the use of cosmic ray tracks. As the final track χ^2 was virtually ideal but the track parameter resolution was not it suggests that the detector was deformed in some form of χ^2-invariant manner. To help with the removal of these χ^2-invariant modes they need to be identified. To find these modes the eigenvalues and eigenvector of the matrices produced via the Global χ^2 Alignment technique were inspected. In this section the properties of the alignment system at Level 2 and Level 3 are discussed.

As the full detector contains approximately 35000 DoF inspecting the eigenvalues of the complete system is somewhat difficult. To simplify the investigation into the χ^2-invariant modes of the detector a study of the properties of the Level 2 alignment was performed followed by a study of the Level 3 alignment on portions of the detector.

7.5.1. Level 2 Properties

Initially the barrel of the detector was investigated as its geometry is similar to that used in the toy model presented in the previous chapter. It will be shown that the system exhibits similar properties. Aligning the ATLAS barrel at Level 2 (considering barrel layers as single entities), results in a system with 7 super structures and hence 42 degrees of freedom. The alignment equations were formed with approximately 50000 simulated tracks constrained to originate from common positions in the x-y plane.

It would be expected that there would be six clearly unconstrained degrees of freedom associated to the three translation and three rotations that would normally define the alignments systems frame of reference. Two of these degrees of freedom have been removed by constraining the tracks to originate from a common vertex position. As such the system will not exhibit unconstrained global translation degrees of freedom in the x and y directions.

The otherwise expected global rotations of all layers around the x and y axes are no longer global degrees of freedom when aligning the detector at Level 2 with the magnetic field on. The Inner Detector is enclosed in a magnetic solenoid and as such particles will travel in a helical path. This helical trajectory will have an axis aligned with the magnetic field. A rotation of the whole ID around the x or y axes will cause the hits on the reconstructed track to rotate accordingly. However by rotating the detector around either the x and y axes the hits will be moved into a shape that is no longer helical and as such the global rotations around the x and y axes are constrained.

The remaining unconstrained degrees of freedom are clearly visible (see Figure 7.17) and correspond to global rotations around the z axis (eigenvalue 41) and the global translation in the z direction (eigenvalue 42).

There are another three eigenvalues which are orders of magnitude smaller than the bulk of the eigenvalues, and upon first inspection they all exhibit the property $T_i \propto r$. Closer inspection reveals that the unconstrained movements in the x and y directions are in fact proportional to r^2 (see Figures 7.18 and 7.19). The parabolic nature of the χ^2-invariant movement in the x-y plane can be attributed to the parabolic like nature of path of high momentum particles in the bending plane. It would be expected that such parabolic movements would have three degrees of freedom which would result in three eigenvector displaying such characteristics. However, one degree of freedom (the constant shift) has been removed by the constraint on the track parameter d_0. One has been identified as the predominantly linear translation and the final degrees of freedom is present but well hidden amongst the other eigenvalues which were two orders of magnitude larger. The fact they are two orders of magnitude larger is consistent with the size of the residual shown in Figures 7.18b and 7.19b.

Translations in the z direction of movement seem consistent with $T_z \propto r$ (see Figure 7.20) despite what looks to be independent movement of pixel and SCT detectors. These residual movements are yet to be fully explained.

When considering the whole Silicon Tracker, additional unconstrained degrees of freedom emerge as more structures are being aligned. At Level 2 there are 31 objects to align and hence 186 degrees of freedom. There are six very small eigenvalues for the system with no additional constraints applied (see Figure 7.21). These six modes correspond to global translations in the x and y directions, a global translation in the z direction, a global rotation around the z axis and movements in the x and y direction proportional to the z^2 (see Figure 7.22). Again, no sign rotational degrees of freedom are present around the x and y axes.

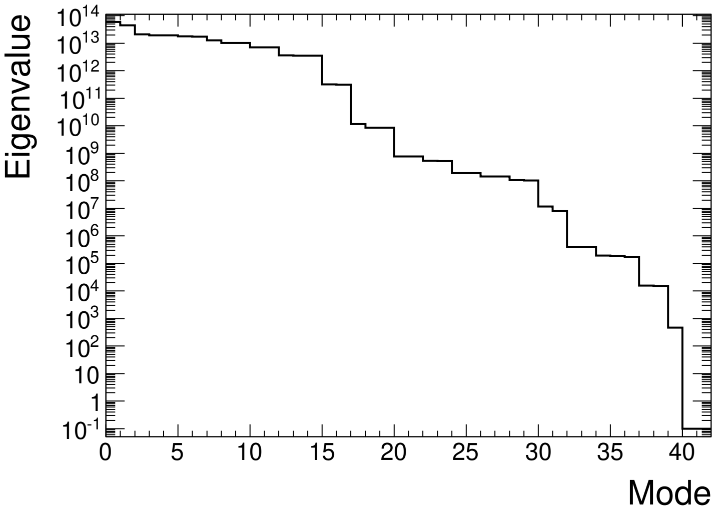

Figure 7.16.: The eigenvalues of the barrel region ATLAS Silicon Tracker at Level 2. Note to aid the visulisation, eigenvalues below 10^{-1} have been set to 10^{-1}

As opposed to the barrel, the parabolic nature of the poorly constrained movements in the x and y direction is strong and clearly evident in the movements with respect to the z position of the super structures (see Figure 7.23 and 7.24). Furthermore the movement of one end-cap is independent of the other.

As the magnitude of the eigenvalues is inversely related to the final error on the alignment parameters, it would be expected that the translations in the z direction would be associated to the smallest eigenvalues, as these movements are only very poorly defined especially in the end-caps. As such the next thirty modes are mainly associated to movements in the z, direction except for four. Those four eigenvalues correspond to movements in the x-y plane proportional to r^2 and z^2. This highlights again the inability of cutting on the eigenvalues to correctly remove unconstrained degrees of freedom.

There are also χ^2-invariant modes that are related to the z position of the super structures and the z translations. Naively, it would be expected that the relationship between these two would be linear, as the track (assuming it is of high enough transverse momentum) will be linear in the r-z plane. In reality this assumption breaks down on two fronts; firstly the magnetic field does have significant components in the radial direction at high $|z|$ (see Figure 3.7), secondly not all tracks have high transverse momentum and as such the track may bend significantly in the magnetic field so that $d\theta/dz$ of the track is not constant. The low transverse momentum tracks are easy to eliminate while the effect of the magnetic field is a reality of the detector.

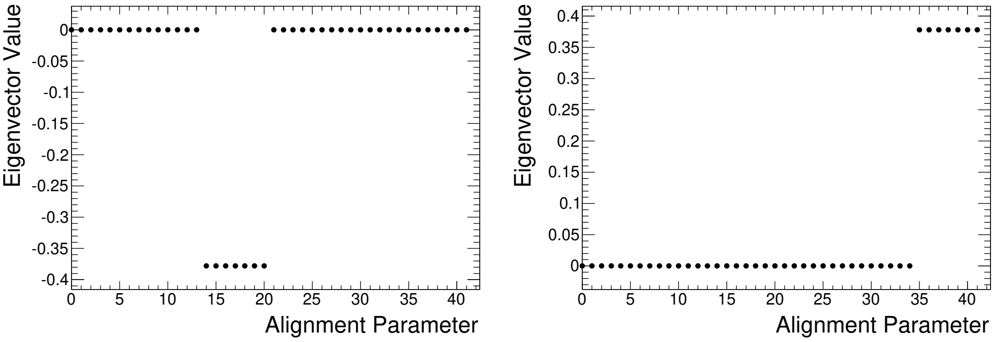

(a) Eigenvector 42: $\Delta T_z \propto 1$

(b) Eigenvector 41: $\Delta R_z \propto 1$

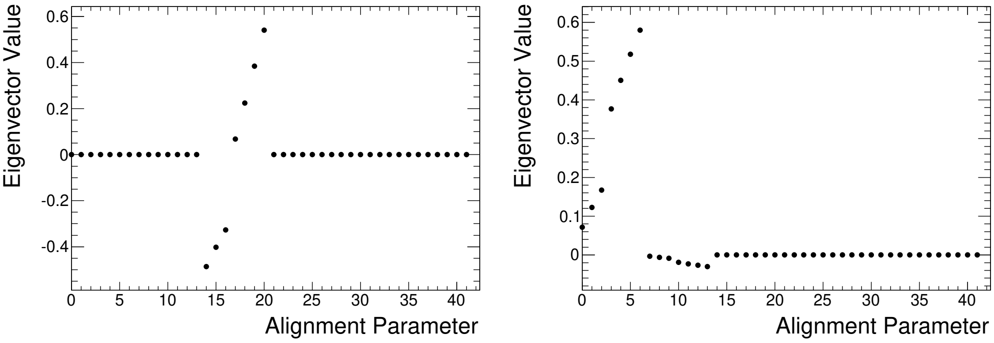

(c) Eigenvector 40: $\Delta T_z \propto r$

(d) Eigenvector 39: $\Delta(aT_x + bT_y) \propto r^2$

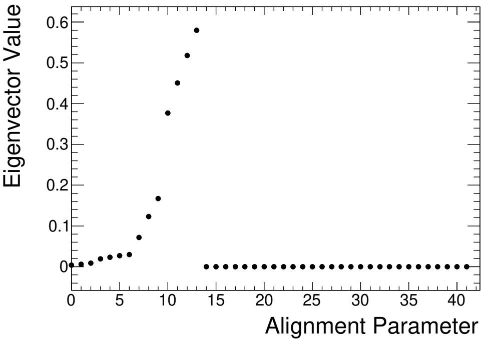

(e) Eigenvector 38: $\Delta(aT_x + bT_y) \propto r^2$

Figure 7.17.: The eigenvectors of the alignment matrix corresponding to the five smallest eigenvalues from the central barrel ATLAS Silicon Tracker at Level 2. Along the x axis of each plot are the alignment parameters while the y axis shows magnitude of the correction. The first seven parameters correspond to a translations in the x direction of module 1-7, parameters 8-14 correspond to a translation in the y direction, parameters 15-21 correspond a translation in z direction, parameters 22-28 correspond to a rotations around the x-axis, parameters 29-35 correspond the rotations around the y-axis, and parameters 35-42 correspond a rotation around the z-axis.

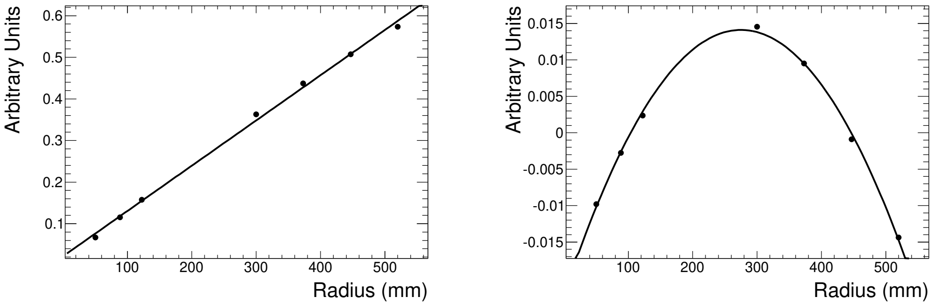

(a) T_x component of the eigenvector fit with a first order polynomial

(b) Residual after the removal of the linear component fit with a second order polynomial

Figure 7.18.: The T_x components of eigenvector 39 of the as a function of module radius.

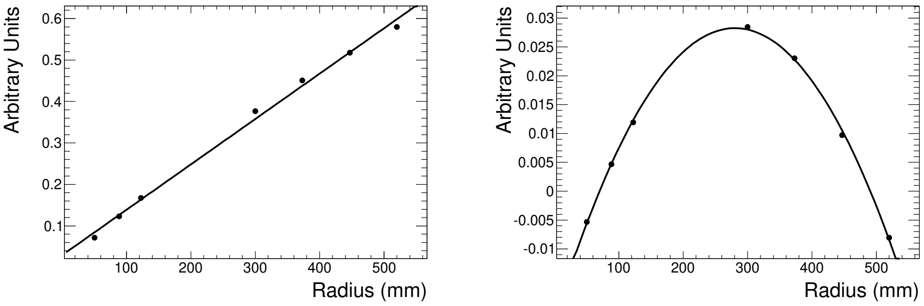

(a) T_y component of the eigenvector fit with a first order polynomial

(b) Residual after the removal of the linear component fit with a second order polynomial

Figure 7.19.: The T_y components of eigenvector 38 of the as a function of module radius.

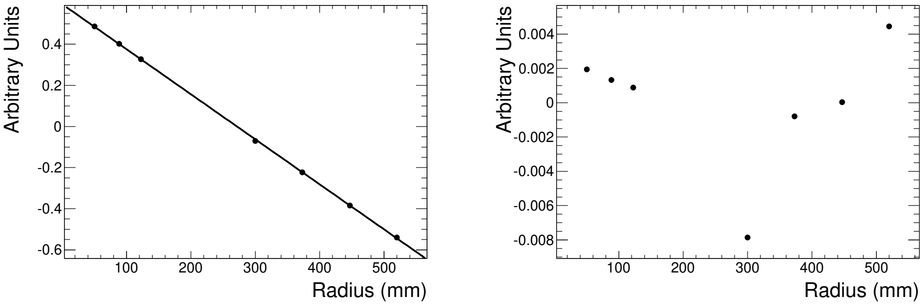

(a) T_z component of the eigenvector fit with a first order polynomial

(b) Residual after the removal of the linear component

Figure 7.20.: The T_z components of eigenvector 40 of the as a function of module radius.

When applying a linear fit to the systematic movement of the super structure in the z direction with respect to the z position of the structure (see Figure 7.25), the fit is reasonable when excluding the outer most disk. This further suggests that these effects seen are due to the changes in the magnetic field given that last SCT disk is surrounded by a rather weak and non axial magnetic field.

For the full ATLAS silicon tracker nineteen poorly constrained modes or χ^2-invariant degrees of freedom were identified. To constrain these modes required that the following movements are constrained:

- Global translations of the detector

$$\sum_{Module} T_i = 0 \text{ where } i = x, y, z$$

- Global rotations around the z axis

$$\sum_{Module} R_z = 0$$

- Shearing of the modules with respect to the module radius

$$\sum_{Module} T_i \cdot r_{Module} = 0 \text{ where } r_{Module} \neq 0 \text{ and } i = x, y, z$$

$$\sum_{Module} T_i \cdot r^2_{Module} = 0 \text{ where } r_{Module} \neq 0 \text{ and } i = x, y$$

- Shearing of the modules with respect to the module z position

$$\sum_{Module} T_i \cdot z_{Module} = 0 \text{ where } z_{Module} > 0 \text{ and } i = x, y, z$$

$$\sum_{Module} T_i \cdot z_{Module} = 0 \text{ where } z_{Module} < 0 \text{ and } i = x, y, z$$

$$\sum_{Module} T_i \cdot z^2_{Module} = 0 \text{ where } z_{Module} > 0 \text{ and } i = x, y$$

$$\sum_{Module} T_i \cdot z^2_{Module} = 0 \text{ where } z_{Module} < 0 \text{ and } i = x, y$$

To further stabilise the ends caps a very loose constraint on the z position $\mathcal{O}(1mm)$ can be imposed to constrain those movements.

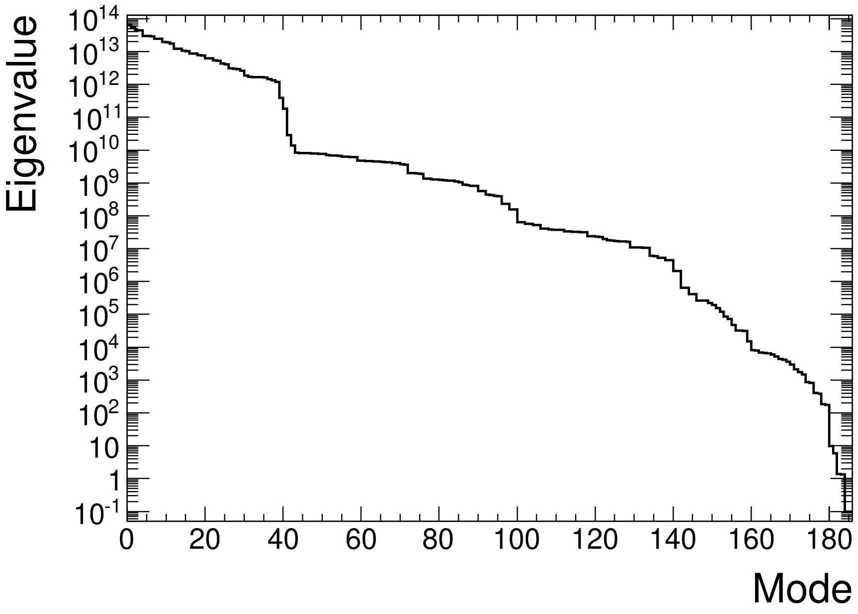

Figure 7.21.: The eigenvalues of the ATLAS Silicon Tracker at Level 2. Note to aid the visualisation, eigenvalues below 10^{-1} have been set to 10^{-1}

7.5.2. Level 3 Properties

To study the χ^2-invariant modes that are present when aligning the individual modules, the system was broken into sections in order to make it more computationally manageable. To study the barrel, a half cone geometry was constructed. The half cone geometry consists of every module between $\eta = 0$ and $\eta = 0.8$. This system has 1030 silicon modules within it and as such has 6180 degrees of freedom. To study the end-caps, modules with $\eta > 1.6$ were selected providing a system with 712 modules or 4272 degrees of freedom.

The tracks in both cases were required to have at least two hits in the pixel detector and five hits in the SCT detector. In addition to this the tracks were constrained in the transverse plane to the beams spot via a track parameter constraint on the transverse impact parameter.

Barrel - Half Cone

The unconstrained global degrees of freedom that are present during the Level 2 alignment are still present at Level 3, however they manifest themselves in a slightly different manner. The global rotation around the z axis and translation in z are clearly displayed in the eigenvectors associated to the smallest eigenvalues (see Figure 7.26) as they are at Level 2.

The other movements identified at Level 2 are now ϕ dependent (shown in Figures 7.28 to 7.33). The ϕ dependent nature is quite simple to explain. The invariant movements identified at Level 2 still apply to the whole detector. However, now there is no need for the movements to occur uniformly to the whole detector as the movements of the individual modules on a particular layer are not strongly correlated. Adjacent modules will be relatively well correlated (due to the overlap between them) but beyond that the correlations are quite small.

The ϕ dependant nature of the χ^2-invariant modes manifest themselves as harmonics of the detector (see Figures 7.28 to 7.33). Examination of the eigenvectors shows that there are four clearly distinguishable harmonics of the movements in the x-y plane across all layers of the ID. In total six modes are present but the last two are not as clean as the previous four. The number of harmonics is most likely related to the number of modules present and the amount of overlap between the modules. This suggests that a high degree of overlap between the modules will reduce number of harmonics. In addition to the modes in the x-y plane there are also modes in the z plane although they are less prevalent.

Additional poorly constrained degrees of freedom are introduced into the system that are not present at Level 2. Rotations around the x and y axes are possible (see Figure 7.27). These rotations were not allowed at level 2 as they would not leave the track helical and as such are not χ^2-invariant. However it appears that movements of the individual modules can allow for the rotation with a minimal impact on the χ^2. This is most likely due to the linearisation of the alignment problem.

In addition to these rotations a radial expansion of the detector becomes an unconstrained movement of the detector, despite the fact that these movements should be constrained by the inter module overlap. These movements are characterised by the position of the module $\vec{x}$ transforming to $a \cdot \vec{x}$ where a is a constant proportional to the magnitude of the position vector $\vec{x}$.

Another point of interest is that these modes lead to no net movement of the detector on a layer per layer or disk by disk basis. As such constraining the modules to the super structures that they are built on by ensuring that modules movements sum to zero would be clearly ineffective in this particular case.

End-cap - $\eta > 1.5$

Inspecting the eigenvectors from the end-cap system reveals a similar story. Again a global translation in the z direction and global rotation around the z axis are present as the first two χ^2-invariant modes of the detector (Figure 7.34).

The next modes exhibit a ϕ dependence but as opposed to the barrel situation the movements are predominately in the z direction (see Figure 7.35). In the case of the end-caps, movements in the z direction are poorly defined when compared to x and y directions, as they are not directly related to the measurement residual. As such the lower order modes are expected to be dominated by movements in the z direction.

The amount of information available for the alignment also differs significantly in both cases. In the barrel case each module had between 5000 and 1000 hits while in the end-cap case the modules have anywhere between 1000 and 50 hits, and as such alignment corrections can be quite poorly defined due to the lack of statistics. This, combined with greater distance the track has to be extrapolated between measurement planes, does increase the uncertainty on the residuals and as a result, on the alignment parameters.

Difference between the barrel and the end-cap harmonics is that the barrel harmonics were propagated through all layers (see Figure 7.36). This suggests that in the end-cap case the modules at either end of the detector are not very correlated to each other.

In summary, the study of the modes at Level 3 showed that the same movement allowed at Level 2 are still present at Level 3. However to constrain them completely the detector cannot be treated as a whole and would need to be broken into sectors.

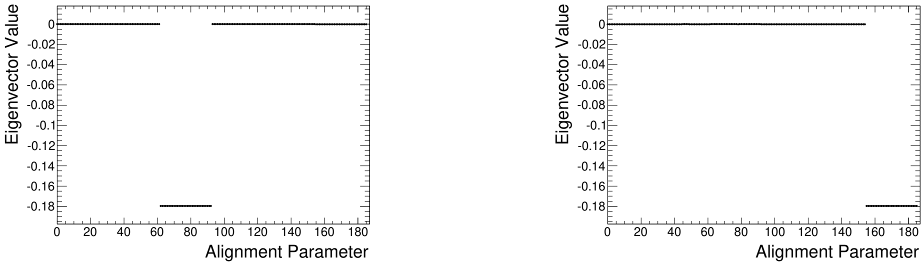

(a) Eigenvector 186: $\Delta T_z \propto 1$

(b) Eigenvector 185: $\Delta R_z \propto 1$

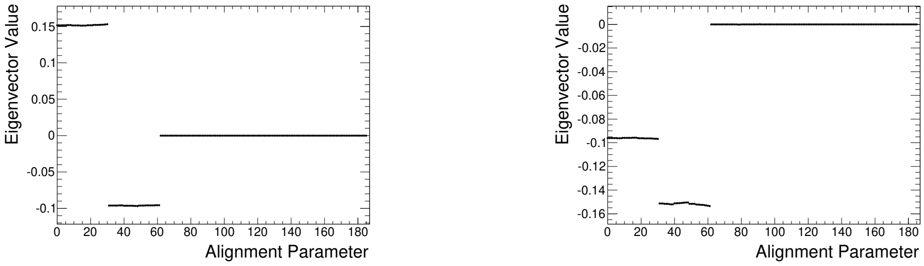

(c) Eigenvector 184: $\Delta(aT_x + bT_y) \propto 1$

(d) Eigenvector 183: $\Delta(aT_x + bT_y) \propto 1$

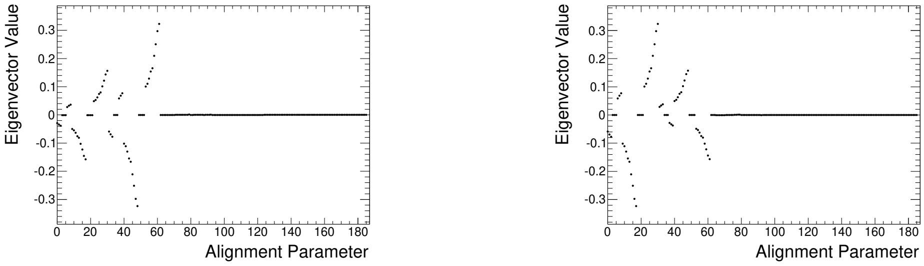

(e) Eigenvector 182: $\Delta(aT_x + bT_y) \propto z^2$

(f) Eigenvector 181: $\Delta(aT_x + bT_y) \propto z^2$

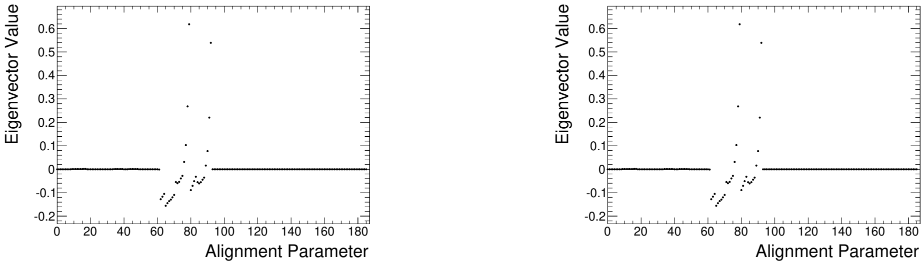

(g) Eigenvector 180: $\Delta T_z \propto z^2$

(h) Eigenvector 179: $\Delta T_z \propto z^2$

Figure 7.22.: The eigenvectors of the alignment matrix corresponding to the six smallest eigenvalues from the unconstrained ATLAS Inner Detector at Level 2. Along the x axis of each plot are the alignment parameters while the y axis shows magnitude of the correction. The first thirty one parameters correspond to a translations in the x direction of super structure 1-31, parameters 12-62 correspond to a translation in the y direction, parameters 63-93 correspond a translation in z direction, parameters 94-124 correspond to a rotations around the x-axis, parameters 125-155 correspond the rotations around the y-axis, and parameters 156-186 correspond a rotation around the z-axis.

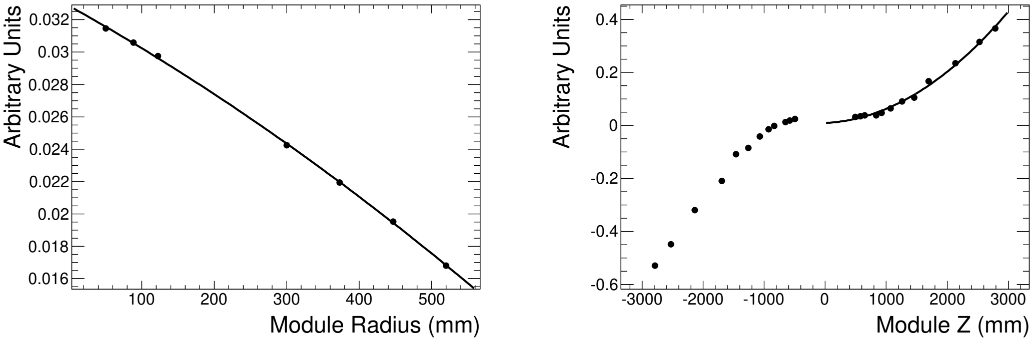

(a) R - Fit with a second order polynomial

(b) Positive Z - Fit with a second order polynomial

Figure 7.23.: The T_x components of the 182th mode the full Silicon Tracker at Level 2.

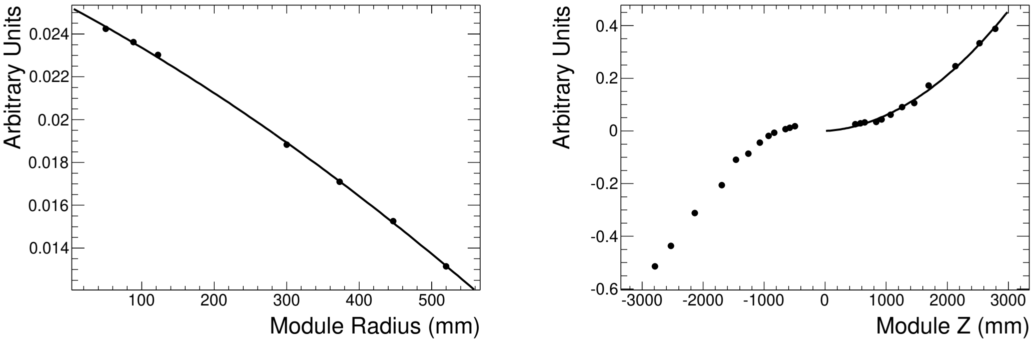

(a) R - Fit with a second order polynomial

(b) Positive Z - Fit with a second order polynomial

Figure 7.24.: The T_y components of the 182th mode the full Silicon Tracker at Level 2.

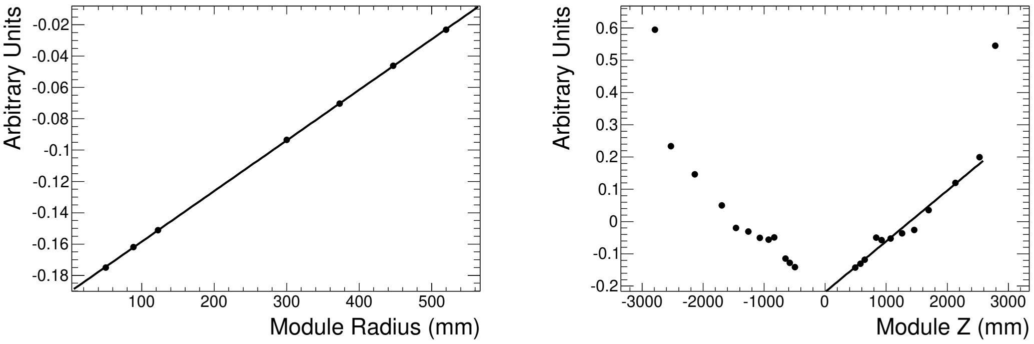

(a) R - Fit with a first order polynomial

(b) Z - Fit with a first order polynomial (excluding the furthest point)

Figure 7.25.: The T_z components of the 180th mode the full Silicon Tracker at Level 2.

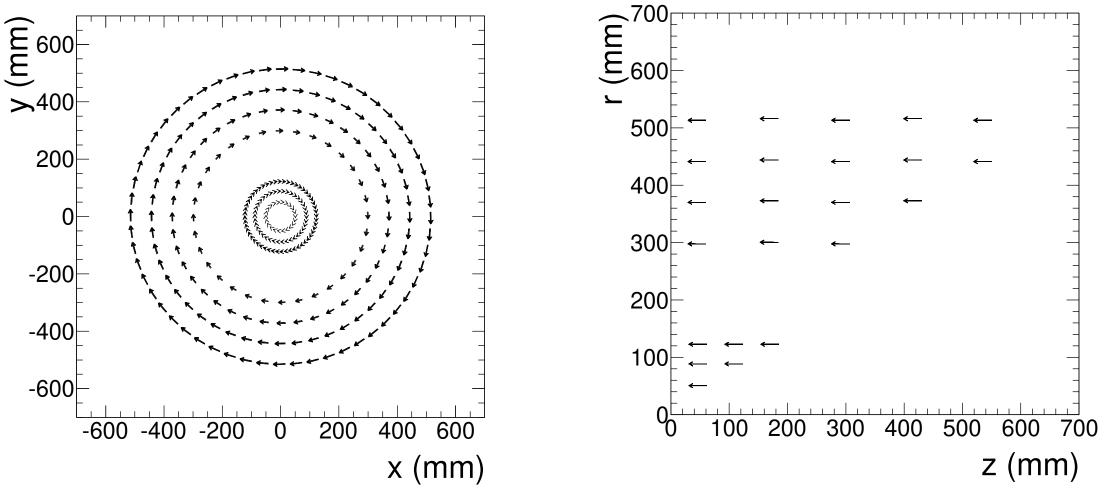

(a) Global Rotation around the z axis

(b) Global Translation in the z direction

Figure 7.26.: Movements represented by the first two χ^2-invariant modes of the barrel system

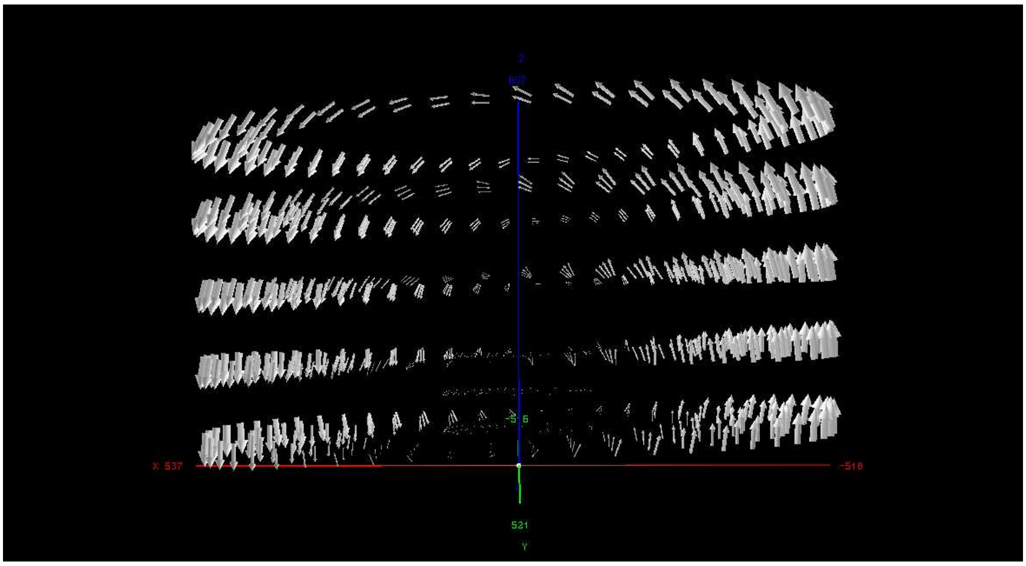

Figure 7.27.: A three dimensional representation of the seventh mode of the central barrel cone. The mode seems to exhibit rotation around the y axis.

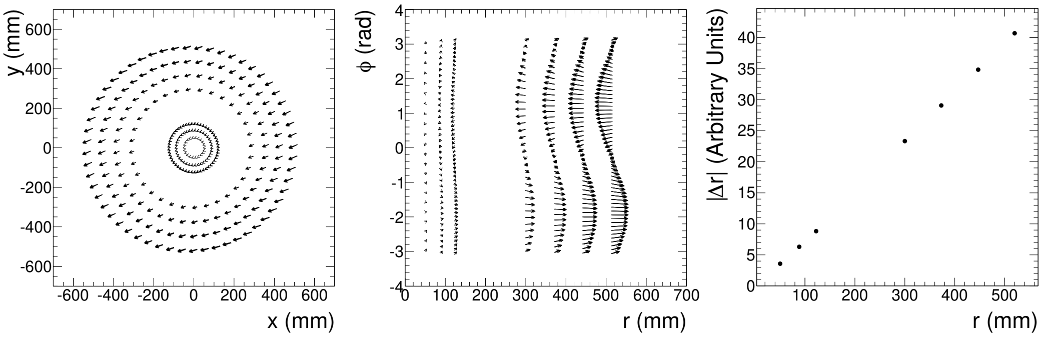

(a) **(b)** **(c)**

Figure 7.28.: The first harmonic of the movement $aT_x + bT_y \propto r$ in the barrel.

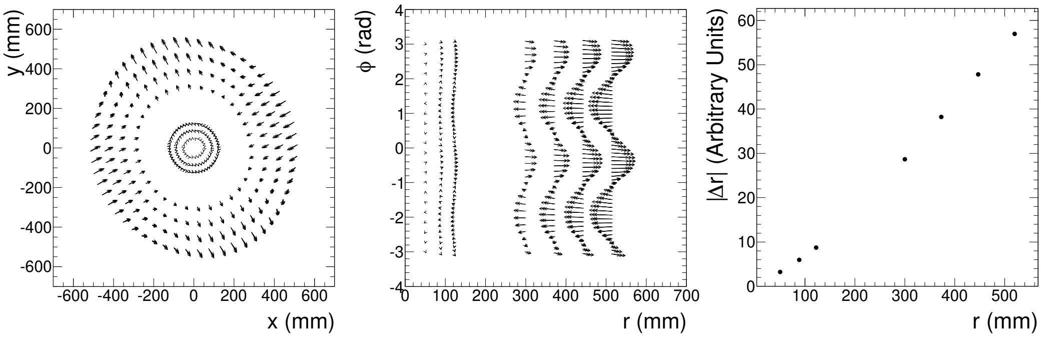

(a) **(b)** **(c)**

Figure 7.29.: The second harmonic of the movement $aT_x + bT_y \propto r$ in the barrel.

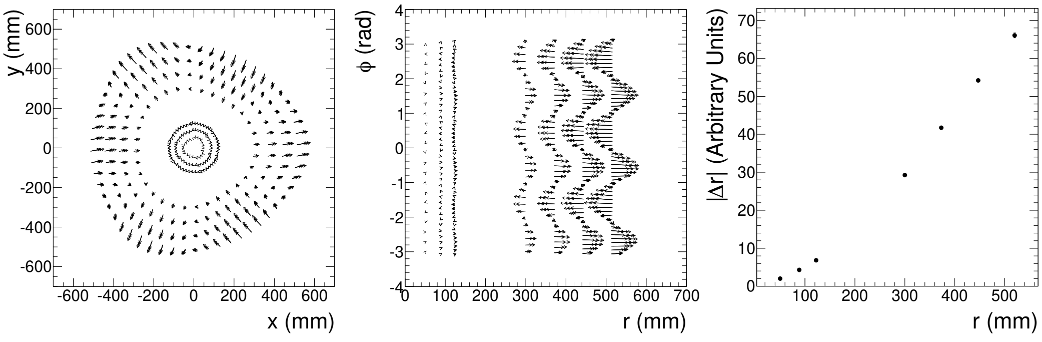

(a) **(b)** **(c)**

Figure 7.30.: The third harmonic of the movement $aT_x + bT_y \propto r$ in the barrel.

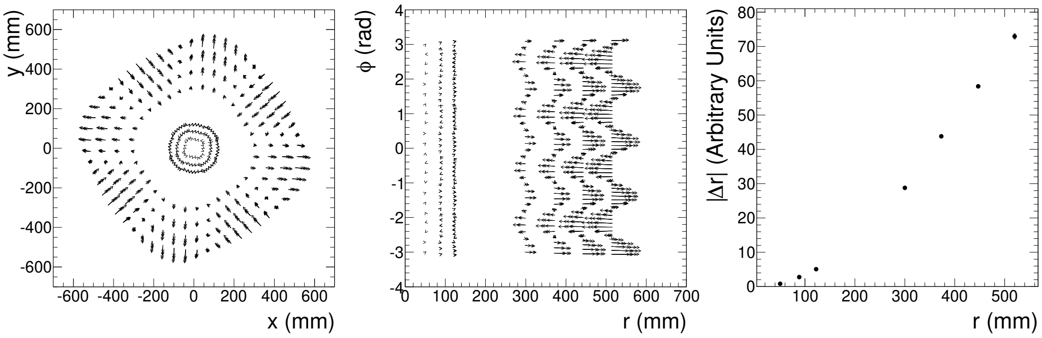

(a) **(b)** **(c)**

Figure 7.31.: The forth harmonic of the movement $aT_x + bT_y \propto r$ in the barrel.

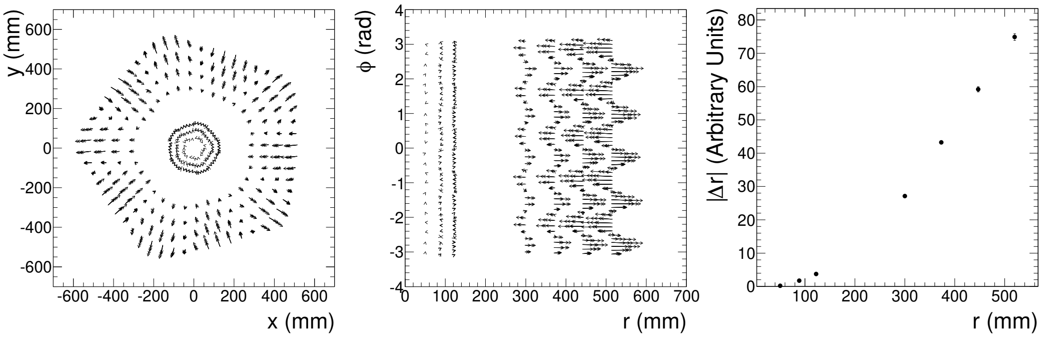

(a) **(b)** **(c)**

Figure 7.32.: The fifth harmonic of the movement $aT_x + bT_y \propto r$ in the barrel.

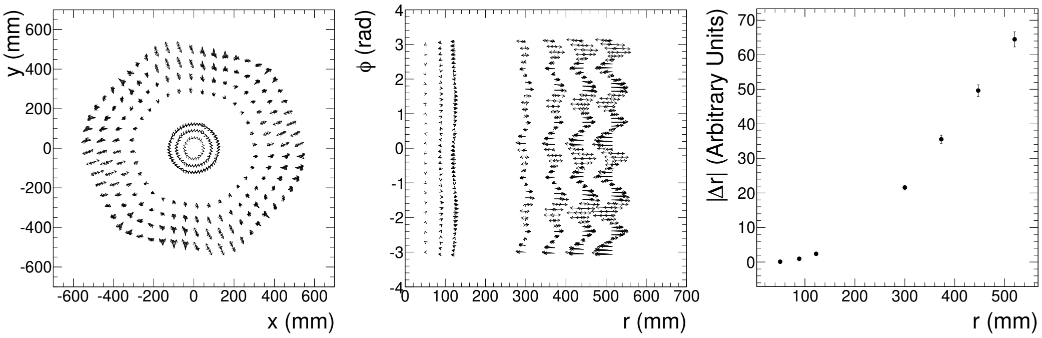

(a) **(b)** **(c)**

Figure 7.33.: The sixth harmonic of the movement $aT_x + bT_y \propto r$ in the barrel.

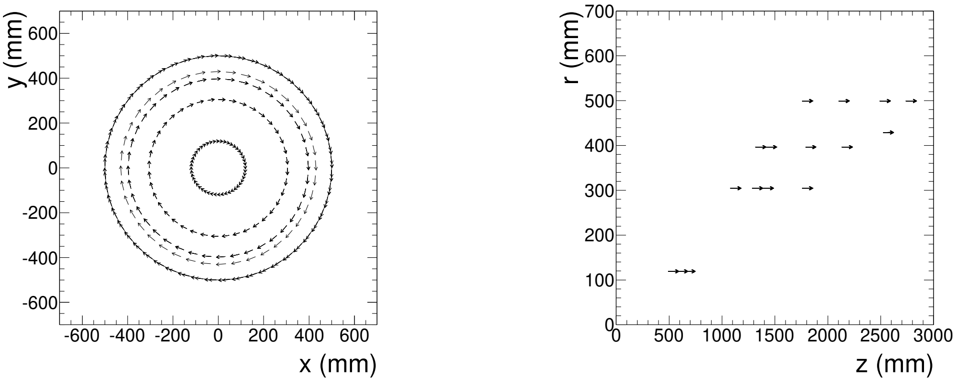

(a) Global Rotation **(b)** Global Translation

Figure 7.34.: The first modes of the end-cap system at Level 3

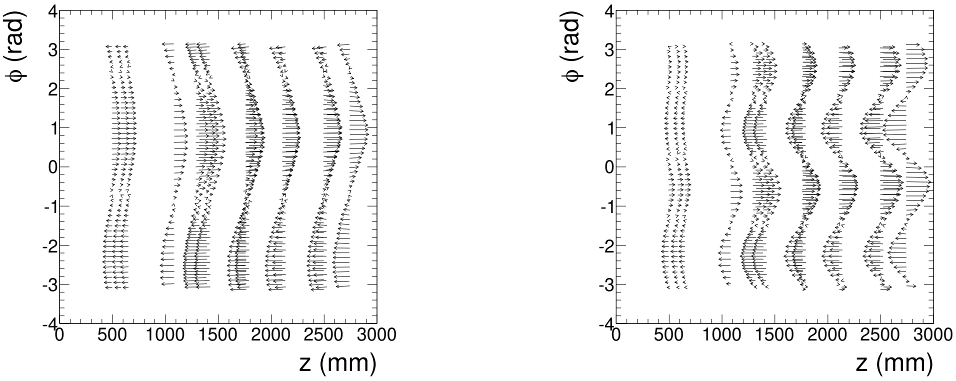

(a) First Harmonic **(b)** Second Harmonic

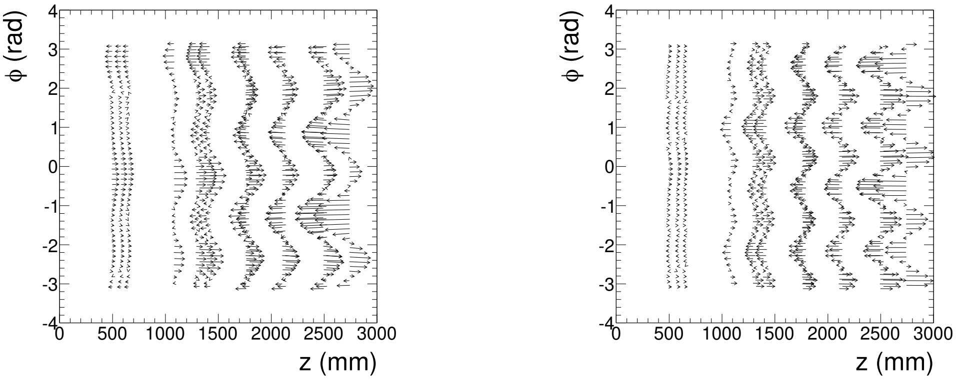

(c) Third Harmonic **(d)** Forth Harmonic

Figure 7.35.: The first four harmonics of the corrections in the end-caps

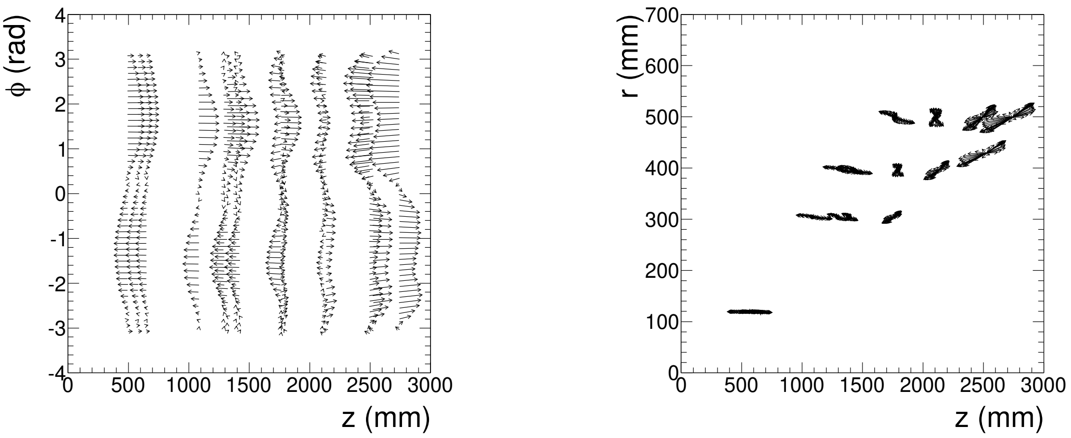

(a) **(b)**

Figure 7.36.: The seventh mode of the Level 3 alignment of the end-caps displaying a η dependence on the movements

7.6. Modification of Standard Alignment Procedure

As was mentioned the standard CSC alignment procedure (Section 7.3) is not fail safe, as some χ^2-invariant modes are not constrained. A safer recipe consists of explicit elimination of the χ^2-invariant modes identified in the previous section. The use of Lagrange Multipliers to explicitly eliminate the unconstrained movements of the detector was shown to be an effective method of constraining the χ^2- invariant modes of the toy model (see Section 6.4.1) and was applied to the alignment of the full ATLAS detector system.

In this section a discussion of how to apply the constraint through the use of Lagrange Multipliers on the ATLAS detector is presented. This is followed by results of applying the constraints to the Level 2 and Level 3 alignment of the ATLAS detector.

7.6.1. Implementation of Lagrange Multiplier Constraints

To apply Lagrange multiplier constraints, a knowledge of rate change of the alignment parameters with respect to each of the detector movements that are to be constrained is required .

$$\frac{dQ}{d\alpha}, \tag{7.1}$$

must be calculated for each constraint, Q. In most cases this is best achieved numerically. The movement associated with the constraint, for each module, can be represented by the transformation $\mathscr{T}_Q$ in the reference frame of the module. As the transformation is actually a function of the alignment parameters $(T_x, T_y, T_z, R_x, R_y, R_z)$, and assuming that the magnitude of the transformation is infinitesimally small (i.e. $|\mathscr{T}_Q| = \epsilon$) the derivatives of the alignment parameters of the module can be represented by the transformation $\mathscr{T}_Q$ given by

$$\frac{dQ}{d\alpha} \approx (T_x/\epsilon, T_y/\epsilon, T_z/\epsilon, R_x/\epsilon, R_y/\epsilon, R_z/\epsilon). \tag{7.2}$$

As the application of the constraints requires knowledge of the relationship between the effect of certain global movements on the position of the module, application of the constraints at Level 2 is very simple, as every super module's position is defined in the global frame. At Level 3 more work needs to be done as the modules are defined in their local reference frame and the invariant movements are all defined with respect to the global frame.

The transformation from the local frame into global is defined to be $\mathscr{T}_G$ and the movement in the global frame is given by $\mathscr{T}_M$. Therefore the transformation that defines the global movement in the local frame is

$$\mathscr{T}_Q = \mathscr{T}_G^{-1} \mathscr{T}_M \mathscr{T}_G. \tag{7.3}$$

When aligning the individual modules of the detector (Level 3 alignment) the χ^2-invariant modes of the detector present themselves as ϕ dependent harmonics (as discussed in Section 7.5.2). In order to constrain the movements of the modules well the detector is divided into twelve equal ϕ sectors. Within each sector the following constraints were applied:

- Shear of the modules with respect to the module radius

$$\sum_{Module} T_i \cdot r_{Module} = 0 \text{ where } i = x, y, z$$

$$\sum_{Module} T_i \cdot r^2_{Module} = 0 \text{ where } i = x, y$$

- Shearing of the modules with respect to the module z position

$$\sum_{Module} T_i \cdot z_{Module} = 0 \text{ where } z_{Module} > 0 \text{ and } i = x, y, z$$

$$\sum_{Module} T_i \cdot z_{Module} = 0 \text{ where } z_{Module} < 0 \text{ and } i = x, y, z$$

$$\sum_{Module} T_i \cdot z^2_{Module} = 0 \text{ where } z_{Module} > 0 \text{ and } i = x, y$$

$$\sum_{Module} T_i \cdot z^2_{Module} = 0 \text{ where } z_{Module} < 0 \text{ and } i = x, y$$

- Radial expansion of the modules

$$\sum_{Module} T \cdot |\vec{x}| = 0 \text{ where } \vec{x} \text{ is the position of the module}$$

These in combination with the six constraints that define the frame of reference require a total of 198 constraints. It could be foreseen that these constraints will need to be further segmented in η, however at this stage it is not required.

7.6.2. Level 2 Alignment

Applying constraints to a perfectly aligned system enables the study of their effectiveness in stabilising the system. The results of aligning the perfect system should ideally return zero for all parameters (within statistical accuracy) hence any statistically significant change of the alignment parameters should be the result of poorly constrained χ^2-invariant modes. Aligning the system using the constraints described in Section 7.5 resulted in a relatively stable system except for the parameters relating to rotations around the z axis.

On closer inspection the parameters exhibited a strong dependence on the radius and z position of the modules. Figures 7.37a and 7.38a show the R_z corrections as a function of r and z respectively (the movements with respect to z direction are independent in each end-cap). The rotations of the modules with respect to the radius exhibits a $R_z \propto 1/r$ like behavior. To understand what this means for the measurements, assume that that the point $(r, 0, 0)$ is rotated around the z axis as such

$$R_z(\varphi/r) \rightarrow x \approx r, \;\; y \approx \varphi.$$

To first order approximation this is a constant translation of the measurement in the $r\phi$ direction. However, given the cylindrical nature of the detector it cannot be expected to be truly a χ^2-invariant movement and as such is corrected for in the next iteration (see figure 7.37b).

Similarly the z dependence of the rotation is of the form $R_z \propto z$. Again to understand the effect of this rotation on the measurements consider the point $(r, 0, z)$

$$R_z(z\varphi) \rightarrow x \approx r, \;\; y \approx rz\varphi.$$

Which again is not a truly χ^2-invariant movement as such is corrected for in the next iteration (see Figure 7.38b).

As these modes are only *pseudo* χ^2-invariant modes the question must be asked how did they arise? A possible answer is that they emerge because of the linearisation of the problem. A number of assumptions are made during the formation of the χ^2 minimisation the biggest is that problem is linear. The linearisation may over simplify the problem and miss nuances.

The identification of the pseudo χ^2-invariant modes is, in general, rather simple as after the movement is introduced it will be corrected for in subsequent iterations.The only real concern of these modes is the random nature of the magnitude of these pseudo χ^2-invariant deformations. An understanding of the cause of which is yet to be completely determined. It may be that the other constraints somehow force these rotations of the detector however no further evidence can be found to support this hypothesis.

These psuedo χ^2-invariant deformations not only effect the principle movement but they also effect the accuracy of other alignment parameters (see Figure 7.39) which

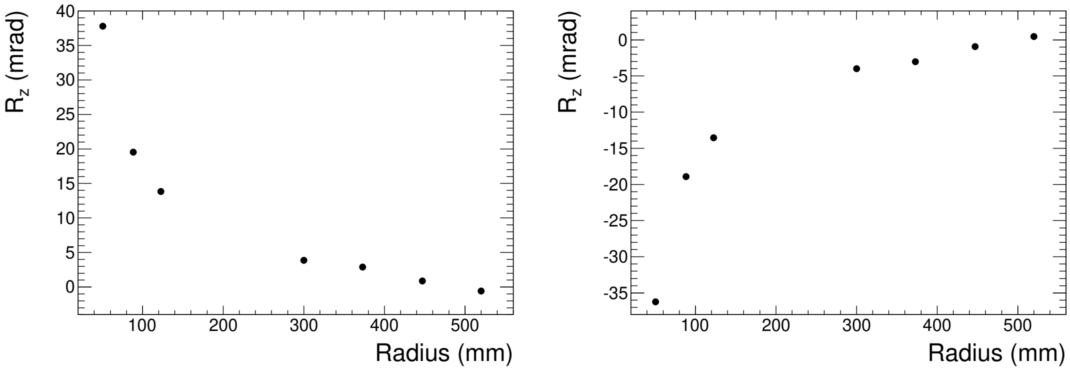

(a) Eighth Iteration **(b)** Ninth Iteration

Figure 7.37.: The R_z corrections, at Level 2, of the perfect aligned system.

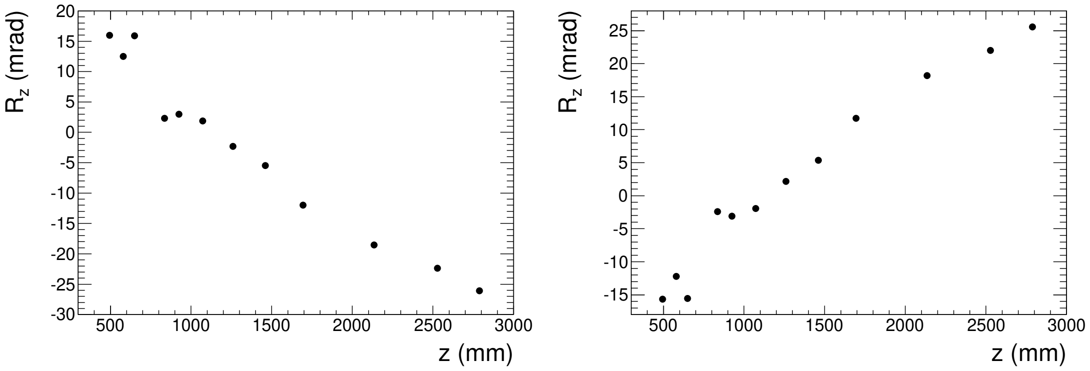

(a) Eighth Iteration **(b)** Ninth Iteration

Figure 7.38.: The R_z corrections, at Level 2, of the perfect aligned system.

is expected to a certain extent. By adding an additional three constraints

$$\sum_{Module} R_z / r_{Module} = 0$$

$$\sum_{Module} R_z \cdot z_{Module} = 0 \text{ where } z_{Module} > 0$$

$$\sum_{Module} R_z \cdot z_{Module} = 0 \text{ where } z_{Module} < 0$$

to the original nineteen it is possible to compare the effect that the additional constraints have on the other parameters.

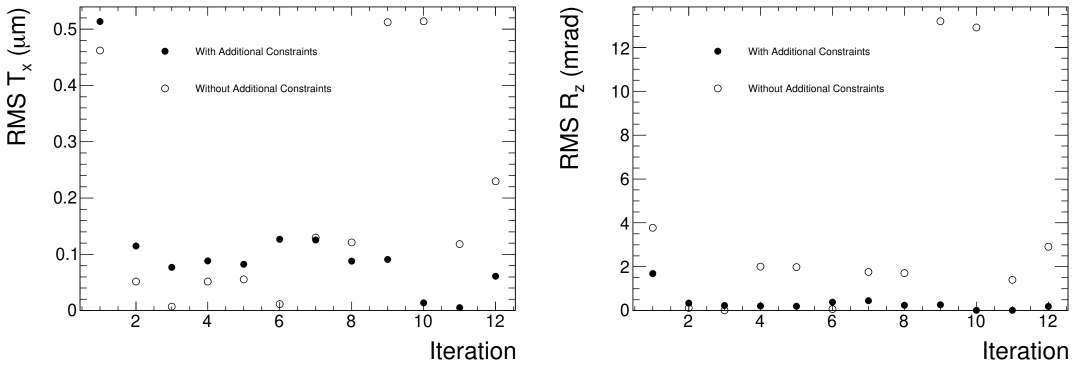

(a) T_x

(b) R_z

Figure 7.39.: The RMS of the T_x and R_z corrections, at Level 2, of the perfect aligned system across a number of iterations using Lagrange multipliers to constrains the system.

Figure 7.40 shows the effect of the 22 constraints on the results of the alignment on a perfect detector over a number of iterations in comparison to the standard CSC alignment procedure.

The first thing to note is that, as expected, the average movement of the super structures at Level 2 is consistent with zero for the all movements when Lagrange multipliers are used. This shows that the constraints behaved as designed and ensure that the detector does not deviate from its mean starting position. This also shows that the RMS of the corrections after the second iteration are effectively zero for the constrained system, while for the standard alignment procedure the modules continue to display significant fluctuations.

Although Lagrange multipliers are an effective way to constrain the alignment of the detector caution is required when using them in conjunction with other techniques. Incorrect application can lead to the alignment parameters being totally compromised. For example, a ϕ dependence on the momentum can be introduced if the full suite of constraints are applied to the detector at Level 2 in conjunction with an impact parameter constraint if the detector is displaced from its ideal position. The impact parameter constraint has the effect of trying to move the pixel layers in a certain manner while the Lagrange multipliers fix the detector into a certain shape. As the pixel detector needs to move a large distance ($\sim 2\ mm$) to correct for CSC misalignment, this imparts a large ϕ dependence on the reconstructed momentum (see Figure 7.41).

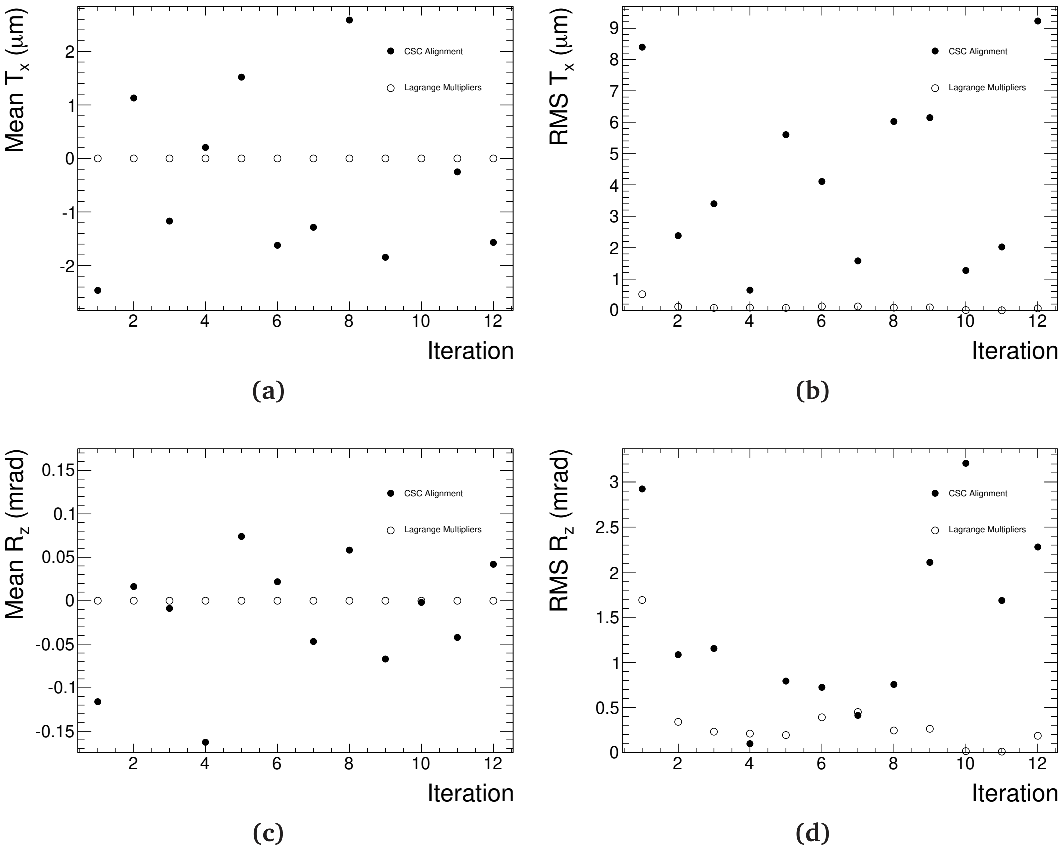

Figure 7.40.: The effectiveness of the Lagrange multipliers at stabilising the alignment of the Silicon Tracker at Level 2.

What Constraints Should be Used on a Misaligned System?

There is a minimum number of constraints required to ensure that the system it not singular. As was shown from the properties of the toy model there are six eigenvalues which are approximately zero. To eliminate these six singular modes, a frame of reference must be defined, for example through the use of Lagrange multipliers or with a combination of track parameter constraints. If there is a need for the whole detector to move globally to accommodate another constraint of the system (e.g. a common vertex constraint), careful consideration is needed when considering the impact of the other alignment parameter constraints. As such only five constraints were applied to the system; a track parameter constraint on the impact parameter, Lagrange multiplier constraints on global translation z, and finally constraints on global rotations around the three axes. These constraints define the frame of reference for the

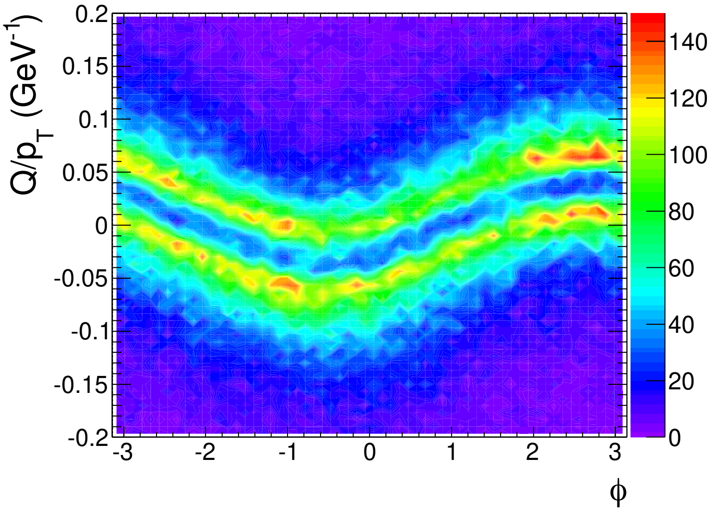

Figure 7.41.: ϕ dependence of the reconstructed momentum introduced by a combination of track parameter constraints and Lagrange Multiplier constraints.

alignment system. Defining the frame of reference should be considered a minimum requirement for an alignment problem.

The convergence of the alignment takes significantly longer to obtain a suitably stable solution than what was shown in the CSC exercise. Using 20,000 muon events twelve iterations were performed at Level 2 before end-cap disks of the SCT reached a somewhat stable solution. The outer most end-caps, having the least hits, take a long time to converge to a reasonable solution. Figure 7.42 shows the improvement of the track quality and track finding ability of during Level 2 alignment iterations. The average number of tracks per event, hits per track and holes per track approach their ideal, but do not quite reach them. The individual modules misalignments, which have not been taken into account, do not allow the track finding to perform optimally. A clearer effect of the Level 3 misalignments is the average value of the χ^2/DoF of a track, which is still approximately three times larger than its desired value.

This method of aligning the Level 2, like the CSC method, makes no effort to constrain any possible χ^2-invariant modes. As it is unknown if any undetectable deformations are present it was decided that there was no need to stop them from being introduced as they will need to be corrected for at a later date.

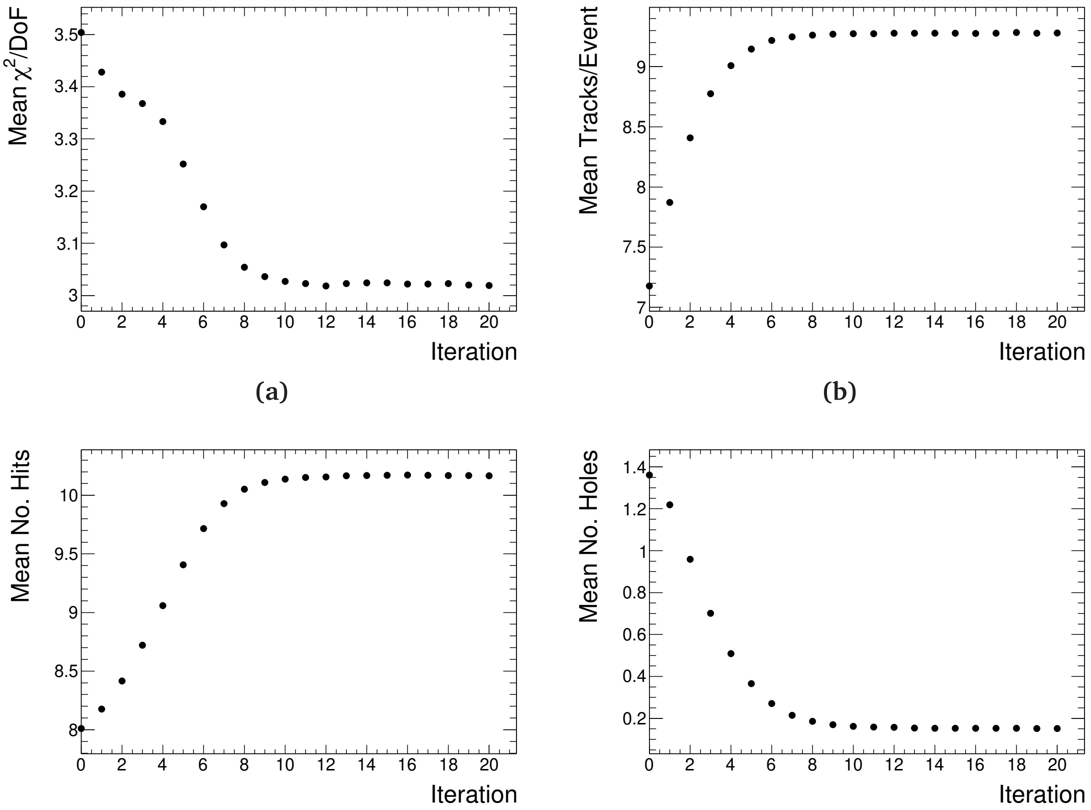

(a) (b) (c) (d)

Figure 7.42.: The improvement of the track quality during L2 alignment of the misaligned detector. The last eight iterations using information from the TRT to remove certain systematic distortions

7.6.3. Removal of χ^2 Invariant Distortions

After the Level 2 alignment a significant momentum scale bias is present. As the alignment system has converged there it would be safe to assume that the detector is now aligned but deformed in a χ^2-invariant manner. The standard information obtained from collision data is going to be unable to eradicate this bias hence the need for additional information. In the CSC exercise, simulated collision data was combined with track from cosmic rays. These tracks link the upper and lower half of the detector allowing for some radially dependent movement to be constrained. As tracks only are reconstructed in the barrel of the detector they will have a limited ability in removing the χ^2-invariant modes in the end-caps.

An alternative technique in trying to remove the χ^2-invariant modes is to place a momentum constraint of the reconstructed tracks within the alignment procedure.

Almost all of the χ^2-invariant modes will have an effect on the reconstructed momentum and as such constraining the track to its correct value should correct the alignment of the detector.

The information required for such a constraint can be obtained from the TRT. Starting from a perfectly aligned TRT, tracks extended from the silicon tracker into the TRT are combined to provide a track using all hit information. The track is then split into two parts one containing only hits from the TRT, the other only containing hits from the silicon detectors. The TRT portion of the track is then refitted using constraints on the tracks θ, z_0 and d_0 extracted from the full track fit. The track parameters θ and z_0 are constrained as in the barrel of the detector the TRT alone is unable to determine them to any reasonable accuracy. The track parameter d_0 is also constrained but to an error 25 times larger than the uncertainty of the original track fit to reduce the effects of any biases. This constraint significantly improves the resolution and reduces the uncertainty on the reconstructed momentum thus increasing the strength of the constraint (see Figure 7.43).

The silicon portion of the track is then refitted using a constraint on the track parameter d_0, ϕ_0 and Q/p extracted from the TRT only measurement. It is this silicon only track that is used for the alignment of the detector and in addition to this the information from the TRT only track is propagated into the alignment to allow for a track parameter constraint.

Despite the fact that the TRT's standalone momentum resolution is not as good as the standalone Silicon Tracker (see Figure 7.43), the system is able to correct for the momentum bias present given enough tracks. Additionally the TRT does not cover the whole Inner Detector. As such a mixture of tracks that contain the TRT constraint and tracks that don't were used to align the detector. Figure 7.44 illustrates the improvement in momentum scale bias in central barrel and the end-caps for silicon only tracks after the application of constraints on the tracks ϕ_0 and Q/p_T derived from the TRT to the alignment procedure for eight iterations of the alignment procedure.

This form of constraint has its dangers, as any bias in the measured quantities from the TRT will be propagated to the Silicon Tracker. Given that the χ^2-invariant modes of the TRT will be similar to those of the Silicon Tracker it would be possible to correct for the modes introduced in the Silicon Tracker. A safer way to use a momentum constraint would be to use high momentum muon tracks as measured in the muon spectrometer. As the magnetic field in the muon detector is entirely different to that

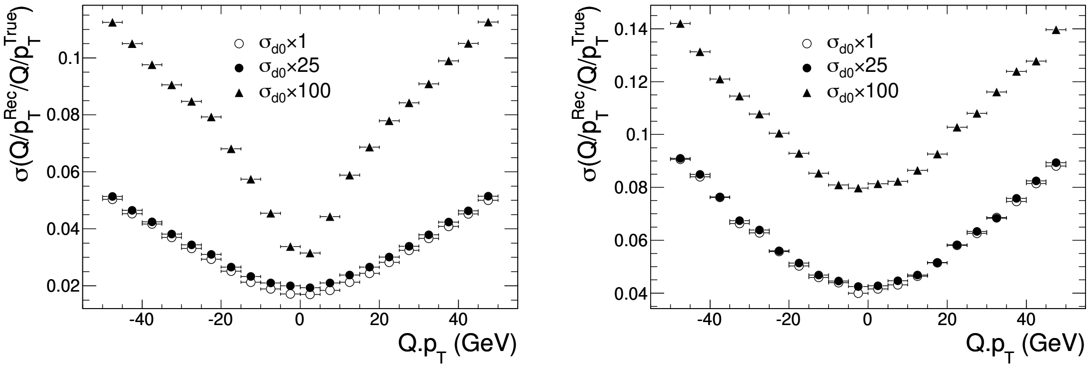

(a) $|\eta| < 0.8$ **(b)** $|\eta| > 1.5$

Figure 7.43.: The momentum resolution of the TRT only tracks used to constrain the alignment of the silicon tracker. The effect of increasing the uncertainty of the transverse impact parameter is shown.

in the ID, the geometrical nature of the χ^2-invariant modes in the muon spectrometer should also be different. As such, aligning the detector with constraints derived form the muon spectrometer should ensure that the detector is free from systematic biases that cannot be removed by the alignment procedure. This is yet to be tested, and the results using the TRT to extract a momentum constraint act as proof of the momentum constraint principle. Also the Muon spectrometer has better momentum resolution than the Inner Detector, and as such the constraints applied should be much more stringent than those of the TRT.

It should be pointed out that constraints aimed at restricting the χ^2-invariant movements present should be removed, as these will hamper the efforts of trying to correct for any χ^2-invariant distortion of the detector.

The question may be asked of the point of constraining the system if the χ^2-invariant modes can be removed at a later date. Imparting constraints improves the convergence of the system as the system has fewer degrees of freedom as was shown with the toy model. However the gross misalignment of the detector does not allow for the detector to move freely enough if constrained from the start. Additionally it may take a significant effort to obtain an unbiased system and as such it would nice to have the assurance that the system will contain the same systematic biases before and after alignment.

The TRT constraint alone will not and can not remove all χ^2-invariant modes as the TRT does not provide any information about the track parameters z_0 and θ. This means that modes involving the translations in the global z direction cannot be cor-

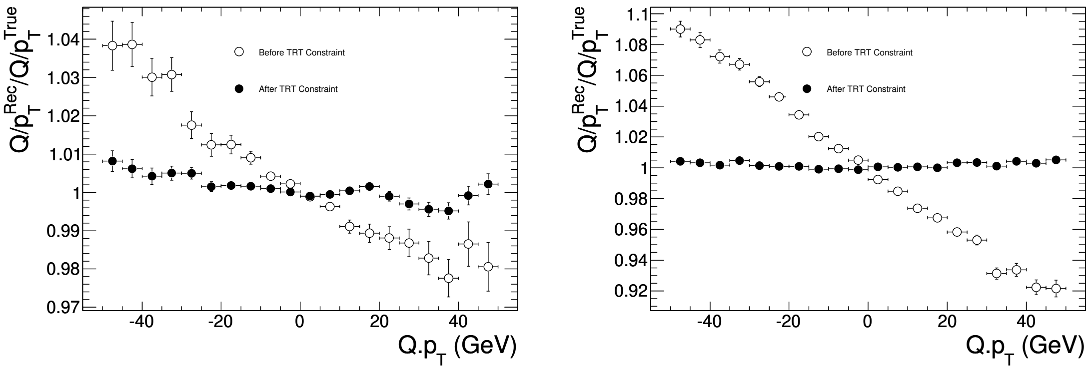

(a) $|\eta| < 0.8$ **(b)** $|\eta| > 1.5$

Figure 7.44.: The reduction in the momentum bias and after the application of the TRT constraint.

rected, for example $T_z \propto z$. Movements of this kind will significantly bias the reconstructed θ and hence the momentum of the track. To correct these modes more information is required. Cosmic rays link the lower and upper half detector meaning that any radially dependant shift of the detector modules can be removed including z translations. As the cosmic tracks do not illuminate the full detector a mix of cosmic tracks with collision tracks was used during the alignment.

To highlight the effects of using cosmic rays the results of aligning the detector at Level 2 including the additional information obtained from cosmic ray tracks was performed for three iterations. The results can be seen in Figure 7.45. The reconstructed θ had a distinct asymmetry prior to alignment with cosmic ray which is removed. Also rather fortuitously the track parameter z_0 becomes less biased. This is the result of the pixel detector moving the most to correct for the misalignments (see Figure 7.46).

7.6.4. Level 3 Alignment

The alignment at Level 3 proved successful during the CSC alignment procedure. The only possible issue was the lack of constraints on the χ^2-invariant modes. Although it was not determined if any deformations were introduced during the CSC alignment procedure it is clear that such deformations are possible and are detrimental to the overall performance of the ATLAS detector.

To ensure that these deformations do not enter the solution of the alignment parameter, the detector was constrained using the constraints described in Section 7.6.1.

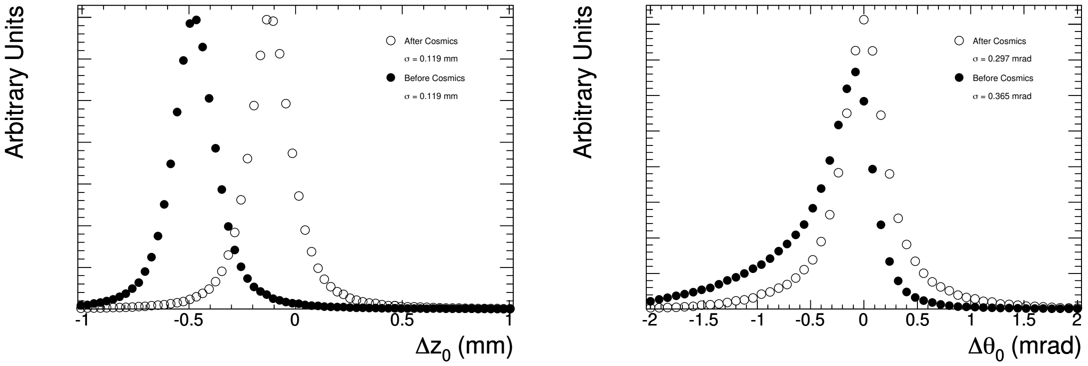

(a) **(b)**

Figure 7.45.: Difference between the reconstructed track parameter resolution before and after the use if cosmic tracks in the alignment

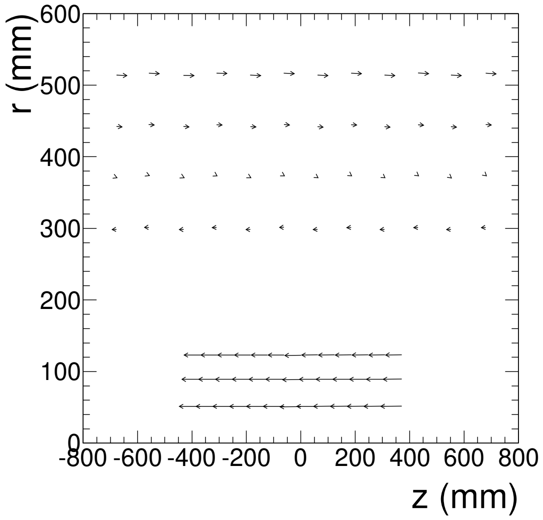

Figure 7.46.: The difference between the alignment constants,for the barrel only, before and after the application cosmic tracks to help align the detector. The arrows indicate the magnitude and direction of the corrections. (The magnitude of the differences has been increased by a factor of 250 to aid visualisation)

After three iterations the alignment looked to have converged yielding a much better resolution on all of the track parameters especially the momentum (see Figure 7.47). In addition, measures of the track quality and track finding quality (Figure 7.48) obtain their ideal values.

Two further iterations at Level 2 were performed using cosmic tracks and constraints derived from the TRT. This effectively removes all of the remaining biases from the detector besides a ≈ 100 μm shift of the detector in the global z direction (see Figure 7.50).

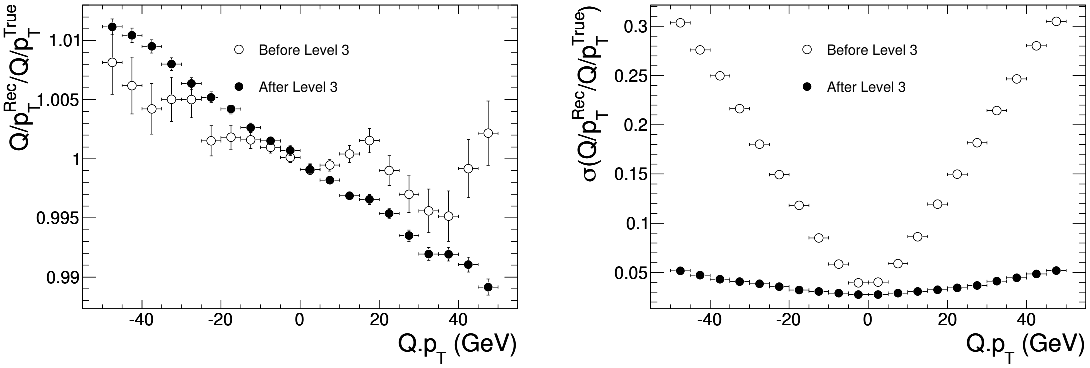

(a) $|\eta| < 0.8$ **(b)** $|\eta| < 0.8$

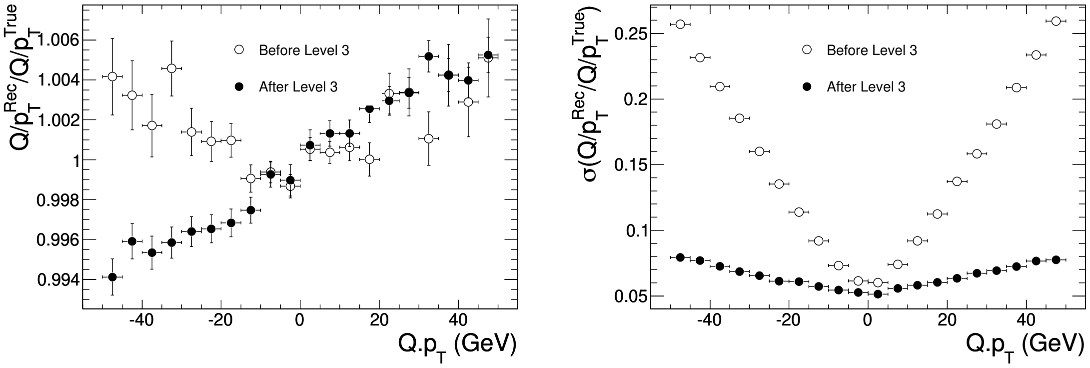

(c) $|\eta| > 1.5$ **(d)** $|\eta| > 1.5$

Figure 7.47.: Reconstructed momentum bias and resolution after application of Level 3 alignments

The effectiveness of the tracking (Figure 7.48) is identical to that of the perfectly aligned detector. The general track quality is also identical to that of the perfectly aligned detector, needless to say that track hit residuals are virtually perfect.

The resolution of the reconstructed track parameters is only compromised marginally (maximum of less than 3%) and only the longitudinal impact parameter is biased. Further statistics would be expected to improve the Level 3 alignment allowing the detector to reach the ultimate precision.

Close inspection of the reconstructed momentum suggests that some form of systematic bias was introduced in the end-caps (0.3% at $p_T = 50$ GeV)(see Figure 7.49). At this stage it is unknown if this bias was introduced during level 3 alignment or if it can not be removed at Level 3 using the information that has been used. This is a major improvement over the standard alignment procedure.

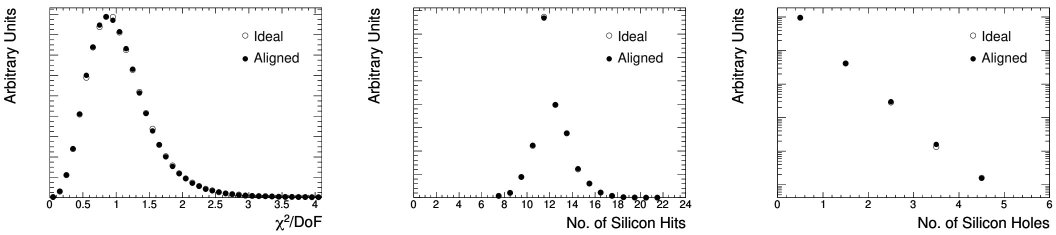

(a) **(b)** **(c)**

Figure 7.48.: Track quality of the aligned detector.

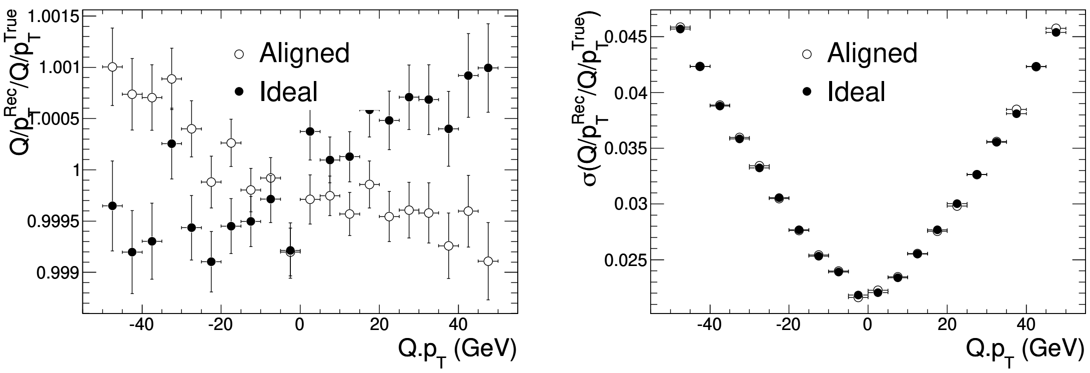

(a) $|\eta| < 0.8$ **(b)** $|\eta| < 0.8$

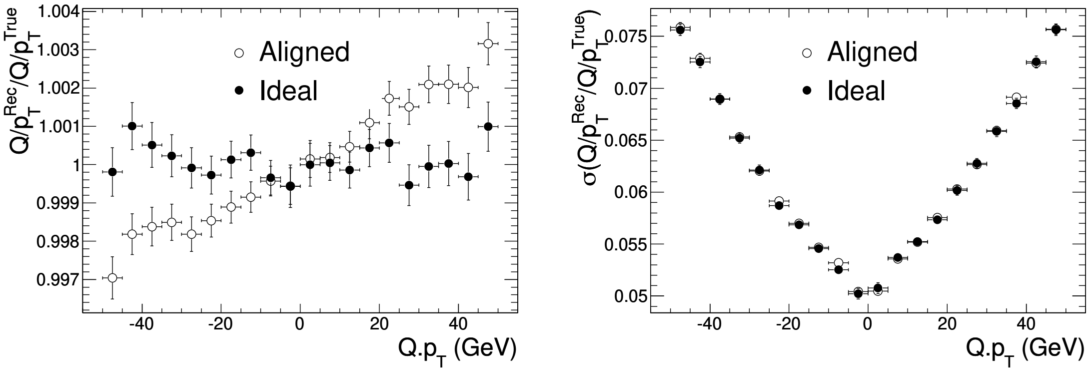

(c) $|\eta| > 1.5$ **(d)** $|\eta| > 1.5$

Figure 7.49.: Reconstructed momentum bias and resolution of the aligned detector.

7.7. Outlook

The alignment of the CSC geometry showed that the Global χ^2 alignment algorithm is functioning properly and is able to recover a nearly perfectly aligned detector. A method for controlling the systematic distortions which degrade the track parameter resolutions has been shown to work effectively at removing χ^2-invariant distortions.

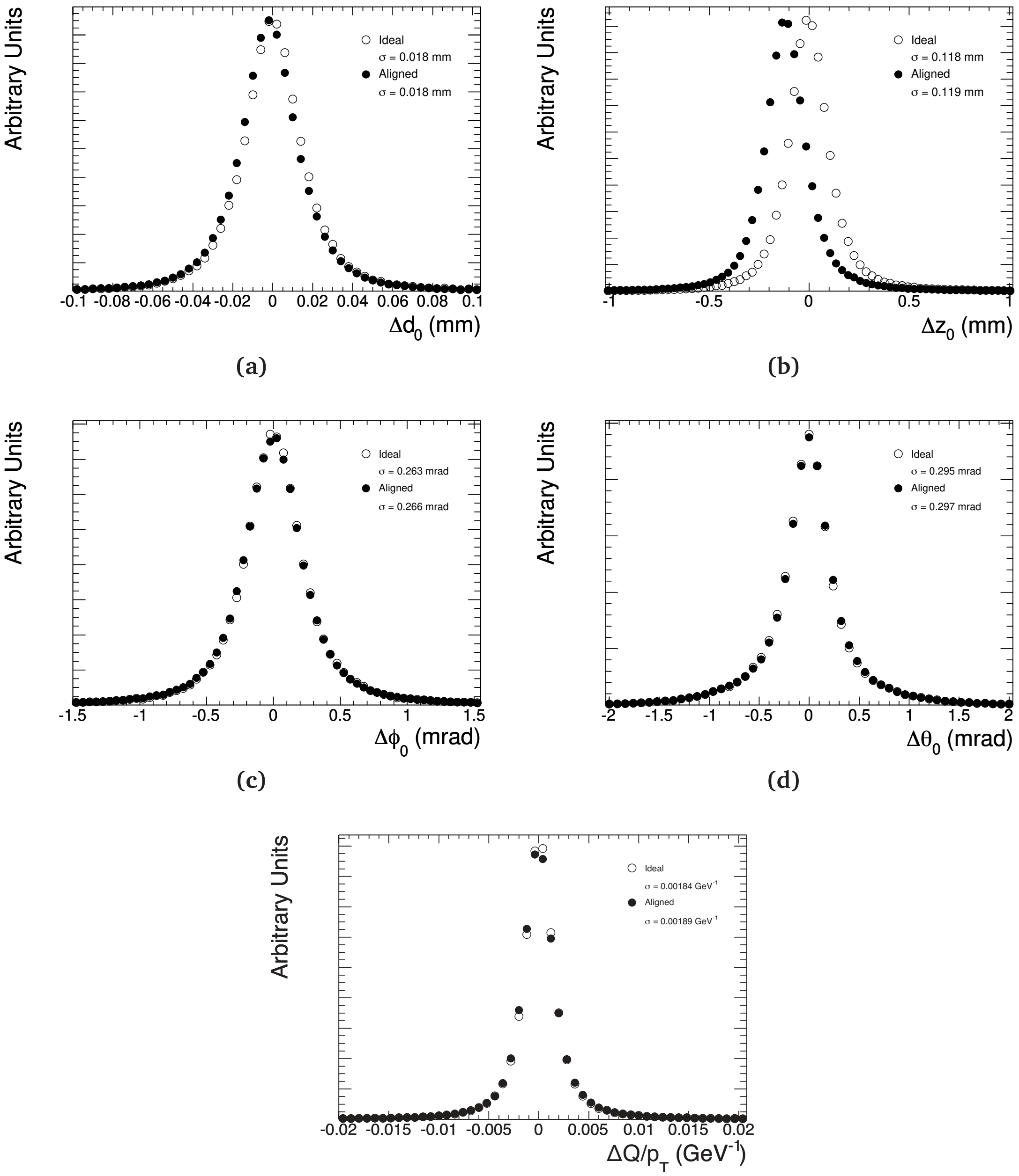

(a) (b) (c) (d) (e)

Figure 7.50.: Track parameter resolution of the aligned detector.

Further studies are required to investigate the effects of the simplifications made in the study presented. Firstly these studies used what is a rather idealistic data set, that being a pure set of muons. Without the effects of pileup and the underlying events on the track reconstruction and identification procedure the number of misallocated hits is kept to an absolute minimum. Tests of the alignment procedure have been performed during the ATLAS Full Dress Rehearsals (FDR's). The FDR's were intended to test the performance of the ATLAS software in collision like events. In these tests a variety of events were simulated and pass through the full ATLAS reconstruction chain[93].

To test the alignment procedures simulated dijet events were were passed through a trigger algorithm which selected high momentum tracks ($p_T > 5$ GeV). This recovered about $\mathcal{O}(10^6)$ tracks. Using a mildly modified version of the CSC alignment procedure the results obtained were eventually qualitatively quite similar to that of the CSC procedure [93]. This suggests that the results of this study are directly applicable to the real world case.

Secondly this study shows that the procedure does not introduce any systematic deformation at the individual module level. The effects of systematic deformations at Level 3 has been investigated to some extent in [120]. Mainly focusing on a curl misalignment of the detector ($\Delta\phi = c_1\, r + c_2/r$), which is equivalent to $R_z \propto r$, the study showed this misalignment will have significant effects on the physics performance of the detector.

The extension to the alignment process described utilised the knowledge that the detector was unbiased at the individual module level (Level 3) and any systematic biases could only be introduced at Level 2. This is clearly a simplification of the problem, however the technique described for removing χ^2-invariant distortions would work at any alignment level. Despite this I would be apprehensive about applying track parameter constraints at individual module level unless the detector from which the track parameter constraints are derived from is very well understood.

Prior to the LHC operation the alignment activities focus on information from cosmic ray tracks alone. The cosmic ray tracks present their own problems as they will not illuminate the detector uniformly and will have there own χ^2-invariant transformations. Much progress has been made with alignment of the detector however recent comparisons between the ATLAS detector constants produced by the local and global χ^2 indicate do exhibit what appears to be a χ^2-invariant distortions of the one of the two sets of constants.

8

CHAPTER

ELECTRON BREMSSTRAHLUNG IDENTIFICATION AND ESTIMATION

In Section 4.3 the properties of a helical track model were discussed. It was noted that material interactions (energy loss and scattering) perturb a particle from its “ideal” path and these interactions must be taken into account if one wishes to have a properly estimated trajectory. To be able to account for the material interactions they must be incorporated into the model. Radiative energy losses are an ever-present problem for the reconstruction of electrons at ATLAS due material within the Inner Detector and the high energy of the electrons.

In Section 8.1 the reconstruction of electrons is briefly discussed. The impact of bremsstrahlung on electron and track reconstruction is explored in Section 8.2, and a method of incorporating the position of the electromagnetic clusters, to improve track reconstruction, into track fitting (“CaloBrem”) is presented in Section 8.3. The tracking properties of the calorimeter are discussed in Section 8.4, with solution techniques, and performance of CaloBrem outlined in sections F and 8.6 respectively.

8.1. Electron Reconstruction in ATLAS

The reconstruction of electrons and photons is performed within the same algorithm in the ATLAS software due to their common use of electromagnetic clusters as a “seed” for the reconstruction [27]. The sliding window algorithm [126] is used to find and reconstruct electromagnetic clusters forming rectangular clusters with a fixed size, positioned to maximise the amount of energy within the cluster.

The optimal cluster size depends on the particle type being reconstructed and the region of the calorimeter in which the cluster is being reconstructed. For example, electrons need larger clusters than photons due to their greater interaction probability in the upstream material, and also because they bend in the magnetic field, radiating soft photons along a range in angle ϕ. Multiple of collections of clusters are therefore built by the reconstruction software, corresponding to different window sizes. These clusters are the starting point for the identification of electron and photon candidates.

For each of the reconstructed clusters, a search is made for tracks, that when extrapolated to the calorimeter, match the cluster within a $\Delta\eta \times \Delta\phi$ window of 0.05 rad × 0.10 rad with momentum, p, compatible with the cluster energy, E $(E/p < 10)$. If one or more matching tracks is found, the reconstruction checks for the presence of an associated photon conversion. An electron candidate is created if a matched track is found and no conversion is flagged. Otherwise, the candidate is classified as a photon. The reconstruction procedure allows for multiple tracks to be associated to the clusters, to maximise electron reconstruction efficiency. Any electromagnetic cluster with an associated track is classified as an electron. As a result, reconstructed electrons may be converted photons. Furthermore QCD jets may also be reconstructed as electrons.

The classification of electrons and photons allows for the application of different corrections to electron and photon candidates. Furthermore it is the starting point for a more refined identification based largely on shower shapes [27].

8.1.1. Standard Electromagetic Cluster Reconstruction

The sliding window algorithm [126] is used to find and reconstruct fixed-size rectangular electromagnetic clusters which are positioned to maximise the amount of energy within the cluster. The energy and position reconstruction is an involved process requiring a number of corrections which take into account factors such as the accordion geometry of the electromagnetic calorimeter and the origin of the particle. The properties of the ECAL and their effects on reconstruction is extensively documented in [27] and is briefly summarised here.

The amount of absorber material crossed by incident particles varies as a function of ϕ due to the ECAL's accordion geometry. If uncorrected this would produce a ϕ modulation of the reconstructed energy. If the electromagnetic shower is not fully contained in the η window chosen for the clusters, a modulation in the energy and a bias in the measured position will be observed which is dependent on the particle impact point within a cell. After the energies of the cells are corrected the energy deposited in the cells of each individual layer of a cluster are summed, and an energy-weighted cluster position is calculated for each layer. The ϕ position of the cluster is calculated solely from the energy weighted average in the second sampling layer of the calorimeter, while the η position is calculated using all layers.

8.2. The Impact of Bremsstrahlung on Electron Reconstruction

In the following section the effects of bremsstrahlung on electron reconstruction are described.

8.2.1. Bremsstrahlung Classification

To highlight the effects of bremsstrahlung, electrons will be classified into three separate categories: A *Hard* bremsstrahlung electron classification is designated as an electron which looses more than 20% of its energy in a single interaction prior to the electron reaching a radius of 300 mm. *Low* bremsstrahlung electrons are electrons that lose less than 20% of its energy before reaching a radius of 600 mm. Finally *medium* bremsstrahlung events are those that are neither hard or soft.

The fraction of electrons within each classification group is constant with energy, as the fractional energy loss due to bremsstrahlung is almost independent of energy. However, the electron reconstruction efficiency does depend on the electron energy

(Figure 8.4) and the amount of energy lost, and as a result the fraction of electrons within each classification will vary (see figure 8.1).

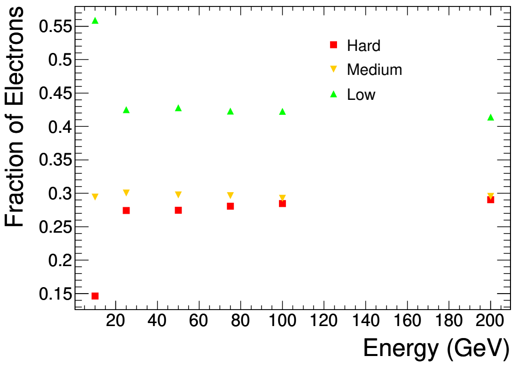

Figure 8.1.: Fraction of reconstructed electrons within each bremsstrahlung classification

In an attempt to emphasise the effect of bremsstrahlung, an effective mean ($M(x)$) and width ($R(x)$) have been defined in terms of the minimum half-width enclosing a fraction, x, of all events. Values of $R(68\%)$ and $R(95\%)$ have been determined for various reconstructed parameters and correspond to $\pm 1\sigma$ and $\pm 2\sigma$ coverage respectively. The value of $R(68\%)$ quantifies the width of the core of the distribution, while the $R(95\%)$ interval is determined by the size of the bremsstrahlung tail.

A "Crystal Ball function" is a probability density function commonly used to model "lossy" processes and consists of a Gaussian core portion and a power-law low-end tail.

$$f(x;\alpha,n,\bar{x},\sigma) = N\cdot\begin{cases}\exp(-\frac{(x-\bar{x})^2}{2\sigma^2}), & \text{for } \frac{x-\bar{x}}{\sigma} > -\alpha \\ A\cdot(B-\frac{x-\bar{x}}{\sigma})^{-n}, & \text{for } \frac{x-\bar{x}}{\sigma} \le -\alpha\end{cases}, \tag{8.1}$$

where $\bar{x}$ is the mean of the Gaussian core, σ is the width of the Gaussian core, $-\alpha$ is the point where the fit switches to a power law tail, n is the strength of the power,

$$A = \left(\frac{n}{|\alpha|}\right)^n \cdot \exp\left(-\frac{|\alpha|^2}{2}\right),$$

and

$$B = \frac{n}{|\alpha|} - |\alpha|.$$

8.2.2. Bremsstrahlung Location

The distribution and amount of material within the Inner Detector determines the location and magnitude of the electrons bremsstrahlung. Figure 8.2 shows the average energy loss as a function of radius along two different planes through the detector. The electrons traversing the low material region ($\eta = 0.5$) have an average energy loss of about 15% prior to the first layer of the SCT and 30% prior to the TRT. Through the high material region ($\eta = 1.5$) the average amount of energy lost prior to the first layer of the SCT is 25% and 50% prior to the TRT. Figure 8.3 displays the true positions of bremsstrahlung vertices within the Inner Detector clearly depicting the structures within the Inner Detector.

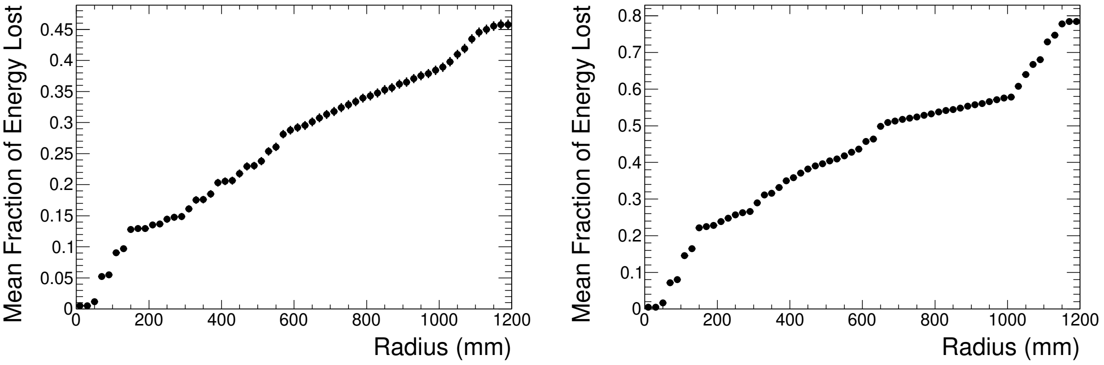

(a) $\eta = 0.5$ **(b)** $\eta = 1.5$

Figure 8.2.: Average energy loss of electrons as a function of radius with in the Inner Detector generated from a sample of single electrons with an initial transverse energy of 25 GeV

8.2.3. Impact on Cluster Reconstruction

Calorimeters estimate the energy of electrons and photons by inducing electromagnetic showers via bremsstrahlung and pair production, within the detector. If bremsstrahlung occurs prior to the active calorimeter material, the calorimeter may interpret this early showing as a lower energy electron. The cluster reconstruction tries to take into account the effects of the material located in front of the calorimeter, however their performance is degraded by this material.

Cluster reconstruction efficiency is very dependent upon the density and amount of energy deposited within the calorimeter. As electromagnetic clusters are attempted to

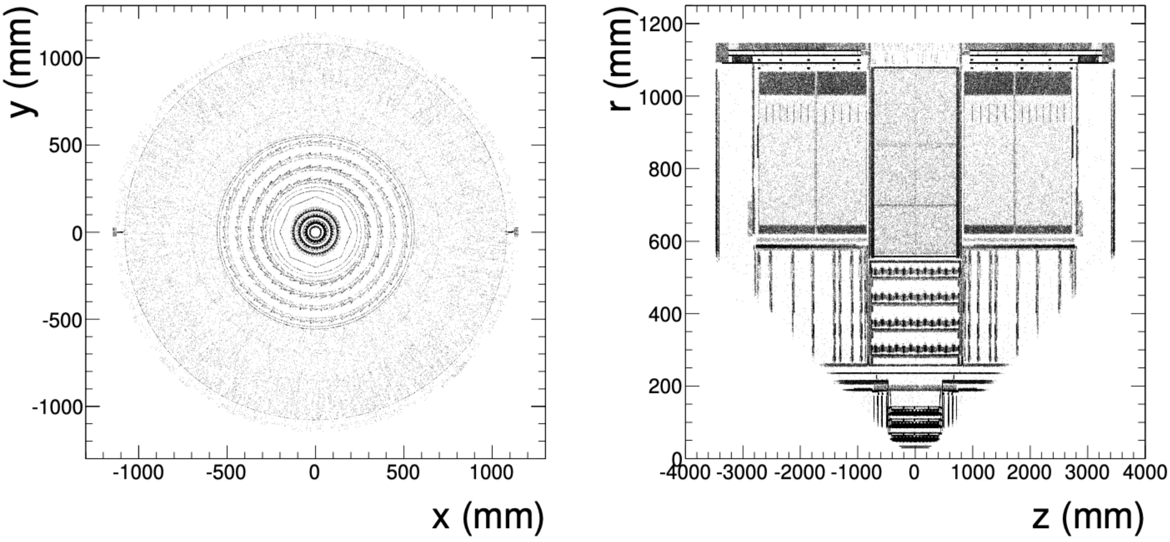

(a) x-y plane $|\eta| < 0.8$ **(b)** z-r plane

Figure 8.3.: The true positions of bremsstrahlung vertices in the Inner Detector. The plots were generated from 50,000 simulated single electrons with an initial transverse energy of 25 GeV

be recostructed below a raw deposited transverse energies of 2.5 GeV, low momentum electrons that lose a large fraction of their energy through bremsstrahlung early in the Inner Detector may not deposit enough energy in a small enough area to allow the sliding window algorithm to build a cluster (see Figure 8.4). Moreover if there if an electron losses enough energy, two or more clusters may be formed. This is one consquence of using fixed cluster size as opposed to a dynamic cluster size.

The energy reconstruction of an electromagnetic cluster already tries to take into account some of the effects of bremsstrahlung by compensating for the material in front of the calorimeter. As successful as these methods are, there is still a significant low energy tail resulting from bremsstrahlung (see Figure 8.5a). Due to the bremsstrahlung classification focussing on effects upon the track reconstruction, only small differences can be seen between what have been classified as hard and medium bremsstrahlung events. The medium and hard bremsstrahlung events clearly degrade the energy resolution of the calorimeter. Low bremsstrahlung events are almost unbiased and provide the ultimate precision of the calorimeter system.

The fractional energy resolution is conventionally parametrised as

$$\sigma(E)/E = a/E \oplus b/\sqrt{E} \oplus c, \tag{8.2}$$

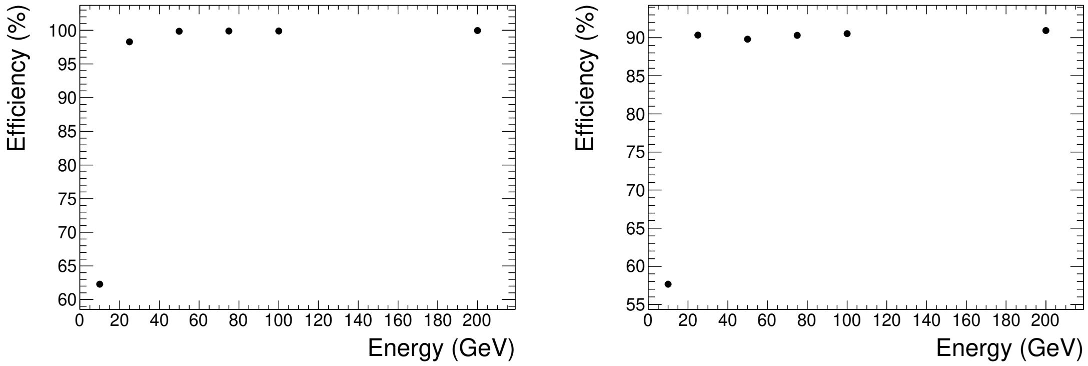

(a) Cluster Reconstruction **(b)** Electron Reconstruction

Figure 8.4.: Reconstruction efficiency of electromagnetic clusters and electrons a function of energy averaged across the active area of the detector.

where a is the noise term, b is the sampling term and c is the constant term [27]. The values for the parameterisation of the energy resolution can be found in appendix E.

8.2.4. Impact on Track Parameters

The track reconstruction efficiency of electrons is significantly degraded by bremsstrahlung. The main cause of this degradation is large energy loss processes which cause the pattern recognition to fail[1]. Figure 8.4 shows a large discrepancy between the cluster reconstruction efficiency and the electron reconstruction efficiency, which is due to deficiencies of the tracking.

The standard track reconstruction assumes that the particle is a pion and as such all material interactions are assumed to be pion like. By not allowing bremsstrahlung the overall track parameters for electrons are biased, especially those in the bending plane (Q/p, ϕ_0, d_0). Table 8.1 displays effective mean and width of the track parameter for 50 GeV electrons and muons within the Inner Detector. It is noted here that the bending plane parameters for the electrons are biased, while the muons are at their ideal value. In addition to these biases, the resolution is also heavily compromised. In the case of the reconstructed momentum the effective 1σ resolution of the events is increased by a factor of eight while the average momentum is 13% lower than its real value.

---

[1] The pattern recognition does not allow for major changes in track parameters consistent with bremsstrahlung

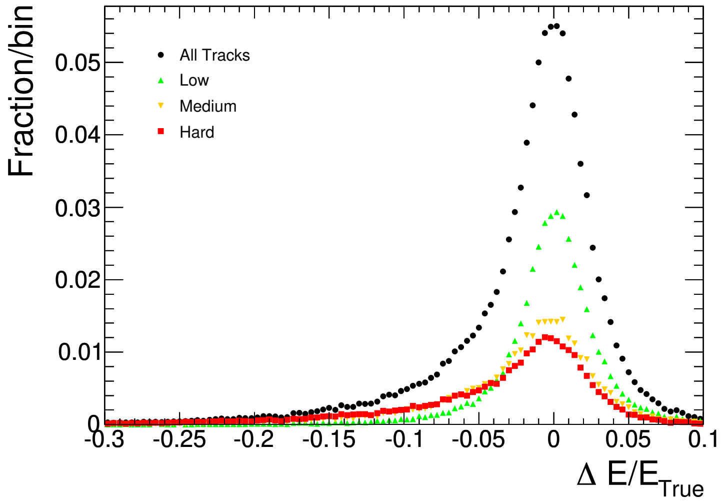

(a) 50 GeV Electrons

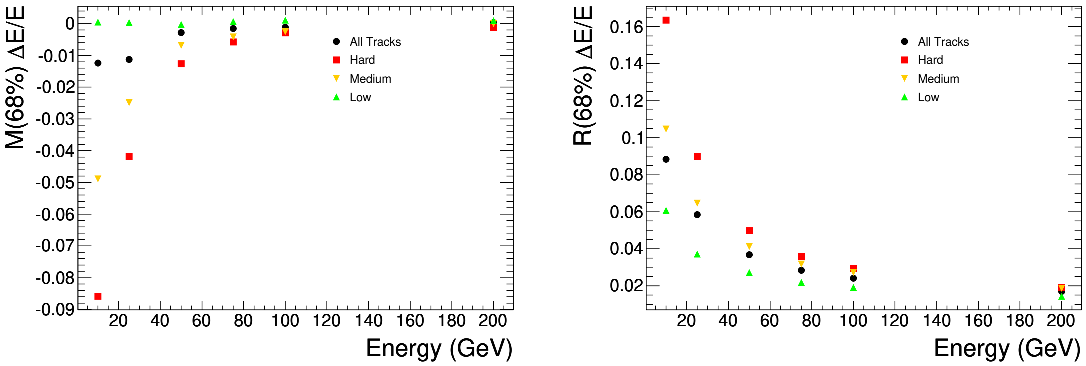

(b) **(c)**

Figure 8.5.: Energy reconstruction for electromagnetic clusters associated to electrons

Figure 8.6 shows the reconstructed track parameters broken down into the three different bremsstrahlung classes (see Section 8.2.1) highlighting again the effect of bremsstrahlung on track reconstruction. For the bending plane parameters it can be clearly seen that as one progresses from low to medium then to hard bremsstrahlung cases, the reconstructed track parameters become more biased with poorer resolution. This is further emphasised in Figure 8.7 where the variation of the effective 1σ mean and width with energy are shown. For reference, the performance of the default tracking on electrons of various energies is detailed in Table 8.2.

The non-bending plane parameters (θ, z_0) are not overly effected by bremsstrahlung. There is still an increase in the overall resolution, but the effects are almost negligible in comparison to the bending plane parameters.

Electrons				
Parameter	Mean 68%	Width 68%	Mean 95%	Width 95%
p_{True}/p_{Rec}	1.137	0.242	1.353	1.270
ϕ_0 (mrad)	0.431	0.828	0.990	3.819
d_0 (mm)	-0.0242	0.0466	-0.0479	0.1634
θ (mrad)	-0.0242	0.3423	-0.0587	1.120
z_0 (mm)	-0.0132	0.1187	-0.0116	0.3548
Muons				
Parameter	Mean 68%	Width 68%	Mean 95%	Width 95%
p_{True}/p_{Rec}	1.000	0.0294	1.000	0.0744
ϕ_0 (mrad)	0.002	0.180	0.001	0.630
d_0 (mm)	-0.0007	0.0129	-0.0011	0.0379
θ (mrad)	-0.0207	0.3411	-0.0283	0.939
z_0 (mm)	-0.0092	0.0955	-0.0057	0.2599

Table 8.1.: The effective 1σ and 2σ mean and width for the reconstructed track parameters of electrons and muons with $\mathrm{E} = 50$ GeV

The track parameter uncertainty measurements are also seriously compromised. Incorrect error estimation has implications when reconstructing vertices and evaluating their viability and hence the physics performance of the detector. The pull distributions (see Section 4.6 for the definition of the pull), Figure 8.8, show that besides the track parameters being biased the uncertainties are vastly underestimated. For example the uncertainty of the reconstructed momentum is six times too small.

Energy	Δd_0 (μm)		$\Delta\phi_0$ (mrad)		p_{True}/p_{Rec}	
(GeV)	M(68%)	R(68%)	M(68%)	R(68%)	M(68%)	R(68%)
10	-27.9	54.1	0.576	1.12	1.069	0.114
25	-27.1	50.1	0.539	1.01	1.110	0.183
50	-25.7	45.3	0.438	0.80	1.140	0.236
75	-22.1	40.8	0.379	0.67	1.161	0.278
100	-19.4	37.4	0.324	0.61	1.174	0.307
200	-12.9	29.7	0.200	0.43	1.197	0.390

Table 8.2.: The effective 1σ width and mean of the bending plane parameters for the default tracking on electrons

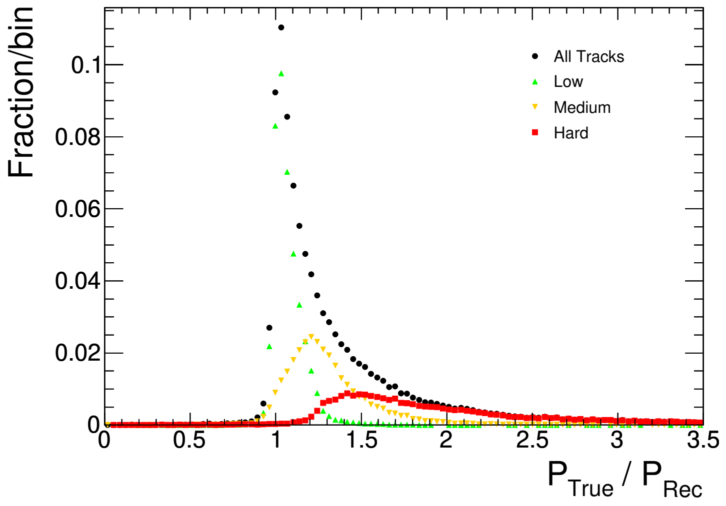

(a) Momentum

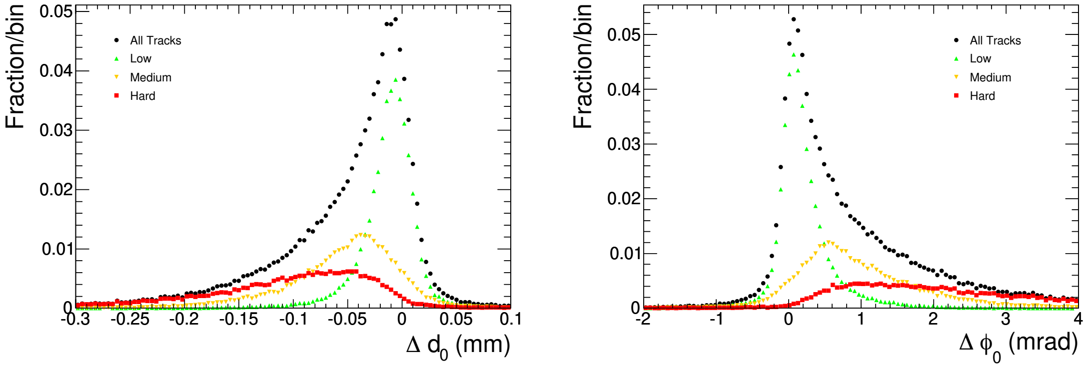

(b) Transverse impact parameter **(c)** Azimuthal angle

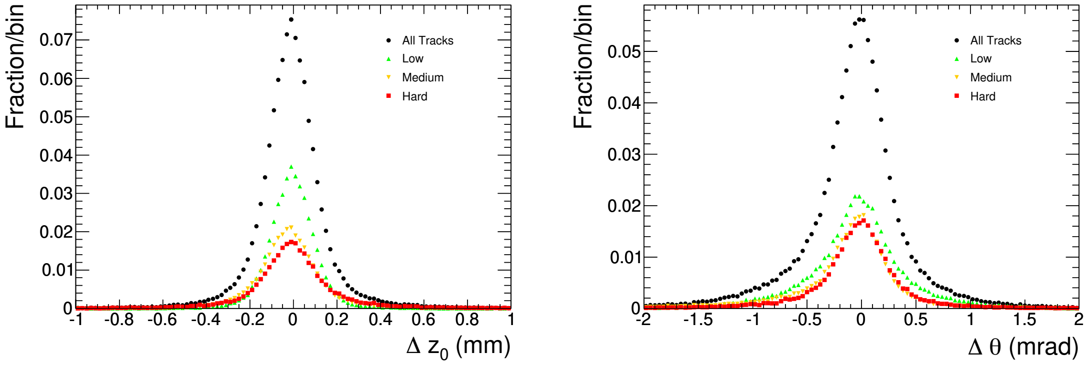

(d) Longitudinal impact parameter **(e)** Zenith Angle

Figure 8.6.: Track parameter resolution for E = 50GeV electrons using a the default track fitter (Global χ^2 fitter)

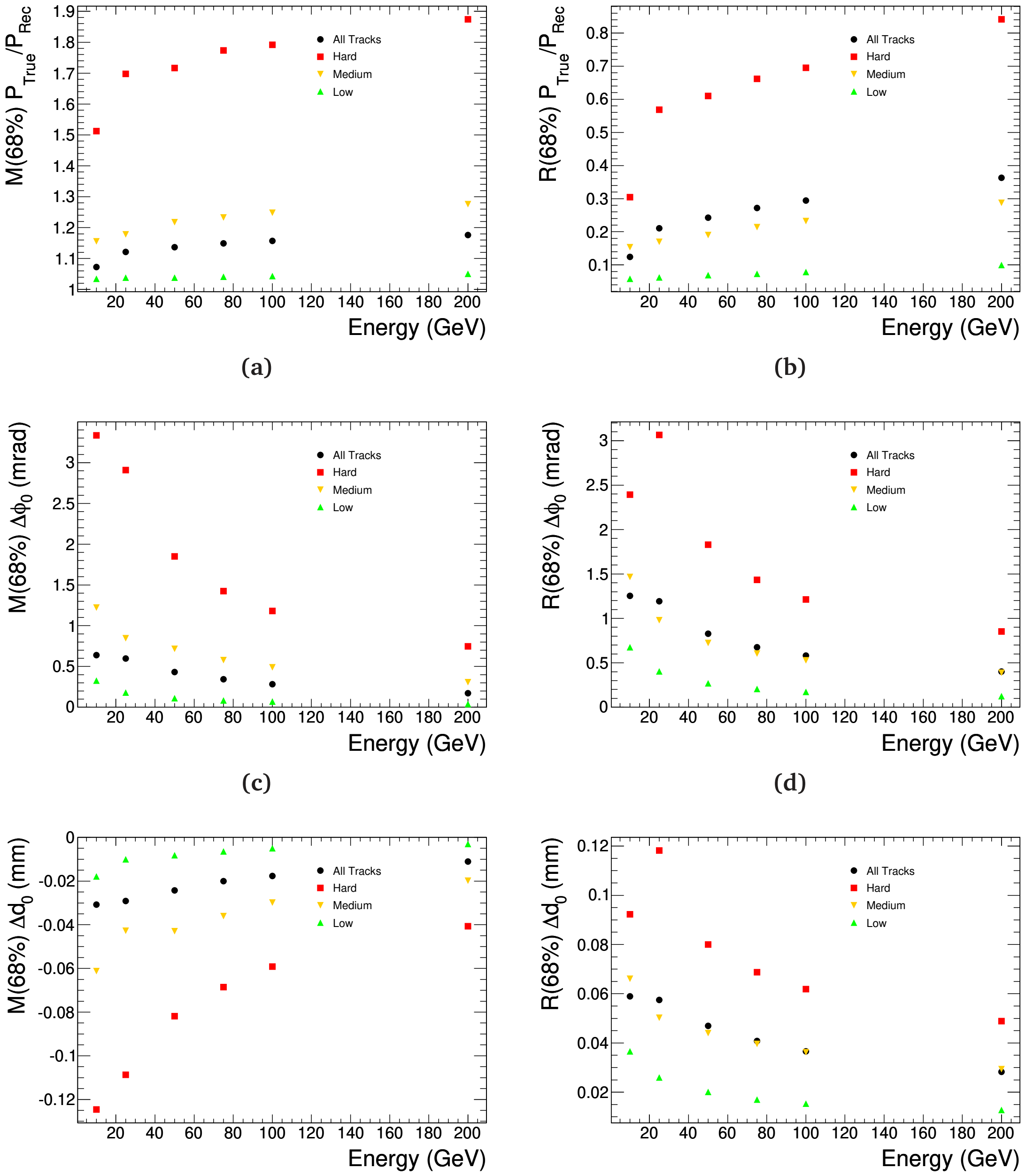

(a) (b)

(c) (d)

(e) (f)

Figure 8.7.: The effective 1σ mean and width of the bending plane parameters for the default track reconstruction as a function of energy.

Again hard bremsstrahlung events are the most effected and have their uncertainties estimated most poorly, especially the momentum reconstruction. It is interesting to note that low bremsstrahlung events still do not obtain the ideal uncertainty measurements, suggesting that even small amounts of radiative energy loss adversely affect the track parameter error estimation.

8.3. Track Fitting Incorporating Calorimeter Information

The primary purpose of the calorimeter is to measure energy. In addition, the calorimeter provides information about the location of the energy deposits. The positions of the clusters are determined by two independent measurements in the η and ϕ direction. The measurement in the η direction is not able to aid the recovery of bremsstrahlung energy losses significantly as it is in the non-bending plane. However the ϕ position measurement of the cluster is in the bending plane and proves to be useful for electron measurements.

To illustrate how the ϕ position of an electromagnetic cluster can be used in electron track reconstruction a simplified linearised helical model will be used (see Section 4.3.3). Consider the case of a barrel-like system. The position in the $r\phi$ plane, t, with respect to the radius of the particle can be written as

$$t(r) = -d_0 + \phi_0 r + \frac{1}{2R} r^2, \tag{8.3}$$

where d_0 is the transverse impact parameter of the electron, ϕ_0 is the original azimuthal angle of the particle and R is the radius of curvature of the particle. Assume that at a particular radius, R_B, the electron loses a fraction of its energy, $1 - Z$ (Z being the fraction of energy retained by the electron). To ensure that the electrons path is continuous at R_B

$$t(R_B) = -d_0 + \phi_0 R_B + \frac{1}{2R} R_B^2 = -d_0^B + \phi_0^B R_B + \frac{1}{2Z\,R} R_B^2, \tag{8.4}$$

and

$$\left.\frac{dt}{dr}\right|_{r=r_B} = \phi_0 + \frac{1}{R} r_B = \phi_0^B + \frac{1}{zR} r_B. \tag{8.5}$$

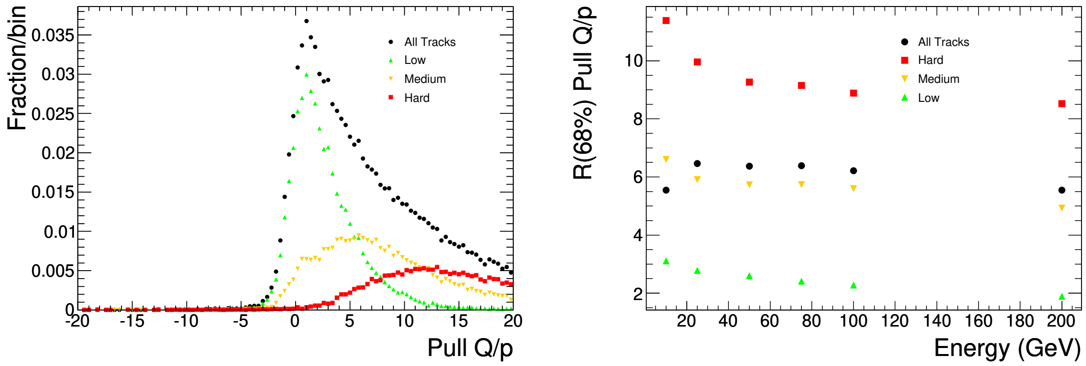

(a) E = 50 GeV **(b)**

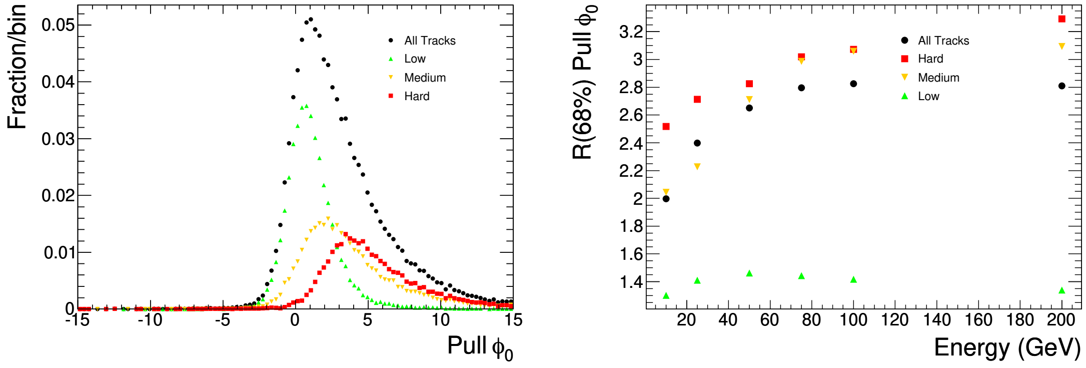

(c) E = 50 GeV **(d)**

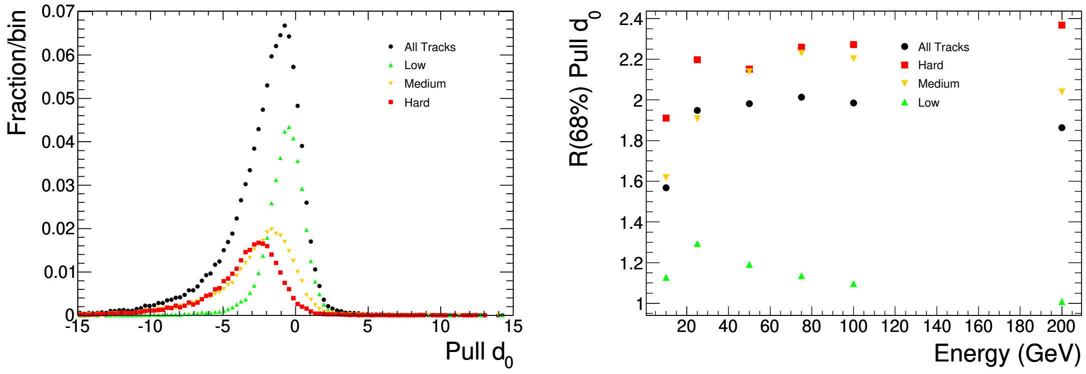

(e) E = 50 GeV **(f)**

Figure 8.8.: The pull distributions of bending plane parameters for E = 50 GeV electrons and the effective 1σ width as a function of energy.

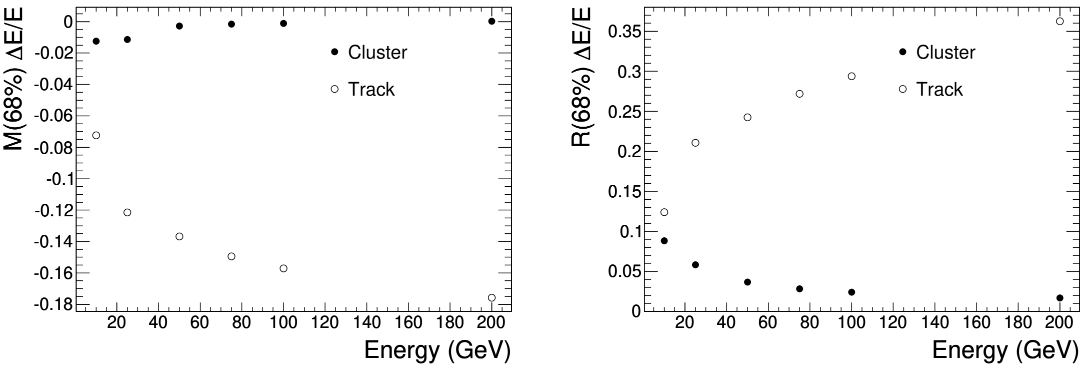

(a) **(b)**

Figure 8.9.: The variation of the effective 1σ mean and width with electron energy.

Hence

$$\phi_0^B = \phi_0 + \frac{R_B}{ZR}(Z-1), \tag{8.6}$$

and

$$\begin{aligned} -d_0^B &= -d_0 + (\phi_0 - \phi_0^B)R_B + \frac{R_B^2}{2ZR}(Z-1) \\ &= -d_0 - \frac{R_B^2}{2ZR}(Z-1). \end{aligned} \tag{8.7}$$

Using the above expressions the equations of motion for the path of the electron after the bremsstrahlung can be written in terms of only the original particle's path, the fraction of energy retained and the bremsstrahlung radius

$$t^B(r,R_B,Z) = -d_0 - \frac{R_B^2}{2ZR}(z-1) + \left(\phi_0 + \frac{R_B(z-1)}{zR}\right) r + \frac{1}{2zR}r^2. \tag{8.8}$$

If it is assumed that the photon is emitted collinear with the electron, then the photon's $r\phi$ position can be written as a function of r

$$t^P(r) = t(R_B) + \left.\frac{dt}{dr}\right|_{r=R_B}(r-R_B) \tag{8.9}$$

$$= t(R_B) + \left(\phi_0 + \frac{1}{R}R_B\right)(r-R_B). \tag{8.10}$$

Assuming that all of the energy from the electron and photon is contained in one cluster the barycentre can be calculated in the following way:

$$\begin{aligned} t^{Barycentre} &= Zt^B + (1-Z)t^P \qquad (8.11) \\ &= Z\left(-d_0 - \frac{R_B^2}{2ZR}(Z-1) + \left(\phi_0 + \frac{R_B(Z-1)}{ZR}\right)r + \frac{1}{2ZR}r^2\right) \\ &\quad +(1-Z)\left(-d_0 + \phi_0 R_B + \frac{1}{2R}R_B^2 + (\phi_0 + R_B/R)(r - R_B)\right) \\ &= d_0 + \phi_0 r + \frac{1}{2R}r^2. \qquad (8.12) \end{aligned}$$

Hence the barycentre of the cluster containing all of the energy from the original electron will be located along the path of the track prior to energy loss. This is also true when the full helical model is used to describe the passage of the electron. To incorporate the information of the cluster position into the track fit, this position must be located along the path of the electron before radiative energy loses occur. To accomplish this the track model is simply a charged particle that loses some fraction of its energy at some yet to be determined radius (see Figure 8.10).

$$t(r) = \begin{cases} d_0 + \phi_0 r + \frac{1}{2R}r^2 & r \leq R_B \\ -d_0 - \frac{R_B^2}{2zR}(z-1) + \left(\phi_0 + \frac{R_B}{ZR}(Z-1)\right)r + \frac{1}{2ZR}r^2 & r > R_B \end{cases} \qquad (8.13)$$

It is interesting to note that the final distance between the track and the photon in the calorimeter is:

$$\begin{aligned} \Delta t &= t^B(r_C) - t^P(r_C) \\ &= \frac{\left(r_C - r_B\right)^2}{2zR} \qquad (8.14) \end{aligned}$$

and the distance between the track and centre of the cluster at the radius of the cluster (X_B) is

$$\begin{aligned} X_B &= t^B(r_C) - t(r_C) \\ &= \frac{1-z}{2zR}(r_C - r_B)^2 \qquad (8.15) \\ z &= \frac{(r_C - r_B)^2}{2X_B R - (r_C - r_B)^2}. \qquad (8.16) \end{aligned}$$

What is presented here is a very simplified model which can not be directly applied to the ATLAS Inner Detector. Although the magnetic field is quite homogeneous in the very central part of the detector, towards the ends of the solenoid the effects of its limited length result in an in-homogeneous magnetic field(see Figure 3.7).

To account for these inhomogeneities the particle must be extrapolated through the field using a numerical tool referred to as an extrapolator. The default choice in ATLAS is based upon the Runge-Kutta-Nystrøm integration technique[127, 128].

As such the final track model is:

$$f(\mathbf{p}, R_B, Z) = \begin{cases} f(\mathbf{p}) & r \leq R_B \\ f(\mathbf{p}_B) & r > R_B \end{cases} \tag{8.17}$$

where $\mathbf{p}_B = \mathbf{p}$ at $r = R_B$ except for q/p which changes to q/Zp. Solving such a problem is rather troublesome as it is an inherently non-linear problem. A discussion of some possible solution techniques can be found in Appendix F.

A fit using this track model is referred to CaloBrem in the ATLAS community.

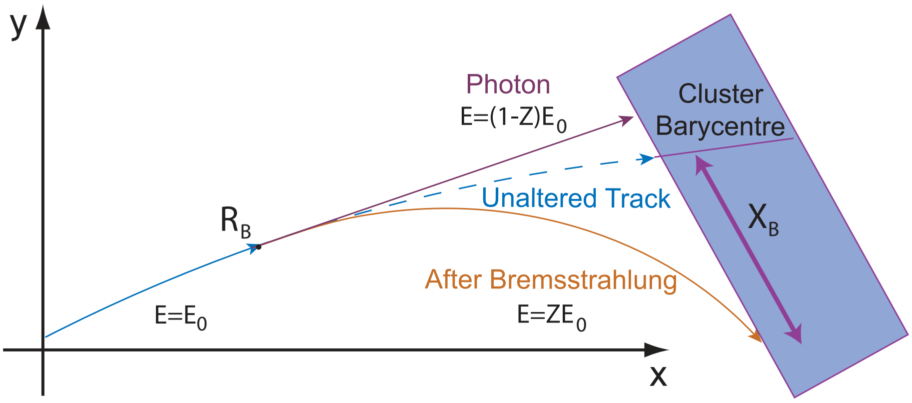

Figure 8.10.: A schematic diagram of the parameters in CaloBrem

8.4. Calorimeter Information For Tracking

In order to use the information available from the EM cluster measurement they need to be unbiased and have a known uncertainty[2]. The most important piece of information for the bremsstrahlung recovery is the position of the cluster, in particular, the azimuthal angular position.

8.4.1. Angular resolution

For a calorimeter cluster to be used in tracking the uncertainty on the position of the electromagnetic cluster must be known. To determine this a large sample of single electrons with energies ranging from 10 GeV to 200 GeV were used. Simulated electrons were extrapolated through the magnetic field to the surface of the second sampling layer of the electromagnetic calorimeter, where the difference between the reconstructed cluster position and the true cluster position was measured. The difference between the reconstructed position and the measured position is mostly Gaussian, but has a charge dependent tail (see figure 8.11).

This tail is a result of not all the energy being deposited within the cluster window, due to bremsstrahlung. The tail will increase as the energy of the original electron is reduced because the energy will spread over a large area (due to the electron bending in the magnetic field).

To account for this tail a Crystal Ball function was used when fitting the angular resolution distribution. An example of the fit is shown in Figure 8.11 and Table 8.3. The fit reveals that the mean of the distribution is biased, the reason for which will be detailed in Section 8.4.2. The azimuthal angular resolution of the cluster was taken to be the width of the Gaussian component of the Crystal Ball function.

Charge	α	n	$\bar{x}$ (mrad)	σ (mrad)
Positive	1.523 ± 0.080	1.89 ± 0.22	0.607 ± 0.027	1.317 ± 0.024
Negative	1.465 ± 0.075	2.15 ± 0.22	-0.626 ± 0.027	1.310 ± 0.024

Table 8.3.: Results of a fit of a Crystal Ball function to distributions shown in figure 8.11.

---

[2] The uncertainty of the energy measurement has been extensively studied elsewhere and the results of the parameterisation of its performance can be found in Appendix E

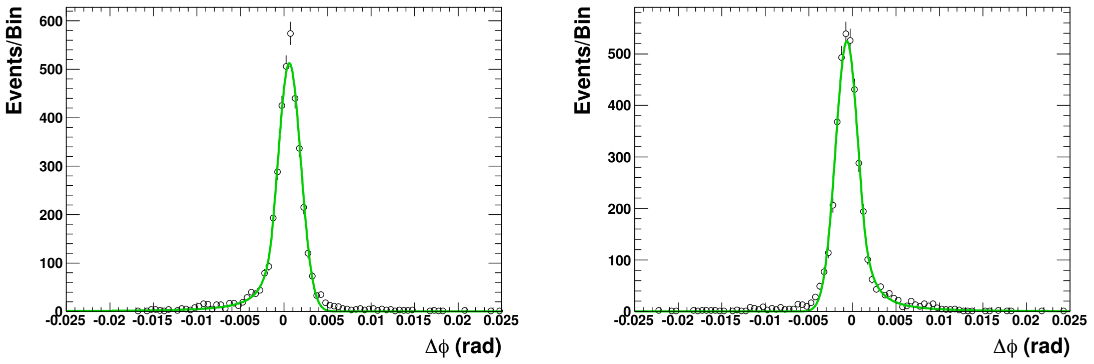

(a) Positive Tracks

(b) Negative Tracks

Figure 8.11.: The difference between the measured ϕ position and true ϕ position of 25 GeV electrons $\eta = 0.2$ at the surface of the second sampling layer of the calorimeter. The green solid line is the result of a fit with Crystal Ball function (see table 8.3).

The azimuthal angular resolution of electromagnetic clusters was calculated at various energies as a function of η. The results are shown in Figure 8.12. The structure of the resolution as a function η corresponds well to the geometry of the calorimeter. For example, the change in absorber thickness at $\eta = 0.8$ can be seen as well as the crack between the barrel and the end-cap at $\eta = 1.5$. There is also a clear energy dependence on the resolution.

The energy dependence of the ϕ-resolution is proportional to the inverse of the energy of the cluster (see Figure 8.12b)

$$\sigma(\phi) = a/E + c, \tag{8.18}$$

unlike the resolution of energy of the cluster, which is proportional to the inverse of the square root of the energy.

The variation of the two fit parameters a and c as a function of η are shown in Figure 8.13. These parameters were then parameterised as a function of η and results can be seen in Appendix E.

8.4.2. Depth

As was seen in Table 8.3 the reconstructed ϕ position of the cluster is biased. The helical path of electrons within the Inner Detector means that they will most likely

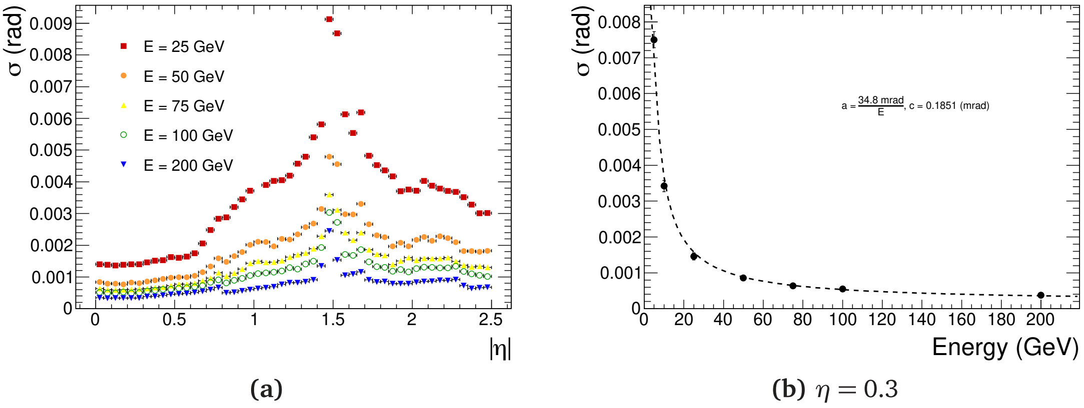

(a) **(b)** $\eta = 0.3$

Figure 8.12.: The azimuthal angular resolution of electromagnetic clusters from electrons as function of energy.

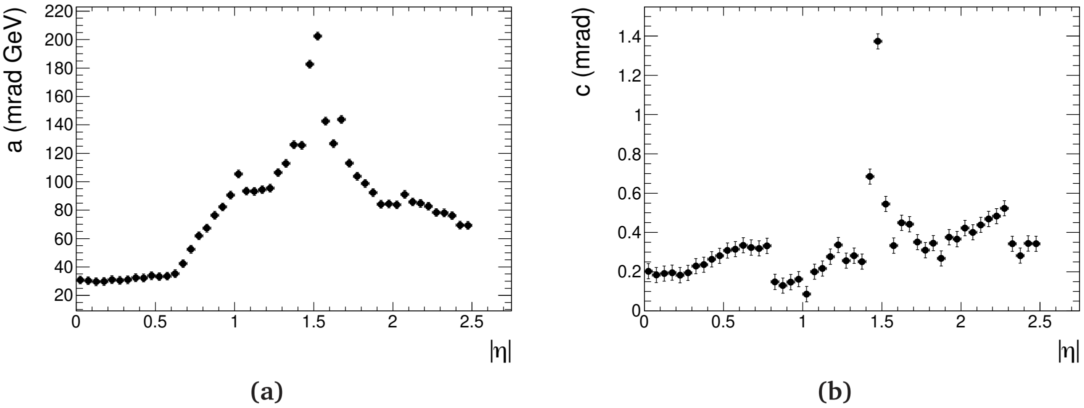

(a) **(b)**

Figure 8.13.: Parameterisation of the angular resolution of the electromagnetic calorimeters

not enter the calorimeter perpendicular to the surface of the detector. The electromagnetic shower has finite length, which is determined by the energy of the electron, and the energy will be asymmetrically spread in the ϕ direction due to the electron not entering the calorimeter perpendicular to the surface.

Figure 8.11 shows the average difference between the reconstructed cluster position and the position of the simulated electron in the calorimeter. The figure indicates that there is a bias in the reconstructed position at the surface of the second sampling layer of the calorimeter. By varying the depth that the truth particle is extrapolated into the calorimeter this bias can be eliminated (see Figure 8.14). The depth at which the bias is eliminated corresponds to the depth at which the resolution of the cluster position is optimal (see Figure 8.15).

The depth at which there is no bias in the reconstructed ϕ will be referred to as the apparent depth of the cluster. The apparent depth of the cluster could only be calculated in the barrel region. The apparent depth of the cluster does not behave like the longitudinal position barycentre of the electromagnetic shower as it becomes shallower as the energy increases (see Figure 8.16).

Use of the apparent depth during fitting yielded negligible improvement to the performance of CaloBrem and as a result the depth of the cluster was fixed to be the surface of the second sampling layer of the calorimeter.

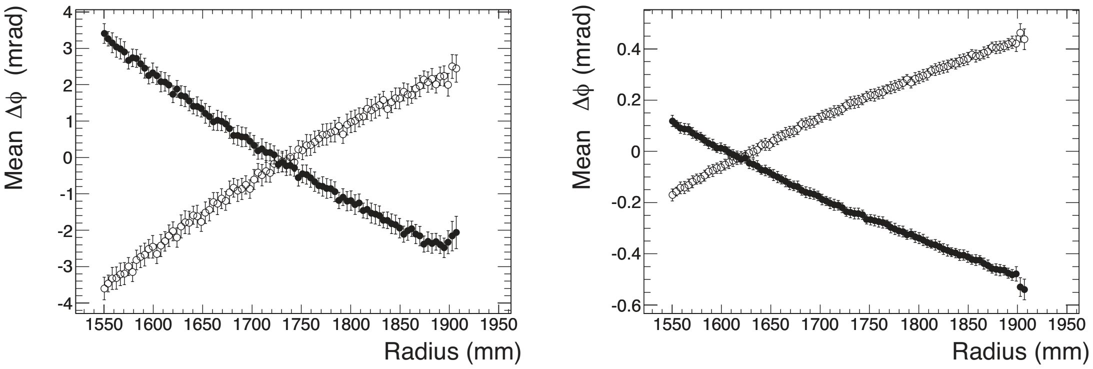

(a) E = 10 GeV **(b)** E = 100 GeV

Figure 8.14.: Mean cluster angular position bias as a function of radius at $\eta = 0.4$. Negative tracks represented by the open circles and positive tracks by the full circles.

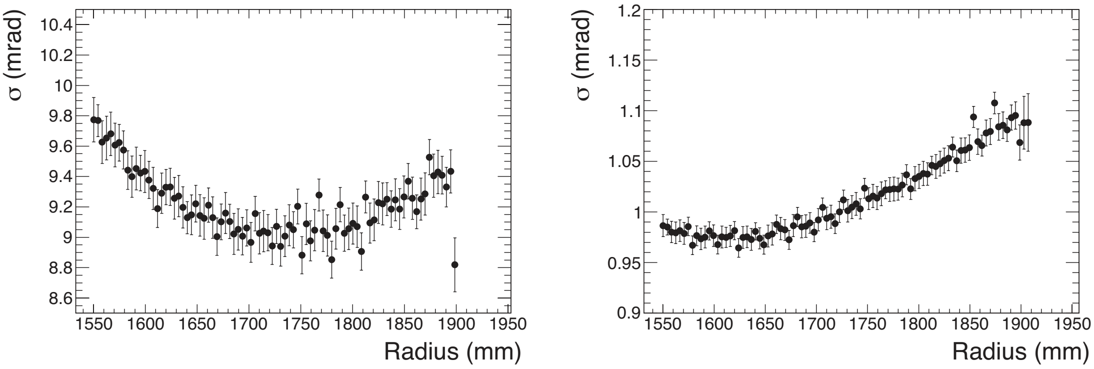

(a) E = 10 GeV **(b)** E = 100 GeV

Figure 8.15.: Azimuthal angular resolution of electromagnetic clusters in the second sampling layer as a function of radius.

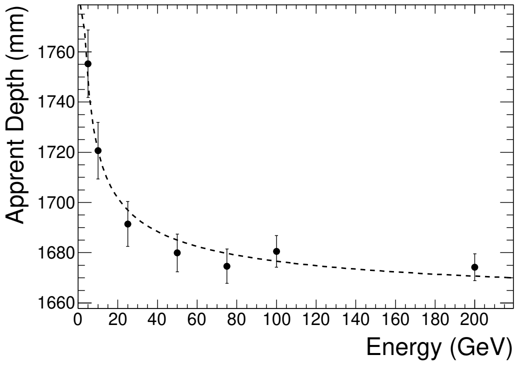

(a) $\eta = 0.4$

Figure 8.16.: The apparent depth of a cluster as a function of energy for a cluster at $\eta = 0.4$.

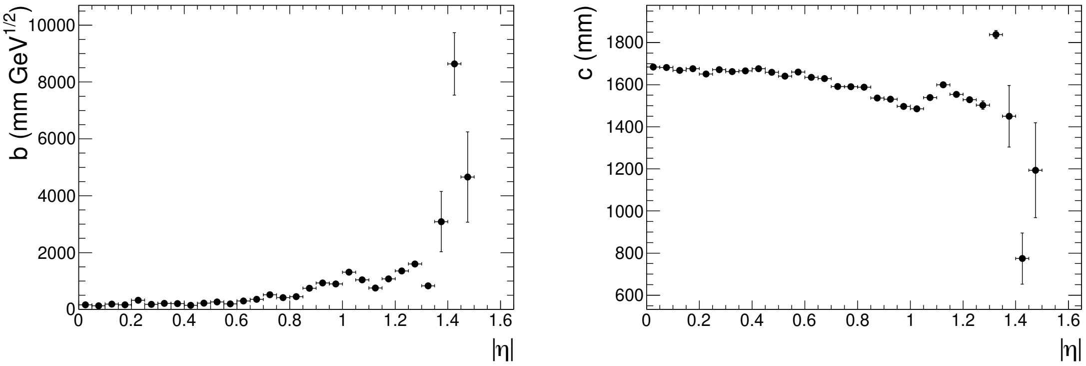

(a) **(b)**

Figure 8.17.: The parameterisation of the the apparent depth of the electromagnetic clusters.

8.5. Choice of Parameters

The choice parameters to be solved is crucial when solving any problem. If the parameters are too correlated the minimisation procedure will converge slowly (if at all) causing fitting to become very inefficient and time consuming. For this particular problem the amount of energy retained (Z_B) is very highly correlated to the initial azimuthal direction of the electron and the initial momentum of the electron. In order to reduce the level of correlation the amount of energy retained can be replaced by the distance separating the cluster position and the impact of the electron in the calorimeter, X_B (see Equation 8.15).

The fit needs to be seeded with an initial guess of all of the track parameters as well as the two bremsstrahlung parameters. The track parameters are seeded with the results of the standard track reconstruction. The radius of the bremsstrahlung begins at a radius of 250 mm and X_B is seeded with the distance between the cluster and the default track at the calorimeter. The starting position of the bremsstrahlung radius had negligible effect on the convergence of the algorithm as long as there were enough hits either side of the bremsstrahlung position to define the track.

The range that the parameters can fit with is also limited (see Table 8.4). Although this is not entirely necessary it does ensure the solution is physically reasonable.

As bremsstrahlung only effects the bending plane parameters little is to be gained by trying to fit all seven parameters. To reduce the computation time only the three bending plane parameters (d_0, ϕ_0, Q/p) are fit, with the two bremsstrahlung parameters (R_B, X_B).

Parameter	Lower Limit	Upper Limit
$d_0(mm)$	-10	10
$z_0(mm)$	-500	500
ϕ_0 (rad)	$-\pi$	π
θ (rad)	0	π
Q/p (MeV^{-1})	-0.002	0.002
R_B (mm)	10	1000
X_B	-1000	10

Table 8.4.: The allowed range for fit parameters in CaloBrem

8.6. Performance

To find the optimal track parameters a χ^2 minimisation procedure is employed. The performance of this procedure and the improvements of track reconstruction caused by the new track model are discussed in the following section.

8.6.1. Minimisation Performance

The performance of the χ^2 minimisation technique is vital to the overall performance of the track fitting with CaloBrem. As explained in Appendix F the minimisation process works by mapping the χ^2 landscape, in an intelligent manner, to find a minimum.

This requires a function that calculates the χ^2 to be called a number of times. However the number of times the function is called varies depending on the how well the problem is defined.

To ensure that the minimisation does not enter some form of infinite loop a limit is set on the maximum number of function calls. However, limiting this maximum to a number that is too small does not allow the system to converge. Figure 8.18 shows both the average time for a single fit and the fraction of events that has converged for a given maximum number of iterations. Incidentally it is interesting to note that for events that will eventually fail to converge take loner to do so.

Little overall computation cost is incurred by increasing the maximum number of iterations allowed once more than 90% of the tracks converge. To ensure that no one fit would take longer than one second, and that more than 99% would converge, an upper limit of 2000 function calls was set. This function takes on average 330 μs per call[3].

Lower energy electrons require more iterations in the minimisation process as the problem is less well defined. This is a result of the large uncertainty of the cluster position, which is in fact vital for the minimisation. This uncertainty increases as the energy decreases.

It should be noted that there is a significant number of events where the problem fails to converge, particularly at low energy (see Figure 8.19). In the limit of very low energy loss due to bremsstrahlung, when fitting, the radius of the bremsstrahlung will be totally undefined and as a result the fit will fail to converge. As it is difficult to ascertain if bremsstrahlung has occurred prior to fitting, it is impossible to avoid such situations.

8.6.2. Track Parameter Reconstruction

The ultimate goal is to accurately estimate the track parameters, as it is these that determine the usefulness of the technique. Figure 8.20 displays the three bending plane track parameters for 50 GeV electrons. When compared to Figure 8.6 an obvious improvement can be seen in both the resolution and level of bias of the track

---

[3] These tests were ran in a single threaded process on a system with dual Intel Xeon E5450 CPU's running at 3.00 GHz with 16 GB of memory

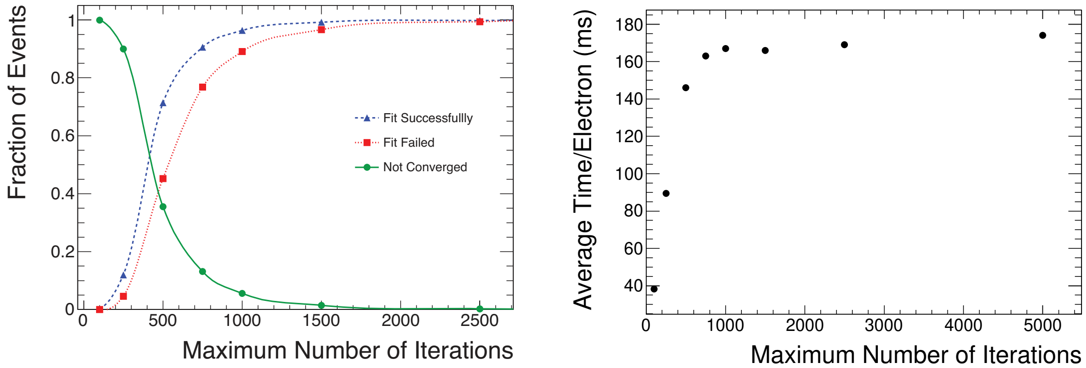

(a) Convergence **(b)** Average Time

Figure 8.18.: The effect of varying the maximum number of iterations on the convergence of `MINUIT` and the average time taken to process one electron (50 GeV).

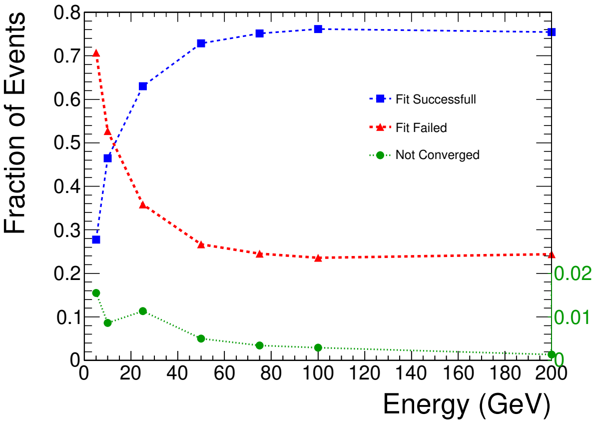

(a) Convergence. Note that the fraction that is yet to converge uses the right hand axes

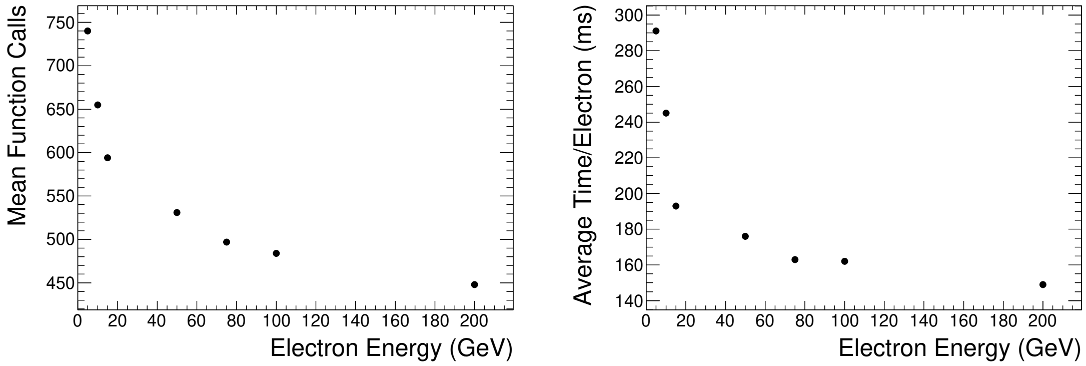

(b) Average Number of Calls **(c)** Average Time

Figure 8.19.: Efficiency of `MINUIT` as a function of electron energy.

parameters, especially in the hard bremsstrahlung case. Figure 8.22 compares the effective 1σ mean and width (Table 8.5) to that of the default track fitter (Table 8.2), again showing the large improvement reconstructed track parameters. Also of note is that the degree of improvement increases as the energy increases. This is a result of the cluster position being better defined.

Figure 8.21 displays the mean momentum for all the bremsstrahlung categories as a function of η. CaloBrem makes major improvements across the whole η range with the largest improvement evident in the central barrel region. The performance is much poorer in the region around $|\eta| = 1.5$, which coincides with the crack in the calorimeter and hence where the energy and position of clusters are most poorly defined. This is unfortunate as this is the region of the Inner Detector containing the largest amount of material and hence the region where bremsstrahlung would most likely occur.

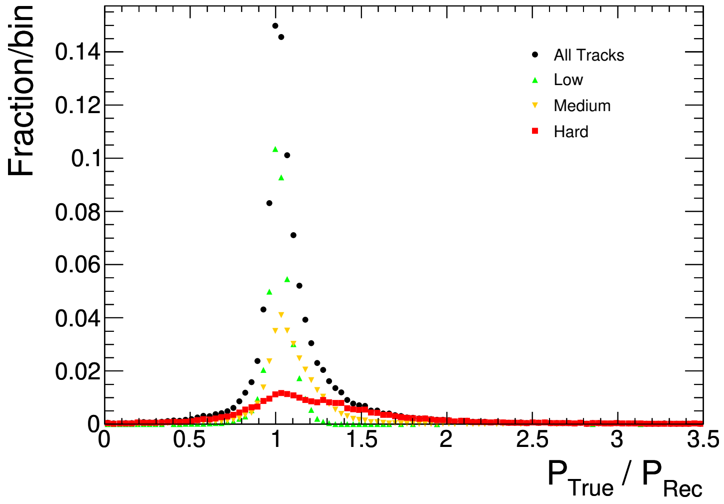

(a) Momentum

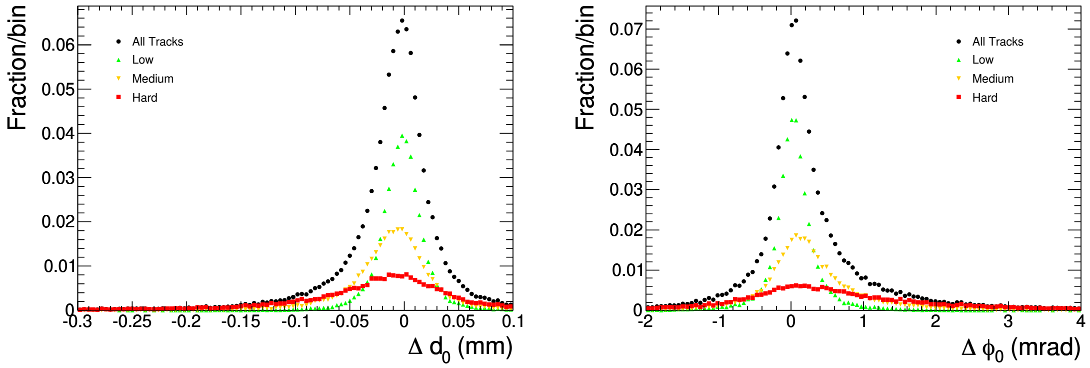

(b) Transverse impact parameter

(c) Azimuthal angle

Figure 8.20.: Track parameter resolution for E = 50GeV electrons using CaloBrem.

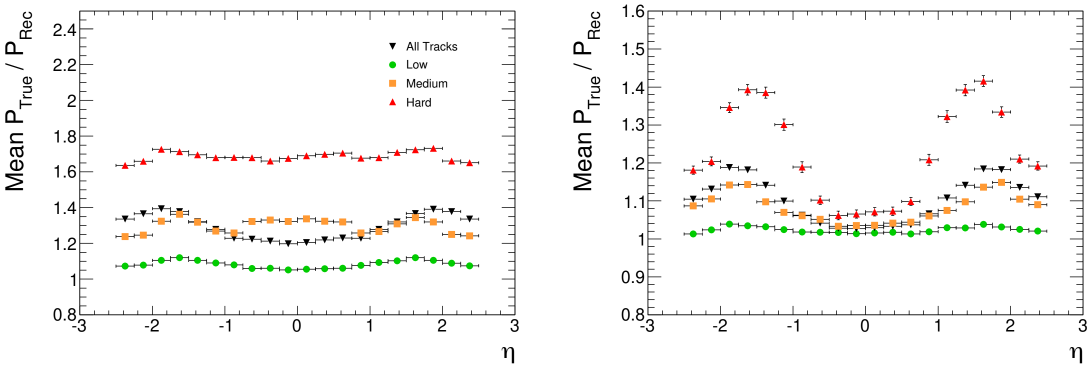

(a) Default **(b)** CaloBrem

Figure 8.21.: The mean reconstructed momentum for E = 50 GeV electrons as function of η for the default track fitter and CaloBrem.

Energy	Δd_0 (μm)		$\Delta\phi_0$ (mrad)		p_{True}/p_{Rec}	
(GeV)	M(68%)	R(68%)	M(68%)	R(68%)	M(68%)	R(68%)
10	-9.72	52.4	0.183	0.951	1.0216	0.077
25	-8.01	43.9	0.170	0.820	1.0369	0.128
50	-4.37	31.3	0.095	0.525	1.0378	0.141
75	-3.06	26.2	0.059	0.419	1.0399	0.155
100	-2.26	23.5	0.046	0.358	1.0400	0.169
200	-0.30	19.0	0.015	0.256	1.0341	0.218

Table 8.5.: The effective 1σ width and mean of the bending plane parameters for CaloBrem

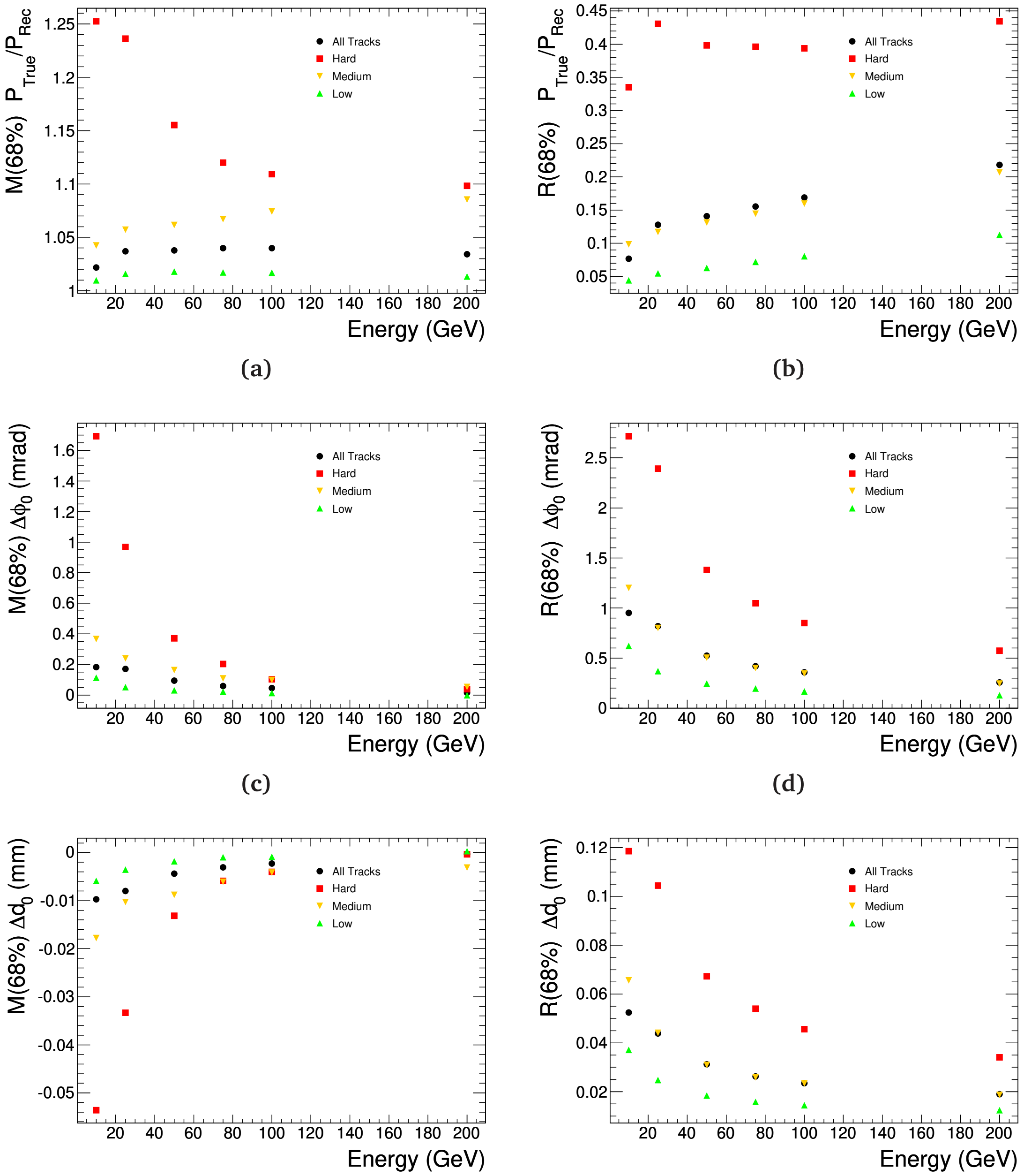

(a) (b)

(c) (d)

(e) (f)

Figure 8.22.: The effective 1σ mean and width of the bending plane parameters of CaloBrem as a function of energy. The three bremsstrahlung categories are shown.

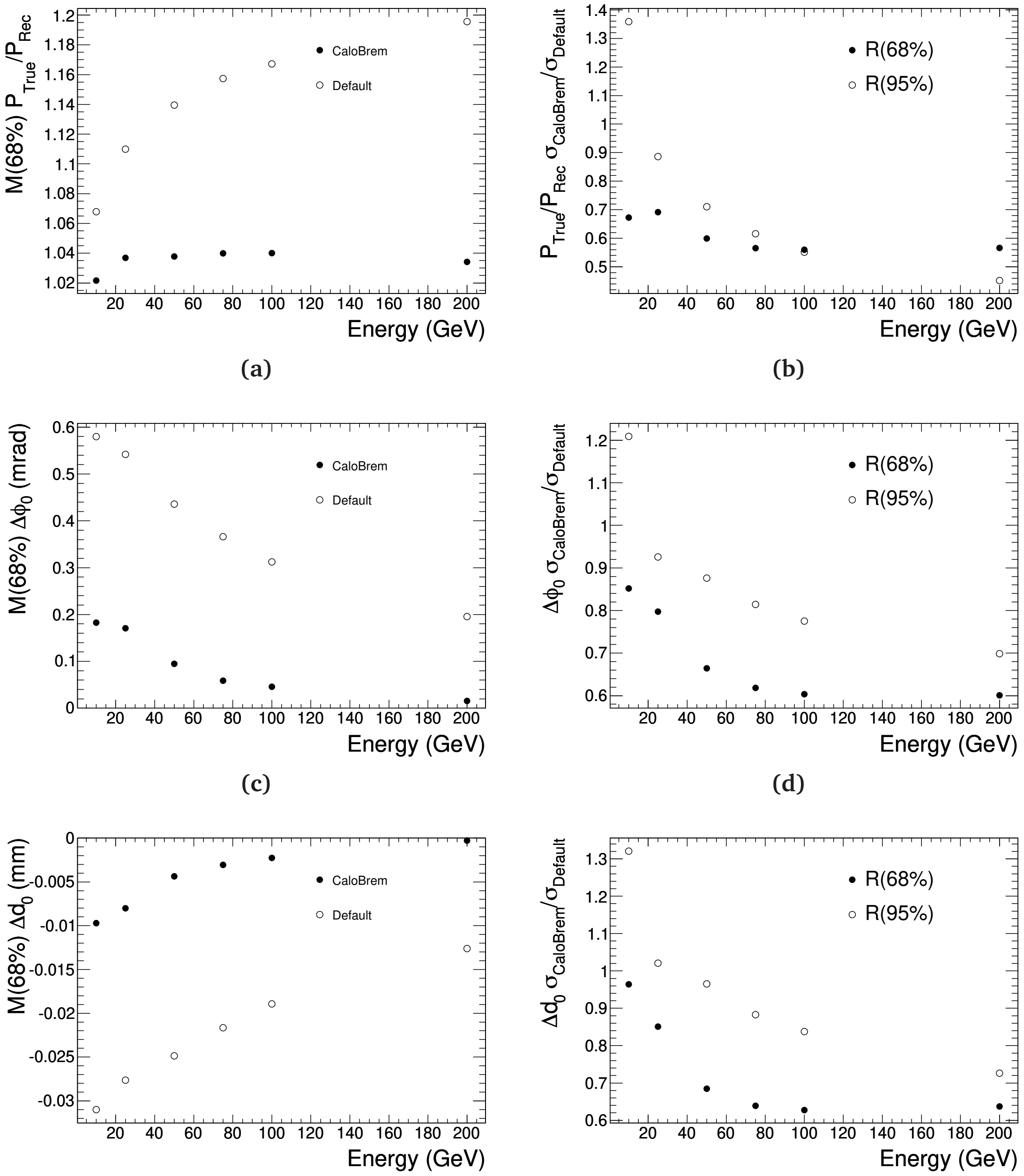

(a) **(b)**

(c) **(d)**

(e) **(f)**

Figure 8.23.: The effective 1σ mean and width of the bending plane parameters of CaloBrem and the default track fitter as a function of energy.

Error Estimation

For the uncertainty on the track parameters to be estimated correctly, the track model and the uncertainty on the measurements must also be optimal. The standard track reconstruction severely underestimated the uncertainty on the bending plane parameters as the energy losses due to bremsstrahlung are not incorporated into the track model. Our modified track model should improve the estimation of the uncertainty.

The pull distributions (see Figure 8.24) show large improvements when compared with the default track reconstruction. However, the uncertainty on all the track parameters, especially the reconstructed momentum, is still underestimated.

The reason for the underestimated uncertainty is most likely the result of the track model not being a true representation of what has actually occurred. The model is limited to a single bremsstrahlung, which is a rather large simplification. In fact, the error estimation on events where there is only one significant bremsstrahlung is much better, although still not ideal, suggesting that some of the problem may lie in the way that `MINUIT` estimates the uncertainty. Although the standard error estimation can be improved upon by using such tools as `MINOS`, the added computation time proved to make these techniques unfeasible.

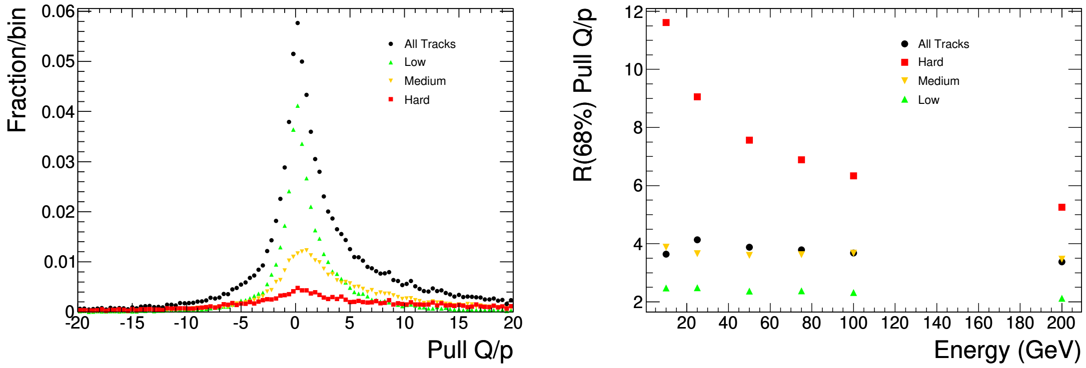

(a) E = 50 GeV **(b)**

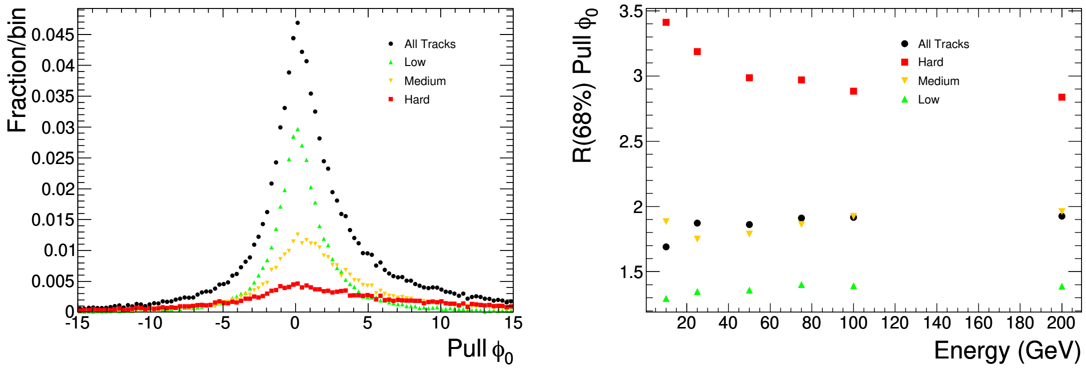

(c) E = 50 GeV **(d)**

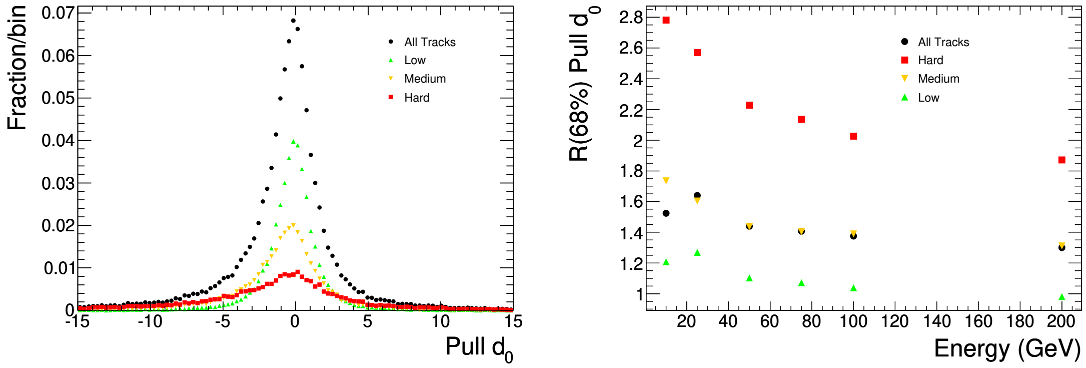

(e) E = 50 GeV **(f)**

Figure 8.24.: The pull distributions of bending plane parameters for E = 50 GeV electrons and the effective 1σ width as a function of energy.

8.6.3. Additional Constraints

Additional constraints can be added to the track fit to improve the trajectory estimation. A constraint on the transverse impact parameter derived from the position of the beam spot proved to be especially useful and improved the accuracy of all of the track parameters. Care must to be taken when using this constraint to ensure that it is only considered on “prompt” electrons, those that originate from the primary collision vertex.

The constraint is applied on the transverse impact parameter. The beam spot position, given in Cartesian coordinates, is converted into an apparent transverse impact parameter based upon the initial direction of the track

$$d_0^{BS} = -x_{BS} \sin\phi_0 + y_{BS} \cos\phi_0, \tag{8.19}$$

where x_{BS} and y_{BS} are the x and y positions of the beam spot and ϕ_0 is the initial direction of the electron. This constraint makes the assumption that the distances involved are small.

The uncertainty attributed to the impact parameter due to the uncertainty on the beam spot position is

$$\sigma(d_0^{BS}) = (\sigma_x \sin\phi_0)^2 - 2\sigma_{xy} \sin\phi_0 \cos\phi_0 + \left(\sigma_y \cos\phi_0\right)^2, \tag{8.20}$$

where σ_x, σ_y and σ_{xy} are the uncertainty on the position of the beam spot in the x and y direction and the correlation between them. Finally the χ^2 contribution of the beam spot constraint is:

$$\chi^2_{BS} = \left(\frac{d_0 - d_0^{BS}}{\sigma(d_0^{BS})}\right)^2. \tag{8.21}$$

Significant improvements can be seen in the resolution for low momentum electrons and the bias is also much reduced (see Table 8.6). The improvements decrease as the energy increases. This is not surprising as the resolution of the impact parameter improves as the energy of the electron increases reducing the impact of the constraint.

The calorimeter provides a completely independent measurement of the energy of the electron and can be used to provide a constraint on the momentum of the track.

Energy	Δd_0 (μm)		$\Delta\phi_0$ (mrad)		p_{True}/p_{Rec}	
(GeV)	M(68%)	R(68%)	M(68%)	R(68%)	M(68%)	R(68%)
10	-3.58	23.6	0.0865	0.623	1.0167	0.068
25	-3.04	20.5	0.0871	0.489	1.0302	0.109
50	-1.77	16.1	0.0571	0.330	1.0329	0.121
75	-1.01	14.8	0.0406	0.273	1.0336	0.135
100	-0.57	14.0	0.0245	0.242	1.0369	0.147
200	-0.075	12.7	0.0070	0.187	1.0358	0.191

Table 8.6.: The effective 1σ width and mean of the bending plane parameters for CaloBrem including information from the beam spot

Energy	Δd_0 (μm)		$\Delta\phi_0$ (mrad)		p_{True}/p_{Rec}	
(GeV)	M(68%)	R(68%)	M(68%)	R(68%)	M(68%)	R(68%)
10	-9.08	49.2	0.171	0.865	1.0176	0.0668
25	-5.08	40.5	0.103	0.688	1.0216	0.0763
50	2.48	27.6	-0.0243	0.394	1.0070	0.0475
75	3.63	22.6	-0.0393	0.288	1.0041	0.0355
100	3.83	20.2	-0.0427	0.240	1.0021	0.0299
200	2.69	15.7	-0.0311	0.158	1.0001	0.0215

Table 8.7.: The effective 1σ width and mean of the bending plane parameters for CaloBrem including a constraint on the tracks energy derived from the cluster energy.

The energy resolution of the calorimeter is superior to that of the Inner Detector at energies above 10 GeV.

The χ^2 contribution of the constraint is

$$\chi^2_E = \left(\frac{|Q.p| - E}{\sigma(E)}\right)^2. \tag{8.22}$$

This constraint improves the resolution of the track parameters, especially at high momentum. However the track parameters d_0 and ϕ_0 are now biased in the opposite direction (see Table 8.7). The resolution of the momentum of the track is dictated by the resolution of the calorimeter cluster and is no longer determined by the accuracy of the tracking.

Energy	Δd_0 (μm)		$\Delta \phi_0$ (mrad)		p_{True}/p_{Rec}	
(GeV)	M(68%)	R(68%)	M(68%)	R(68%)	M(68%)	R(68%)
10	-3.83	23.3	0.108	0.576	1.0134	0.0611
25	-2.38	20.6	0.072	0.425	1.0188	0.0722
50	0.791	15.3	-0.00463	0.265	1.0092	0.0487
75	2.01	13.8	-0.0199	0.204	1.0046	0.0367
100	1.96	13	-0.0266	0.175	1.0029	0.0305
200	1.94	11.4	-0.024	0.124	1.0002	0.0217

Table 8.8.: The effective 1σ width and mean of the bending plane parameters for CaloBrem including both the information from the beam spot and the energy of the calorimeter

Finally both constraints can be combined. At high energy the constraint on the beam spot adversely effects the resolution of the reconstructed momentum resolution when compared to that of the just energy constraint alone. While the resolution of the other two track parameters is improved upon (see Table 8.8).

8.6.4. Summary

This technique for incorporating the bremsstrahlung into the track model shows significant improvements in the reconstructed track parameters at high energy. Even at low energy there is definite improvement to the reconstructed track parameters as they become less biased. The resolution is also mildly improved, however given the low fraction of events that are actually successfully fit, the true strength of the technique lies at higher energies (E > 25 GeV). Tables 8.9, 8.10 and 8.11 summarise the improvements of the track parameters resolution when using the CaloBrem technique with various constraints over the default track reconstruction.

8.6.5. Bremsstrahlung Parameter Reconstruction

Although the normal track parameters are the key parameters for physics analysis, the final two parameters of the model, the bremsstrahlung radius and the amount of

Energy (GeV)	Default	Beamspot	Energy	Beamspot + Energy
10	0.964	0.436	0.900	0.432
25	0.851	0.408	0.778	0.410
50	0.685	0.356	0.607	0.341
75	0.639	0.362	0.554	0.342
100	0.628	0.374	0.542	0.353
200	0.637	0.427	0.533	0.390

Table 8.9.: The ratio between the effective 1σ width of d_0 for the default track reconstruction and CaloBrem with different constraints

Energy (GeV)	Default	Beamspot	Energy	Beamspot + Energy
10	0.852	0.555	0.767	0.519
25	0.798	0.486	0.662	0.427
50	0.664	0.413	0.496	0.338
75	0.618	0.399	0.426	0.304
100	0.604	0.401	0.403	0.297
200	0.601	0.432	0.371	0.296

Table 8.10.: The ratio between the effective 1σ width of ϕ_0 for the default track reconstruction and CaloBrem with different constraints

energy lost, can provide useful information about the detector itself. Using a combination of the location of reconstructed bremsstrahlung vertices and the amount of energy lost, a material map of the Inner Detector could be produced.

Bremsstrahlung Radius

An electron will generally bremsstrahlung multiple times as it travels through the detector. Hence to define the true position of the bremsstrahlung is rather difficult as only one bremsstrahlung vertex is reconstructed. As such, the reconstructed vertex will be a sort of weighted average of the bremsstrahlung positions. To simplify the situation the reconstructed bremsstrahlung position will be compared to that of the position of the largest bremsstrahlung, the vertex where the largest amount of energy is lost. This simplification is not ideal. When there are multiple significant bremsstrahlung it will act as a first order approximation.

Energy (GeV)	Default	Beamspot	Energy	Beamspot + Energy
10	0.673	0.599	0.576	0.537
25	0.692	0.594	0.404	0.397
50	0.600	0.515	0.200	0.208
75	0.566	0.485	0.128	0.134
100	0.560	0.479	0.097	0.101
200	0.566	0.489	0.056	0.057

Table 8.11.: The ratio between the effective 1σ width of p_{True}/p_{Rec} for the default track reconstruction and CaloBrem with different constraints

The χ^2/DoF of the track was set between 0.8 and 2.0. In addition, the bremsstrahlung radius (R_B) was required below 990 mm and above 12 mm to ensure that the reconstructed bremsstrahlung radius was not too close to the limits defined in for the minimisation process. This left approximately 70% of the electrons that were successfully fit.

Comparing the reconstructed bremsstrahlung resolution to the reconstructed fraction of energy retained (Figures 8.25 and 8.26), a clear trend emerges. As the reconstructed energy loss decreases the resolution on the reconstructed bremsstrahlung radius increases (this is highlighted in Figure 8.26). There are two reasons for this. Firstly as the bremsstrahlung radius is more accurate at higher energy losses it suggests that the bremsstrahlung vertex is reconstructed more accurately when there is a greater separation between the track's point of impact in the calorimeter and the position of the electromagnetic cluster. Secondly if the energy loss estimate is accurate then it suggests that the electron must lose $\gtrapprox$ 50% of its energy in order to have accurately reconstructed the bremsstrahlung vertex. As such it is impossible to have another bremsstrahlung that loses more energy, hence the other bremsstrahlung will more than likely be relatively small. Furthermore, the true bremsstrahlung position, which is estimated by the position of the largest bremsstrahlung, is accurate.

These results show that the use of all constraints improves the bremsstrahlung radius resolution, and helps to eliminate the majority of the unphysical bremsstrahlung events, where $Z_B > 1$. This allows for the reconstruction of bremsstrahlung in the pixel detector.

To map the material of the Inner Detector, a relatively fine granularity is required. Only events with Z_B resolution below 5 cm were selected. This drastically reduces the

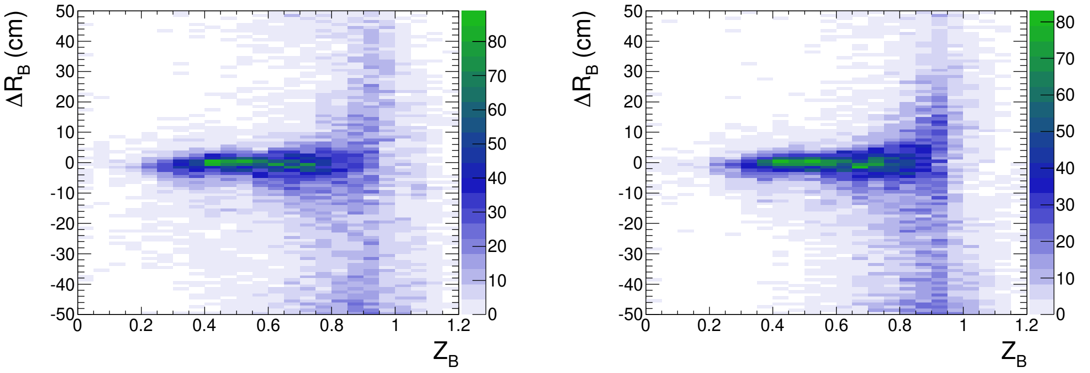

(a) 10 GeV, no constraint **(b)** 10 GeV, energy and beam spot

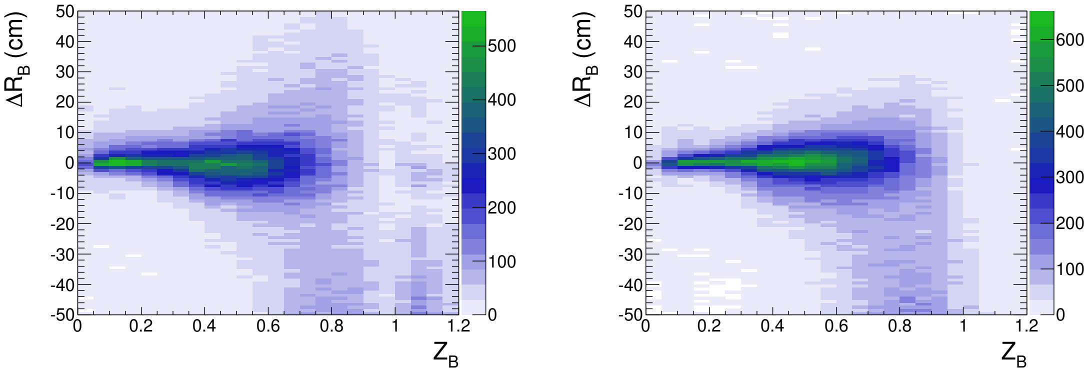

(c) 75 GeV, no constraint **(d)** 75 GeV, energy and beam spot

Figure 8.25.: The difference between the reconstructed bremsstrahlung radius and the radius of the largest bremsstrahlung as function of the measured fraction of energy retained.

remaining fraction of events with just under 5% of events remaining. The difference between the reconstructed bremsstrahlung radius and the largest radius is shown in Figure 8.27.

For both of the selected energy points there is a significant non-Gaussian tail present. At low energy it is biased towards underestimating the radius of the bremsstrahlung, while at high energy it is biased to overestimating the radius.

In the high energy sample there is clearly some structure in the resolution that is not present at low energy. The structure seems to correlate quite well to material layers but further study is required to understand why it is not present at low energy as seen in Figure 8.28.

Figure 8.28 displays the bias in the mean reconstructed bremsstrahlung radius and its dependence on the true bremsstrahlung radius. For both samples the reconstructed

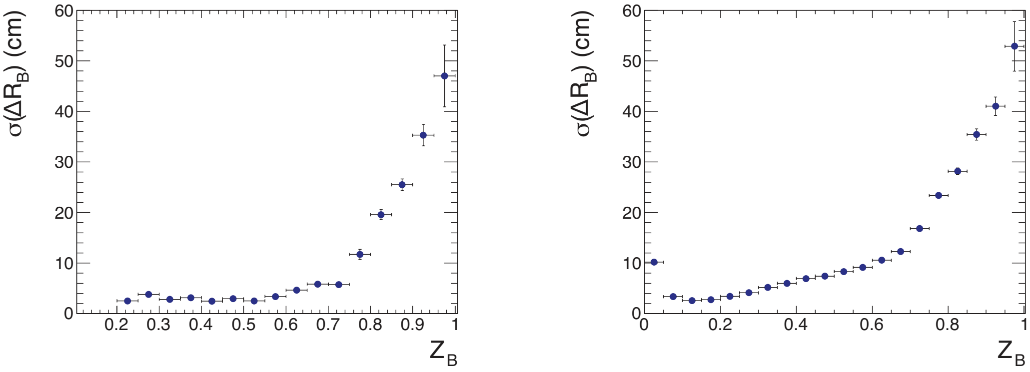

(a) 10 GeV **(b)** 75 GeV

Figure 8.26.: The dependance of the reconstructed bremsstrahlung radius resolution on the reconstructed fraction of energy retained (when using both a beam spot and energy constraint). The results are obtain from a Gaussian fit.

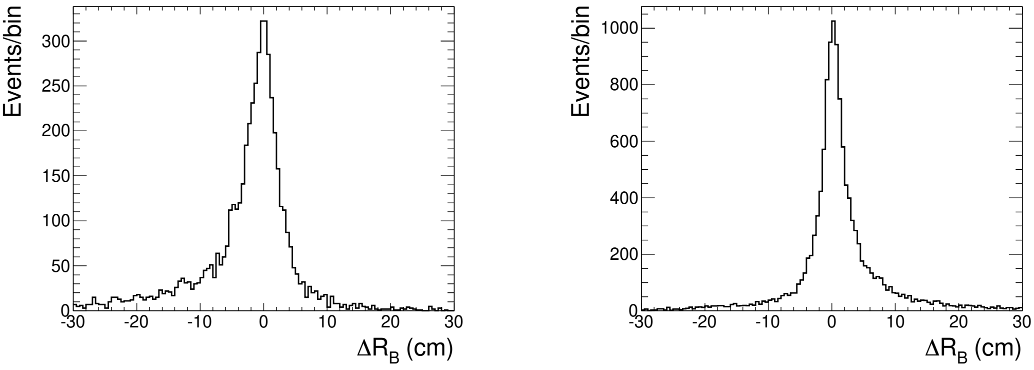

(a) 10 GeV **(b)** 75 GeV

Figure 8.27.: The difference between the reconstructed bremsstrahlung radius and the true radius of largest bremsstrahlung after selection cuts have been applied.

bremsstrahlung radius is relatively unbiased below a radius of 55 cm (the last layer of the SCT) but beyond that the measurement becomes heavily underestimated. This looks to be a result of an inability to determine the occurrence of bremsstrahlung within the TRT detector.

Figure 8.29 displays the reconstructed bremsstrahlung radius when compared to true bremsstrahlung radius smeared by 1.25 cm in central region of the detector. It shows that the 3 pixel layers and the 4 silicon layer can be resolved. The reconstruction bremsstrahlung occurring first pixel layers is not 100% efficient. Also it is clear to see that the majority of bremsstrahlung occurring in the TRT is reconstructed in a radius of approximately 60 cm.

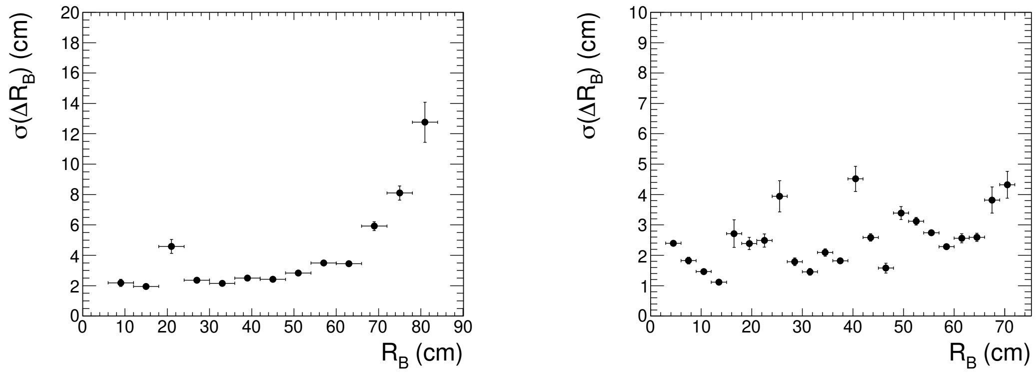

(a) 10 GeV **(b)** 75 GeV

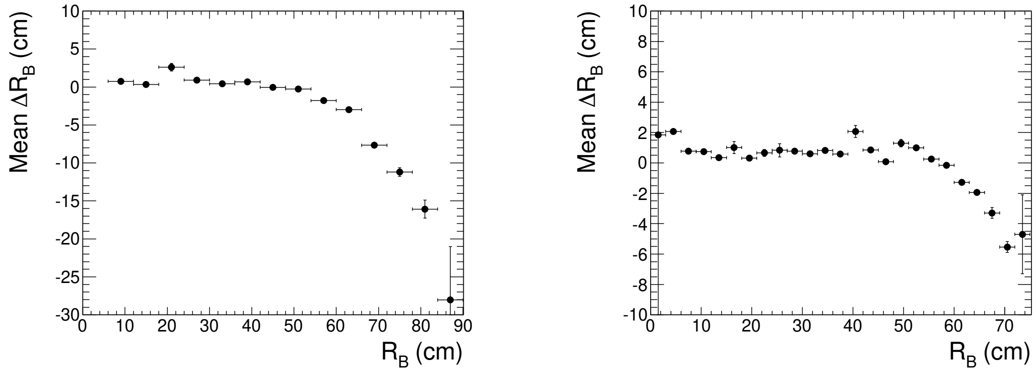

(c) 10 GeV **(d)** 75 GeV

Figure 8.28.: The dependance of mean reconstructed bremsstrahlung radius and resolution on the true of the bremsstrahlung. The results are obtained from a Gaussian fit.

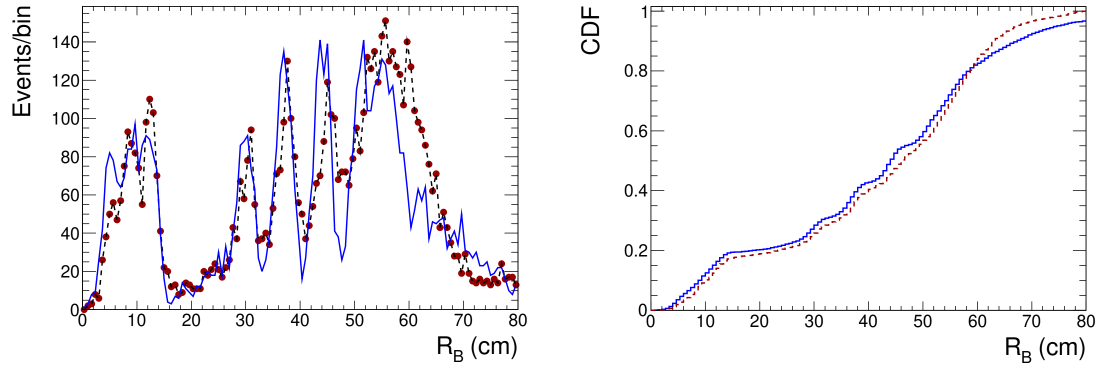

(a) **(b)**

Figure 8.29.: The reconstructed bremsstrahlung radius (dashed line and points) and the true bremsstrahlung radius (solid blue line) which has been smeared by a Gaussian with a width of 1.25 *cm*.

Bremsstrahlung Energy

Using the same event selection as the bremsstrahlung radius study, the fraction of energy remaining after the bremsstrahlung (Z_B) can be reconstructed relatively well. In fact if one inspects events where only one bremsstrahlung has occurred (see Figures 8.30a 8.30c), the resolution of Z_B is 4% at E = 10 GeV and less than 1% at 75 GeV. Looking at the resolution of the Z_B reconstruction in events where multiple bremsstrahlung occur the amount of energy lost is overestimated especially in the high energy electrons. This suggests that the measured energy loss is not just from the largest bremsstrahlung but from all bremsstrahlung that occur. Figure 8.31 confirms this.

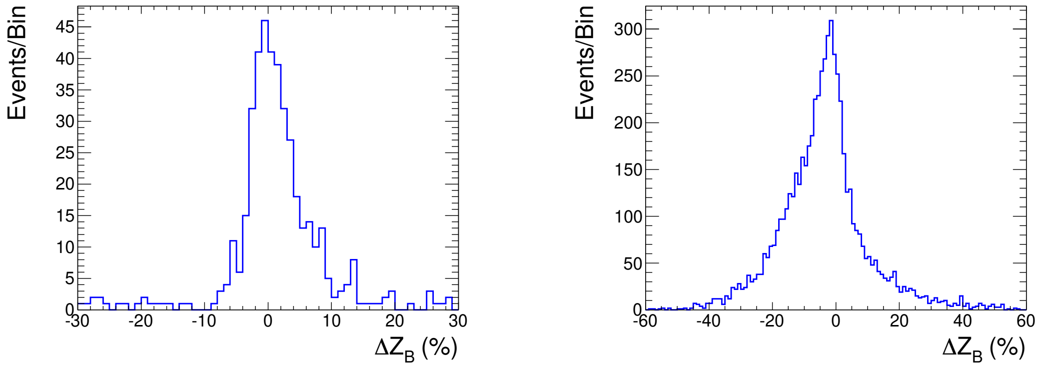

(a) Single Bremsstrahlung - 10 GeV Electrons **(b)** Multiple Bremsstrahlung - 10 GeV Electrons

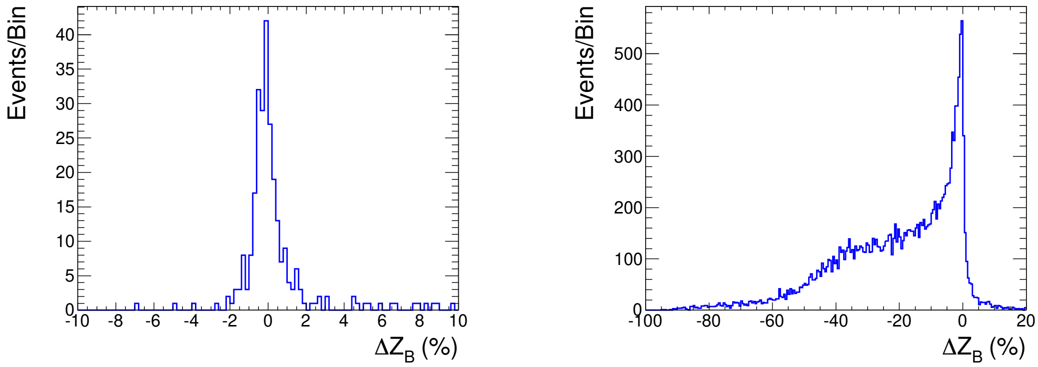

(c) Single Bremsstrahlung - 75 GeV Electrons **(d)** Mulitple Bremsstrahlung - 75 GeV Electrons

Figure 8.30.: The difference between reconstructed Z_B and fraction of energy retained after the largest bremsstrahlung.

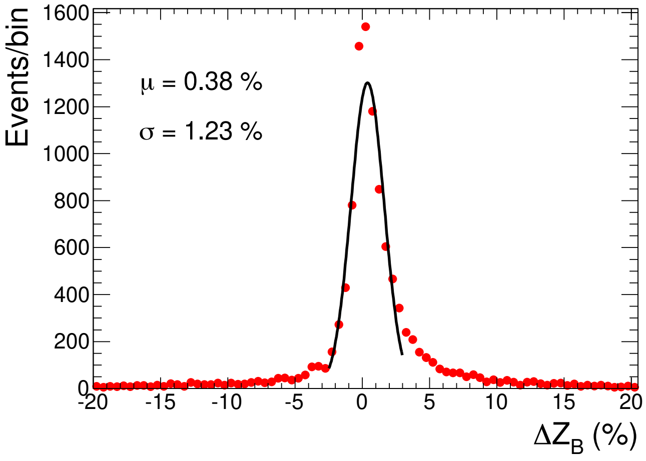

Figure 8.31.: The difference between reconstructed Z_B and fraction of energy retained before the electron reaches a radius of 70 cm for 75 GeV electrons. The core the distribution is fit with a Gaussian.

8.7. Outlook

A new tracking based bremsstrahlung recovery technique that utilises the position of the electromagnetic cluster has been implemented and tested in the ATLAS software framework. The algorithm improves as the energy electron increases where the position of the cluster in the calorimeter is well defined. However useful improvements can be gained at low energies.

These initial studies were performed on an idealised sample of events consisting only of a single electron. The effects of “pile up” and the underlying event on the track, cluster and electron reconstruction have not been taken into account, nor have the effects of misalignments of the Inner Detector and calorimeter. It would be expected that misalignments of the calorimeter with respect to the Inner Detector could significantly degrade the performance of the technique.

From the information gained about the bremsstrahlung location and strength it may be possible, with a more refined study, to create a detailed material map of the Inner Detector. In order to generate this material map understanding of the efficiency of the bremsstrahlung reconstruction as a function of radius, energy and η will be required.

It may also be possible to gain some information from the bremsstrahlung that may help improve the electron identification, however this is yet to be fully explored.

9

CHAPTER

PHYSICS CASE STUDIES

In Chapter 8 a new technique for recovering the effects of bremsstrahlung was introduced and its performance on single electrons was assessed. CaloBrem was shown to significantly improve the momentum estimates of electrons above 25 GeV.

CaloBrem is not the only bremsstrahlung recovery technique implemented in the ATLAS software. Two other techniques that have been developed, the Gaussian Sum Filter (GSF) and Dynamic Noise Adjustment (DNA), both of which are based upon Kalman filtering and give significant improvements over the standard track reconstruction. Their performances are relatively similar for low energy electrons. For high energy electrons the GSF works better than DNA. However, the GSF is 10 times slower than DNA[1].

In this chapter a very preliminary tracking based study of several physics processes are discussed. Three different track fits are considered: The default track fit which is a global χ^2 fit that assumes that energy losses are only due to ionisation; the GSF, which incorporates non Gaussian material effects based upon Geant4 simulation of electron energy loss; CaloBrem, which is not 100% efficient, in events where the CaoBrem fit

---

[1] GSF takes on average 52 ms per track on a Intel Xeon E5450 CPU's running at 3.00 GHz

fails the results of the default track fit are used. Particle identification is performed through the ATLAS reconstruction, however Monte-Carlo is used to identify the origin of those particles.

Electrons from the decay of various mass resonance's will be used to calibrate the electromagnetic calorimeter and help in the validation of the performance of the detector. Some of these techniques require precise estimation of the momentum of tracks and as such the performance of bremsstrahlung techniques should be evaluated.

Three physics processes are considered: $J/\psi \to e^+e^-$ (Section 9.1); $\Upsilon(1S) \to e^+e^-$ (Section 9.2); and $Z \to e^+e^-$ (Section 9.3).

9.1. $J/\psi \to e^+e^-$

The J/ψ, mass of 3096.916 ± 0.011 MeV and width of 93.2 ± 2.1 keV [5], has electron pair decay mode with $\mathrm{BR}(J/\psi \to e^+e^-) = 5.94 \pm 0.06$ %.

A sample of 100,000 $J/\psi \to e^+e^-$ decays, generated and simulated through the full simulation procedure of ATLAS, were inspected. The simulation required that the transverse momentum of both leptons was at least 3 GeV. The requirement was put in-place to reduce simulation time due to the low probability of an electron below 3 GeV being reconstructed. Figure 9.1 shows the true transverse momenta of the leptons, ordered according to their energy. The leading lepton is more energetic than the secondary lepton.

The electrons reconstructed in the event are then matched to the Monte-Carlo truth. If the events contain a reconstructed electron and positron that originated from the $J\psi$, then the event is considered in the study. Such a selection process leaves 45.1% of the generated events for analysis.

The resolution values are given in tables 9.1 and 9.2. As in the previous chapter (see Section 8.2) the effective width is quantified as the narrowest half-width enclosing 68% (1σ) and 95% (2σ) of the distribution. The reconstructed lepton Q/p residuals are shown in Figure 9.2. In all cases the GSF provides the best overall estimate of the momentum. It reduces the effective 1σ width by 37% when compared to the default track reconstruction and the mean of those events are closer to the ideal value.

The invariant mass distributions of the e^+e^- pair are shown in Figure 9.3. The resolution of the reconstructed invariant mass is dominated by the resolution of the momentum of the tracks. The peak of the GSF invariant mass distribution is in good agreement with the accepted mass of the J/ψ. As the electrons momentum is largely underestimated by the standard track reconstruction, the reconstructed invariant mass has no clear peak, but a kinematic edge at the true energy of the J/ψ.

Due to the poor efficiency of CaloBrem at low energy (35% for this sample) the fitter provides little improvements over the standard track reconstruction [2]. For the 12.7% of events that have both tracks successfully fitted by CaloBrem the improvements in the reconstructed invariant mass can be clearly seen (see Figure 9.3b). The effective 1σ width of the reconstructed mass is actually better than the GSF (3% improvement), however the 1σ mean is worse than that of the GSF (10.9% underestimation compared to 5.5% underestimation).

Energy	Leading Lepton		Secondary Lepton		$M_{ee} - M_{J/\psi}$ (GeV)	
	M(68%)	R(68%)	M(68%)	R(68%)	M(68%)	R(68%)
Default	1.075	0.127	1.075	0.127	-0.282	0.298
CaloBrem	1.052	0.116	1.056	0.119	-0.219	0.280
CaloBrem 100%	1.025	0.092	1.022	0.089	-0.109	0.224
GSF	0.999	0.080	1.000	0.080	-0.055	0.232

Table 9.1.: The effective 1σ width and mean momentum of tracks from decay of the J/ψ and the reconstructed mass

Energy	Leading Lepton		Secondary Lepton		$M_{ee} - M_{J/\psi}$ (GeV)	
	M(95%)	R(95%)	M(95%)	R(95%)	M(95%)	R(95%)
Default	1.165	0.440	1.166	0.447	-0.417	0.628
CaloBrem	1.128	0.461	1.130	0.466	-0.339	0.672
CaloBrem 100%	1.061	0.369	1.061	0.370	-0.175	0.687
GSF	1.059	0.376	1.058	0.373	-0.173	0.626

Table 9.2.: The effective 2σ width and mean momentum of tracks from decay of the J/ψ and the reconstructed mass

---

[2] For these studies any failed fits use the default tracking results

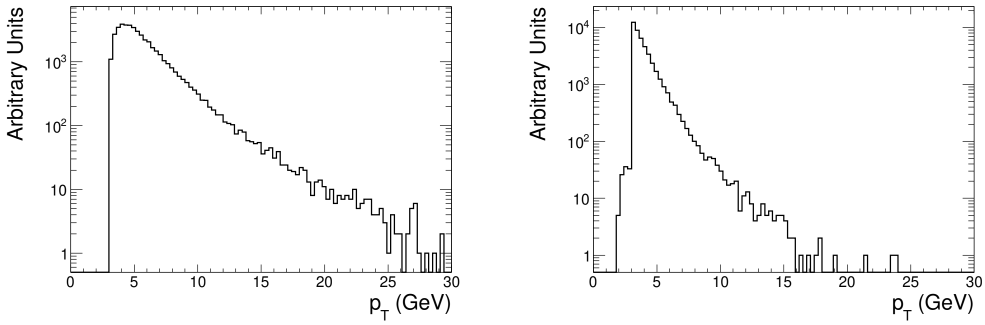

(a) Leading Lepton **(b)** Secondary Lepton

Figure 9.1.: Distributions of the true momenta of the leptons from J/ψ decay. The leptons are ordered according to their energy with the leading lepton being more energetic than the secondary lepton. Both Leptons were required to have transverse momentum 3 GeV.

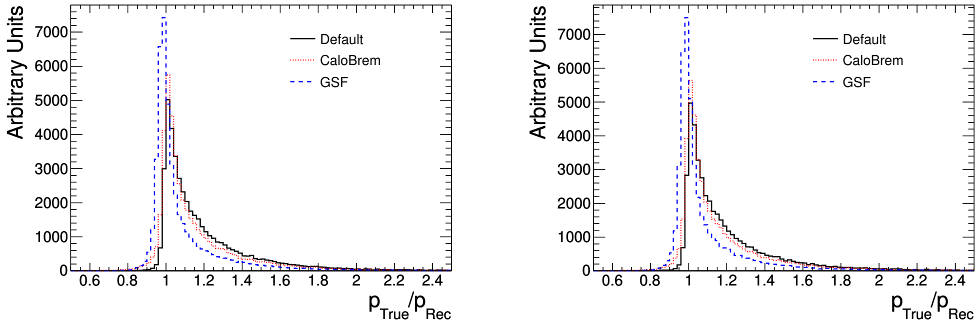

(a) Leading Lepton **(b)** Secondary Lepton

Figure 9.2.: Normalised Q/p residuals of the two leptons originating from the $J/\psi \rightarrow e^+e^-$ decay. Tracks reconstructed with the GSF (blue dashed) are compared to that of CaloBrem (red dotted line) and the default tracking (solid black).

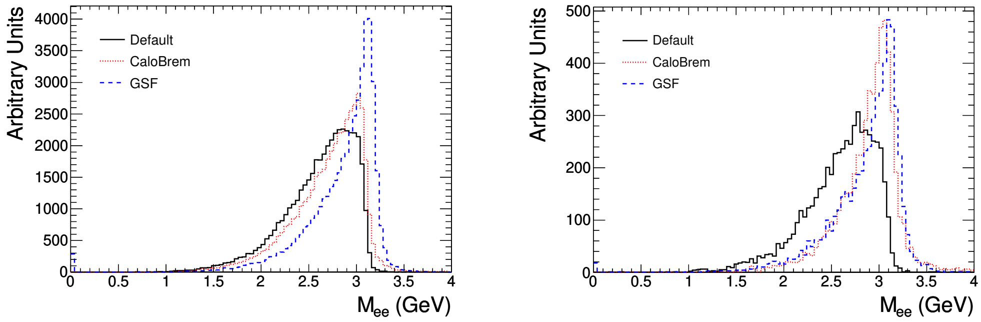

(a) All Events **(b)** CaloBrem Successful

Figure 9.3.: The reconstructed invariant mass of the J/ψ. The effectiveness of CaloBrem can clearly be seen in events where the fit was successful on both leptons (Figure 9.3b). Events reconstructed with the GSF (blue dashed) are compared to that of CaloBrem (red dotted line) and the default tracking (solid black).

9.2. $\Upsilon(1S) \rightarrow e^+e^-$

The $\Upsilon(1S)$, mass of 9460.30 ± 0.26 MeV and width of 54.02 ± 1.25 keV[5], has electronic decay mode with a branching ratio, BR($J/\psi \rightarrow e^+e^-$) = 2.38% ± 0.11%.

A sample of 100,000 $\Upsilon(1S) \rightarrow e^+e^-$ decays, generated and simulated through the full simulation procedure of ATLAS, were inspected. The simulation required that the transverse momentum of both leptons was at least 3 GeV. The requirement was put in-place to reduce simulation time due to the low probability of an electron below 3 GeV being reconstructed. Figure 9.4 shows the true transverse momenta of the leptons, ordered according to their energy. The leading lepton is defined to more energetic than the secondary lepton. Only events with electron truly originating from $\Upsilon(1S)$ where considered in this study.

The resolution values are given in tables 9.3 and 9.4. The reconstructed lepton Q/p residuals are shown in Figure 9.5 There is slight degradation in the momentum resolution of the track reconstruction when compared to that of the track from the J/ψ. This is a result of the average track momentum being slightly larger in the case of the Υ. Again in all cases the GSF provides the best estimate of the momentum of the tracks. It reduces the effective 1σ width by 37% when compared to the default track reconstruction and the mean of those events is now unbiased.

The invariant mass distributions of the e^+e^- pairs are shown in Figure 9.6. The peak of the GSF invariant mass distribution is in good agreement with the accepted mass of the $\Upsilon(1S)$. The standard track reconstruction has very similar features to that of the J/ψ. It is interesting to note that the reconstructed mass resolution is effectively three times larger than that of the J/ψ whose mass is three times smaller than that of the $\Upsilon(1S)$.

Again due to the poor efficiency of CaloBrem at low energy (36% for this sample) it provides little improvements over the standard track reconstruction. For the 13.0% of events that have both tracks successfully fitted by CaloBrem, the improvements in the reconstructed invariant mass can clearly be seen (see Figure 9.6b). In the effective 1σ width of the reconstructed mass is actually better than the GSF (7% improvement). However the 1σ mean is worse than that of the GSF (3.2% underestimation compared to 2.0% underestimation).

The effective 2σ width of the invariant mass suggests that the default track reconstruction encompasses 95% of the events in the smallest width. This happens because for all fitters to ensure that 95% of the events are captured, the window of acceptance must reach into the tails of the distribution. As the default track reconstruction will not overestimate the momentum of the electrons the window will be the smallest.

Energy	Leading Lepton		Secondary Lepton		$M_{ee} - M_{\Upsilon(1S)}$ (GeV)	
	M(68%)	R(68%)	M(68%)	R(68%)	M(68%)	R(68%)
Default	1.078	0.131	1.079	0.133	-0.908	0.944
CaloBrem	1.054	0.121	1.057	0.126	-0.710	0.902
CaloBrem 100%	1.022	0.091	1.019	0.090	-0.307	0.702
GSF	1.001	0.086	1.001	0.086	-0.192	0.756

Table 9.3.: The effective 1σ width and mean momentum of tracks from decay of the $Y(1S)$ and the reconstructed mass

Energy	Leading Lepton		Secondary Lepton		$M_{ee} - M_{\Upsilon(1S)}$ (GeV)	
	M(95%)	R(95%)	M(95%)	R(95%)	M(95%)	R(95%)
Default	1.175	0.481	1.178	0.480	-1.339	1.935
CaloBrem	1.133	0.502	1.139	0.505	-1.085	2.093
CaloBrem 100%	1.058	0.357	1.058	0.364	-0.530	1.952
GSF	1.065	0.402	1.065	0.407	-0.587	1.940

Table 9.4.: The effective 2σ resolution and mean momentum of tracks from decay of the $Y(1S)$ and the reconstructed mass

9.3. $Z \rightarrow e^+e^-$

The Z boson has a mass 91.188 ± 0.002 GeV and a width $\sigma = 2.495 \pm 0.002$ GeV[5]. It has an equal probability of decaying into any pair of charged leptons, BR($Z \rightarrow e^+e^-$) = BR($Z \rightarrow \mu^+\mu^-$) = BR($Z \rightarrow \tau^+\tau^-$) = 1.12%. The large production rate of Z at the LHC will allow the calculation of the W-mass to a high precision.

A sample of 100,000 $Z \rightarrow e^+e^-$ decays were inspected. The sample required that at least one of the electrons is within the Inner Detector acceptance (i.e. $|\eta| < 2.5$).

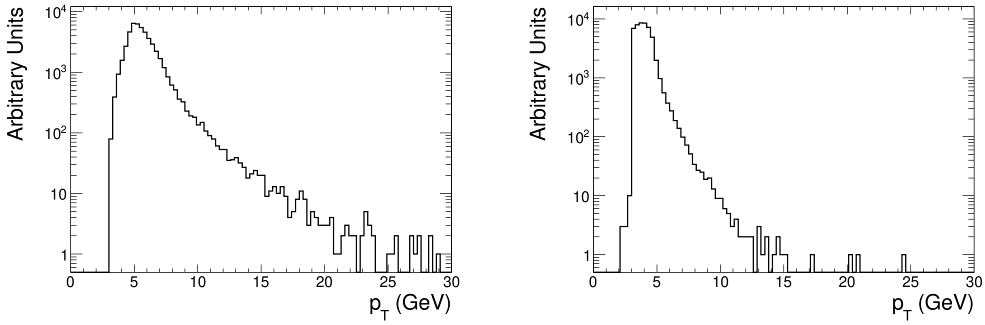

(a) Leading Lepton **(b)** Secondary Lepton

Figure 9.4.: Distributions of the true momenta of the leptons from $\Upsilon(1S)$ decay. The leptons are ordered according to their energy with the leading lepton being more energetic than the secondary lepton. Both Leptons were required to have transverse momentum 3 GeV.

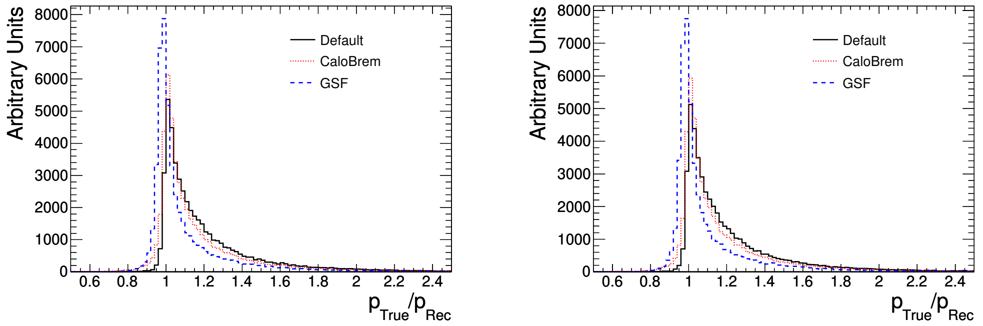

(a) Leading Lepton **(b)** Secondary Lepton

Figure 9.5.: Normalised Q/p residuals of the two leptons originating from the $\Upsilon \rightarrow e^+e^-$ decay. Tracks reconstructed with the GSF (blue dashed) are compared to that of CaloBrem (red dotted line) and the default tracking (solid black).

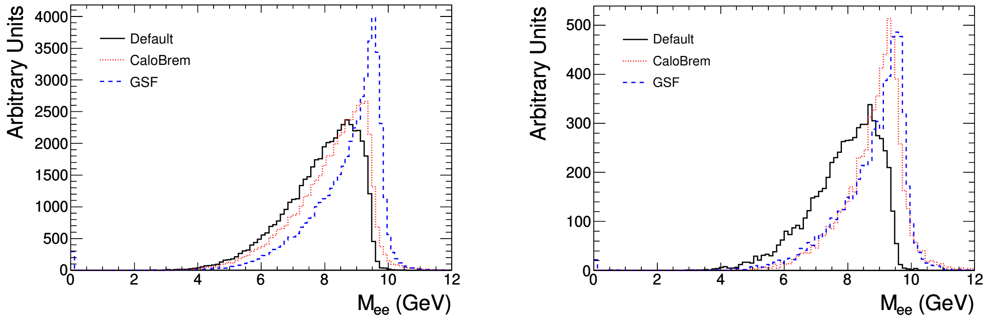

(a) All Events **(b)** CaloBrem Successful

Figure 9.6.: The reconstructed invariant mass of the $\Upsilon(1S)$. The effectiveness of CaloBrem can clearly be seen in events where the fit was successful on both leptons (Figure 9.6b). Events reconstructed with the GSF (blue dashed) are compared to that of CaloBrem (red dotted line) and the default tracking (solid black).

Figure 9.7 shows the true transverse momenta of the final state leptons. After selecting events that have both an electron and a positron that originate from a Z boson (matched using Monte-Carlo truth) 40.2% of events are left for analysis .

The normalised reconstructed Q/p residuals are shown in Figure 9.8 and the corresponding effective 1σ and 2σ width and mean values are provided in tables 9.5 and 9.6. As expected the momentum resolution is worse for leptons from the Z decay than from J/ψ and Υ decays as leptons are significantly more energetic.

The invariant mass of the lepton pair is shown in Figure 9.9. Due to the large width of the Z boson it of greater use to inspect Figure 9.10 which shows the difference between the reconstructed mass and the generated mass of the lepton pair. Large improvements in the reconstructed mass is seen for both CaloBrem and GSF.

The effective 1σ resolution, when compared to the default tracking, is improved by 10% when using the GSF and 18% when using CaloBrem. The effective mean is also significantly improved. In the special case were both tracks are fit by CaloBrem (56% of events) the effective 1σ resolution is improved by 29% while the mass was underestimated by 4.5 GeV.

A high energy tail is present in the reconstructed invariant mass distribution for CaloBrem. This is a result of CaloBrem overestimating the momentum of the electrons. This tail, if considered a problem, can simply be removed by replacing the tracks momentum by the default reconstructed mass. For example this can be done if the ratio between the reconstructed energy of the electromagnetic cluster and the tracks momentum is less than 0.9. This tail results in the effective 2σ resolution of CaloBrem being larger than that of the default tracking but the distribution is generally more symmetric.

Energy	Leading Lepton		Secondary Lepton		$M_{ee} - M_Z$ (GeV)	
	M(68%)	R(68%)	M(68%)	R(68%)	M(68%)	R(68%)
Default	1.130	0.244	1.130	0.241	-13.55	14.87
CaloBrem	1.048	0.160	1.047	0.155	-6.08	12.21
CaloBrem 100%	1.035	0.137	1.035	0.134	-4.46	10.53
GSF	1.024	0.168	1.024	0.168	-5.40	13.36

Table 9.5.: The effective 1σ width and mean momentum of tracks from decay of the Z and the reconstructed mass

Energy	Leading Lepton		Secondary Lepton		$M_{ee} - M_Z$ (GeV)	
	M(95%)	R(95%)	M(95%)	R(95%)	M(95%)	R(95%)
Default	1.375	1.549	1.370	1.552	-20.88	31.15
CaloBrem	1.116	1.117	1.114	1.170	-10.32	43.26
CaloBrem 100%	1.060	0.709	1.064	0.687	-5.34	38.80
GSF	1.195	1.230	1.192	1.239	-12.41	32.77

Table 9.6.: The effective 2σ width and mean momentum of tracks from decay of the Z and the reconstructed mass

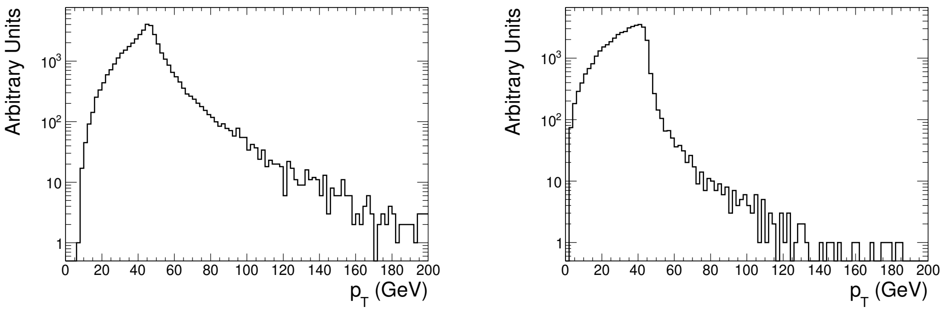

(a) Leading Lepton **(b)** Secondary Lepton

Figure 9.7.: Distributions of the true momenta of the leptons from Z boson decay. The leptons are ordered according to their energy with the leading lepton being more energetic than the secondary lepton.

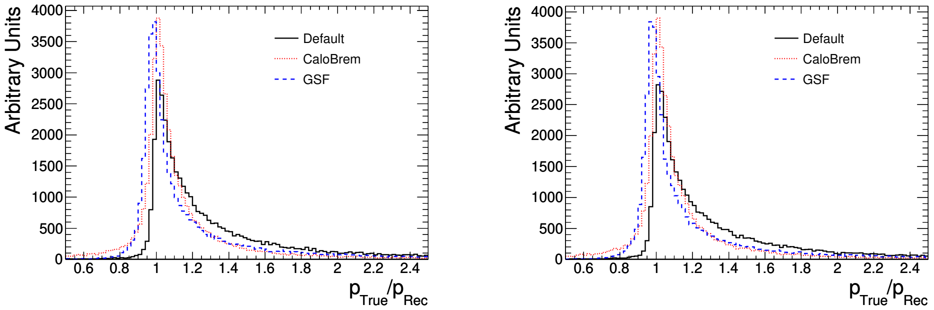

(a) Leading Lepton **(b)** Secondary Lepton

Figure 9.8.: Normalised Q/p residuals of the two leptons originating from the $Z \rightarrow e^+e^-$ decay. Tracks reconstructed with the GSF (blue dashed) are compared to that of CaloBrem (red dotted line) and the default tracking (solid black).

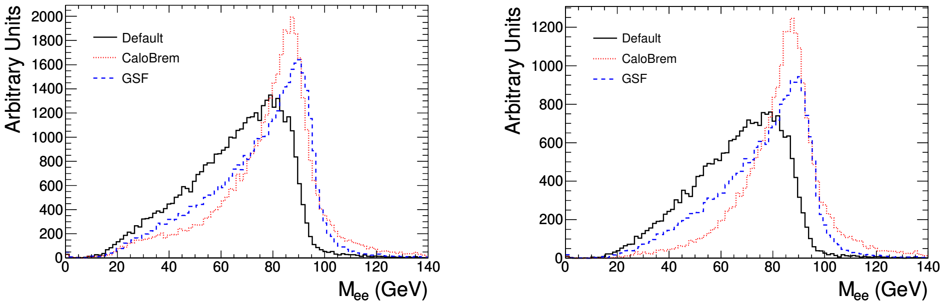

(a) All Events **(b)** CaloBrem Successful

Figure 9.9.: The reconstructed invariant mass of the Z. The effectiveness of CaloBrem can clearly be seen in events where the fit was successful on both leptons (Figure 9.9b). Events reconstructed with the GSF (blue dashed) are compared to that of CaloBrem (red dotted line) and the default tracking (solid black).

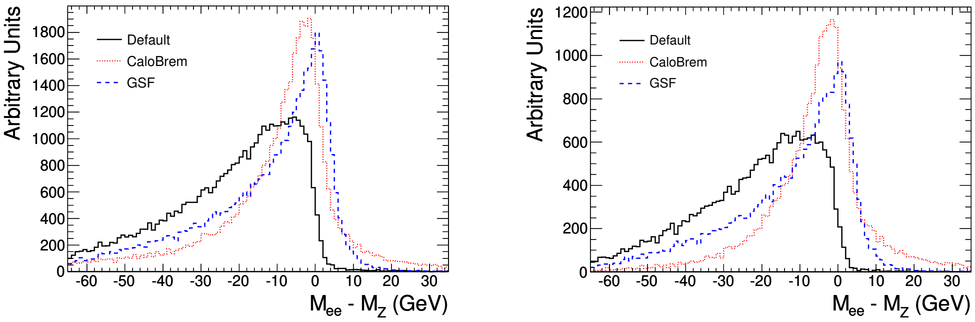

(a) All Events **(b)** CaloBrem Successful

Figure 9.10.: The difference between the reconstructed invariant mass of the Z and the generated. The effectiveness of CaloBrem can clearly be seen in events where the fit was successful on both leptons (Figure 9.10b). Events reconstructed with the GSF (blue dashed) are compared to that of CaloBrem (red dotted line) and the default tracking (solid black).

A

APPENDIX

THE EFFECT OF MATTER ON THE TRAJECTORY

The simple notion of particles traveling undisturbed in a homogenous magnetic field can never be realised in particle physics experiments if we wish to measure the particles. The need to measure the trajectory of particles requires the particle to interact with the active detector elements. The detector not only consists of the active detector but there may also be significant amount of dead material in the form of support structures or services, that will be detrimental to the measurement of the particles trajectory. Disturbances to the particles trajectory can be accounted for in the track model allowing for material interactions to be accounted for.

A.1. Energy Loss

In our track model it was assumed that the energy of charged particle was constant. In reality when a charged particle traverses through matter some energy is transmitted to medium. As a result the supposed constant, p, must be readjusted to account for this loss and an understanding of the mechanisms of energy loss are required.

A.1.1. Ionisation

Energy loss by ionisation is the most prevalent form of energy loss for a charged particle within the tracking volume. The ionisation process is stochastic, however the fluctuation in energy loss is small with respect to the mean. The mean rate of energy loss is normally given by a deterministic approximation, the Bethe-Bloch equation[5],

$$-\frac{dE}{dx} = Kq^2 \frac{Z}{A}\frac{1}{\beta^2}\left[\frac{1}{2}\ln\frac{2m_e c^2\beta^2\gamma^2 T_{max}}{I^2} - \beta^2 - \frac{\delta\left(\beta\gamma\right)}{2}\right], \tag{A.1}$$

where β and γ are the relativistic kinematic variables, E is in MeV and x is in cm. All constants are defined in Table A.1.

Symbol	Definition	Units / Value
K/A	Constant of proportionality	0.3071 $MeV\ g^{-1}\ cm^2$
M	Mass of incident particle	MeV/c^2
q	Elementary charge of incident particle	n/a
m_e	Electron mass	0.511 MeV/c^2
Z	Atomic number	n/a
A	Atomic mass	$g\ mol^{-1}$
ρ	density	$g\ cm^{-3}$
I	Mean excitation energy	eV
$\delta\left(\beta\gamma\right)$	Density effect correction	
T_{max}	Maximum energy a particle can impart to an electron	MeV

Table A.1.: Summary of variables used in the Bethe-Bloch equation.

The maximum energy a particle can impart to an electron, T_{max}, is given by

$$T_{max} = \frac{2m_e c^2\beta^2\gamma^2}{1 + 2\gamma m_e/M + \left(m_e/M\right)^2}. \tag{A.2}$$

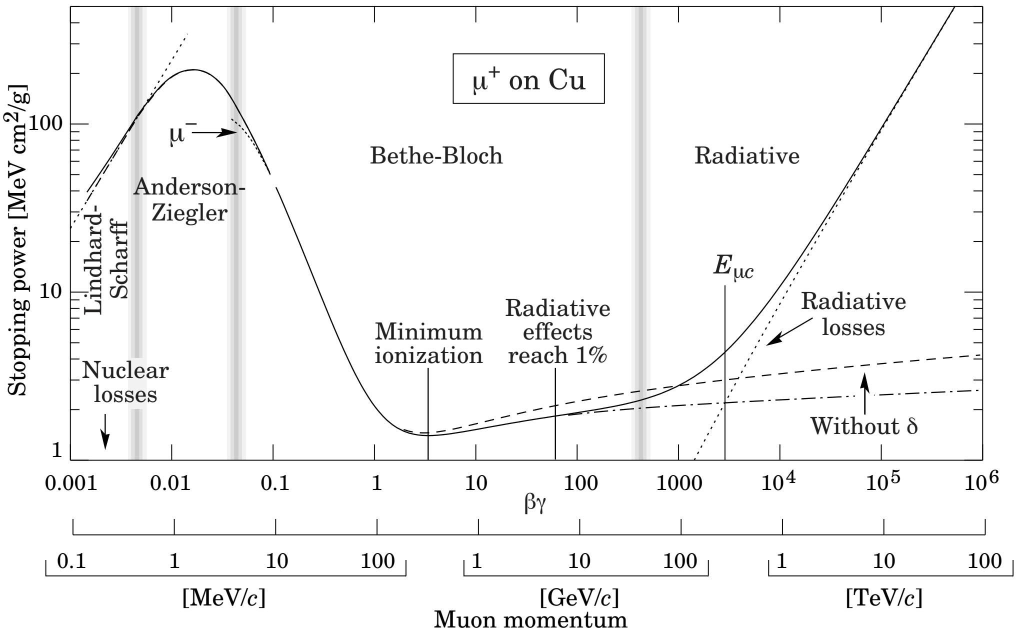

Figure A.1.: Stopping power of for positive muons in copper[5]

A semi-empirical expression for the mean excitation potential is

$$I = 16(eV) \times Z^{0.9}. \tag{A.3}$$

The density effect correction (when I is in eV) is given by

$$\delta\left(\beta\gamma\right) = 2\ln\left(28.816\frac{1}{I}\sqrt{\rho\frac{Z}{A}}\right) + 2\ln(\beta\gamma) - 1. \tag{A.4}$$

The ionisation energy loss rate is mass and energy dependent. As a result the rate of energy loss by ionisation can be used to distinguish between particles of different masses if a knowledge of the momentum of the particle is known. Due to high energies being dealt with at the LHC, this is only likely to be useful in the identification of extremely heavy exotic particles.

A.1.2. Radiation Length, X_0

Radiation length is a scaling variable for the probability of occurrence of bremsstrahlung, pair production and for the variance of the angle of multiple scattering. High energy electrons predominately loose energy through by bremsstrahlung, while high

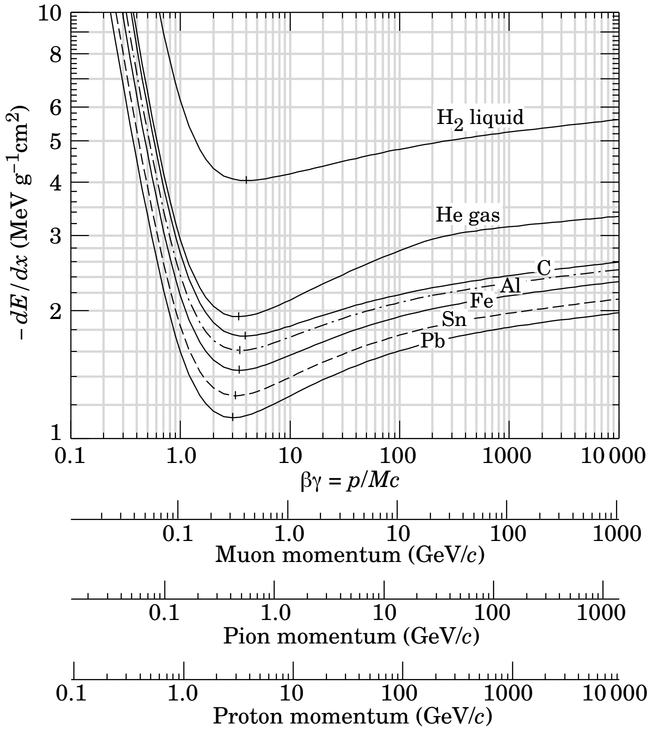

Figure A.2.: Mean energy loss due to ionisation[5]

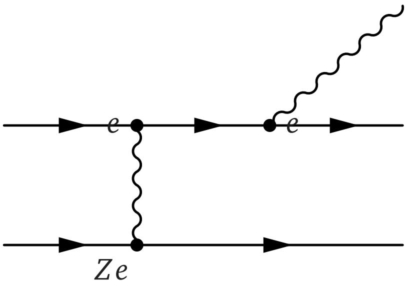

Figure A.3.: Bremsstrahlung Feynman diagram

energy photons by the production of e$^+$e$^-$ pairs. Radiation length is both the mean distance over which a high-energy electron loses all but $1/e$ of its energy by bremsstrahlung and 7/9 of the mean free path for pair production of a high-energy photon. For example $X_0(silicon) = 9.36\ cm$[5].

A.1.3. Bremsstrahlung

Bremsstrahlung is the emission of photons by charges particles accelerated by a field (see figure A.3). Bremsstrahlung, unlike ionisation, must be modeled stochastically as the fluctuation of the magnitude of the energy losses varies significantly when compared to the mean. The Bethe-Heitler probability density function[5, 129] provides a simple and relatively accurate model of the radiative energy losses

$$f(z) = \frac{(-\ln(z))^{c-1})}{\Gamma(c)}, \qquad \text{with} \qquad c = \frac{t}{\ln(2)},\ 0 < z < 1 \tag{A.5}$$

where z is the ratio of the energy of the electron after (E_f) and prior to bremsstrahlung (E_i), i.e. $z = E_f/E_i$. The amount of material traversed by the particle, t, is characterised as a fraction of the material's radiation length

$$t = \frac{x}{X_0}, \tag{A.6}$$

where x corresponds to the physical thickness of material traversed.

The Bethe-Heitler distribution is assumed to be independent of the energy of the incident electron and its dependance on material thickness. The Bethe-Heitler distribution provides a reasonable approximation of fraction of energy retained however the Geant4 [74, 75] simulation is much more accurate. The difference between Geant4 simulation and the Bethe-Heitler simulation can be seen in Figure A.4 with the largest discrepancy being seen at low z.

The emission probability is proportional to $1/m^2$ and has la inear dependance on the energy of incident particle once above a certain critical energy. E_c, the critical energy, as defined by Rossi[130] is the energy at which the ionization loss per radiation length is equal to the electron energy .i.e. the point at which the bremsstrahlung becomes the predominate energy loss mechanism.

At energies greater than $\sim 100\ GeV$, radiative energy losses become significant for muons and pions. In this case, the Bethe-Bloch equation is an inadequate description of energy loss. For muons and pions, the stochastic nature of bremsstrahlung is generally overlooked and, in the limit of $t \ll 1$, it is standard practice simply to add an additional term in Equation A.1 for radiative energy losses [5]

$$-\left.\frac{dE}{dx}\right|_{rad} = \frac{E_i}{X_0}\left(\frac{m_e}{M}\right)^2, \tag{A.7}$$

where E_i is again the initial energy of the charged particle.

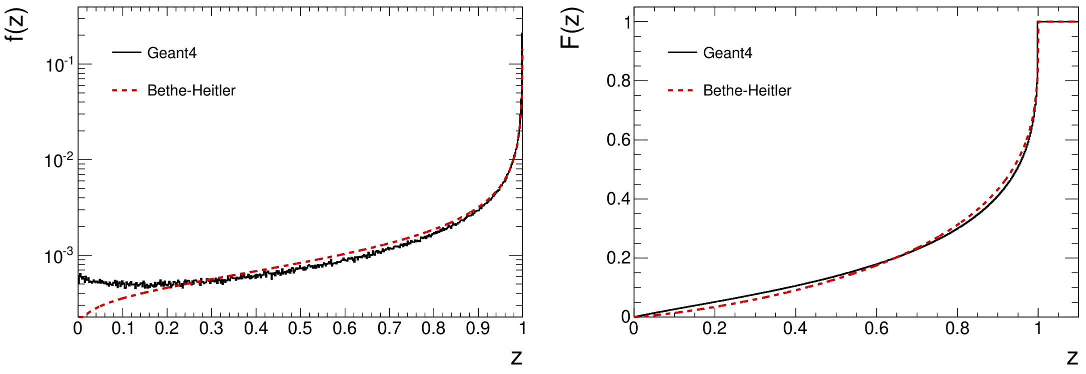

(a) PDF **(b)** CDF

Figure A.4.: The probability and cumulative distribution function of the fraction of energy retained for 10 GeV electrons passing through 0.2 X_0 of silicon. Geant4 simulation is compared to the Bethe-Heitler distribution.

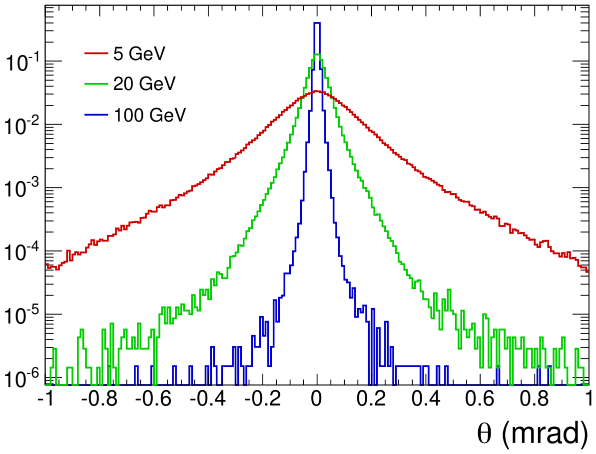

Figure A.5.: Bremsstrahlung angular distribution from Geant4 simulation of electrons passing through 0.1 X_0 of silicon

The angular distribution of the bremsstrahlung with respect to the original particles trajectory is virtually collinear. In the rest frame of the electron this is certainly not true but in the energy regime dealt with at ATLAS and the LHC it can be assumed that the photon is emitted in a collinear direction to that of the original charged lepton.

A.2. Multiple scattering

When an electrically charged particle passes through matter it is deflected off its original path by scattering off the electrons or nuclei of the matter. This process will occur on numerous occasions and is known as either Multiple Coulomb scattering or just multiple scattering. Multiple scattering is stochastic in nature and as such causes a random deviation of the trajectory. Under all but the most extreme circumstances it is sufficient to characterise the angular distribution of scattered particles as a Gaussian, distributed around zero, with a width

$$\sigma(\theta^{proj}) = \frac{13.6\ (MeV)}{\beta c p} q \sqrt{\frac{x}{X_0}} \left[1 + 0.038 \ln \left(\frac{x}{X_0} \right) \right], \tag{A.8}$$

where p is the initial momentum of the particle, q is the charge, x is the thickness of the material being traversed and X_0 is the radiation length of the material. [5, 130, 131].

This approximation covers the central 98% of the angular distribution. Multiple scattering at large angles results in significantly longer tails than produced by a Gaussian (see Figure A.6).

A description of how to treat multiple scattering in global least squares track fitting can be found in section 5.2

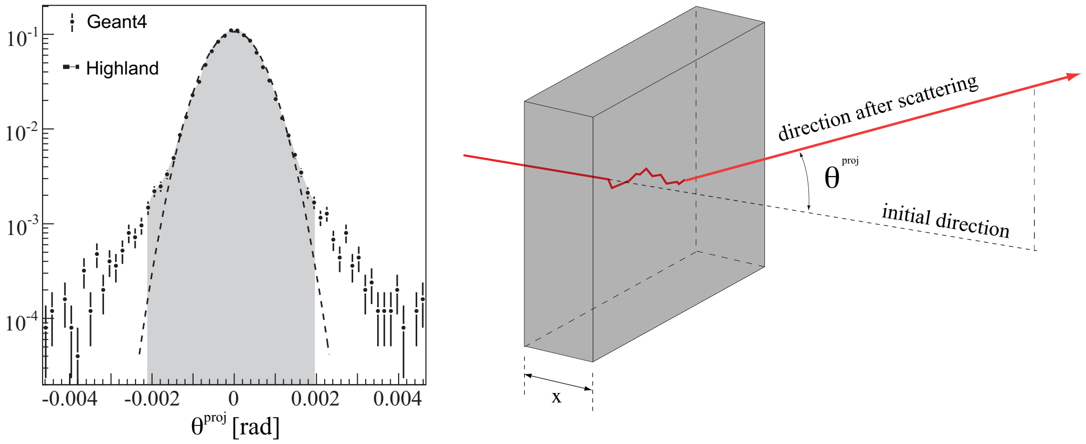

Figure A.6.: The projected scattering angle distribution θ^{proj} (left) of a muon with 5 GeV that traverses a silicon detector with a thickness t that corresponds to 1% of radiation length X_0 . The distribution has been created by Monte Carlo simulation of 25000 muon events using the Geant4 simulation toolkit. It shows the Gaussian distribution originating from the Highland formula (dashed). The shaded area represents a 98% core fraction of the Geant4 distribution. The illustration (right) shows the definition of the projected angle θ^{proj} for an example multiple scattering process [127]

B

APPENDIX

ALTERNATIVE METHOD TO OBTAIN ALIGNMENT PARAMETERS

An alternative way of extracting the alignment parameters from a track χ^2 minimisation is to replace the derivatives with respect to $\boldsymbol{\alpha}$[55] by

$$\frac{d}{d\mathbf{p}} = \frac{\partial}{\partial \boldsymbol{\alpha}} + \frac{d\mathbf{p}}{d\boldsymbol{\alpha}} \frac{\partial}{\partial \mathbf{p}}. \tag{B.1}$$

To obtain the derivative $d\mathbf{p}/d\boldsymbol{\alpha}$, it is assumed that once at a minimum the derivative of the track χ^2 with respect to $\mathbf{p}$ is taken and as such can be expressed as

$$\frac{d}{d\boldsymbol{\alpha}} \frac{\partial \chi^2}{\partial \mathbf{p}} = 0. \tag{B.2}$$

This leads to the final expression for the derivatives of the track parameters with respect to the alignment parameters

$$\frac{d\mathbf{p}}{d\boldsymbol{\alpha}} = -\frac{\partial^2 \chi^2}{\partial \boldsymbol{\alpha} \partial \mathbf{p}} \left(\frac{\partial^2 \chi^2}{\partial \mathbf{p}^2} \right)^{-1}. \tag{B.3}$$

To simplify the notation the following are defined:

$$A \equiv \frac{\partial r}{\partial \boldsymbol{\alpha}}, \qquad H \equiv \frac{\partial r}{\partial \mathbf{p}}. \tag{B.4}$$

A solution can now be obtained for $d\mathbf{p}/d\boldsymbol{\alpha}$

$$\frac{d}{d\boldsymbol{\alpha}} = \frac{\partial}{\partial \boldsymbol{\alpha}} - A^T V^{-1} H C \frac{\partial}{\partial \mathbf{p}}, \tag{B.5}$$

where C is the covariance matrix from the track fit

$$\frac{d\chi^2}{d\alpha} = 2A^T V^{-1}(V - HCH^T)V^{-1}r \tag{B.6}$$

$$\frac{d^2\chi^2}{d\alpha^2} = 2A^T V^{-1}(V - HCH^T)V^{-1}A. \tag{B.7}$$

Comparing these derivative to those of the single track fit one can see that there is an additional term is present (HCH^T). This term is the representation of the covariance of the track parameters in the measurement space. $R = V - HVH^T$ is the covariance matrix of the residuals.

The corrections to the alignment parameters, $\Delta\boldsymbol{\alpha}$, can be evaluated from the first and second derivatives for an initial alignment calibration $\boldsymbol{\alpha}_0$ and estimated track parameters $\mathbf{p}_0$. From a large sample of tracks we solve the equation B.8.

$$\frac{d^2\chi^2}{d\boldsymbol{\alpha}^2}\Delta\boldsymbol{\alpha} = -\frac{d\chi^2}{d\boldsymbol{\alpha}} \tag{B.8}$$

C

APPENDIX

NOTES ON THE CONVERGENCE OF THE NEWTON-RAPHSON ALGORITHM

The Newton-Raphson algorithm is a root finding algorithm. Assume there is a function $f(x)$ and take a Taylor series expansion of $f(x)$ around the point $x = x_0 + \epsilon$

$$f(x_0 + \epsilon) = f(x_0) + f^{'}(x_0)\epsilon + \frac{1}{2}f^{''}(x_0)\epsilon^2 + ... \tag{C.1}$$

If only the first order terms are kept, setting $f(x_0 + \epsilon) = 0$ and solving for $\epsilon = \epsilon_0$ gives

$$\epsilon_0 = -\frac{f(x_0)}{f^{'}(x_0)}, \tag{C.2}$$

which is just the first order correction to the roots position. The next correction is calculated by letting $x_1 = x_0 + \epsilon_0$ and calculating a new ϵ_1. The process can be repeated until it converges to a fixed point (which is precisely a root) using

$$x_{n+1} = x_n - \frac{f(x_n)}{f^{'}(x_n)} \tag{C.3}$$

for $n = 1, 2, 3, ...$ It is clear that if the function is linear the precise solution will be obtained in one iteration.

To gain a better understanding on the convergence of the Newton Raphson method, assume that after iteration $k+1$, x converges toward x^* with $f^{'}(x^*)! = 0$, and define the error after the k^{th} step by

$$x_k = x^* + \epsilon_k. \tag{C.4}$$

Expanding $f(x_k)$ about x^* gives

$$\begin{aligned} f(x_k) &= f(x^*) + f^{'}(x^*)\epsilon_k + 1/2 f^{''}(x^*)\epsilon_k^2 + ... \\ &= f^{'}(x^*)\epsilon_k + \frac{1}{2} f^{''}(x^*)\epsilon_k^2 + ... \qquad \text{(C.5)} \\ f^{'}(x_k) &= f^{'}(x^*) + f^{''}(x^*)\epsilon_k + ... \qquad \text{(C.6)} \end{aligned}$$

But

$$\begin{aligned} \epsilon_{k+1} &= \epsilon_k + (x_{k+1} - x_k) \\ &= \epsilon_k - \frac{f(x_k)}{f^{'}(x_k)} \\ &\approx \epsilon_k - \frac{f^{'}(x^*)\epsilon_k + \frac{1}{2} f^{''}(x^*)\epsilon_k^2}{f^{'}(x^*) + f^{''}(x^*)\epsilon_k} \end{aligned} \tag{C.7}$$

Taking the second-order expansion leads to

$$\epsilon_{k+1} \approx \frac{f^{''}(x^*)}{2 f^{'}(x^*)} \epsilon_k^2. \tag{C.8}$$

Showing that when the method converges it will do so quadratically.

D

APPENDIX

SILICON MISALIGNMENTS FOR THE CSC EXERCISE

This appendic presents the misalignments used during the CSC exercise of the Silicon Tracker. All misalignment numbers that will be shown in the following have been taken from[125].

D.1. Silicon: Level 1 Transforms

In the following table the misalignments to be applied to the Pixel and SCT subdetectors as level 1 transforms are displayed. The reference frame of these transformations is the global ATLAS coordinate system, where x is horizontal, y vertical and z along the beamline, and R_x, R_y and R_z are rotations around each axis respectively. In Table D.1, displacements are given in mm and rotations in $mrads$. The Pixel detector will be treated as a single unit, without relative misalignments between the barrel and the end-caps due to the detector being installed as a single entity.

Level 1 Transforms						
System	T_x	T_y	T_z	R_x	R_y	R_z
Pixel detector	+0.60	+1.05	+1.15	-0.10	+0.25	+0.65
SCT Barrel	+0.70	+1.20	+1.30	+0.10	+0.05	+0.80
SCT End-cap A	+2.10	-0.80	+1.80	-0.25	0.00	-0.50
SCT End-cap C	-1.90	+2.00	-3.10	-0.10	+0.05	+0.40

Table D.1.: Silicon: Level 1 displacements

D.2. Silicon: Level 2 Transforms

In the Table D.2 the misalignments applied to the Pixel and SCT layers/disks at Level 2 are shown. The coordinate system is the same as in the Level 1 transforms and again the global displacements are given in *mm* and rotations in *mrads*.

D.3. Silicon: Level 3 Transforms

In the Table D.3 the misalignments to be applied for the Pixel and SCT modules as Level 3 transforms are displayed. The coordinate x' is along the principle measuring direction of the module(i.e, along short-pixels for Pixel modules, across strips for SCT modules), y' along the perpendicular direction to x' within the module plane (i.e, along long-pixels for Pixel modules, along strips for SCT modules), and z' is defined in the direction out-of the module plane. The three angles, $R_{x'}$, $R_{y'}$ and $R_{z'}$ correspond to rotations around the three local axis, x', y' and z' respectively. Displacements are given in *mm* and rotations in radians. These misalignments must be generated within flat distributions of width defined by the numbers quoted in the Table D.3.

Level 2 Transforms								
System	layer	x	y	z	α	β	γ
Pixel Barrel	0	+0.020	+0.010	0.0	0.0	0.0	+0.6
	1	-0.030	+0.030	0.0	0.0	0.0	+0.5
	2	-0.020	+0.030	0.0	0.0	0.0	+0.4
Pixel End-cap A	1	-0.224	0.030	0.012	1.39	0.00	-1.39
	2	0.443	-0.358	-0.037	-2.27	0.00	2.27
	3	0.271	-0.236	-0.027	-2.38	0.00	2.38
Pixel End-cap C	1	-0.560	-0.031	0.200	-1.59	0.00	1.59
	2	0.366	-0.221	-0.113	1.41	0.00	-1.41
	3	0.111	-0.441	0.052	0.28	0.00	-0.28
SCT Barrel	0	0.0	0.0	0.0	0.0	0.0	-1.0
	1	+0.050	+0.040	0.0	0.0	0.0	+0.9
	2	+0.070	+0.080	0.0	0.0	0.0	+0.8
	3	+0.100	+0.090	0.0	0.0	0.0	+0.7
SCT End-cap A	1	+0.050	+0.040	0.0	0.0	0.0	-0.1
	2	+0.010	-0.080	0.0	0.0	0.0	0.0
	3	-0.050	+0.020	0.0	0.0	0.0	+0.1
	4	-0.080	+0.060	0.0	0.0	0.0	+0.2
	5	+0.040	+0.040	0.0	0.0	0.0	+0.3
	6	-0.050	+0.030	0.0	0.0	0.0	+0.4
	7	-0.030	-0.020	0.0	0.0	0.0	+0.5
	8	+0.060	+0.030	0.0	0.0	0.0	+0.6
	9	+0.080	-0.050	0.0	0.0	0.0	+0.7
SCT End-cap C	1	+0.050	-0.050	0.0	0.0	0.0	+0.8
	2	0.0	+0.080	0.0	0.0	0.0	0.0
	3	+0.020	+0.010	0.0	0.0	0.0	+0.1
	4	+0.040	-0.080	0.0	0.0	0.0	-0.8
	5	0.0	+0.030	0.0	0.0	0.0	+0.3
	6	+0.010	+0.030	0.0	0.0	0.0	-0.4
	7	0.0	-0.060	0.0	0.0	0.0	+0.4
	8	+0.030	+0.030	0.0	0.0	0.0	+0.6
	9	+0.040	+0.050	0.0	0.0	0.0	-0.7

Table D.2.: Silicon: Level 2 displacements

Level 3 Transforms						
System	T'_x	T'_y	T'_z	$R_{x'}$	$R_{y'}$	$R_{z'}$
Pixel Barrel modules	0.030	0.030	0.050	0.001	0.001	0.001
Pixel End-cap modules	0.030	0.030	0.050	0.001	0.001	0.001
SCT Barrel modules	0.150	0.150	0.150	0.001	0.001	0.001
SCT End-cap modules	0.100	0.100	0.150	0.001	0.001	0.001

Table D.3.: Silicon: Level 3 displacements

E

APPENDIX

PARAMETERISATION OF THE CALORIMETER PERFORMANCE

A requirement of using the calorimeter as a tracking detector is to know the quality of the measured quantities. The quality of measurement will vary with energy and position and as such need to be parameterised to ensure their usefulness.

E.1. Angular Resolution

The angular resolution of calorimeter varies a function inversely proportional to the energy deposited in the calorimeter. The constant term of the angular resolution and is variation as a function as absolute value of η is shown in Table E.1 while the energy dependant term is shown in Table E.2.

η	c (mrad)
0.30	0.191492
0.60	$0.09350 + 0.392766\,\eta$
0.80	0.327201
1.05	0.141755
1.35	$-1.07475 + 1.15372\,\eta$
1.55	$-15.2133 + 11.2163\,\eta$
1.85	$1.28452 - 0.53016\,\eta$
2.30	$-0.66562 + 0.52136\,\eta$
2.50	0.327754

Table E.1.: Parameterisation of the azimuthal angular resolution of the calorimeter (constant term)

η	a (mrad GeV)
0.65	$28.5262 + 9.85529\,\eta$
1.05	$-69.0774 + 166.424\,\eta$
1.25	$76.9113 + 14.9434\,\eta$
1.55	$-407.594 + 393.218\,\eta$
1.95	$415.602 - 172.824\,\eta$
2.05	-84.0844
2.40	$187.563 - 47.2463\,\eta$
2.50	69.3652

Table E.2.: Parameterisation of the azimuthal angular resolution of the calorimeter (energy dependant term)

E.2. Depth

The apparent depth cluster within the calorimeter varies as inversely proportional to the square root of the energy deposited in the calorimeter cluster. The constant term and energy dependant term of the depth vary a function as absolute value of η and is shown in Table E.3. it should be noted that the depth of the cluster only work in the barrel region of the calorimeter. In the end-caps very little improvement of the cluster resolution can be seen so the depth of the calorimeter cluster is to be taken to be the surface of the second sampling layer.

η	b (mm GeV$^{1/2}$)	c (mm)
0.65	$190.029 + 44.2047\,\eta$	$1669.29 - 12.6291\,\eta$
1.05	$-826.993 + 1771.17\,\eta$	$1848.43 - 333.571\,\eta$
1.45	$-3172.17 + 3629.60\,\eta$	$1918.48 - 303.562\,\eta$

Table E.3.: Parameterisation of the apparent cluster depth

E.3. Energy Resolution

The energy resolution of calorimeter varies a function proportional to the square root of the energy deposited in the calorimeter cluster. The constant term and energy dependant term of the angular resolution and is variation as a function as absolute value of η is shown in Table E.4.

η	b (MeV$^{3/2}$)	c (MeV)
0.05	9.60832	0.764440
0.15	9.22633	0.778579
0.25	9.36220	0.902059
0.35	9.51660	0.794211
0.45	9.84234	0.772288
0.55	10.8710	0.748239
0.65	12.3186	0.504367
0.75	16.9488	0.309400
0.85	18.2509	0.222931
0.95	19.3125	0.000420
1.05	22.0666	0.005880
1.15	22.4085	0.151410
1.25	23.5868	0.001328
1.35	26.4539	0.007946
1.45	27.6533	0.006253
1.55	35.2674	0.517023
1.65	37.6763	0.002220
1.75	23.6935	0.687641
1.85	20.9790	0.625471
1.95	17.7002	0.627151
2.05	18.0877	0.713889
2.15	18.0476	0.690940
2.25	15.9020	0.709736
2.35	14.9494	0.713798
2.45	18.6565	1.217530

Table E.4.: Parameterisation of the energy resolution

F

APPENDIX

NON-LINEAR PROBLEM MINIMISATION

The track model described in Section 8.3 has features that makes it intrinsically non-linear. The fit of a helix in a uniform magnetic field is a non-linear problem, however it can be linearised by a number of transformations, e.g. a Riemann transform[132]. The fact that the magnetic field is not completely homogenous does affect this linearisation as the path of the particle in the bending plane will no longer be perfectly circular, but as was shown at high momentum the track model is approximately linear so this is not overly problematic.

The difficulty lies in the CaloBrem track model, which is essentially two tracks that sharing a common vertex, where the position of the vertex is not known and can move. In general when fitting a vertex of two tracks you fit the two tracks, the tracks are first fitted individually. These results are then used to perform a fit of the vertex.

However unlike a standard vertex fit the movement of hypothesised vertex position can shift hits from one track to another. This in turn will change the tracks fits and hence require the vertex fit to be performed again. In order to find the best fit result, it would be necessary to fit all possible divisions of the hits between the two tracks. Then determine which of those fits is the best, possibly using a χ^2 as a measure of the final fit quality. However this process can be computationally time consuming as there can be > 40 hits per track.

Another way of dealing with such a problem is to treat it as a multivariate non-linear problem and find the most likely solution. This is known as function optimisation and there are a number of programs that can be employed for this process based upon similar priciples. What follows is summary of [133] which describes the basic principles of iterative function optimisation.

To highlight these principles consider the function $F(\mathbf{x})$, where the aim of the function optimisation is to find the values of the variables $\mathbf{x}$ for which the function $F(\mathbf{x})$ obtains its smallest value. In this case the function to be minimised F is the χ^2 of the bremsstrahlung track. The minimum of $F(\mathbf{x})$ is not known analytically but the function $F(\mathbf{x})$ can be evaluated for any physical values of $\mathbf{x}$. Hence the function $F(\mathbf{x})$ is repeatedly evaluated at different points $\mathbf{x}$ until its minimum value is attained.

To reduce computation time it is desirable to find the solution in the fewest number of function calls. Hence the properties of the function need to be investigated to help reduce the number of function calls. The function $F(\mathbf{x})$ will obtain its smallest value at a point where either:

- all derivatives $\partial F/\partial \mathbf{x} = 0$, or
- some derivative $\partial F/\partial \mathbf{x}$ does not exist , or
- the point x is on the boundary of the allowed region.

As there may be many of these points within the range where the function is well defined it may take some time to find the global minimum. To simplify this problem, we will no longer attempt to find the global minimum but instead find just the local minimum. A local minimum can be defined as a point $\mathbf{x}_0$, where for all points $\mathbf{x}$ in some neighbourhood around $\mathbf{x}_0$, result in $F(\mathbf{x}) > F(\mathbf{x}_0)$. So by varying $\mathbf{x}$ in small steps in a direction which causes F to decrease, and continuing until F increases in all allowed directions from some point $\mathbf{x}_0$, we can find a minimum. However, this does require that an initial guess of the solution is in reasonable agrement to the global minimum.

Although this argument suggests that a solution can be found, it does not indicate how to find the solution. A Taylor's series expansion for F about some point $\mathbf{x}_1$ provides the information required to find the minimum

$$F(\mathbf{x}) = F(\mathbf{x}_1) + \mathbf{g}^T(\mathbf{x} - \mathbf{x}_1) + 1/2(\mathbf{x} - \mathbf{x}_1)\mathbf{V}(\mathbf{x} - \mathbf{x}_1)^T + \cdots ,$$

where $\mathbf{g}$ is the gradient vector $g_i = \partial F / \partial x_i$ and the matrix $\mathbf{V}$ is defined by $V_{ij} = \partial^2 F / \partial x_i \partial x_j$ all evaluated at $\mathbf{x}_1$.

As with any Taylor series expansion the higher order terms only become important when $(\mathbf{x} - \mathbf{x}_1)$ becomes large. As such, a predication based on the lower order terms should be correct if the step size is small. The first term of the series is constant and provides no information about the minimum of the function. The second term is proportional to the gradient $\mathbf{g}$, and provides information about which direction the function is decreasing fastest. This linear term $\mathbf{g} \rightarrow 0$ when approaching a minimum, so an additional term is required. This third term, which is quadratic, describes parabolic behaviour and is the lowest term to predict a minimum. Also $\mathbf{V}$ can be expected to be constant over small regions as it would be constant if the higher order term were zero[133].

`MINUIT`[134] is the standard in minimisation packages used by High Energy Physicists and was chosen as the minimisation program for this problem. The principal algorithm, called `MIGRAD`, is a variable metric method. It exploits the idea that the computation of the second derivative is needed to move to the function minimum, and the matrix need not be computed accurately during the initial steps as it would be expected to be changing significantly. Instead the second derivative can be iteratively improved, so that by the time the method gets near the actual minimum, the matrix is accurate and rapidly converges.

In the future other minimisation techniques may be employed, for example `FUMILI`[135], to see if there are any performance improvements.

BIBLIOGRAPHY

[1] ATLAS Collaboration. The ATLAS Experiment at the CERN Large Hadron Collider. *JINST*, 3:S08003, 2008.

[2] L. Evans, and P. Bryant, editors. LHC Machine. *JINST*, 3:S08001, 2008.

[3] A. Morley *et al.*. Alignment of the inner detector using misaligned csc data. Technical Report ATL-COM-INDET-2008-014, CERN, Geneva, Sep 2008.

[4] A. Einstein. The foundation of the general theory of relativity. *Annalen Phys.*, 49:769–822, 1916.

[5] W-M Yao *et al.*. Review of Particle Physics. *J. Phys. G*, 33, 2006. URL `http://pdg.lbl.gov`.

[6] S. L. Glashow. Partial Symmetries of Weak Interactions. *Nucl. Phys.*, 22:579–588, 1961.

[7] S. Weinberg. A Model of Leptons. *Phys. Rev. Lett.*, 19:1264–1266, 1967.

[8] A. Salam. Gauge Unification of Fundamental Forces. *Rev. Mod. Phys.*, 52: 525–538, 1980.

[9] D. Perkins. *Introduction to High Energy Physics*. Cambridge University Press, 4th edition, 2000.

[10] P. W. Higgs. Broken Symmetries, Massless Particles and Gauge Fields. *Phys. Lett.*, 12:132–133, 1964.

[11] P. W. Higgs. Broken Symmetries and the Masses of Gauge Bosons. *Phys. Rev. Lett.*, 13:508–509, 1964.

[12] G. Arnison *et al.*. Experimental observation of isolated large transverse energy electrons with associated missing energy at. *Physics Letters B*, 122(1):103–116, February 1983. ISSN 0370-2693.

[13] G. Arnison *et al.*. Experimental observation of lepton pairs of invariant mass around 95 GeV/c2 at the CERN SPS collider. *Physics Letters B*, 126(5):398–

410, July 1983. ISSN 0370-2693.

[14] C. Kolda and H. Murayama. The higgs mass and new physics scales in the minimal standard model. *Journal of High Energy Physics*, 2000(07):035, 2000. ISSN 1029-8479.

[15] ALEPH Collaboration, C. D. F. Collaboration, D0 Collaboration, DELPHI Collaboration, L3 Collaboration, OPAL Collaboration, S. L. D. Collaboration, LEP Electroweak Working Group, Tevatron Electroweak Working Group, and SLD electroweak heavy flavour groups. Precision electroweak measurements and constraints on the standard model. *0911.2604*, November 2009.

[16] R. Barate *et al.*. Search for the standard model Higgs boson at LEP. *Phys. Lett.*, B565:61–75, 2003. arXiv:hep-ex/0306033.

[17] The CDF Collaboration, the D0 Collaboration, the Tevatron New Physics, and Higgs Working Group. Combined CDF and d0 upper limits on standard model Higgs-Boson production with 2.1 - 5.4 fb-1 of data. *0911.3930*, November 2009.

[18] M. Gell-Mann. A Schematic Model of Baryons and Mesons. *Phys. Lett.*, 8: 214–215, 1964.

[19] M. Kobayashi and T. Maskawa. CP Violation in the Renormalizable Theory of Weak Interaction. *Prog. Theor. Phys.*, 49:652–657, 1973.

[20] N. Cabibbo. Unitary Symmetry and Leptonic Decays. *Phys. Rev. Lett.*, 10:531–533, 1963.

[21] D. J. Gross and F. Wilczek. Asymptotically Free Gauge Theories. 1. *Phys. Rev.*, D8:3633–3652, 1973.

[22] H. D. Politzer. Reliable perturbative results for strong interactions? *Phys. Rev. Lett.*, 30:1346–1349, 1973.

[23] P. Langacker. Structure of the standard model. *hep-ph/0304186*, April 2003. Precision Tests of the Standard Electroweak Model, ed. P. Langacker (World, Singapore, 1995), p15.

[24] S. Haywood. Offline Alignment And Calibration of the Inner Detector. Technical report, CERN, 1999. ATL-INDET-2000-005.

[25] J. D. Bjorken and E. A. Paschos. Inelastic electron-proton and γ-proton scattering and the structure of the nucleon. *Phys. Rev.*, 185(5):1975–1982, Sep 1969.

[26] J.M. Campbell, J.W. Huston, and W.J. Stirling. Hard interactions of quarks and gluons: A primer for LHC physics. *Rept. Prog. Phys.*, 70:89, 2007. arXiv:hep-ph/0611148.

[27] ATLAS Collaboration. *Expected Performance of the ATLAS Experiment, Detector, Trigger and Physics ("CSC book")*. CERN, Geneva, 2008. CERN-OPEN-2008-020.

[28] S. Dawson. Introduction to electroweak symmetry breaking. *hep-ph/9901280*, 1999. URL `http://arxiv.org/abs/hep-ph/9901280`.

[29] P. Langacker and N. Polonsky. Uncertainties in coupling constant unification. *Phys. Rev. D*, 47(9):4028–4045, May 1993.

[30] A. Djouadi. The anatomy of electroweak symmetry breaking: Tome i: The higgs boson in the standard model. *Physics Reports*, 457(1-4):1 – 216, 2008. ISSN 0370-1573.

[31] K. G. Begeman, A. H. Broeils, and R. H. Sanders. Extended rotation curves of spiral galaxies: Dark haloes and modified dynamics. *Mon. Not. Roy. Astron. Soc.*, 249:523, 1991.

[32] D. Clowe, M. Bradac, A. H. Gonzalez, M. Markevitch, S. W. Randall, C. Jones, and D. Zaritsky. A direct empirical proof of the existence of dark matter. *The Astrophysical Journal Letters*, 648(2):L109–L113, 2006.

[33] J. Dunkley *et al.* . Five-Year Wilkinson Microwave Anisotropy Probe (WMAP) Observations: Likelihoods and Parameters from the WMAP data. *Astrophys. J. Suppl.*, 180:306–329, 2009. arXiv:astro-ph/0803.0586.

[34] A. D. Sakharov. Violation of CP Invariance, C Asymmetry, and Baryon Asymmetry of the Universe. *Pisma Zh. Eksp. Teor. Fiz.*, 5:32–35, 1967.

[35] J. Ellis. Physics beyond the standard model. *Nuclear Physics A*, 827(1-4):187c – 198c, 2009. ISSN 0375-9474. PANIC08 - Proceedings of the 18th Particles and Nuclei International Conference.

[36] J.R. Ellis, K.A. Olive, and Y. Santoso. Constraining supersymmetry. *New J. Phys.*, 4:32, 2002. arXiv:hep-ph/0202110.

[37] G. Jungman, M. Kamionkowski, and K. Griest. Supersymmetric dark matter. *Phys. Rept.*, 267:195–373, 1996. arXiv:hep-ph/9506380.

[38] M. B. Green, J. H. Schwarz, and E. Witten. *Superstring Theory: Volume 1, Introduction*. Cambridge University Press, July 1988. ISBN 0521357527.

[39] L. Randall and R. Sundrum. Large mass hierarchy from a small extra dimension. *Phys. Rev. Lett.*, 83(17):3370–3373, Oct 1999.

[40] N. Arkani-Hamed, S. Dimopoulos, and G. Dvali. The hierarchy problem and new dimensions at a millimeter. *Physics Letters B*, 429(3-4):263 – 272, 1998. ISSN 0370-2693.

[41] O. S. Brüning, P. Collier, P. Lebrun, S. Myers, R. Ostojic, J. Poole, and P. Proud-

lock, editors. *LHC Design Report*, volume 1 : The LHC Main Ring. CERN, Geneva, 2004. ISBN 9290832240. CERN-2004-003-V-1.

[42] O. S. Brüning, P. Collier, P. Lebrun, S. Myers, R. Ostojic, J. Poole, and P. Proudlock, editors. *LHC Design Report*, volume 2 : The LHC Infrastructure and General Services. CERN, Geneva, 2004. CERN-2004-003-V-2.

[43] M. Benedikt, P. Collier, V. Mertens, J. Poole, and K. Schindl, editors. *LHC Design Report*, volume 3 : The LHC Injector Chain. CERN, Geneva, 2004. CERN-2004-003-V-3.

[44] CMS Collaboration. The CMS experiment at the CERN LHC. *JINST*, 3:S08004, 2008.

[45] LHCb Collaboration. The LHCb Detector at the LHC. *JINST*, 3:S08005, 2008.

[46] ALICE Collaboration. The ALICE experiment at the CERN LHC. *JINST*, 3: S08002, 2008.

[47] LHCf Collaboration . The LHCf detector at the CERN Large Hadron Collider. *JINST*, 3:S08006, 2008.

[48] TOTEM Collaboration. The TOTEM experiment at the CERN Large Hadron Collider. *JINST*, 3:S08007, 2008.

[49] ATLAS Collaboration. *ATLAS Detector and Physics Performance: Technical Design Report*, volume 2. CERN, Geneva, 1999. CERN-TDR-015, CERN-LHCC-99-15.

[50] C. Buttar A. Moraes and I. Dawson. Prediction for minimum bias and the underlying event at LHC energies. *Eur. Phys. J.*, C50:435–466, 2007.

[51] ATLAS Collaboration. *ATLAS Detector and Physics Performance: Technical Design Report*, volume 1 of *Technical Design Report ATLAS*. CERN, Geneva, 1999. CERN-TDR-014, CERN-LHCC-99-14.

[52] InDetGeometryFrames twiki. `https://twiki.cern.ch/twiki/bin/view/Atlas/InDetGe` 2009.

[53] S. Haywood. Local coordinate frames for the alignment of silicon detectors. Technical Report ATL-INDET-2004-001, CERN, Geneva, Jan 2004.

[54] R. Hawkings. Coordinate frames for offline reconstruction. Technical Report ATL-COM-SOFT-2006-019, CERN, Geneva, Dec 2006.

[55] A. Bocci and W. Hulsbergen. Trt alignment for sr1 cosmics and beyond. Technical Report ATL-INDET-PUB-2007-009. ATL-COM-INDET-2007-011. CERN-ATL-COM-INDET-2007-011, CERN, Geneva, Jun 2007.

[56] ATLAS Collaboration. *ATLAS Magnet System Technical Design Report*. CERN, 1997. CERN-LHCC-97-18.

[57] ATLAS Collaboration. *ATLAS Barrel Toroid Technical Design Report*. CERN, 1997. CERN-LHCC-97-19.

[58] ATLAS Collaboration. *ATLAS End-Cap Toroids Technical Design Report*. CERN, 1997. CERN-LHCC-97-20.

[59] ATLAS Collaboration. *ATLAS Central Solenoid Technical Design Report*. CERN, 1997. CERN-LHCC-97-21.

[60] ATLAS Collaboration. *ATLAS Inner Detector Technical Design Report*, volume 1. CERN, 1997. CERN-LHCC-97-16.

[61] ATLAS Collaboration. *ATLAS Inner Detector Technical Design Report*, volume 2. CERN, 1997. CERN-LHCC-97-17.

[62] ATLAS Collaboration. *ATLAS Pixel Detector Technical Design Report*. CERN, 1998. CERN-LHCC-98-13.

[63] G. Aad *et al.*. ATLAS Pixel Detector Electronics and Sensors. *JINST*, 3:P07007, 2008.

[64] A. *et al.*Ahmad. The Silicon microstrip sensors of the ATLAS semiconductor tracker. *Nucl. Instrum. Meth.*, A578:98–118, 2007.

[65] E. Abat *et al.*. The ATLAS Transition Radiation Tracker (TRT) proportional drift tube: Design and performance. *JINST*, 3:P02013, 2008.

[66] ATLAS Collaboration. *ATLAS Liquid Argon Calorimeter Technical Design Report*. CERN, 1996. CERN-LHCC-96-41.

[67] ATLAS Collaboration. *ATLAS Tile Calorimeter Technical Design Report*. CERN, 1996. CERN-LHCC-96-42.

[68] ATLAS Collaboration. *ATLAS Calorimeter Performance Technical Design Report*. CERN, 1996. CERN-LHCC-96-40.

[69] ATLAS Collaboration. *ATLAS Muon Spectrometer Technical Design Report*. CERN, 1997. CERN-LHCC-97-22.

[70] ATLAS Collaboration. *ATLAS First-Level Trigger Technical Design Report*. CERN, 1998. CERN-LHCC-98-14.

[71] ATLAS Collaboration. *ATLAS High-Level Trigger, Data Aquisition and Controls Technical Design Report*. CERN, 2003. CERN-LHCC-2003-022.

[72] Athena: The ATLAS Common Framework , 2004. Developer Guide.

[73] Gaudi: Data Processing Applications Framework, 2001. Developer Guide.

[74] S. Agostinelli *et al.*. G4 – a simulation toolkit. *Nuclear Instruments and Methods in Physics Research Section A: Accelerators, Spectrometers, Detectors and Associ-*

ated Equipment, 506(3):250 – 303, 2003. ISSN 0168-9002.

[75] J. Allison *et al.*. Geant4 developments and applications. *Nuclear Science, IEEE Transactions on*, 53(1):270–278, 2006. ISSN 0018-9499.

[76] T. Sjöstrand, S. Mrenna, and P. Skands. Pythia 6.4 Physics and Manual. Technical report, Fermilab, 2006.

[77] T. Cornelissen, M. Elsing, S. Fleischmann, W. Liebig, E. Moyse, and A. Salzburger. Concepts, design and implementation of the atlas new tracking (newt). Technical Report ATL-SOFT-PUB-2007-007. ATL-COM-SOFT-2007-002, CERN, Geneva, Mar 2007.

[78] R. Clifft and A. Poppleton. IPATREC: Inner detector pattern-recognition and track-fitting. Technical Report ATL-SOFT-94-009. ATO-PN-9, CERN, Geneva, Jun 1994.

[79] I. Gavrilenko. Description of global pattern recognition program (xkalman). Technical Report ATL-INDET-97-165. ATL-I-PN-165, CERN, Geneva, Apr 1997.

[80] J. Jackson. *Classical Electrodynamics*. John Wiley and Sons, 1998.

[81] E-J Buis, R J Dankers, S Haywood, and A Reichold. Parameterisation of the inner detector performance. Technical Report ATL-INDET-97-195. ATL-I-PN-195, CERN, Geneva, Dec 1997.

[82] F. Akesson *et al.*. ATLAS Tracking Event Data Model. Technical report, CERN, 2006. ATL-SOFT-PUB-2006-004.

[83] R. L. Plackett. Studies in the history of probability and statistics. XXIX: the discovery of the method of least squares. *Biometrika*, 59(2):239–251, August 1972.

[84] Maurice G Kendall and Alan Stuart. *The Advanced Theory of Statistics*. C. Griffin, London, 2nd edition edition, 1963. ISBN 0852640110. LCCN 519.5.

[85] R. Frühwirth. Application of kalman filtering to track and vertex fitting. *Nuclear Inst. and Methods in Physics Research, A*, 262(2-3):444–450, 1987.

[86] R. Frühwirth, M. Regler, R. Bock, H. Grote, and D. Notz. *Data Analysis Techniques for High-Energy Physics*. Cambridge University Press, 2nd edition, 2001.

[87] G. Kitagawa. Non-Gaussian Seasonal Adjustment. *Comp. and Math. Appl.*, 19: 503–514, 1989.

[88] R. Frühwirth. Track Fitting with non-Gaussian noise. *Comp. Phys. Comm*, 100: 1–16, 1997.

[89] R. Frühwirth, W. Adam, A. Strandlie, and T. Todorov. Reconstruction of electrons with the Gaussian-Sum Filter in the CMS Tracker at the LHC. CMS note

2005/001, 2005.

[90] T. M. Atkinson. *Electron Reconstruction with the ATLAS Inner Detector*. PhD thesis, The University of Melbourne, 2006.

[91] F. Heinemann. *Robust Track Based Alignment of the ATLAS Silicon Detectors and Assessing Parton Distribution Uncertainties in Drell-Yan Processes*. PhD thesis, University of Oxford, 2007.

[92] O. Brandt *et al.*. Extension of the Track-Based Robust Alignment Algorithm for the ATLAS Silicon Tracker. Technical Report ATL-COM-INDET-2009-041, CERN, 2009.

[93] J. Alison *et al.*. Inner detector alignment within the atlas full dress rehearsal. Technical Report To be published, CERN, 2009.

[94] A. Ahmad *et al.*. Alignment of the pixel and sct modules for the 2004 atlas combined test beam. *J. Instrum.*, 3(arXiv:0805.3984):P09004. 22 p, May 2008.

[95] A. Abdesselam *et al.*. The data acquisition and calibration system for the atlas semiconductor tracker. Technical Report ATL-INDET-PUB-2007-012. ATL-COM-INDET-2007-015. CERN-ATL-COM-INDET-2007-015, CERN, 2007.

[96] ATLAS Collaboration. Alignment of the atlas inner detector using cosmic tracks. Technical Report To be published, CERN, 2009.

[97] R. Härtel. Iterative local χ^2 alignment approach for the ATLAS SCT detector. Master's thesis, MPI Munich MPP-2005-174, 2005.

[98] T. Göttfert. Iterative local χ^2 alignment algorithm for the ATLAS Pixel detector. Master's thesis, University Würzburg and MPI Munich MPP-2006-118, 2006.

[99] V. Blobel. A program description for millepede and the code is available via: http://www.desy.de/ blobel.

[100] V. Blobel and C. Kleinwort. A new method for the high-precision alignment of track detectors. Technical report, DESY, 2002.

[101] P. Schleper, G. Steinbrueck, and M. Stoye. Software alignment of the CMS tracker using MILLEPEDE II. Technical report, CERN, 2006. CMS-NOTE-2006-011.

[102] R. McNulty, T. Shears, and A. Skiba. A procedure for the software alignment of the CDF silicon ystem. Technical report, Fermilab, 2001. CDF/DOC/TRACKING/GROUP/5700.

[103] S. Viret, C. Parkes, and D. Petrie. Lhcb velo software alignment, part i : the alignment of the velo modules in their half boxes. Technical report, CERN, 2005. CERN-LHCb-2005-101.

[104] P. Bruckman, A. Hicheur, and S. J. Haywood. Global χ^2 approach to the alignment of the atlas silicon tracking detectors. Technical Report ATL-INDET-PUB-2005-002. ATL-COM-INDET-2005-004. CERN-ATL-INDET-PUB-2005-002, CERN, Geneva, 2005.

[105] T. Cornelissen. CTBTracking: track reconstruction for the testbeam and cosmics. *ATL-INDET-INT-2006-001. ATL-COM-INDET-2006-003*, 2006.

[106] T. Cornelissen. *Track fitting in the ATLAS Experiment*. PhD thesis, Nationaal Instituut voor Kernfysica en Hoge-Energiefysica (NIKHEF), 2006.

[107] E. Anderson *et al.*. *LAPACK Users' Guide*. Society for Industrial and Applied Mathematics, Philadelphia, PA, third edition, 1999. ISBN 0-89871-447-8 (paperback).

[108] M. Karagoz Unel. Parallel computing studies for the alignment of the ATLAS Silicon tracker. In *CHEP*, 2006.

[109] C. C. Paige and M. A. Saunders. Solution of sparse indefinite systems of linear equations. *SIAM Journal of Numerical Analysis*, 12:617–629, 1975. http://www.stanford.edu/group/SOL/software/minres.html.

[110] The Numerical Algorithms Group Limited. *NAG Fortran Library Manual, Mark 21*, 2006.

[111] N.I.M. Gould, J.A. Scott, and Hu Y. A numerical evaluation of sparse direct solvers for the solution of large sparse symmetric linear systems of equations. *ACM Transactions on Mathematical Software*, 33(2):1–32, 2007.

[112] I. Duff. Ma57 – a new code for the solution of sparse symmetric definite and indefinite systems. *ACM Trans. Mathematical Software*, 30(2):118–154, 2004.

[113] O. Schenk and Gärtner K. On fast factorization pivoting methods for symmetric indefinite systems. *Elec. Trans. Numer. Anal.*, 23:158–179, 2006.

[114] O. Schenk and Gärtner K. Solving unsymmetric sparse systems of linear equations with PARDISO. *Journal of Future Generation Computer Systems*, 20(3): 475–487, 2004.

[115] I. Duff and J.K. Ried. Ma27 – a set of fortran subroutines for solving sparse symmetric sets of linear equations. Technical Report AERE R-10533, 1982.

[116] D.C. Sorensen. Implicitly restarted arnoldi/lanczos methods for large scale eigenvalue calculations. Technical report, Rice University, 1995.

[117] ATLAS Collaboration. ATLAS Inner Detector: Technical Design Report, volume 1. Technical report, CERN, 1997. CERN-LHCC-97-016.

[118] S. Snow and A. Weidberg. The effect of inner detector misalignments on track reconstruction. Technical report, CERN, 1997. ATL-INDET-97-160.

[119] S. Correard *et al.*. b-tagging with dc1 data. Technical Report ATL-COM-PHYS-2003-049, CERN, 2003.

[120] E. Bouhova-Thacker *et al.*. Studies into the impact of inner detector misalignments on physics. Technical Report ATL-PHYS-PUB-2009-080. ATL-COM-PHYS-2009-281, CERN, 2009.

[121] E. Bouhova-Thacker *et al.*. Impact of inner detector and muon spectrometer misalignments on physics. Technical report, CERN, 2009. ATL-COM-GEN-2009-022.

[122] ATLAS Collaboration. Misalignment and b-tagging. Technical report, CERN, 2009. ATL-PHYS-PUB-2009-020.

[123] A. Ahmad, D. Froidevaux, S. González-Sevilla, G. Gorfine and H. Sandaker. Inner detector as-built detector description validation for CSC. Technical report, CERN, 2007. ATL-INDET-INT-2007-002.

[124] http://gridui03.usatlas.bnl.gov:25880/server/pandamon/query?mode=showtask0&reqid=64

[125] https://twiki.cern.ch/twiki/bin/view/Atlas/SiliconMisaCSC.

[126] W. Lampl, S. Laplace, D. Lelas, P. Loch, H. Ma, S. Menke, S. Rajagopalan, D. Rousseau, S. Snyder, and G. Unal. Calorimeter clustering algorithms: Description and performance. Technical Report ATL-LARG-PUB-2008-002. ATL-COM-LARG-2008-003, CERN, Geneva, Apr 2008.

[127] A. Salzburger. The atlas track extrapolation package. Technical Report ATL-SOFT-PUB-2007-005. ATL-COM-SOFT-2007-010, CERN, Geneva, Jun 2007.

[128] J.R. Dormand and P.J. Prince. A family of embedded runge-kutta formulae. *Journal of Computational and Applied Mathematics*, 6:19–26, March 1980.

[129] H. Bethe and W. Heitler. On the stopping of fast particles and on the creation of positive electrons. *Proceedings of the Royal Society of London. Series A.*, 146: 83 – 112, 1934.

[130] B. Rossi and K. Greisen. Cosmic-Ray Theory. *Rev. Mod. Phys.*, 13:240–309, 1941.

[131] V. Highland. Some Practical Remarks on Multiple Scattering. *Nucl. Instrum. Meth.*, 129:497 – 499, 1975.

[132] R. Frühwirth, A. Strandlie, and W. Waltenberger. Helix fitting by an extended riemann fit. *Nuclear Instruments and Methods in Physics Research Section A: Accelerators, Spectrometers, Detectors and Associated Equipment*, 490(1-2):366–378, September 2002. ISSN 0168-9002.

[133] CERN. *CERN Computing and Data-processing School*. Geneva, 1972.

[134] F. James and M. Roos. Minuit-a system for function minimization and analysis of the parameter errors and correlations. *Comput. Phys. Commun.*, 10(6):343–67, 1975.

[135] V.S. Kurbatov and I.N. Silin. New method for minimizing regular functions with constraints on parameter region. *Nuclear Instruments and Methods in Physics Research Section A: Accelerators, Spectrometers, Detectors and Associated Equipment*, 345(2):346–350, June 1994. ISSN 0168-9002.